Graphene: Synthesis, Characterization, Properties and Functional Behavior as Catalyst Support and Gas Sensor

TECHNISCHE UNIVERSITÄT DARMSTADT

Vom Fachbereich Chemie
der Technischen Universität Darmstadt

zur Erlangung des akademischen Grades eines

Doctor rerum naturalium (Dr. rer. nat.)

genehmigte

Dissertation

vorgelegt von

MSc. Emine Kayhan
aus Cankiri, Turkei

Referent: Prof. Dr. Jörg J. Schneider
Korreferent: Prof. Dr. Gerd Buntkowsky

Tag der Einreichung: 03. Juni 2013
Tag der mündlichen Prüfung: 12. Juli 2013

Darmstadt 2013
D17

To My Daughter Ikra Asya scented paradise, my eternal love Mehmet and My Parents Elif & Adil

ACKNOWLEDGEMENTS

I would like to extend my gratitude to Prof. Dr. Jörg J. Schneider for his encouragement, supervision, and patience throughout my studies with his immense knowledge. This thesis would not have been possible without his support, great patience and invaluable feedback.

I am grateful to Prof. Dr. Barbara Albert for her invaluable help, time and support during that exciting and stressful process. I express my thanks to my co-examiner Prof. Gerd Buntkowsky for his valuable time for me.

I reserve my special thanks to Prof. Hess for letting me use Raman in his group, Dr. Ravi Mohan Prasad for gas sensor measurements, MSc. Mehmet Kayhan for XRD measurements, Dr. Emanuel Ionescu, Thorsten Heinlein, Sandeep Yadav for Raman measurements, Dr. Jörg Engstler for TEM analysis, Dr. Rudolf Hoffmann for TGA analysis, Ildiko Balog for oximato precursors, Julia Patzsch for BET analysis and Silvio Heinschke for diffuse reflectance measurements. I would like to also thank Dr. Oktay Yılmazoglu and Dr. Önder Metin for collaboration work.

I would like to thank all of my colleges from inorganic chemistry department especially to Jetmire Mersini, Julia Patzsch, Sandeep Yadav, Ildiko Balog and XiaoXiao for their friendship, help and support not only at the university but also in my personal life as well.

I am grateful to my friends in particularly in Turkey, Germany and America and many families in particular family Özçelik, Dogan, Ciyanoglu and Bayram that have become our family here. Many thanks to our landlords Mrs. and Mr. Bernhard for their friendly attitude during our stay in Darmstadt.

And last but not least, I want to thank my daughter Ikra Asya Kayhan. It was not possible to write this thesis without looking into her lovely blue eyes, hugging her and inhaling her paradise smell. Words cannot express how much I am grateful to Mehmet Kayhan who is my best friend, college, beloved love and husband for his endless support and love. I am so fortunate having such a self-sacrificing parents; Elif and Adil; sister Ayyüce and brothers Ertugrul and Ali Kutalmıs, my grandparents Emine and Ali and mother- and father- and sister-in law Seviye, Yakup and Hatice that continuously support and help me through my life.

Abstract:

Graphene has attracted intense scientific interest due to its exceptional electrical, mechanical and chemical properties over the last couple of years. This strictly two-dimensional (2D) material has potential applications in advanced electronic devices and composite materials. The challenge is to produce large area defect-free graphene necessary for electronic applications while bulk-production at gram scale of graphene with defects enabling anchoring sites for nanoparticles is required for applications like catalysis. Herein, we report the Ni-catalyzed ambient pressure chemical vapor deposition of (APCVD) synthesis of few-layer graphene, the spatial characterization of the few-layered transparent graphene by micro Raman spectroscopy, its electrical characterization showing p-semiconductor behavior, as well as studies on the gas-sensing properties towards low concentrations of CO and H_2. Moreover, APCVD and low pressure CVD (LPCVD) growth of graphene have been carried on Cu-catalyst surfaces. Effect of metal catalyst thickness and CVD growth parameters (concentrations of the gases, growth time, cooling effect etc.) were studied in detail to optimize the quality of graphene with respect to the number of layers and defects. Chemical synthesis of graphene was established by oxidation of graphite to graphite oxide (GO) and followed by reduction process. Different methods (Staudenmaier's, Hummers', Modified Hummers' and Tour's Methods) to synthesize GO were studied comparatively to have highly oxidized GO. Various reduction techniques were studied to improve the quality of chemically derived graphene (CDG). Metal nanoparticles (NPs of Au, Ni and Pd) were successfully supported on CDG and employment of Pd/CDG as catalysts in the dehydrogenation and hydrolysis of ammonia borane (AB). Moreover, metal oxide NPs of titanium dioxide (by UV-assisted method and hydrothermal method), tungsten oxide (by sonochemical method) and zinc oxide (via thermal decomposition method), were successfully deposited on CDG. Composites of CDG with TiO_2 and WO_3 were applied successfully in photodegradation reactions of methylene blue (MB) under UV-light. Sensing measurements of ZnO/CDG hybrid materials were conducted towards hydrogen gas at room temperature and elevated temperatures (200^{o}C and 300^{o}C).

Zusammenfassung:

Graphen steht seit mehreren Jahren im Mittelpunkt des wissenschaftlichen Interesses, dies aufgrund seiner außergewöhnlichen elektrischen, mechanischen und chemischen Eigenschaften. Dieses zwei-dimensionale (2D) Material besitzt potenzielle Anwendungsmöglichkeiten in einer Vielzahl von elektronischen Bauteilen sowie als Kompositmaterial. Die besondere Herausforderung besteht darin große Stücke von defektfreiem Graphen herzustellen, welche für den Einsatz in der Elektronik benötigt werden. Ein weiterer Anwendungsaspekt liegt in der in der Herstellung von nicht defektfreiem Graphen im Grammmaßstab, wobei diese Defektstellen als Verankerungsstellen für Nanopartikel dienen können und so für den Einsatz als Komposit beispielsweise in der Katalyse geeignet sind. In der vorliegenden Arbeit wird zunächst auf die Synthese von Graphen mit einer geringen Zahl an Lagen mittels Nickel katalysierter Gasphasendeposition unter Raumdruck (APCVD) eingegangen, danach auf die Charakterisierung des erzeugten Graphens, mittels Micro-Ramanspektroskopie sowie weiterhin auf die elektrischen p-leitenden Eigenschaften dieses Materials eingegangen. Zusätzlich wurde das gassensorische Verhalten bezüglich geringer Konzentrationen von CO und H_2 untersucht sowie das Wachstum von Graphen mittels Gasphasenabscheidung (APCVD und LPCVD) auf Kupferkatalysatoroberflächen untersucht. Der Einfluss der Katalysatorabscheidung und der CVD Wachstumsparameter, wie z.B. Gaskonzentration, Wachstumszeit und Abkühlungzeit wurden intensiv studiert um die Qualität des erzeugten Graphens in Hinblick auf die Zahl der Graphenlagen und -defekte zu optimieren. Desweiteren wurde die nasschemische Synthese von Graphen durch Oxidation von Graphit zu Graphitoxid (GO) und anschließender Reduktion untersucht. Verschiedene Methoden (nach Staudenmaier, Hummers, modifizierte Hummers und Tour Methoden) wurden vergleichend untersucht. Ebenso wurden verschiedene Reduktionstechniken studiert, um die Qualität des chemisch erzeugten Graphens (CDG) zu steigern. Gold-, Nickel- und Palladium-Nanopartikel konnten erfolgreich auf die Oberfläche des CDG aufgebracht werden. Das so erhaltene Pd/CDV Komposit konnte als wirksamer Katalysator in der Dehydrierung und Hydrolyse von Amminboran getestet werden. Darüber hinaus wurden Nanopartikel aus Titandioxid mittels UV-Deposition und Hydrothermalmethode, Wolframoxid mittels Ultraschall und Zinkoxid mittels thermischer Zersetzung erzeugt. Die TiO_2 und WO_3 basierten CDG Materialien zeigten sich katalytisch aktiv für den Photoabbau von Methylenblau (MB) unter UV-Bedingungen. Gassensorische Messungen an den ZnO/CDG Hybridmaterialien zeigten eine Sensoraktivität gegenüber Wasserstoff bei Raumtemperatur sowie erhöhten Temperaturen (200°C und 300°C).

Results from this work already published in peer reviewed journals

1. "Palladium nanoparticles supported on chemically derived graphene: An efficient and reusable catalyst for the dehydrogenation of ammonia borane"
   Metin Ö.*[1], Kayhan E.[1], Özkar S., Schneider J. J ([1]contributed equally) *Int. J. Hydrogen Energ. 2012, 37 (10) 8161*
2. "Synthesis, Characterization, Electronic and Gas Sensing Properties towards H_2 and CO of Transparent, Large Area, Low Layer Graphene"
   Kayhan E., Prasad R. M., Gurlo A., Yilmazoglu O., Engstler J., Ionescu E., Yoon S., Weidenkaff A., Schneider J. J.* *Chem. Eur. J.*, (**2012**), *18 (47)*, 14996-15003

Conference presentations

April 10-13, 2012 Graphene 2012 (poster presentation with the title of "Graphene as gas-sensor and catalyst support: Fabrication, Characterization and Application")
August 31-September 2, 2011 German French Workshop on Nanoscience in Landau, Germany (oral presentation with the title "Fabrication and Characterization of Large Scale Continuous, Highly Transparent Graphene Films by Chemical Vapor Deposition")
September 13-19, 2010 6th EFCATS Summer School "Catalysis and Surface Sciences for Renewables & Energy" İzmir, Turkey (oral presentation with the title of "Adventures into Flatland. Fabrication and Characterization of Large Scale Continuous, Highly Transparent Graphene Films by Chemical Vapor Deposition")

1. Introduction

1.1. Background and Discovery of Graphene

Graphite of which the term was derived from the Greek word “graphein” (to write) in, is a layered planar structure composed of carbon atoms that are arranged in a honeycomb lattice. The separation between carbon atoms in the lattice is 0.142 nm, and the distance between planes is 0.335 nm in graphite structure. In graphite, isolated single layer that is composed of sp^2 hybridized carbon atoms is called graphene. The term of graphene originates from the combination of graphite and suffix –ene that is earlier used in the nomenclature and terminology of polycyclic aromatic hydrocarbons[1]. The possibility of wrapping up graphene into 0D fullerenes, rolling it into 1D carbon nanotubes (CNTs) and stacking of it into 3D graphite makes graphene the central building block of all graphitic materials (see Figure 1)[2].

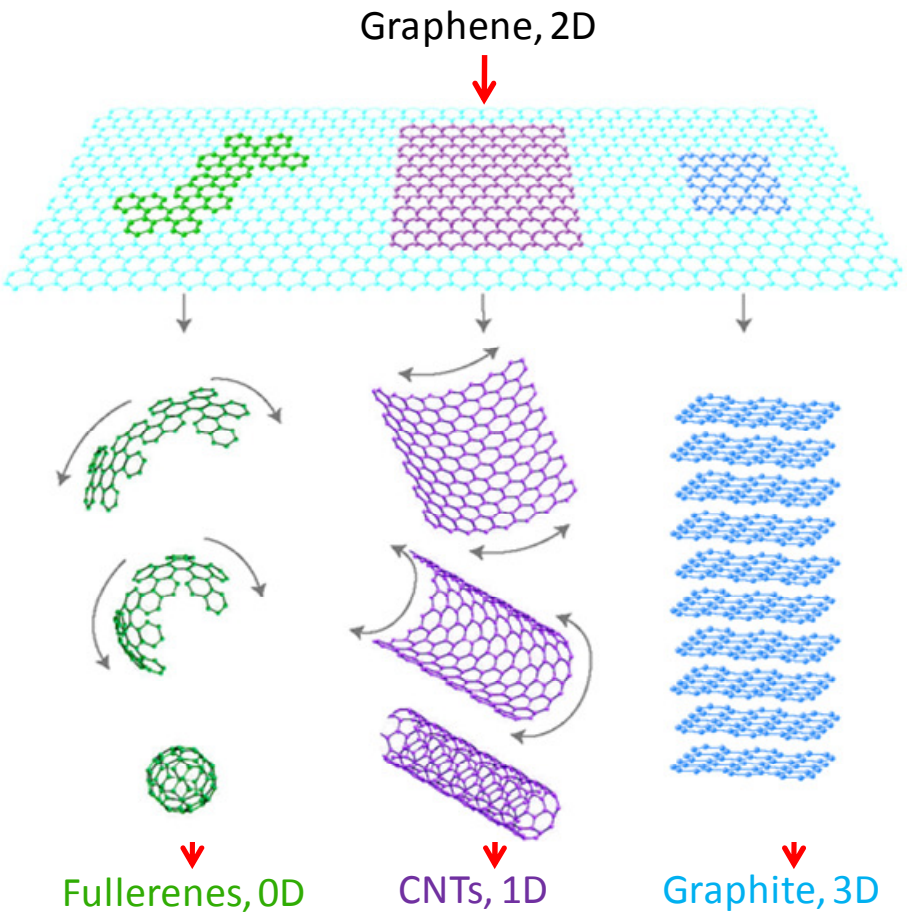

Figure 1: Carbon materials as fullerenes, carbon nanotubes (CNTs) and graphite (0D, 1D and 3D respectively) can be derived from single layer graphene (2D) [2]

Despite the discovery of fullerenes in 1985 by Kroto, Curl, and Smalley[3] and shortly thereafter of CNTs in 1991 by Iijima[4], graphene had already been studied theoretically for the first time in 1947 by P.R.Wallace[5], later in 1956 by J.W. McClure[6] and in 1984 by G.W. Semenoff[7]. The isolation of graphene was thought to be not possible thermodynamically according to Peierls[8], Landau, and later Mermin[9] reporting that a 2D lattice melts due to thermal fluctuations and long range crystalline order is prevented. However, A.K. Geim and K. Novoselov in 2004 isolated the graphene by adhesive Scotch tape and characterized it successfully [10]. They used mechanical exfoliation method to produce single graphene sheet from graphite. Then, graphene was transferred onto silicon dioxide substrate, characterized by optical microscopy and AFM as well as electrical measurements were conducted for it. These two Russian scientists both from Manchester University were awarded the 2010 Nobel Prize in Physics for these "groundbreaking experiments regarding the two-dimensional material graphene". However, it should be noted that graphene like structures (graphite intercalation compounds GICs, graphite oxide GO and reduced graphene oxide rGO) have been already known since 1840s by German scientist Schafhaeutl who reported the insertion of acid or alkali metal between the carbon lamellae (intercalation) and exfoliation of graphite with sulfuric and nitric acids [11]. After Schafhaeutl, Brodie (in 1859)[12], Staudenmaier (in 1898)[13] and Hummers (in 1958)[14] also produced GO by exfoliating the graphite via high oxidizing reagents. In 1962, Boehm (he originally coined the term "graphene" in 1986) and coworkers for the first time reported thin, lamellar carbon containing small amount of hydrogen and oxygen via chemical reduction of dispersions of GO in dilute alkaline media with hydrazine, hydrogen sulfide, or iron(II) salts. Just after this report, thermal reduction of GO was also published by the same group in 1962[15]. Boehm et al. made an assumption that thinnest lamella consisted of a single carbon layer and tried to prove that the thinnest lamella by transmission electron microscopy (TEM) micrograph densitometry measurements. Experimental error due to the thickness calibration standards, however prevented the exact identification of monolayer carbon at that time [15]. It is worth to note that graphene (reduced graphene oxide rGO or chemically derived graphene CDG) not pristine graphene (without heteroatomic contamination) was for the first time described by H. P. Boehm and coworkers.

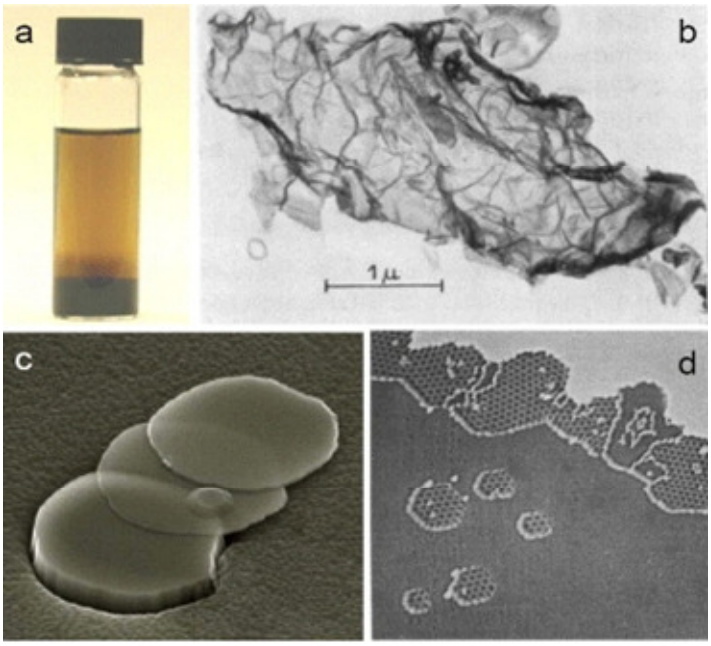

Figure 2: (a) graphite oxide suspension in water (b) TEM image of ultra-thin graphitic flakes from the early 1960s (c) SEM image of thin graphite platelets by mechanical cleavage (d) STM of graphene grown on Pt (image size is 100×100 nm^2) [16].

Besides RGO sample synthesized by Boehm, ultrathin graphitic films and even monolayer pristine graphene was grown epitaxially on metal substrates (Ru, Rh and Ni in 1970) [17], on insulating carbides (SiC in 1975 and TiC, TaC in 1993) [18] and on graphite in 2001 [19] (see Figure 2 d).

Not only the production of pristine graphene was known by epitaxial growth in pre-2004 graphene research, paper from the Kurz's group had shown that a tape method (mechanical exfoliation) to get ultra-thin graphite films had been already used in 1990 [20]. After peeling optically thin layers of graphite from highly ordered pyrolytic graphite (HOPG) with transparent tape, carrier dynamics of the sample was studied as well. Then after, visualization of few-nm thick graphite was reported in 1995 using atomic force microscopy (AFM) on top of HOPG [21] and using a scanning electron microscope (SEM) in 1999 [22] (Figure 2 c).

Besides production and visualization of ultra-thin graphite samples, electrical properties were also analyzed for the samples with thickness down to 60 layers in 1997-2001 [23].

Graphene monolayers for their cleavage on top of HOPG in 2003 [24] by STM and ultrathin epitaxial growth of graphite films composed of typically 3 graphene sheets from SiC in 2004 were reported by W. A. de Heer and coworkers [25].

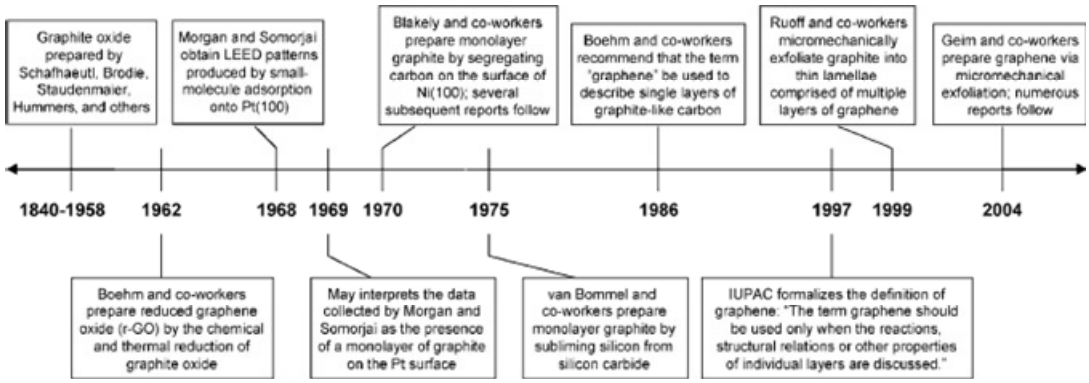

Figure 3: Timeline of graphene showing attempts for preparation, isolation, and characterization [26].

Geim declared his awareness of such earlier reports on the ultra-thin graphitic films and even the monolayers of graphene production, visualization and measurements (Figure 3). However, he finds all the previous reports as observational with the lack of reporting distinguishing properties of graphene [16]. He explains further that not only the ease of method (Scotch tape) that they have used to produce graphene, but also the isolation, identification, characterization and electronic measurements showing the astonishing electronic quality of graphene took researchers by surprise. Therefore their work did not disappear into oblivion to previous literature.

1.2. Properties of Graphene

Graphene is composed of sp^2 hybridized carbon atoms arranged in a 2D honeycomb crystal lattice. Three valence electrons of carbon atoms in graphene form bonds (σ) with their next neighbours while the fourth electron of each carbon atom localized in the p_z (π) orbitals perpendicular to the planar sheet form highly delocalized bonds (π) with the others. Graphene is a zero band gap semiconductor and charge carriers in graphene have very small effective mass so that carrier mobilities are as high as up to 200000 $cm^2V^{-1}s^{-1}$ at a carrier density of 10^{12} cm^{-2} [27]. Electrons can flow through graphene more easily than even through copper. Edges of graphene are called as an armchair or a zig-zag edge due to the individual lattice arrangement on the atomic scale (see Figure 4a).

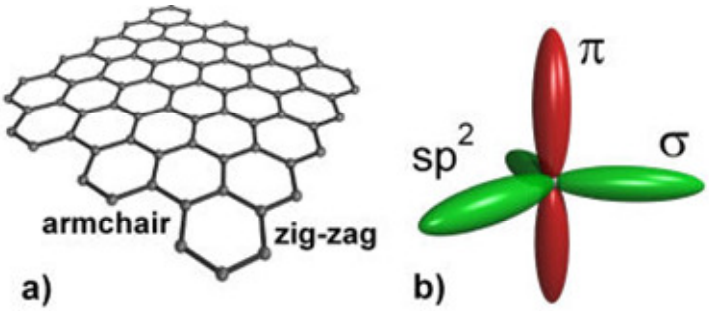

Figure 4: a) armchair and zig-zag edges in graphene b) sp^2 hybridization illustrated in graphene c) Band diagram of graphene at k = 0 [28]

The opacity of a single layer graphene is 2.3 % so its optical transparency is 97.7 % observed in the visible range decreases linearly as the number of layers increases (Figure 5). Graphene, however, becomes visible when it is transferred onto a silicon wafer with a silicon dioxide layer (usually 300 nm). Therefore, detection of the number of graphene layers is possible via the color shifts due to the thickness variations on the silicon wafer [29].

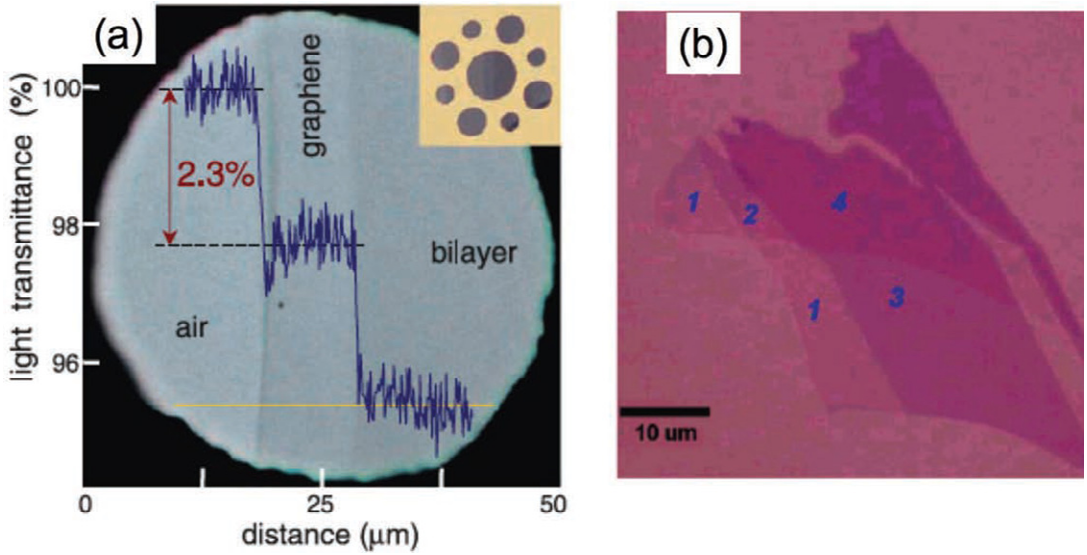

Figure 5: (a) Photograph of a 50- μm aperture that is partially covered by graphene and a graphene bi-layer structure. The line scan profile shows the intensity of transmitted white light along the yellow line. Inset shows the sample design (b) Optical image of graphene flakes with one, two, three, and four layers on a 285-nm thick SiO_2 -on-Si substrate [30]

The mechanical properties of graphene have been investigated by numerical simulations and experimental measurements using Atomic Force Microscopy (AFM) [31]. Graphene is

found to be one of the strongest materials with a mechanical strength higher than diamond and over 300 times greater than a steel film of the same thickness [31b]. Reported values for defect-free graphene are Young's modulus of 1.0 TPa and a fracture strength of 130 GPa that are higher than CNTs [31]. Graphene is flexible and stretchable up to 20% of its initial length. Besides those outstanding properties, graphene has a thermal conductance (>5000 W/m K) [32] that is also higher than all the other carbon structures and theoretical surface area of 2600 m^2/g [33].

Adsorption and desorption of gases such as hydrogen and carbon monoxide is possible on graphene surface like on graphite [34]. Besides forming weak adsorbate on graphene surface, graphite can be also oxidized to graphene oxide (GO) that is the functionalized form graphene with functional groups like epoxy and carboxyl [35]. Further chemical or thermal reduction of so called graphene oxide yields chemically derived graphene (CDG or reduced graphene oxide; rGO) [33].

1.3. Potential Applications of Graphene

Application oriented attractive properties of graphene such as its high carrier mobilities which are 40 times higher than the typical electron mobility for Si and its high current carrying capability makes graphene relevant to be used in electronic devices. Moreover, owing the huge thermal conductivity that is important for electronic devices shrinking as circuit density increases, graphene keeps the devices cool by dissipating heat efficiently. However, large-scale growth of graphene is necessary and crucial to exploit those properties of graphene further. Figure 6 shows the state-of-the art evolution of the size of synthesized graphene from μm to inch levels. After isolation of only μm size monolayer graphene for the first time by Geim and Novoselov [10], 30 inch size of single layer graphene was produced by chemical vapor deposition (CVD) method. The largest monolayer graphene reported so far is in 24" by 300" size grown on copper with CVD technique. Graphene was used in touch panels [36] by utilizing its high transparency, flexibility and high conductivity.

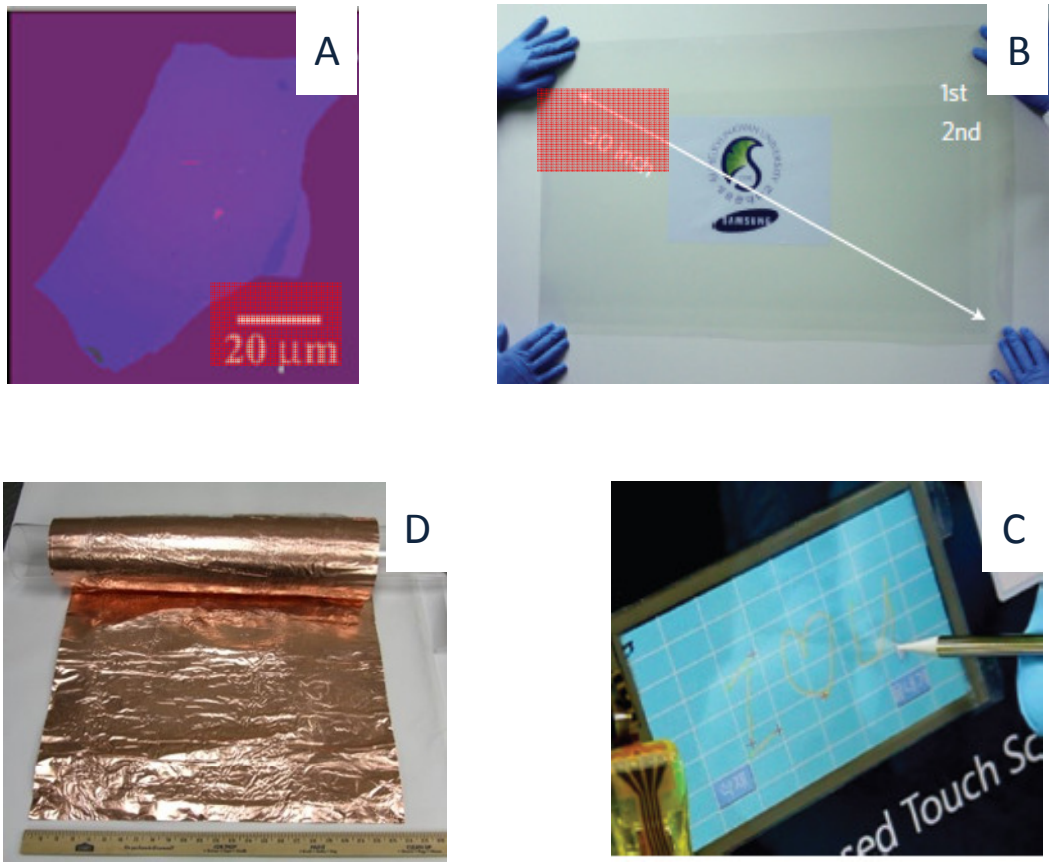

Figure 6: A. Optical microscope image of isolated single layer graphene with µm size for the first time by Geim and Novoselov [10]. Photographs of; B. 30-inch size graphene produced by CVD process, C. First 30-inch flexible touch screen from graphene [36] and D. The largest monolayer graphene produced on copper reported so far (24'' by 300'') by Bluestone Globa; Tech (USA) in February 2013.

Not only for electronics, graphene is one of the most promising material for gas-sensors as well. As gas molecules land on graphene, its electronic properties are affected in a measurable way that enables the detection of a gas [37].

Graphene also finds potential applications as support material in catalysis field due to its huge surface area [38], as an electrode material in electrochemical applications such as batteries and supercapacitors. Layered nature of graphene acts as a barrier against aggregation of nanoparticles in the catalyst or electrode material. The use of chemically derived graphene (or reduced graphene oxide (CDG or RGO)) based materials as anode or cathode in Li-ion battery technology promotes the improvement in the recent field due to the large surface-to-volume ratio and highly conductive nature of graphene. The formation of nanopores and disorders in the CDG through chemical synthesis promotes as lithium insertion active sites that are crucial in Li battery technology. So the process

fastens in the presence of graphene in the electrode (Figure 7, A). In addition, both anode and cathode of a battery might become bendable due to the flexibility feature of graphene (Figure 7, B).

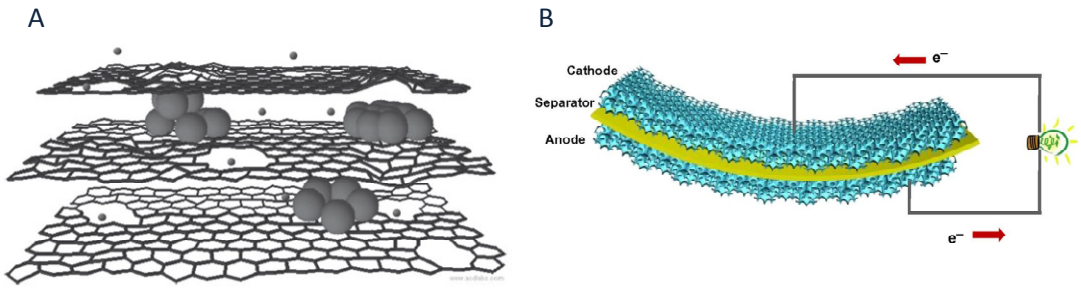

Figure 7: Examples of CDG graphene-based electrodes in Li-ion battery. A. Si/Graphene as an anode [39] B. Flexible $Li_4Ti_5O_{12}$ /Graphene Anode and $LiFePO_4$ /Graphene Cathode [40]

1.4. Synthesis of Graphene

There are currently four main approaches to synthesize graphene. These are mechanical exfoliation, liquid phase exfoliation of graphite, epitaxial growth and chemical synthesis methods.

1.4.1. Mechanical Exfoliation of Graphite (Scotch-tape method)

This simple tape method was reported for the first time by Heinrich Kurz et al. in 1990 to get ultra-thin films of graphite from HOPG [20] that refers to graphite with an angular spread between the graphite sheets of less than 1°. However, Novoselov and Geim succeeded to produce and identify monolayer graphene by using that method in 2004 [10]. That method starts with sticking HOPG onto adhesive tape and folding the two sticky sides against the tiny crystals (Figure 8). After pulling the tape apart, flakes are cleaved in two individual flakes. By repeating that splitting process a couple of times, thinner slices can be achieved. Finally, tape with the pieces is stuck on the silicon wafer with silicon dioxide layer on and tape is pulled away. At the end, one can see graphene by naked eye due to the optical contrast differences.

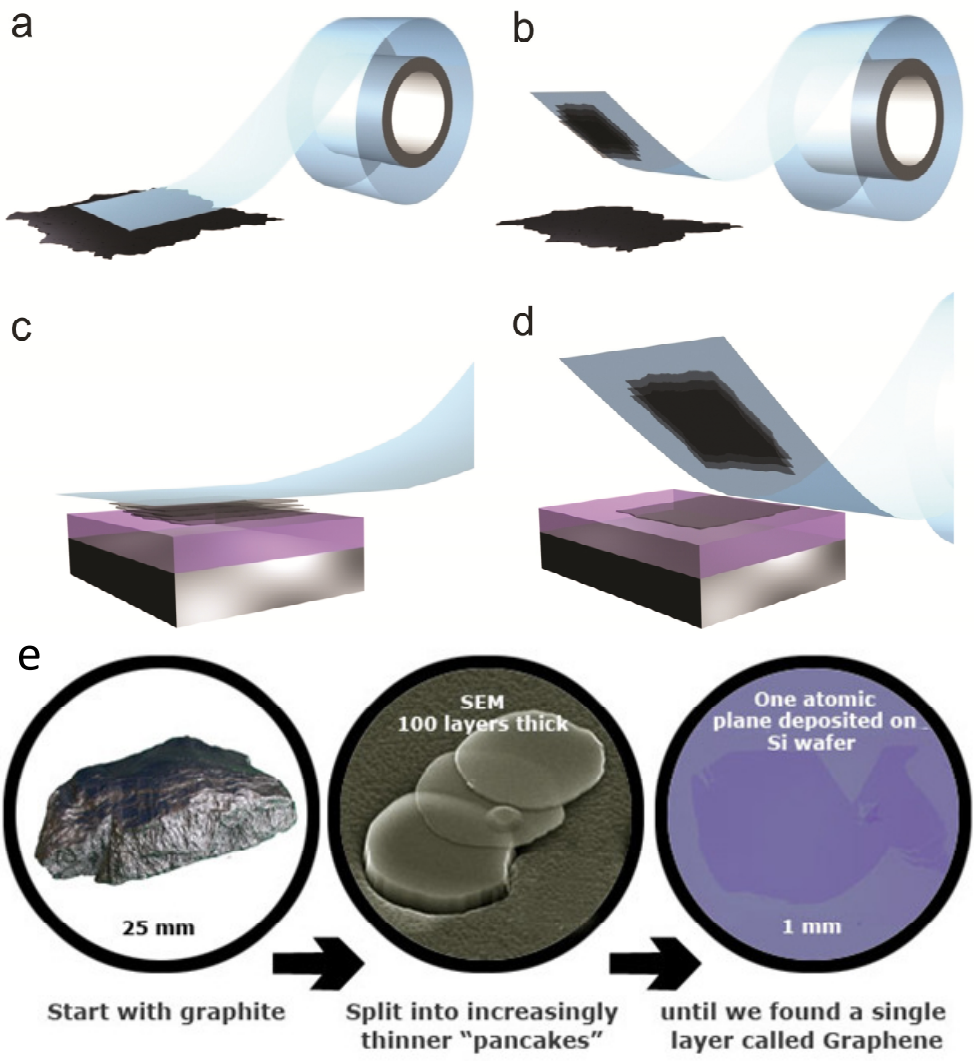

Figure 8: Step by step formation of graphene via Scotch-tape method (a to d) and overview of the process using this method (e) [41]

Despite the ease of the method, it is not likely to produce large quantities. Using this technique, however, Chen J. et al has recently reported a study called "Continuous mechanical exfoliation of graphene sheets via three-roll mill" suggesting a scale up process for effective fabrication of polymer/graphene (single to few layers) nanocomposites [42].

1.4.2. Liquid Phase Exfoliation of Graphite

Hernandez and coworkers [43] carried out the dispersion of graphite typically in N-methylpyrrolidone (NMP) followed by ultrasonication to separate the non-exfoliated

graphite. Graphene dispersions with concentrations up to ~0.01 mg ml^{-1} were achieved. The reason for production of graphene flakes is attributed to the solvent-graphene interaction. The energy necessary for exfoliation is balanced by that interaction for solvents if surface energies match that of graphene [43]. Furthermore, Mariani et al. improved the concentration of graphene in NMP (2.1 mg/ml) by exfoliating polymer-graphite composite [44] and further enhanced it (5.33 mg/ml) by exfoliating the graphite in ionic liquids [45]. Although this technique has the advantage of low cost and scalability, graphene flakes tend to restack and scroll easily.

1.4.3. Epitaxial Growth

1.4.3.1. Epitaxial Growth from SiC

Walt de Heer and coworkers from Georgia Institute of Technology initiated the graphene growth by epitaxial growth method from silicon carbide (SiC) substrates [25]. This method involves thermal desorption of silicon at high temperatures (>1250 °C) and low pressures ($\sim 10^{-6}$ Torr) that results in a formation of carbon-rich surfaces that subsequently graphitized as carbon islands (see Figure 9a). STM analysis showed that graphene with long-range order and a low density of defects was successfully grown epitaxially from SiC (see Figure 9b).

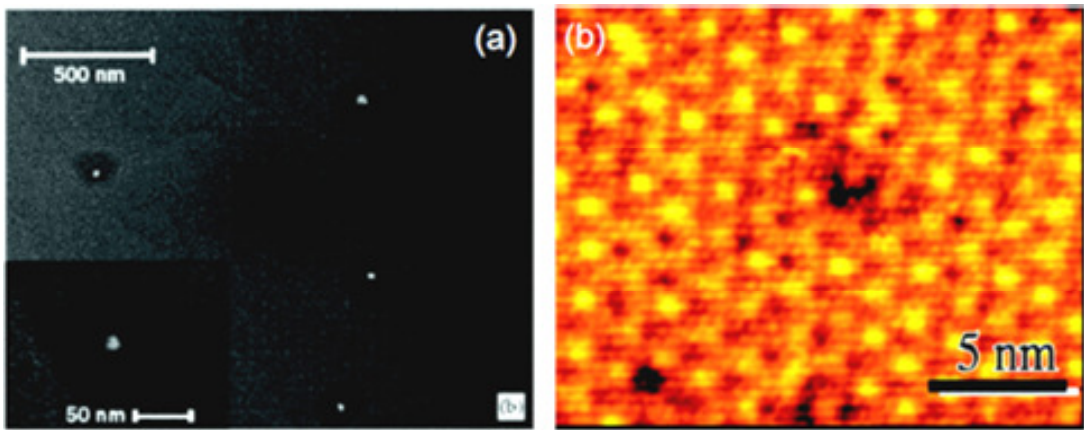

Figure 9: a) SEM image shows small hexagonal crystallites after epitaxial growth process on SiC substrate (b) STM image of epitaxial graphene with long-range order and a low density of defects [46].

Moreover, the method has been recently optimized to give mono- to few layer graphene [47]. Epitaxial growth of graphene from SiC has been achieved on predetermined locations that enable making electronic devices using graphene.

This process is more controllable and scalable than exfoliation method but it is too expensive due to the high cost of SiC substrate and the necessity of high processing temperatures. Moreover, compared to graphene via exfoliation method, more fragile and defective graphene tends to be formed due to the large lattice mismatch between SiC and graphene during epitaxial method.

1.4.3.2. Epitaxial Growth on transition metals or transition metal deposited substrates

Epitaxial growth of thin graphitic films on metal substrates such as Ru, Rh by Grant in 1970 and Ni by Blakely *et al* in 1970 has been already known for nearly half century [17]. After explosion of the interest in graphene by 2004, this method was extensively studied again to get controllable deposition of graphene. Chemical vapor deposition (CVD) of hydrocarbons at elevated temperatures is catalyzed by metal and indeed results in the growth of graphene. Carbon isotope labeling experiments clarify that the mechanism of graphene formation is dependent on carbon solubility of metal and CVD growth conditions [48]. Graphene is formed via adsorption on a metal surface of Cu in which carbon solubility is too low (0.008 wt% C at 1084^{o}C) during CVD process. On the other hand, graphene is produced on Ni surfaces where the carbon solubility is higher (0.6 wt % C at 1326 ^{o}C). Graphene is formed during cooling step in the CVD process via surface segregation-precipitation of carbon from a metastable carbon–metal solid solution [49] (see Figure 10).

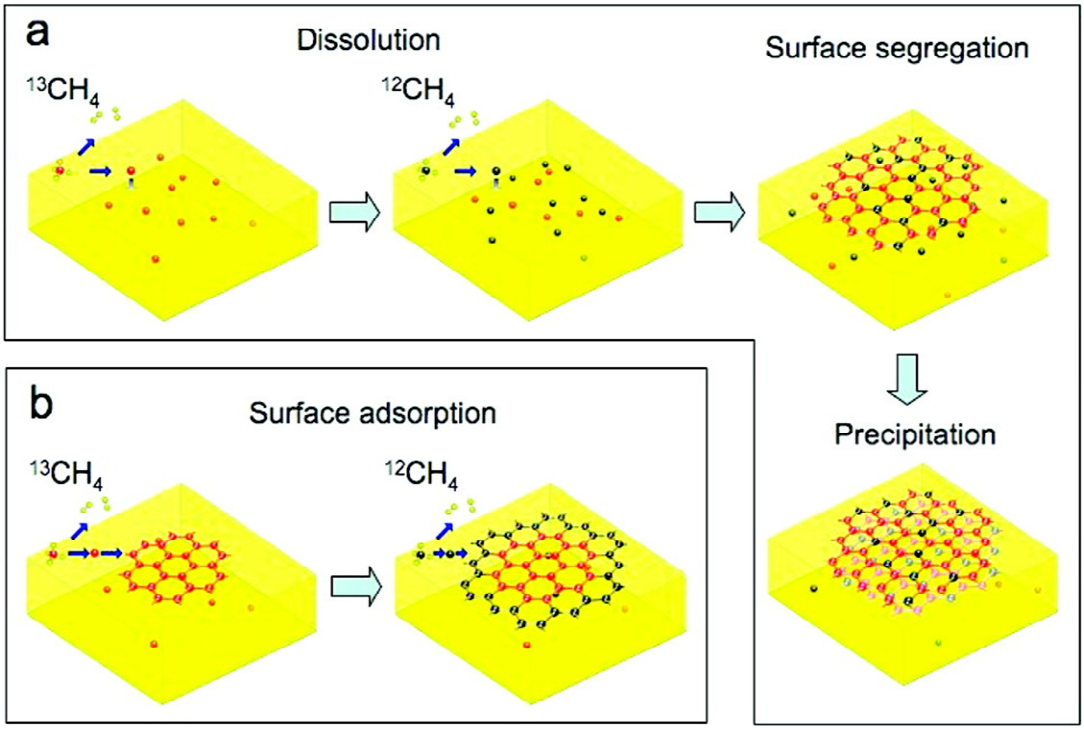

Figure 10: Diagrams showing carbon isotope labeling experiments on (a) Ni, Graphene with randomly mixed isotopes as a result of surface segregation and/or precipitation mechanism. (b) Cu, Graphene with separated isotopes by surface adsorption mechanism [48].

One of the important advantages of this method is that it can be extended to large area substrates (Figure 6D).

1.4.4. Chemical Synthesis

In common, the fabrication methods described so far are for the synthesis of graphene with less defective sites and low number of functional groups. For instance, defects are barriers for transport in electronics while defects can act as additional anchoring sites for nanoparticles to form graphene nanoparticle hybrid materials. Moreover, while continuous layers of graphene are required for transparent displays, graphene at a gram scale is needed e.g. for catalysis or battery applications. Chemical synthesis technique allows bulk production of (defective) graphene which cannot be achieved by the so far mentioned synthesis techniques. This method consists of oxidation and reduction steps. In a typical procedure, graphite is oxidized to graphite oxide (GO) by strongly oxidizing agents such as $KClO_3$, HNO_3, H_2SO_4, H_3PO_4 and $KMnO_4$. That oxidation step leads to extension of intersheet spacing of carbon layers due to the insertion of functional groups

on the layer. As the oxidation degree is higher, the probability to achieve high quality graphene also increases since graphene is formed by the reduction of oxidized graphite. Oxidation degree is improved from Brodie's to Staudenmaier's, Hummers', modified Hummers' and currently Tour's method. Tour's method yields GO with higher oxidation degree with the high intersheet spacing value of 9.5 Å (Table 1). For an overview of different synthesis procedures for chemically derived graphene formation, see Table 1.

Table 1: Methods for the synthesis of graphite oxide from graphite [50]

	Brodie	Staudenmaier	Hummers	Modified Hummers		Tour
Year	1859	1898	1958	1999	2004	2010
Oxidants	$KClO_3$,HNO_3	$KClO_3$ or $NaClO_3$ HNO_3,H_2SO_4	$NaNO_3$, $KMnO_4$,H_2SO_4	$K_2S_2O_8$, P_2O_5, $KMnO_4$,H_2SO_4	$NaNO_3$,$KMnO_4$,H_2SO_4	H_2SO_4,H_3PO_4 $KMnO_4$
C:O ratio	2.28	1.85	2.25	1.3	1.8	--
Reaction time	3-4 days	1-2 days	2-10 h	8 h	5 days	12 h
Intersheet spacing (Å)	5.95	6.23	6.67	6.9	8.3	9.5

GO attains hydrophilic character with the polar oxygen functional groups that makes GO easily dispersable in many solvents, particularly in water. Introducing oxygen functional groups to the GO structure weakens van der Waals cohesive forces, resulting in a partially degradation of the sp^2 lattice into a sp^2-sp^3-sheet with less π-π stacking ability (Figure 10B). Hence, GO becomes nonconducting due to the lack of the conducting graphitic network. Reduction of GO into CDG by chemically (e.g. via hydrazine hydrate) or thermally (e.g. via annealing at 1000°C under Ar flow) recovers the conducting graphitic network by elimination of functional groups through reduction process [33] (Figure 10).

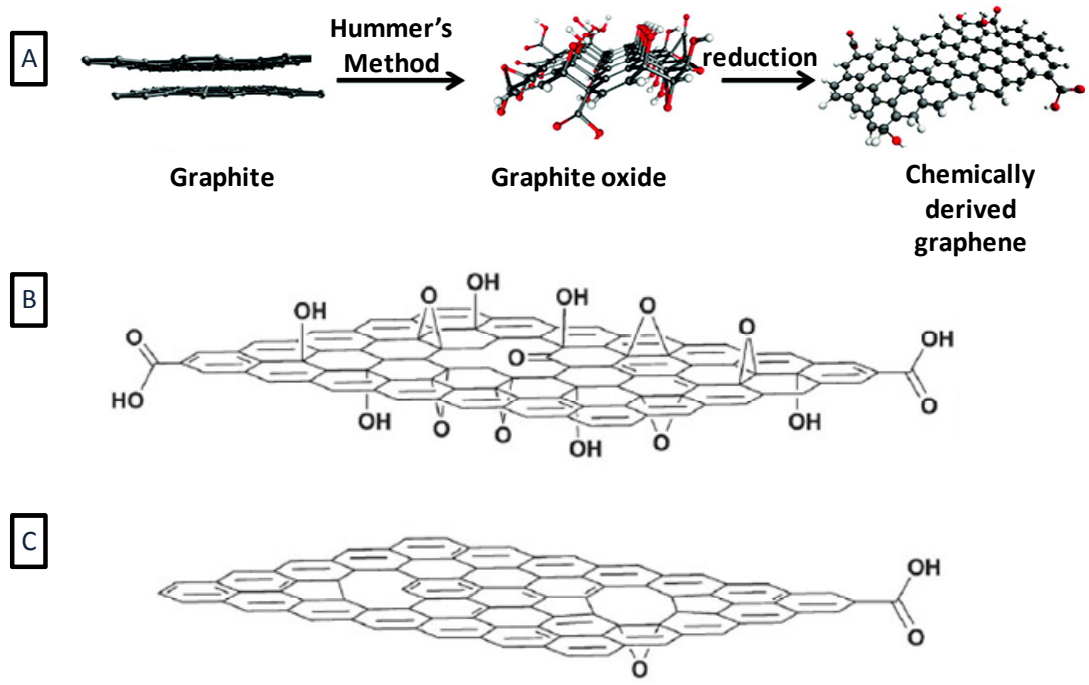

Figure 11: Molecular models showing A. Oxidation and reduction processes from graphite to chemically derived graphene (CDG) [51]. B. Graphite oxide (GO) and C. CDG [50]

In summary, several methods of formation of graphene, including micromechanical cleavage[10], chemical exfoliation[52], and epitaxial growth by chemical vapor deposition (CVD)[53], have been utilized to fabricate high-quality, large-area monolayer graphene on various substrates. The highest quality graphene in terms of its monolayered defect-free structure is obtained by mechanical cleavage of highly oriented pyrolytic graphite (HOPG)[10] and by decomposition of SiC[46]. However, both methods have drawbacks in scalability. Other methods, such as the combined chemical exfoliation and reduction technique, which allow scalability on the one hand, suffer of aggregation caused by strong π–π stacking and van der Waals aggregation of individual graphene sheets on the other hand and thus have the problem of obtaining few-layer graphene. However, when using high-quality metallic substrates with the high purity, such as Ir [54], Ru [55], Ni [53], or Cu [56] in a CVD process and employing a strict control of synthesis temperature and control of the cooling rate and substrate quality, the graphene layer aggregation can be avoided, and formation of graphene with controllable thicknesses down to a monolayer is possible.

Therefore it can be concluded that CVD technique is best to give large scale growth of pristine graphene suitable for electronic applications and chemical synthesis method is the method of choice that allows even a gram scale formation of graphene.

2. Chemical Vapor Deposition (CVD) of Graphene

Epitaxial growth of graphene via methane assisted CVD on transition metal (Ni and Cu foils) and transition metal deposited substrates (Ni or Cu/SiO_2/Si wafers) was conducted to obtain pristine graphene. Different procedures reported in the literature were used but they were modified to optimize the graphene growth via CVD. For instance, effect of thickness and pre-treatment of the metal catalyst and growth conditions (concentration and combinations of the gases, growth time, cooling rate etc.) are discussed in Section 2.1. Experimental Parameters. Besides, method to transfer as-grown graphene samples on a desired substrate and post-treatment of the samples to improve the quality of the sample are described. Samples were characterized qualitatively by means of Raman spectroscopy. Morphological analysis was performed by confocal optical microscopy, SEM-EDX, TEM and AFM techniques.

2.1. Experimental Parameters

2.1.1. Substrate

Two different types of wafers as Si and SiO_2/Si (600 nm thermally oxide layer on Si), quartz plates, 25μm thick Ni foil and 25μm thick Cu foils with different purity (99.8% and 99.999%) were used as a substrate for graphene synthesis. After deposition of nickel as a catalyst on the 1x1 cm^2 wafers and quartz piece, chemical vapor deposition of H_2/CH_4 mixture with various concentrations was performed. Figure 12 represent how the samples grown on Si and SiO_2/Si wafers appear after CVD. Figure 12 belongs to graphene synthesized on SiO_2/Si that there is rough coverage formed on the wafer whereas no visible change was seen for Si.

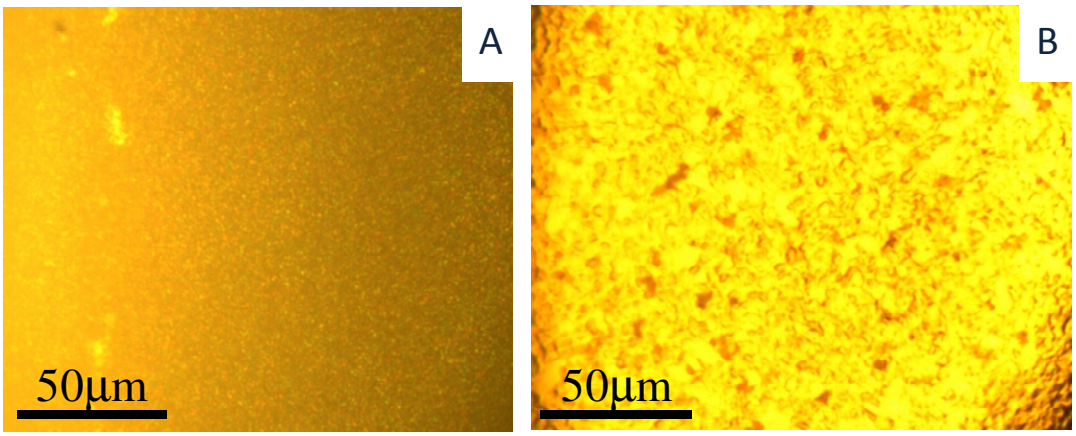

Figure 12: Confocal microscope images taken after the CVD growth (500/25 sccm (H_2/CH_4)) on Ni deposited substrates of A. Si wafer B. SiO_2/Si wafers

Raman spectroscopy is a versatile and precise technique to probe graphene quality, especially the number of layers[57] [58]. Thus, shape, position and relative intensities of D, G and 2D bands allow for estimating the quality of the graphene films [59] [60]. The D band [61] (~1350 cm^{-1}) is related to the breathing mode of the rings of sp^2 hybridized carbon and is activated by the presence of defects. Thus, the intensity of the D band does not relate to the number of layers, but is affected by the amount of disorder. The G band [62] (~1579 cm^{-1}) relates to the in-plane vibration of sp^2 C atoms in single-layer graphene and is located at slightly higher wavenumbers than in graphite (Figure 32 a). The 2D band [58] (~2716 cm^{-1}), which is the 2nd order zone boundary phonon signal of the D band, usually appears as a sharp and one-signal peak in single-layer graphene, with a full width at half maximum (Γ) of around 30 cm^{-1} [58]. The intensity ratio I_G/I_{2D} allows for estimating the numbers of layers in graphene-based materials. It is therefore most often used to discriminate single-layer from multi-layer graphene or graphite.

Therefore, to see whether the production of graphene was successful on the substrates, Raman spectra were recorded. As shown in Figure 13, characteristic signals of graphene (D, G and 2D) were not seen for Si and quartz case means that graphene was formed only on SiO_2/Si wafer. The reason might be attributed to the better adhesion of the catalyst layer on SiO_2 compared to Si and quartz.

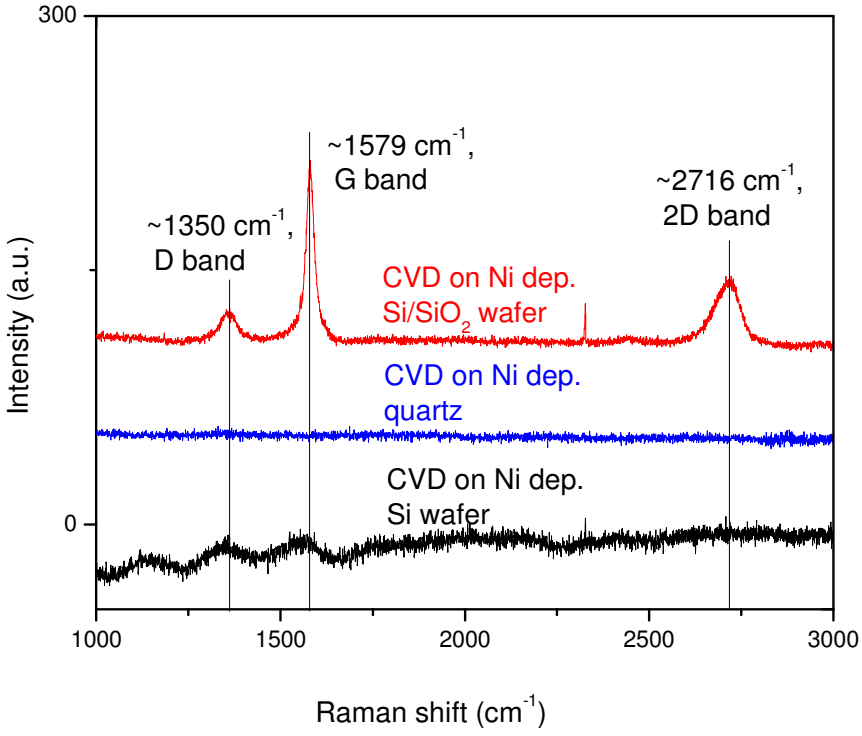

Figure 13: Raman spectra of Ni catalyzed CVD grown samples on different substrates; on Si/SiO_2, quartz and Si from top to bottom in the graph. Samples were treated with (25/1000) sccm of CH_4/H_2 for 10 min at 950°C.

Since the graphene resembles the underlying layer, morphological analysis was carried out for the samples where Ni foil was a substrate and catalyst as well. Samples were heat-treated at 950°C for 40 minutes under Ar and/H_2 flow by keeping CVD growth conditions on Ni-deposited substrate for graphene same except using carbon source (details given in 2.1.3.1 Ni). Below, representative SEM micrographs show that micrometer-sized (>20 μm) grains consisting of hundreds nm sized subgrains were formed during the heating process (Figure 14). However, the metal grains in Ni foil that was not cleaned with HCl appear rough (Figure 14 A-B). When Ni foil was pre-treated with HCl prior to CVD, morphological analysis revealed that Ni grains formed smoother and more uniform after heat-treatment (Figure 14 C-D). After heat treatment and CVD process, distinct evolution of sharp grain boundaries can be easily seen (Figure 14 C-F).

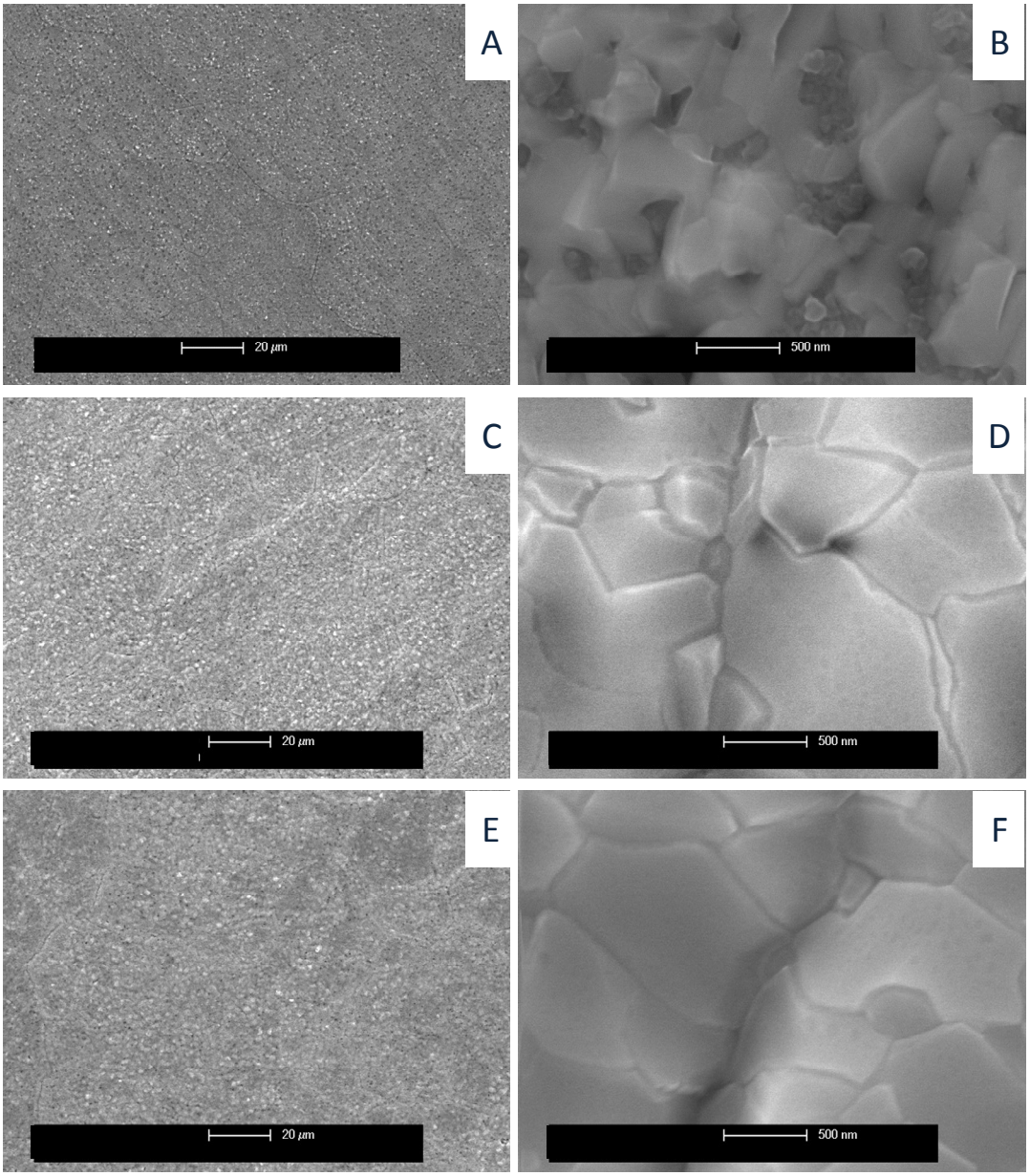

Figure 14: SEM micrographs of Ni foils: heat treated (A, B), pre-treated with HCl prior to heat treatment (C, D), after CVD process (E, F)

Since as-received copper foils have native oxide layers composed of CuO and Cu_2O [17b], these layers reduce the catalytic activity of copper for graphene formation. It has been reported that pre-treatment of the copper foils is essential to obtain high quality large-graphene domains [56] [36]. Therefore, pre-treatment of copper foils prior to CVD growth was conducted by wet-chemical method, cleaning with acetic acid for 10 minutes at 35°C. Then, similar to the treatment of Ni foils given above, Cu foils (with 99.8% and 99.999% purity) were thermally annealed by keeping CVD graphene growth conditions for Cu-

deposited substrates same except using an additive carbon source (details given in 2.1.3.2 Cu). Foils treated with acetic acid appear to have cleaner and flatter grains than the ones not cleaned. Foils of 99.999% purity have well-defined more uniform and smoother grains than the foils of 99.8% purity (Figure 15).

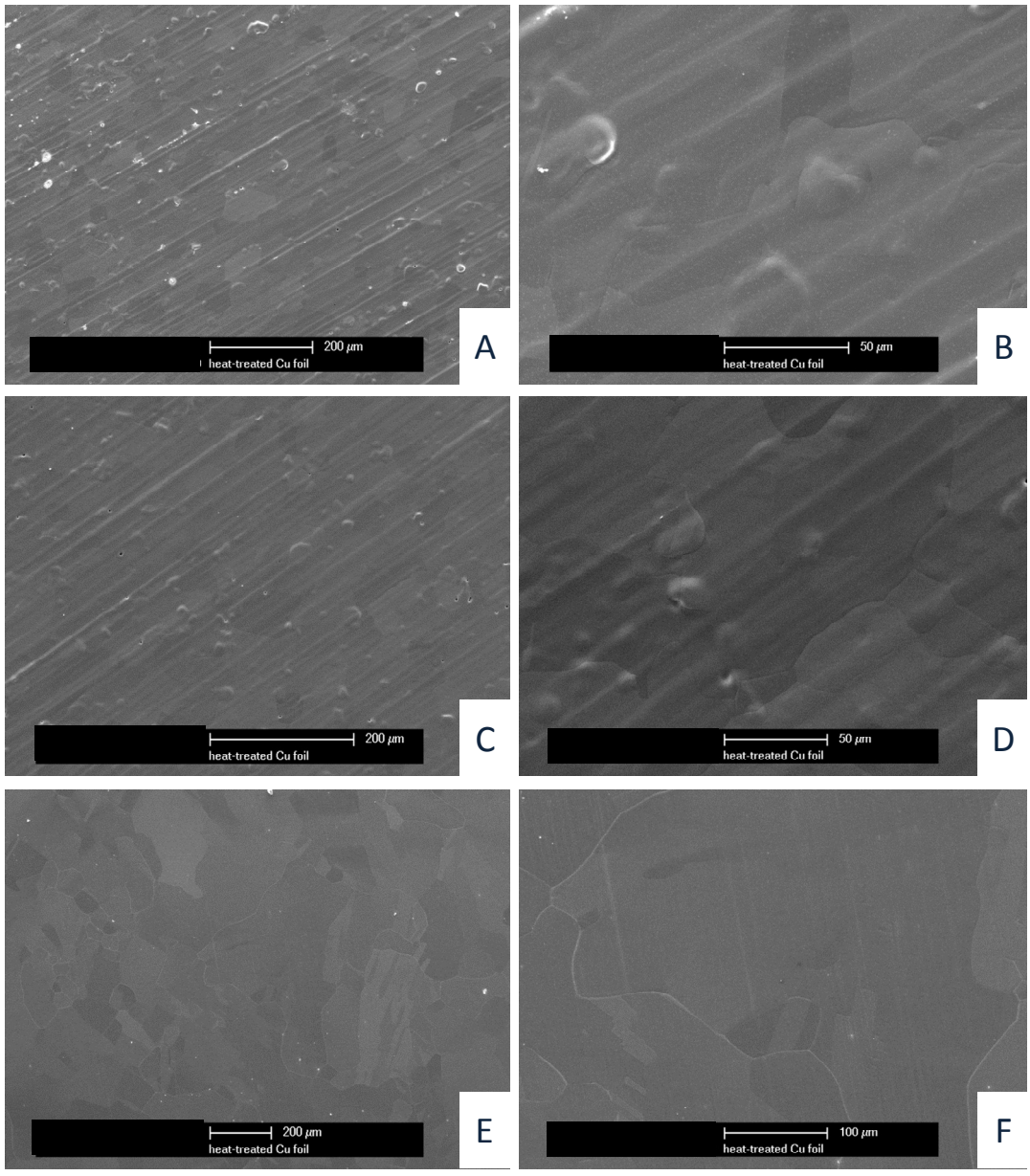

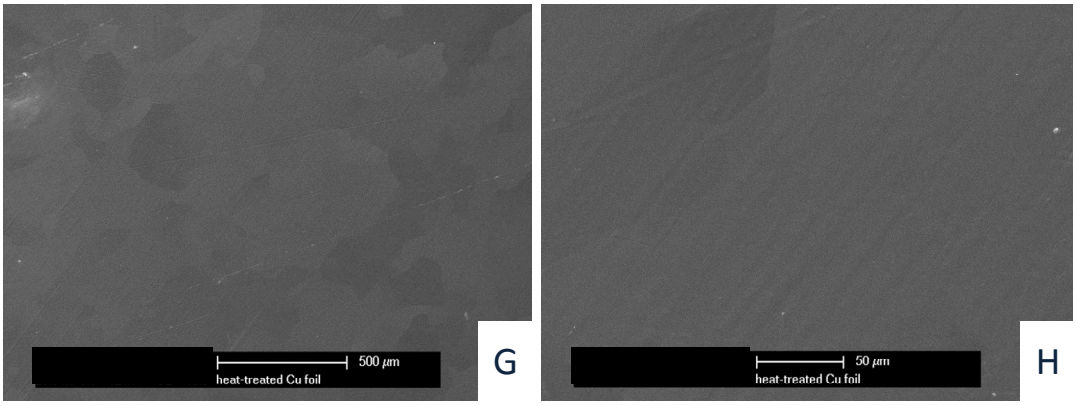

Figure 15: SEM micrographs of Cu foils of different purity: heat treated of 99.8% and 99.999% (A –B and G-H) and pre-treated with acetic acid prior to heat treatment of 99.8% (C, D), and of 99.999% (E, F)

2.1.2. Metal catalyst (type and thickness of metal catalyst) for graphene growth

2.1.2.1. Ni

Nickel was used as catalyst to grow graphene by CVD. To see the effect of Ni thickness on the graphene growth, a series of e-beam deposition experiments of Ni with various thicknesses from 100 nm to 500 nm was examined. Due to the better adhesion of Ni on SiO_2/Si substrate wafers compared to bare Si wafers, SEM images for the heat-treated (by keeping the CVD conditions the same except using CH_4 for graphene growth) Ni deposited samples on SiO_2/Si wafers were given in Figure 16. It is obvious to see that μm-sized Ni grains were formed after thermal annealing of 100 nm, 200 nm and 500 nm Ni thick films. The Ni coverage of the wafer decreases from 500 nm to 200 nm and 100 nm Ni samples as expected (Figure 16).

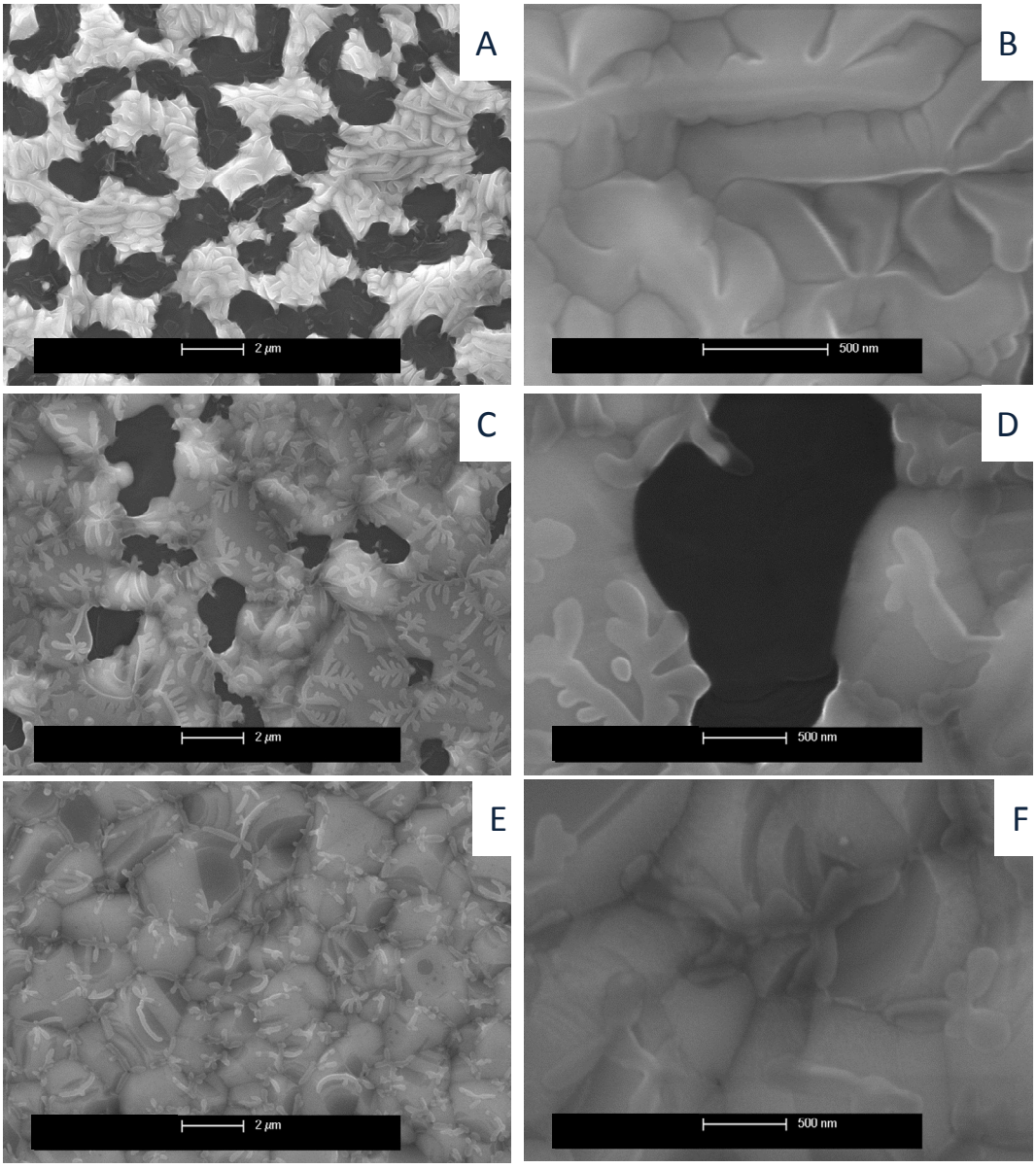

Figure 16: SEM micrographs of heat treated Ni deposited Si/SiO_2 samples. Thickness of Ni is 100 nm (A, B); 200 nm (C, D) and 500 nm (E, F)

The μm-sized Ni grains contain multiple grain-boundaries which are formed during the thermal treatment of the sample. This can be clearly detected in an AFM image of the annealed Ni catalyst film before the CVD graphene growth starts.

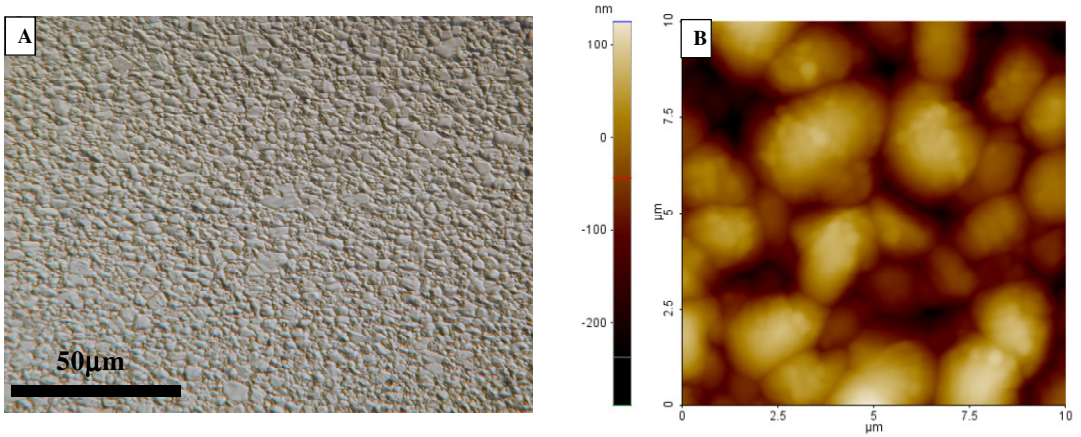

Figure 17: (A) Optical image of the thermally annealed e-beam deposited Ni on SiO_2/Si wafer. (B) AFM image of the corresponding sample.

Raman spectra at 514 nm were given for the samples that were grown on nickel deposited substrates of which the Ni thickness varies from 100 nm to 500 nm (Figure 18). The existence of G and 2D band and no D band in Figure 18 show that high quality graphene was successfully synthesized on each Ni/SiO_2/Si substrates except 100 nm Ni/SiO_2/Si.

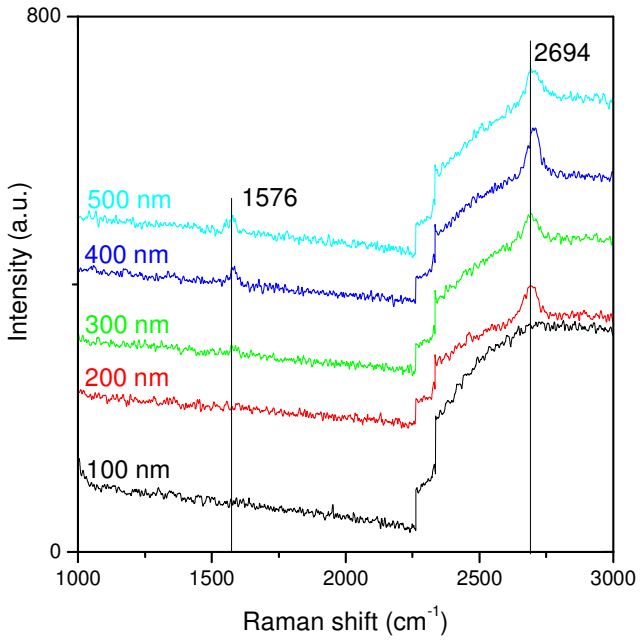

Figure 18: Raman spectra of CVD grown samples on Ni with different thickness; 500-400-300-200-100 nm from top to bottom in the graph. Raman spectroscopy has an offset at 2250 cm^{-1} due to the grating in the spectrometer.

To observe the morphology of the samples through CVD process, SEM analysis of the sample before (annealed 200 nm Ni substrate) and after CVD was conducted (Figure 19). Figure 19 depicts that 200 nm thick of nickel deposited sample did not cover the whole surface of the wafer at all upon heating and CVD processes. Interestingly those Ni-free areas were covered with flat and layered structure after CVD. Confocal Raman analysis was performed to characterize the areas on the nickel part and the empty areas between nickel grains qualitatively.

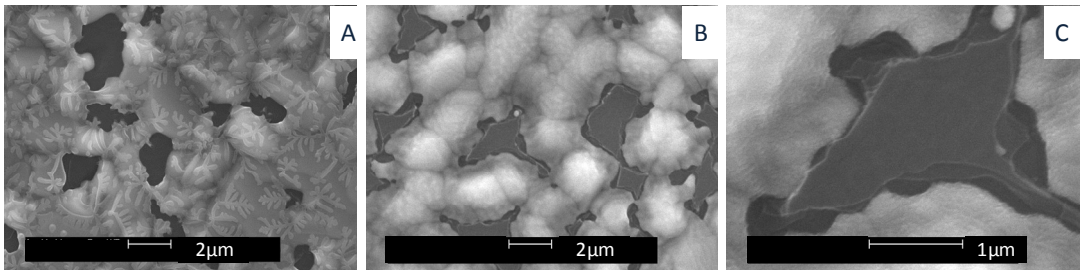

Figure 19: SEM micrographs of 200 nm Ni-SiO_2/Si samples; A. heat-treated , B and C are after CVD process.

In agreement with Figure 19, Ni-free parts are also visible by confocal optical microscope coupled to Raman spectroscopy (Figure 20). Raman spectra were taken at Ni-containing (yellowish) and Ni-free (greenish) parts and given comparably. Both spectra have characteristic bands (D, G and 2D) of graphene revealing that graphene is formed both on the nickel part and between nickel grains (Figure 20). However, relative intensity ratios of 2D/G differ at the areas depicting the inhomogeneity in the number of layers through the sample. The existence of graphene on the metal-free areas can be explained by the dewetting of the metal layer during CVD as reported for the direct CVD growth of copper catalyzed graphene on dielectric substrates [63]. If the dewetting of the metal during temperature ramping (prior to the CVD) takes place, then the graphene layer will be discontinuous in metal-free areas. That means large area coverage with graphene can be provided only by an initially formed and continuous metal catalyst film [63]. Confocal image and Raman spectra were also taken for samples catalyzed by 500 nm Ni. Compared to graphene grown on a 200 nm Ni catalyst layer, sample on 500 nm Ni layer covers the whole wafer and looks morphologically more homogenous (Figure 21). Moreover, two different spectra taken from randomly chosen areas resemble each other suggesting the formation of similar quality of graphene on the surface (Figure 21).

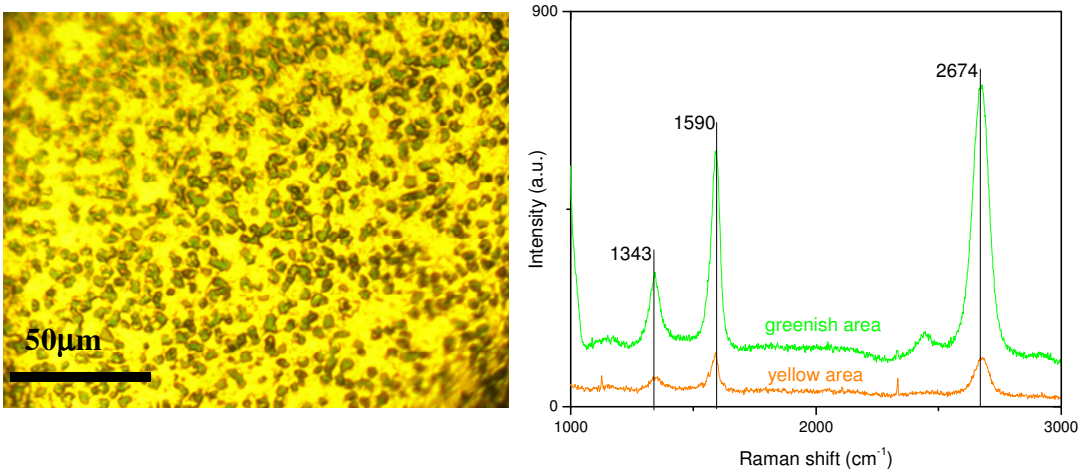

Figure 20: Confocal optical microscopy image of CVD grown sample on 200 nm Ni-Si/SiO_2 wafer (left side), Raman spectra performed on randomly chosen areas Ni-containing (yellowish) and Ni-free (greenish) parts on the sample.

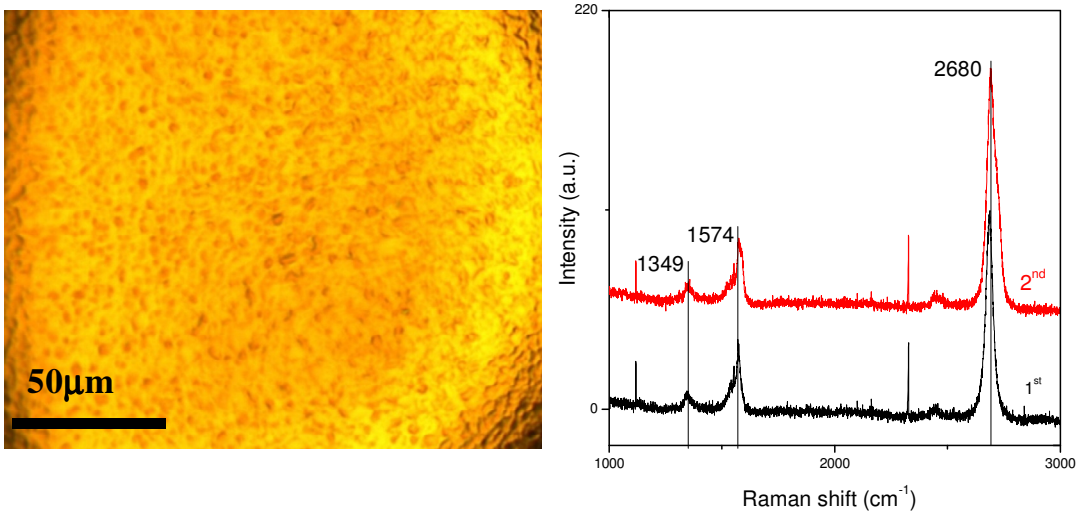

Figure 21: Confocal optical microscopy image of CVD grown sample on 500 nm Ni-Si/SiO_2 wafer (left side), Raman spectra performed on two randomly chosen areas.

2.1.2.2. Cu

Besides nickel, copper was used as a metal catalyst to fabricate CVD graphene. Effect of thickness of the Cu layer on the graphene synthesis was examined by deposition of Cu with various thicknesses from 200 nm to 1000 nm (200, 400, 500, 600, 800, 900, 1000

nm). Similar as in the case of nickel, SiO_2/Si wafers were chosen as substrates due to the better adhesion of Cu on SiO_2/Si wafers compared to Si. In some cases, to increase the adhesion of metal layer on the wafers, 5 nm nickel layer was first deposited on wafers and then the required amount of copper was deposited onto nickel layer. As described for the pre-treatment of Cu foil prior to CVD, copper deposited wafers were also cleaned with acetic acid first (for 10 minutes at 35°C). In Figure 22, sample treated with acetic acid appear more homogeneous than the sample which was not cleaned. Therefore, it is decided to use acetic acid treatment for Cu-deposited wafers prior to CVD process.

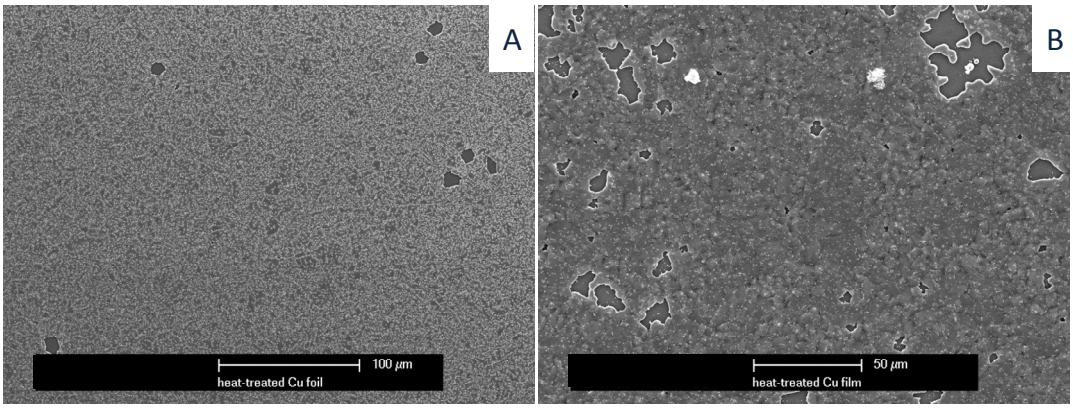

Figure 22: SEM micrographs of heat treated 600 nm Cu-Si/SiO_2 samples; A. pre-treated sample with acetic acid prior to heat treatment B. not pre-treated.

The effect of thickness on the coverage of the wafer is investigated for the copper deposited (200 nm to 1000 nm thick) wafers after CVD process by SEM. It is reported that thinner copper films (<450 nm) tend to break into parts in dot- or finger- shape during temperature ramping [48]. Parallel to that finding, similar elongated structures are seen for chemical vapor deposited copper film with the thickness of 200 nm (Figure 23). The empty areas decrease with increasing the thickness of copper deposited in the order of 200 nm, 400 nm, 900 nm and 1000 nm as expected. The grain size of the copper also gets larger with the same order. Most of the grains are a few μm-sized (<5 μm) in 400 nm whereas tens of μm-sized (>20 μm) (besides few μm-sized ones) are seen in 1000 nm thick copper catalyzed sample.

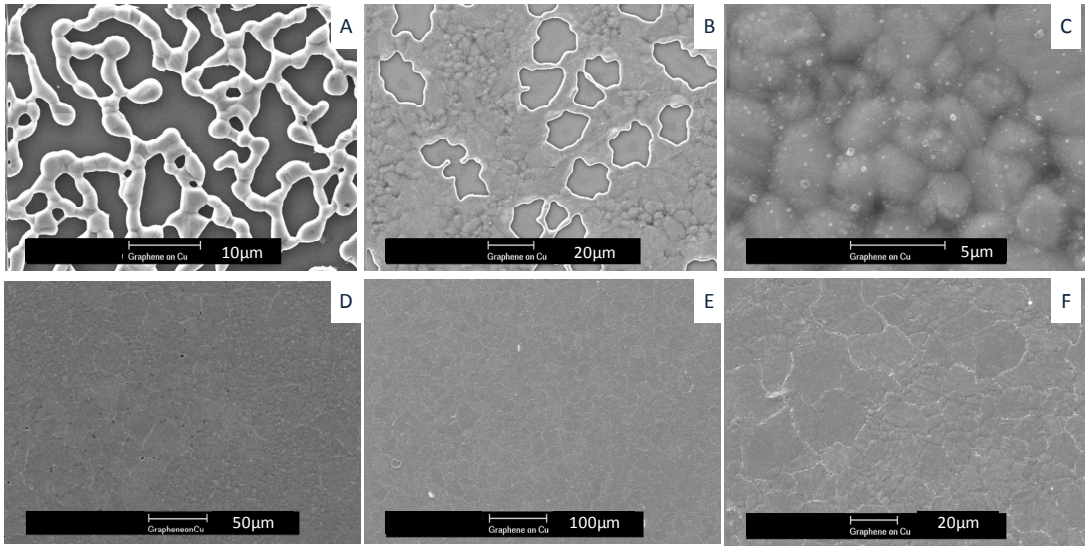

Figure 23: SEM micrographs of (various thickness of Cu deposited Si/SiO_2) samples after CVD process; thickness of Cu is 200-400-400-900-1000-1000 nm from A to F respectively.

2.1.3. CVD Conditions

Employing the methane based CVD growth process at 950°C-1000°C, I have obtained large-scale, high quality crystalline single- to few layer graphene films using nickel or copper as a catalyst. For that purpose, nickel or copper metals are used as a thin film on the substrate or foils of nickel or copper metals are used directly as substrates. The procedure starts with deposition of the metal with required thickness on SiO_2/Si wafers by an e-beam technique and then passing $Ar/H_2/CH_4$ gases with varying mixture and amount at high temperatures (950-1000°C) under ambient pressure (For copper case, low-pressure CVD growth of graphene was also conducted). During a cooling step, graphene is formed on the metal catalyst. Transfer of the graphene onto the desired substrate is possible by etching the metal part completely. The quality of the deposited metal catalyst layer mainly determines the crystalline quality of the obtained graphene film which could be monitored by spatially resolved micro Raman investigations on the graphene films. The overall synthesis process leading routinely to the formation of ca. 1 x 1 cm^2 transparent graphene films is shown in Figure 24.

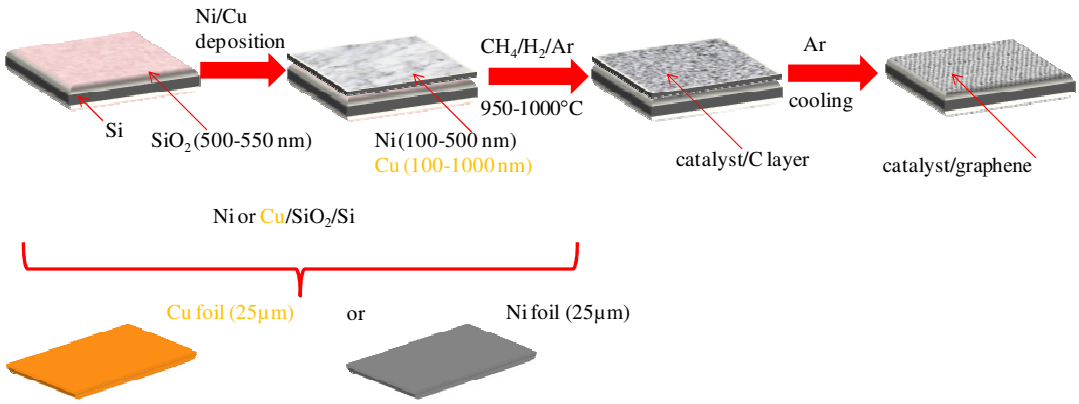

Figure 24: Synthesis steps for CVD-graphene

In the following two sections, graphene growth on nickel and copper catalyst is discussed. In the experiments, Ni and Cu layers on the substrates (deposited by e-beam on SiO_2/Si wafer substrates) and Ni and Cu foils were used as substrates.

2.1.3.1. Ni

Graphene is synthesized with chemical vapor deposition method using Ni film deposited silicon wafer as a substrate. The process starts with deposition of 200-500 nm Ni using electron beam evaporation system (e-beam) on SiO_2 (600 nm)/Si wafer.

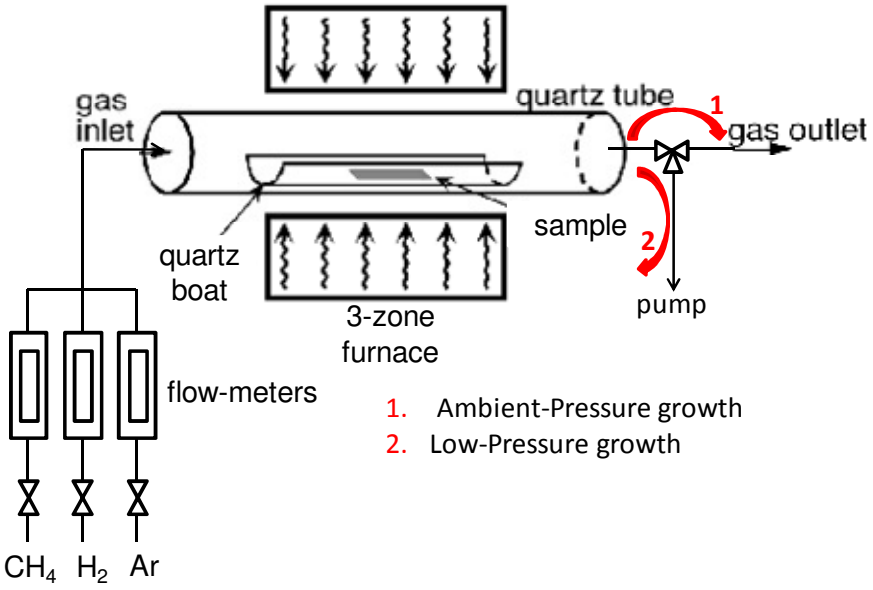

Figure 25: CVD set up for epitaxial growth of graphene

Five processing steps are used for Ni-catalyzed CVD growth of graphene (Figure 26). First, substrates are heated to 950°C under the flow of argon (Ar; 600 sccm) and hydrogen (H_2; 500 sccm).

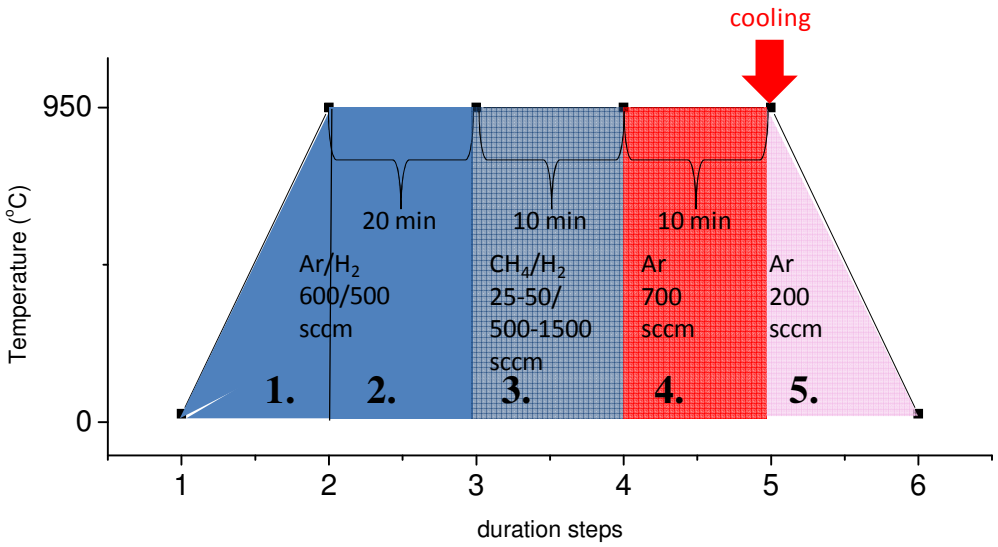

Figure 26: Chart showing an overview of the individual processing steps for Ni catalyzed CVD growth of graphene.

The substrates are further heated at that temperature under Ar and H_2 flow for 20 min to generate µm-sized atomically flat Ni grains. It is stated that the quality of graphene is enhanced by the help of this step and gets similar to graphene grown on a single crystal substrate [64]. Accordingly and in order to get high quality graphene films, an additional thermal annealing step of Ni-SiO_2/Si substrates was conducted. The graphene growth is carried out at 950°C using H_2 (900-1500 sccm) and CH_4 (25 sccm) for 10 min. After the growth step, in contrast to the procedure described [64], the CVD-chamber is purged with Ar (700 sccm) for 10 min to flush the remaining CH_4. In order to see the effect of cooling rate, the sample is either slowly cooled down to room temperature (with 0.1°C/s cooling rate) under a flow of Ar (200 sccm) or directly taken out of the oven at 950°C. It's obvious to see that slow-cooling rate results in a uniform and non-cracked metal film where extremely fast cooling rate gives a cracked film (Figure 27).

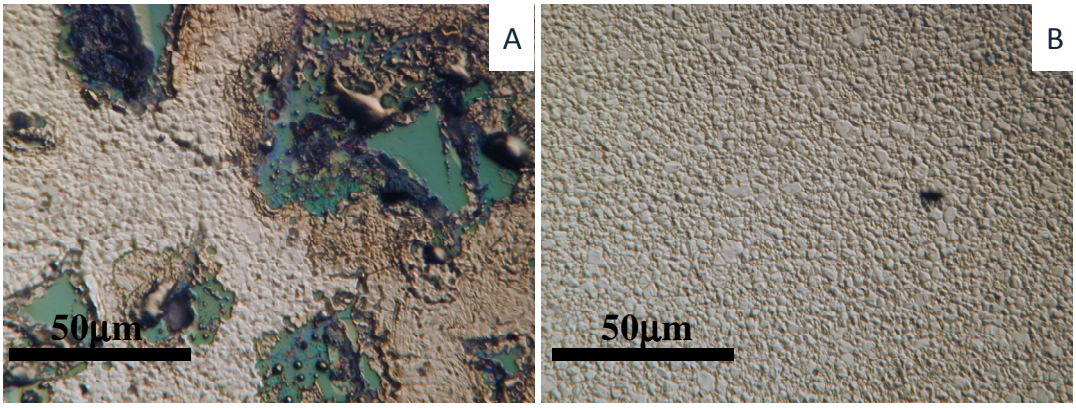

Figure 27: Optical microscope images of CVD grown on 500 nm Ni-Si/SiO_2 samples with different cooling rates; A. shock cooling (sample was dragged out of the oven held at 950°C to room temperature) B. slow cooling with 0.1°C/s.

It has been reported that fast/medium cooling rates (10°C/s) results in graphene formation due to the finite amount of C segregation at the surface whereas slow cooling rates (0.1°C/s) and extremely fast cooling rates (20°C/s) do not lead to graphene formation[65]. Contradictory to that, graphene is formed on Ni/SiO_2/Si substrates and Ni foils with slow cooling rates as shown in the Raman spectra (Figure 28 and Figure 29).

To see the effect of carbon concentration on graphene growth, the supply of the carbon source (CH_4) was kept constant as 25 sccm but diluted with H_2 gas with varying concentrations in the range from 900 to 1500 sccm. In all cases, graphene was formed (Figure 28). Sample c gives less-defective few-layered graphene with high 2D/G and low D/G ratios. Therefore a ratio of (1000/25 sccm) (H_2/CH_4) was chosen as optimum CVD conditions to form graphene on nickel film and conducted on Ni foil as well. The Raman spectroscopy characterization reveals that when employing the same CVD conditions, graphene forms on Ni foil as well (Figure 29). However, a shift of the 2D band to higher wavenumber indicates that the number of graphene layers is higher on Ni foil compared to on Ni films. This is probably due to the fact that more carbon dissolves and segregates on the surface as expected.

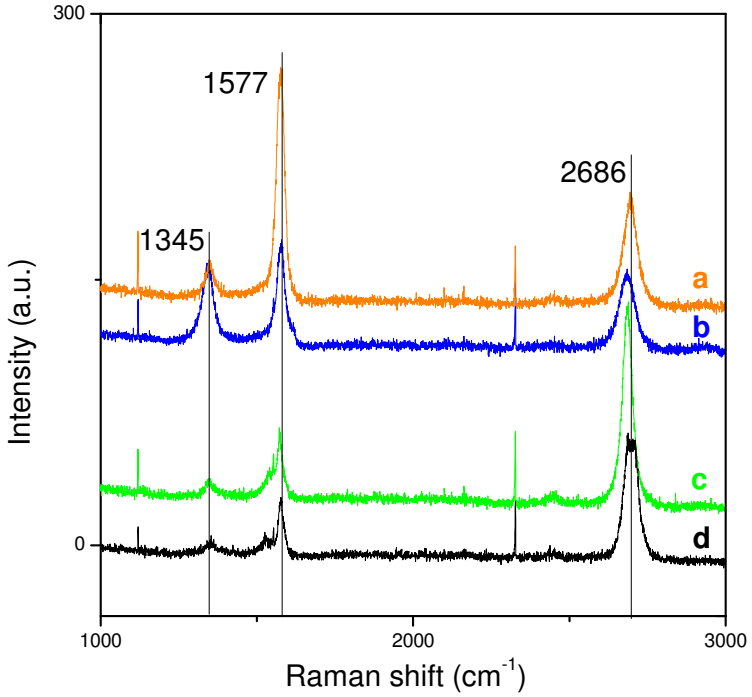

Figure 28: Raman spectra of CVD grown on 500 nm Ni-Si/SiO_2 samples with different sccm/sccm of H_2/CH_4 ratio; a. 1500/25, b. 1100/25, c. 1000/25 and d. 900/25 from top to bottom in the graph.

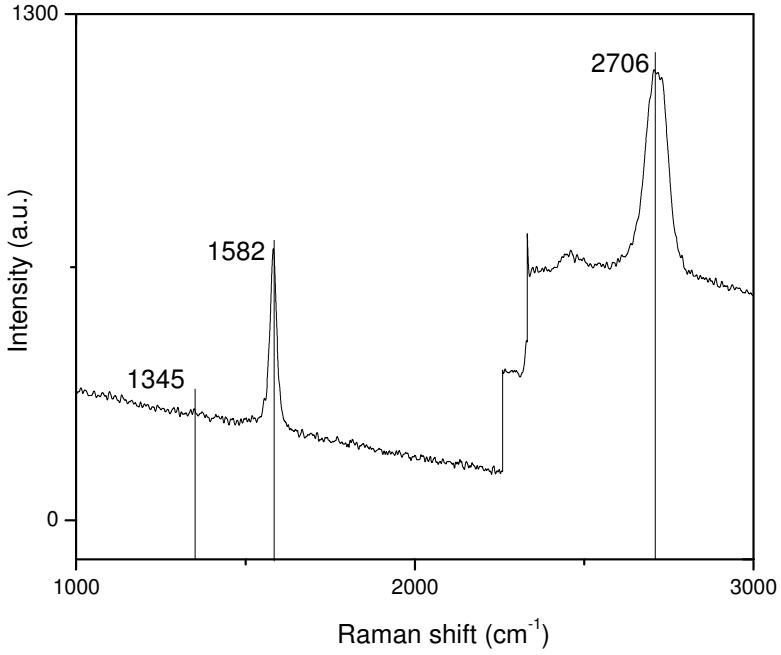

Figure 29: Raman spectrum of CVD grown graphene on Ni foil with 1000 sccm/25 sccm of H_2/CH_4. Raman spectroscopy has an offset at 2250 cm^{-1} due to the grating in the spectrometer.

Ni catalyst layer was separated from graphene by etching process (see Section 2.1.4 “Transfer of graphene”). SEM investigations reveal the formation of a continuous graphene film showing some wrinkles and scrolls which can be associated with the thermal expansion coefficient difference between the Ni catalyst layer and the graphene formed (Figure 30 a) [56] [66]. The corresponding EDX spectrum shows only a carbon peak due to graphene besides the signals of the substrate (Si and O). No signals of Ni could be detected, revealing complete removal of the catalyst layer from the graphene (Figure 30 b).

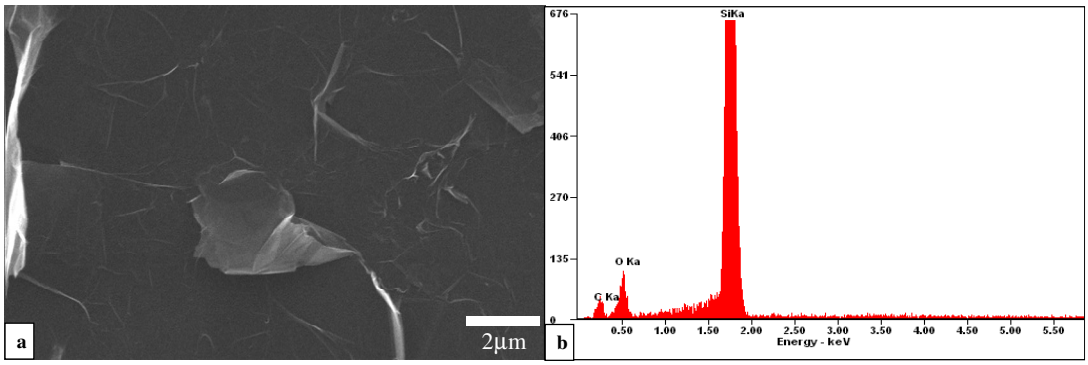

Figure 30: (a) SEM image of a transferred graphene film. (b) EDX spectrum of the corresponding area given in (a) [34].

TEM examination of the graphene films show a honeycomb lattice structure with a six fold symmetry associated with the graphene structure (Figure 31 a) [67]. A single area electron diffraction (SAED) pattern (inset in Figure 31 a) reveals two rings corresponding to the diffractions of the <002> and <101> planes of nanocrystalline, hexagonally ordered graphitic sheets. Grazing incidence X-ray diffraction (GIXRD) showed a characteristic weak and broad peak at ~22.2° which can be indexed to the <200> reflection, the most prominent signal for the graphitic structure (Figure 31 b) [68] [37].

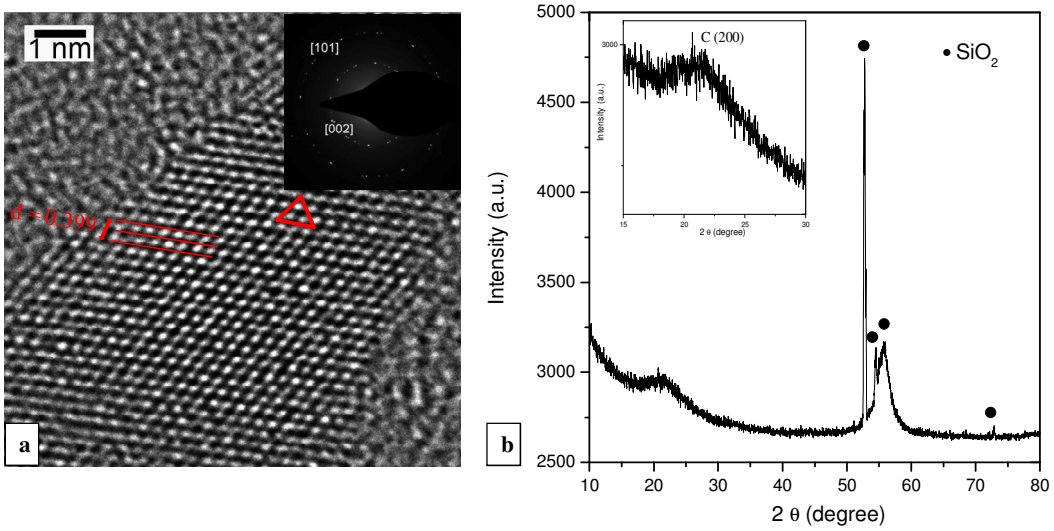

Figure 31: (a) High resolution TEM image of a transferred graphene film. Representative SAED pattern of the graphene sample is given as inset of (a). (b) XRD spectrum of the transferred graphene on SiO_2/Si wafer. Focused pattern between 15-30 2θ is given as inset of (b) [34].

TEM and XRD results for the graphene film give same interlayer spacing between graphene sheets, corresponding to the <002> (0.399 nm is calculated from XRD and TEM). The interlayer distance d of graphene is larger than that of graphite (0.335 nm) which in turn explains the lowering of the shift of the <002> peak of graphite towards lower 2θ values (26.5° to 22.2° according to Bragg's equation).

Besides X-ray diffraction, a detailed micro Raman analysis on the prepared graphene sample was performed (Figure 32). For CVD derived graphene specimens, a full width at half maximum (Γ) of 2D band is 30 cm^{-1} indicating formation of single layer and 2D band gets broader at some randomly chosen areas indicating few layer graphene. The ratio I(G)/I(2D) decreases with increasing number of layers. Thus, the determination of this ratio for different areas over the sample should provide reliable information with respect to the quality of large area, transparent graphene. Two randomly chosen areas are marked with arrows 1 and 2 in Figure 32 b. Their distance is significantly larger than the diameter of the Raman laser spot (ca. 2 μm). As can be seen, the intensity of the D band is very low for all areas studied, indicating a highly ordered graphene structure. However, the sharpness of the G band and intensity ratio I(G)/I(D) varies between 0.2-1.1, indicating that the number of layers is lower than 10 [69] (Figure 32 c and d). The Raman-line mapping studies are thus a valuable experimental proof to suggest that almost single- up to a few-layer graphene is obtained by the employed CVD method.

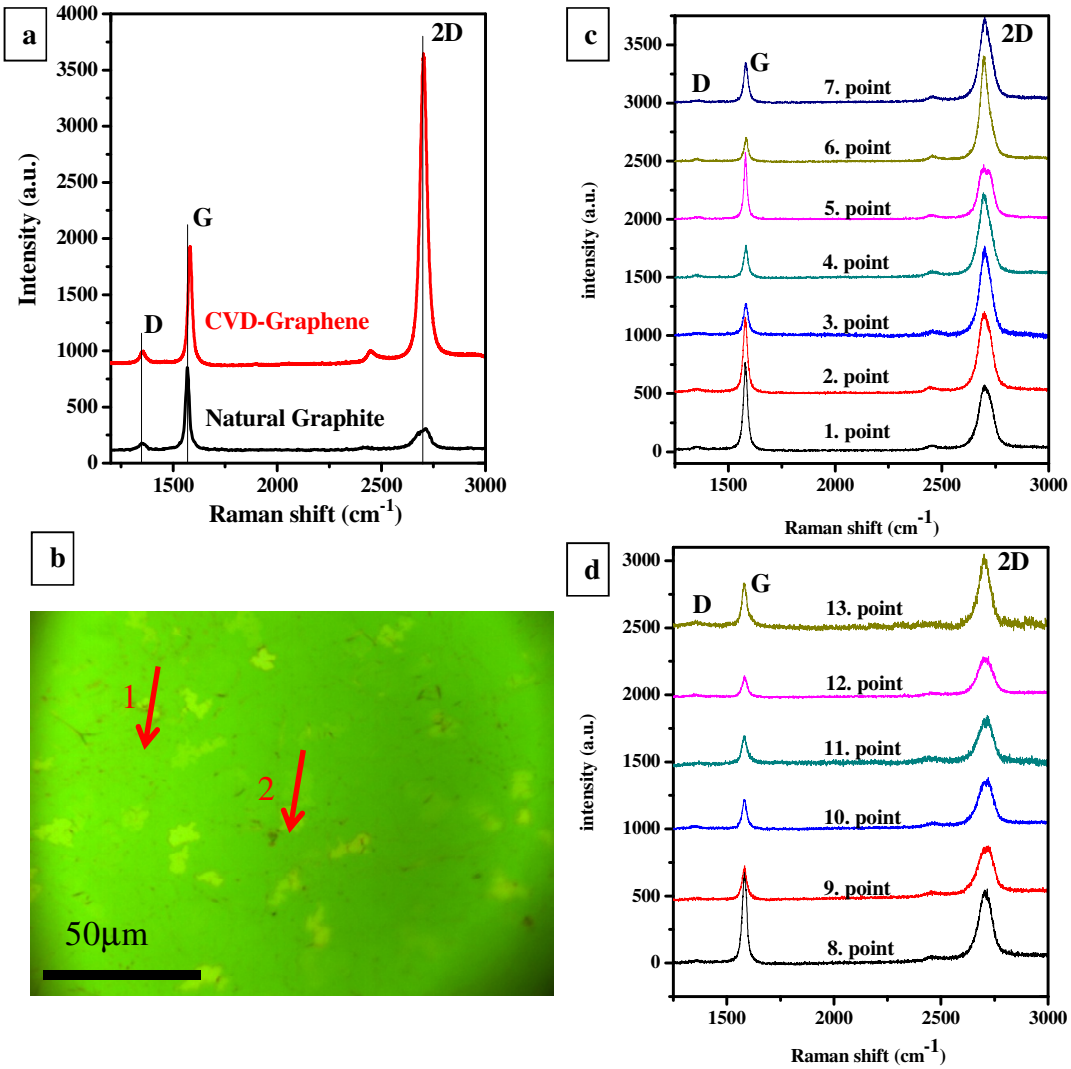

Figure 32: (a) Raman spectra for graphene film and graphite. (b) Optical image of graphene transferred on SiO_2/Si wafer. (c) and (d) Raman line mappings of the areas depicted with arrows 1 and 2 in (b), respectively. Spectra of 1-7 are from area 1, and 8-13 are from area 2 [34].

The reason for the thickness inhomogeneity within the sample can be attributed to the microstructure of the Ni catalyst layer responsible for the formation of graphene. Substrates onto which Ni is deposited are thermally annealed in order to form μm-sized nearly atomically flat Ni grains before the CVD growth process was started [64]. The μm-sized Ni grains with multiple grain-boundaries formed during the thermal treatment of the sample are shown previously with an AFM image (Figure 17 B). Accordingly, the uneven and rough surface of the Ni surface with its particulate surface morphology and the presence of inter grain boundaries is strongly affecting the graphene film growth [70].

Table 2: CVD growth procedures for the synthesis of Cu catalyzed graphene

Procedure #, growth Pressure, Temperature	**Pre-annealing Conditions**	**H_2/CH_4 ratio, growth time**	**cooling step**	**Substrate**
#1, 760 Torr, 990°C	heating up to 990°C with H_2/200scm flow	5-20-120 min H_2/CH_4 (200/200-600-875-1000 sccm)	1. slow cooling with H_2/CH_4 (200/200-600-875-1000 sccm) flow until 200°C or to 600°C 2.Ar/1000 sccm until RT	200-500-600-800-900-1000 nm on SiO_2/Si wafers and 25 μm thick Cu foil
#1', 760 Torr, 990°C	heating up to 990°C with H_2/200scm flow	5-20 min H_2/CH_4 (200/200-875 sccm)	slow cooling until RT under Ar/1000 sccm flow	600-800 nm on SiO_2/Si wafers and 25 μm thick Cu foil
#2, 760 Torr, 990°C	1. heating up to 990°C with Ar/H_2 (1000/325-500 sccm) flow 2. 15 min, 990°C with Ar/H_2 (1000/325-500 sccm) flow	5 min, H_2/CH_4/Ar (325-500/25-100/1000 sccm)	slow cooling until RT under Ar/1000 sccm flow	25 μm thick Cu foil
#3, 760 Torr, 990°C	heating up to 990°C with Ar/H_2 (500/100 sccm) flow	5-15 min, Ar/H_2/CH_4 (500/100/50-200 sccm)	1. shock-cooling -dragging sample with magnet- with Ar/500 sccm or 2. slow-cooling under Ar/500 sccm	25 μm thick Cu foil
#3', 760 Torr, 990°C	heating up to 990°C with Ar/H_2 (1000/1000 sccm) flow	1-5-15-60 min, Ar/H_2/CH_4 (1000/1000/5-13-25-100 sccm)	slow cooling until RT under Ar/1000 sccm flow	25 μm thick Cu foil
#4, 760 Torr, 990°C	1. evacuated to a vacuum of 20 mTorr for 10 min 2. Pump is switched off, 760 Torr with 500 sccm of Ar/H_2 (467/33 sccm) 3. 60 min, 990°C Ar/H_2 (467/33 sccm)	60-120 min, H_2/CH_4/Ar (30/50/420 sccm)	slow-cooling under Ar/500 sccm	25 μm thick Cu foil
#5, 5-15 Torr, 990°C	1. heating up to 990°C with H_2 (1-5 sccm) 2. 30 min, 990°C with H_2 (1-5 sccm)	10 min, H_2/CH_4 (1-2/5 and 5/25 sccm)	shock-cooling -dragging sample with magnet- under H_2 (1-5 sccm)	25 μm thick Cu foil
#5', 2-5-15-20-70 Torr, 990°C	1. heating up to 990°C with H_2 (1-5 sccm) 2. 30 min, 990°C with H_2 (1-5 sccm)	10 min, H_2/CH_4 (1-2/5 and 5/25 sccm)	slow cooling under H_2 (1-5 sccm)	25 μm thick Cu foil

2.1.3.2. Cu

The growth of graphene is obtained in few to tens of microns regions with utilizing Ni as the catalyst and number of graphene layers varied from single to few over the entire substrate that is discussed above (Figure 32). In contrast to Ni, uniform deposition of high quality single layer graphene over large areas as of 30-inches has been reported when using polycrystalline copper foil as a catalyst substrate [56]. Not only Cu foil but also thin film Cu (>500 nm) deposited on SiO_2/Si wafers have been used to catalyze CVD growth of graphene [63]. Therefore, I studied copper foils and as well as e-beam deposited copper thin films on SiO_2/Si wafer to achieve low layer graphene growth.
There are 5 different procedures that I have used for Cu-catalyzed CVD graphene growth (see Table 2).

Procedure#1 and 1'

Table 3. CVD growth procedure#1 and procedure#1' for the synthesis of Cu catalyzed graphene

Procedure #, growth Pressure, Temperature	**Pre-annealing Conditions**	**H_2/CH_4 ratio, growth time**	**cooling step**	**Substrate**
#1, 760 Torr, 990°C	heating up to 990°C with H_2/200scm flow	5-20-120 min H_2/CH_4 (200/200-600-875-1000 sccm)	1. slow cooling with H_2/CH_4 (200/200-600-875-1000 sccm) flow until 200°C or until 600°C 2.Ar/1000 sccm until RT	200-500-600-800-900-1000 nm on SiO_2/Si wafers and 25 μm thick Cu foil
#1', 760 Torr, 990°C	heating up to 990°C with H_2/200scm flow	5-20 min H_2/CH_4 (200/200-875 sccm)	slow cooling until RT under Ar/1000 sccm flow	600-800 nm on SiO_2/Si wafers and 25 μm thick Cu foil

Table 3 summarizes CVD steps used in procedure#1. Procedure#1 starts with heating up the copper deposited substrates or copper foils to 990°C with a flow H_2 flow of 200 sccm flow at ambient pressure of 760 Torr [71]. Then the CVD growth is conducted with the addition of CH_4 (200-600-875-1000 sccm) to H_2 (200 sccm) for 5-20-120 minutes. The system is cooled down without altering the gas mixture (under H_2/CH_4) (until 600°C or 200°C) and further allowed to cool to room temperature under Ar flow of 1000 sccm. Subsequently, graphene was successfully grown on different thick Cu-films (200-600-800-1000 nm) on SiO_2/Si wafers and Cu foil (25μm). Corresponding spectra were plotted

(Figure 33) and relative intensity ratios of D to G bands (I_D/I_G), and 2D to G bands (I_{2D}/I_G) were calculated (see Table 4 below). The decrease in I_D/I_G ratio revealed that defects were diminished by increasing the thickness of metal catalyst. The reason for that can be attributed to an increase in grain size of the copper catalyst with the increased thickness of copper film (Figure 23). As the thickness of copper deposited on wafer increases, number of grain boundaries that cause defects in graphene growth decrease.

In Figure 33, the spectra belonging to graphene via copper with different thicknesses with same CVD conditions are given (200 sccm H_2/875 sccm CH_4 at 990°C for 20 minutes and during cooling with the same gas flow until 200°C). Baselines in the Raman spectra increase due to the fluorescence effect of copper, however, the bands can be still detected. I_{2D}/I_G ratio is almost 1 in each spectrum and the smallest value was obtained for graphene grown on 25 μm thick Cu foil substrate (Table 4). That means the number of graphene layers is higher on a sample grown on Cu foil. Lower I_D/I_G value for the sample on Cu foil substrate shows the less defective formation of graphene compared to ones on Cu film deposited substrates (Table 4).

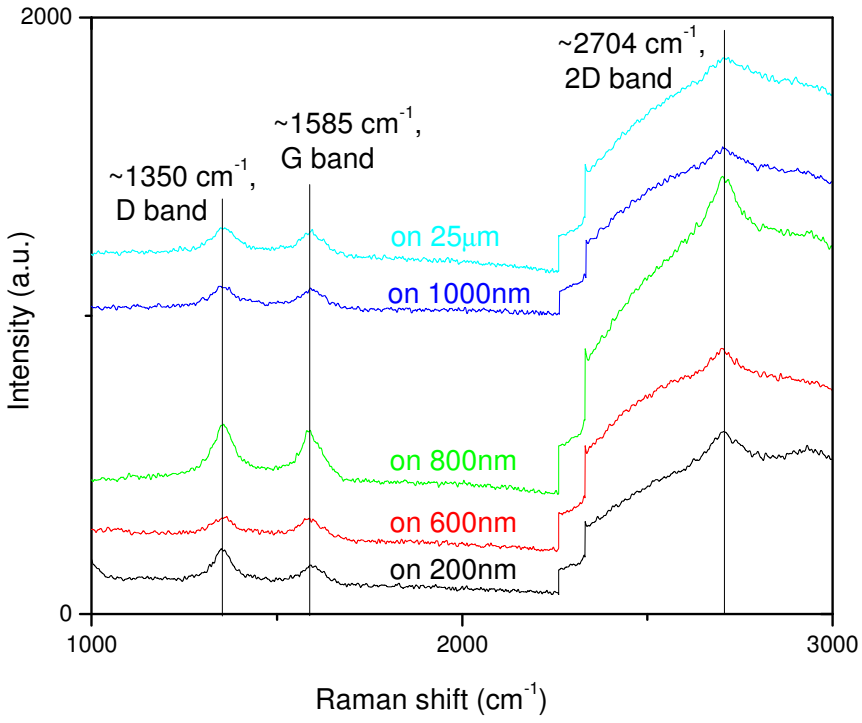

Figure 33: Raman spectra of CVD grown samples on 200-600-800-1000 nm Cu-SiO_2 and 25 μm thick Cu foil using procedure #1 (with same CVD conditions: (200 sccm H_2/875 sccm CH_4 at 990°C for 20 minutes and during cooling with the same gas flow until 200°C). Raman spectroscopy has an offset at 2250 cm^{-1} due to the grating in the spectrometer.

Table 4: Calculated intensity ratios of the Raman bands (I_D/I_G and I_{2D}/I_G) for Cu catalyzed CVD grown samples (given in Figure 33) by using Procedure#1.

--	CVD graphene growth by procedure#1	--
Copper thickness	I_D/I_G	I_{2D}/I_G
200 nm	1.5	1.2
600 nm	1.0	1.6
800 nm	1.0	1.1
1000 nm	0.89	0.89
25 μm	0.79	0.77
	CVD graphene growth by procedure#1'	
25 μm	0.89	1.1

Besides the role of copper thickness on the formation of graphene, the relative ratio of methane to hydrogen at the CVD growth step was changed to analyze the effect of methane concentration on the graphene formation and quality. For that purpose, in addition to 200 sccm/875 sccm (H_2/CH_4) value reported [71], hydrogen amount was kept constant as 200 sccm while the methane amount was varied from 875 sccm to 20-200-400-600-1000 sccm. Growth time was used as 20 minutes as given, but effect of increasing the growth time was considered by using 5 minutes and 120 minutes as well. After the growth step, the methane and hydrogen flow was maintained during cooling to to 200°C. In addition to that, the gas mixture was used during cooling until 600°C instead 200°C.

Raman data belongs to the samples grown on 600 nm, 1000 nm Cu-SiO_2/Si and 25 μm Cu foils by procedure#1 are given in different plots below (Figure 34, Figure 35 and Figure 36, respectively).

The detailed description of the sample codes and overall calculations of relative intensity ratios of the Raman bands of those samples are summarized in Table 5.

Table 5: Calculated intensity ratios of the Raman bands (I_D/I_G and I_{2D}/I_G) for Cu catalyzed CVD grown samples using procedure#1 and 1'.

Procedure 1-on 600nm Cu-SiO_2/Si	**I_D/I_G**	**I_{2D}/I_G**
EK485-20 min(at 990°C) (200/20 sccm) (H_2/CH_4) and cooling until 200°C w/H_2/CH_4	0.56	2.2
EK457-20 min(at 990°C) (200/200 sccm) (H_2/CH_4) and cooling until 200°C w/H_2/CH_4	1.0	1.2
EK482-20 min(at 990°C) (200/200 sccm) (H_2/CH_4) and cooling until 600°C w/H_2/CH_4	0.88	1.4
EK509-20 min(at 990°C) (200/400 sccm) (H_2/CH_4) and cooling until 200°C w/H_2/CH_4	1.0	0.62
EK500-20 min(at 990°C) (200/400 sccm) (H_2/CH_4) and cooling until 600°C w/H_2/CH_4	0.88	0.63
EK463-20 min(at 990°C) (200/600 sccm) (H_2/CH_4) and cooling until 200°C w/H_2/CH_4	0.99	1.4
EK422-20 min(at 990°C) (200/875 sccm) (H_2/CH_4) and cooling until 200°C w/H_2/CH_4	1.0	1.6
EK423-20 min (at 990°C) (200/1000 sccm) (H_2/CH_4) and cooling until 200°C w/H_2/CH_4	0.98	1.1
EK444-2 hrs (at 990°C) (200/875 sccm) (H_2/CH_4) and cooling until 200°C w/H_2/CH_4	1.2	1.2
Procedure 1-1000nm Cu-SiO_2/Si		
EK416- 20 min (at 990°C) (200/200 sccm) (H_2/CH_4) and cooling until 200°C w/H_2/CH_4	1.0	1.2
EK415- 20 min (at 990°C) (200/875 sccm) (H_2/CH_4) and cooling until 200°C w/H_2/CH_4	0.89	0.91
Procedure 1-25 μm Cu foil		
EK458- 20 min (at 990°C) (200/200 sccm) (H_2/CH_4) and cooling until 200°C w/H_2/CH_4	0.91	1.1
EK465- 20 min (at 990°C) (200/600 sccm) (H_2/CH_4) and cooling until 200°C w/H_2/CH_4	0.86	0.71
EK471- 20 min (at 990°C) (200/875 sccm) (H_2/CH_4) and cooling until 200°C w/H_2/CH_4	0.79	0.77

Procedure1'		
EK424-on 600nm Cu-SiO_2/Si-20 min (at 990°C) (200/875 sccm) (H_2/CH_4)	--	--
EK425-on 800nm Cu-SiO_2/Si-20 min (at 990°C) (200/875 sccm) (H_2/CH_4)	--	--
EK587-on 25μm Cu foil-20 min (at 990°C) (200/875 sccm) (H_2/CH_4)	0.89	1.1
EK581-on 25μm Cu foil-5 min (at 990°C) (200/200 sccm) (H_2/CH_4)	0.56	1.4

Table 5 continued

For 600 nm deposited copper case, graphene is successfully grown with different methane concentration (20-200-400-600-875-1000 sccm CH_4 with 200 sccm H_2) (Figure 34). 20/200 sccm (CH_4/H_2) for 20 minutes at 990°C is found to reflect the optimum growth parameters on 600 nm copper catalyst layers deposited on wafers with the low defects (lower I_D band) (Table 5). When more than 20 sccm of methane is used (200-1000 sccm), the defective sites increase in the graphene structure. However, the use of either 200 sccm or more (400-1000 sccm) methane gave a close I_D/I_G and I_{2D}/I_G values suggesting that 200 sccm of methane is enough to saturate the catalyst surface (Table 5). When the samples are cooled under CH_4/H_2 mixture until 600°C instead 200°C, the samples are less defective (see Table 5 for EK457-EK482 and EK509-EK500). If a growth time of 120 minutes instead 20 minutes is used, the intensity of D band increases. It can thus be concluded that the use of 20 minutes as growth time and cooling until 600°C under CH_4/H_2 flow in our CVD set-up gives better quality graphene.

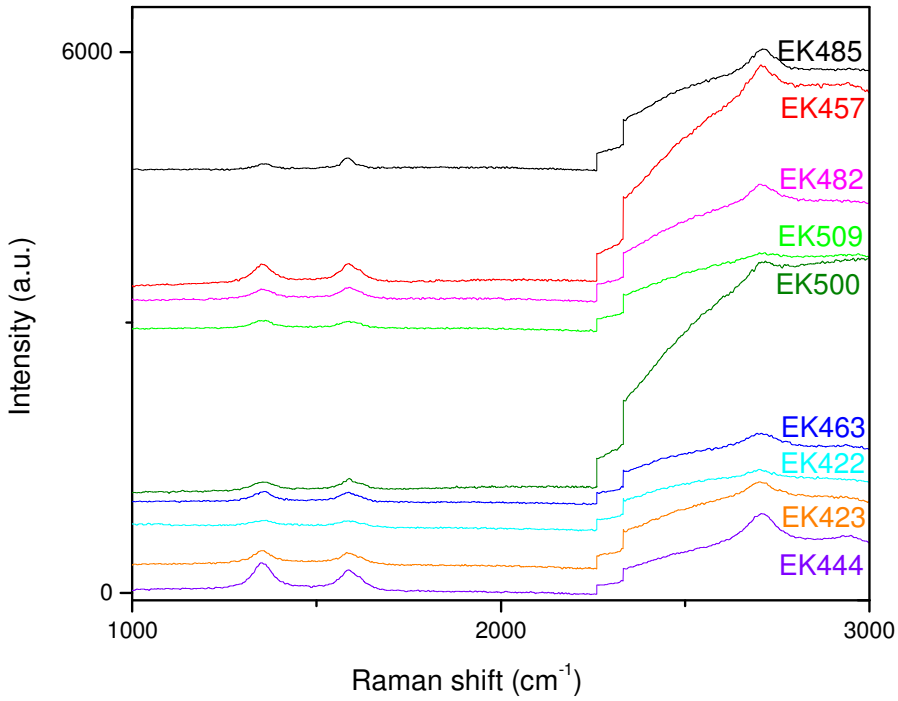

Figure 34: Raman spectra of CVD grown (on 600 nm Cu-Si/SiO_2) samples under different growth conditions by procedure#1. Raman spectroscopy has an offset at 2250 cm^{-1} due to the grating in the spectrometer.

The growth of graphene on 1000 nm Cu-SiO_2/Si and 25 μm Cu foils was also successful (Figure 35 and Figure 36). Similar to the findings for samples grown on 600 nm copper deposited film on SiO_2/Si, samples grown with different concentrations of carbon source have both close I_D/I_G and I_{2D}/I_G values (see Table 5, EK416 and EK415). The increase of methane concentration from 200 sccm to 875 sccm did not result in significant change in the quality of graphene.

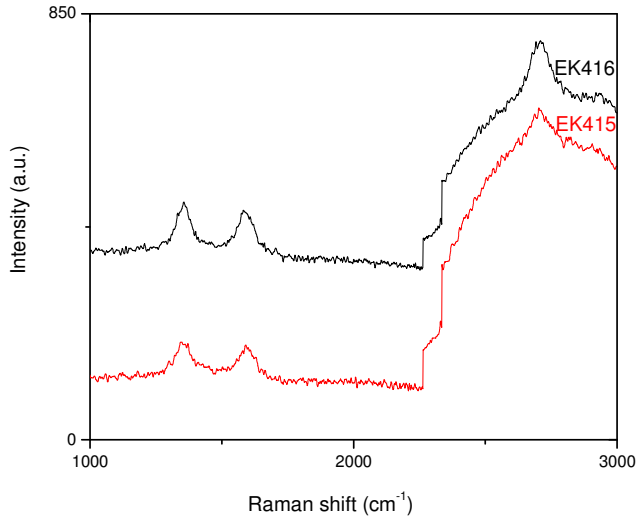

Figure 35: Raman spectra of CVD grown (on 1000 nm Cu-Si/SiO_2) samples under different growth conditions by procedure#1. Raman spectroscopy has an offset at 2250 cm^{-1} due to the grating in the spectrometer.

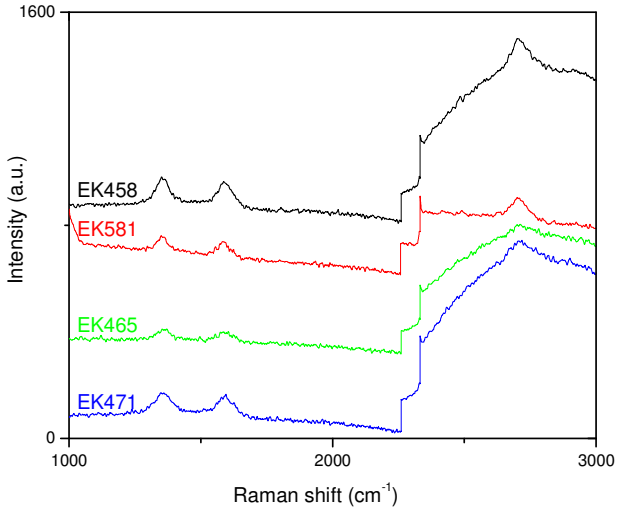

Figure 36: Raman spectra of CVD grown (on 25µm thick Cu foil) samples under different growth conditions by procedure#1. Raman spectroscopy has an offset at 2250 cm^{-1} due to the grating in the spectrometer.

The homogeneity of the graphene samples grown on 600 nm- and 1000 nm Cu-SiO_2/Si was checked by performing spectra from randomly selected areas (black and red spectra in Figure 37). Different than Raman data for Ni-catalyzed graphene samples, the spectra are almost identical meaning that the graphene is homogenous in the means number of

layers and defective sites. Figure 37 shows that homogeneous graphene layer is grown on copper layer using procedure#1.

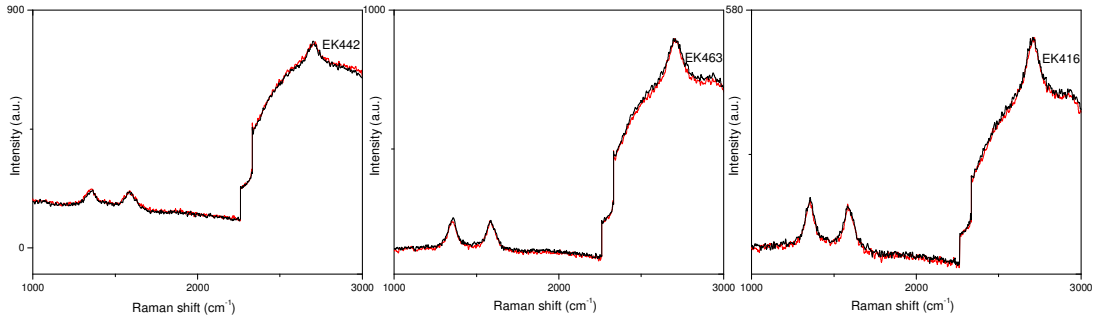

Figure 37: Raman spectra taken on two randomly chosen areas for each CVD grown (on 600 nm and 1000 nm Cu-Si/SiO_2) samples under different growth conditions by procedure#1. (see Table 5 for the detailed description of the samples EK442, EK463 and EK416 from left to right). Raman spectroscopy has an offset at 2250 cm^{-1} due to the grating in the spectrometer.

In procedure#1', all CVD steps except cooling were kept same as described in procedure#1. The mixture of methane and hydrogen was not used after CVD growth during cooling until 200°C in procedure#1'. It was aimed to understand the role of excluding the methane as a carbon source during cooling. The formation of graphene was not seen for 600 nm and 800 nm copper deposited wafers (EK424 and EK425) while seen on 25μm thick copper foils (EK581 and EK587, Figure 38).

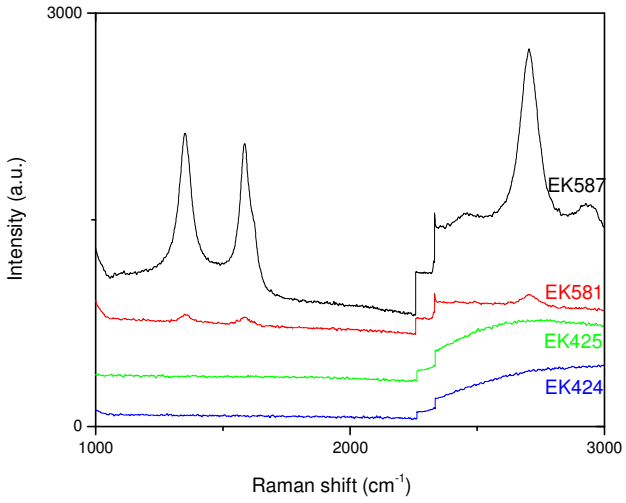

Figure 38: Raman spectra of CVD grown samples on 600-800 nm Cu-SiO_2 and 25 µm thick Cu foil by procedure #1'. Raman spectroscopy has an offset at 2250 cm^{-1} due to the grating in the spectrometer.

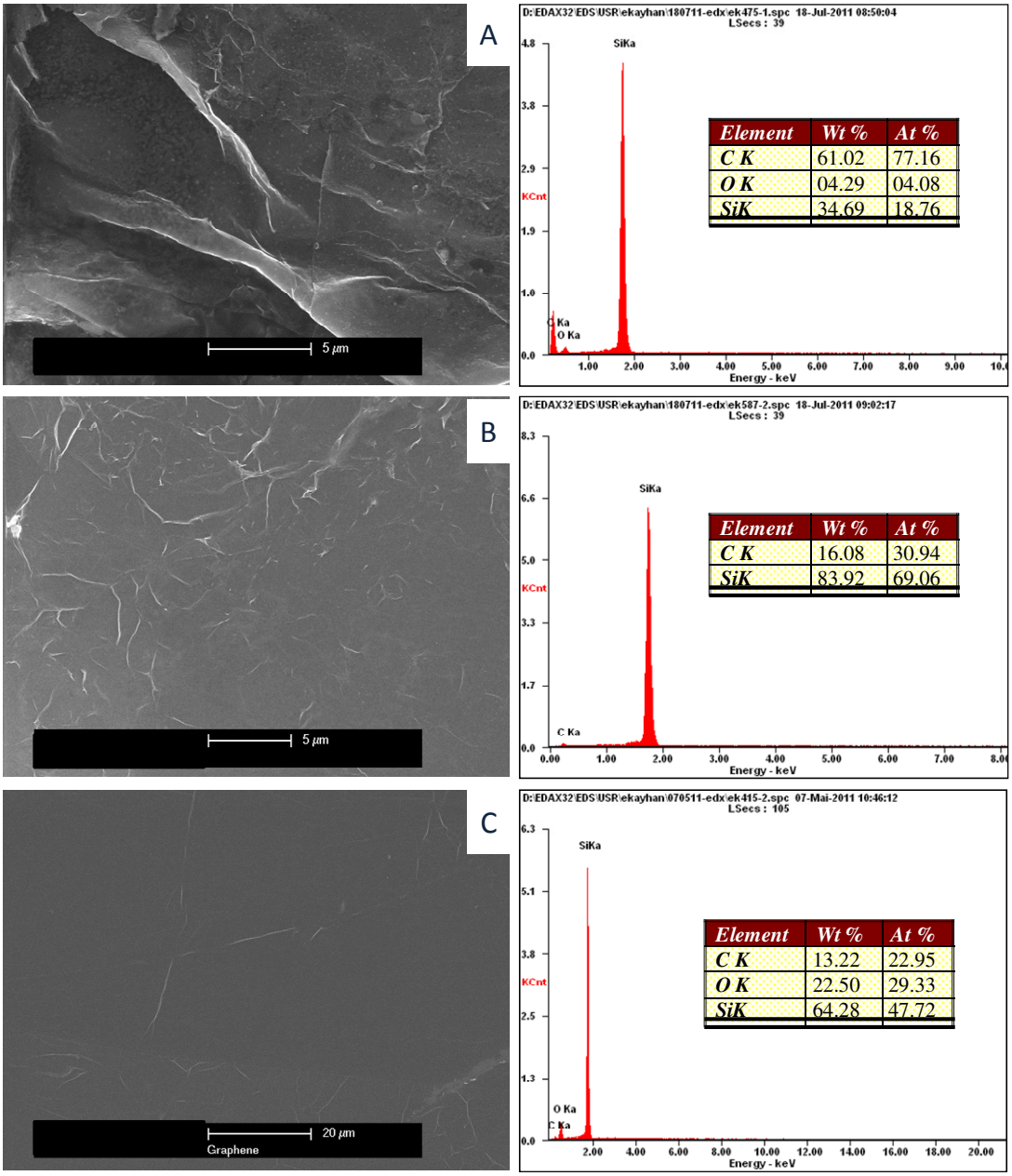

Figure 39: SEM images (left) and EDX data (right) of transferred Cu catalyzed samples on SiO_2 A. EK471, B. EK587 and C. EK415 (EK415 and EK471 are by procedure#1, whereas EK587 is by procedure#1', see Table 5 for the detailed description of the samples)

Graphene samples via 25μm Cu foil by procedure#1' are found to have similar defective structures like the ones used in procedure#1 (see I_D/I_G values, from the Table 5). This means that it is enough to use methane (as a carbon source) only at CVD growth stage and there is no need to use methane flow during cooling to grow graphene on copper foil

substrates. 200/200 sccm (H_2/CH_4) for 5 minutes at 990°C was found as optimum conditions to grow CVD graphene on copper foils at ambient pressure.

Besides, it should be noted that the growth of graphene on both copper deposited SiO_2/Si wafers and on Cu foil as substrates was achieved. Copper catalyzed graphene samples (EK415 and EK471 were by procedure#1, whereas EK587 was by procedure#1') were transferred on SiO_2 wafers (detailed in the 2.1.4 Transfer of graphene section below). SEM micrographs with EDX data are given in Figure 39. The sample grown on copper foil without using carbon source during cooling (EK587 by procedure#1') seems flat and thinner compared to samples grown by procedure#1 (EK415 and EK471). Similarly, EDX data also gives relatively lower carbon content for EK587 compared to others. This also suggests the formation of thinner graphene with procedure#1' in which methane was not used in the cooling step during CVD.

Procedure#2

Table 6. CVD growth procedure#2 for the synthesis of Cu catalyzed graphene

Procedure #, growth Pressure, Temperature	**Pre-annealing Conditions**	**H_2/CH_4 ratio, growth time**	**cooling step**	**Substrate**
#2, 760 Torr, 990°C	1. heating up to 990°C with Ar/H_2 (1000/325-500 sccm) flow 2. 15 min, 990°C with Ar/H_2 (1000/325-500 sccm) flow	5 min, $H_2/CH_4/Ar$ (325-500/25-100/1000 sccm)	slow cooling until RT under Ar/1000 sccm flow	25 μm thick Cu foil

That procedure has been reported for ambient pressure CVD (APCVD) growth of graphene where nickel was the catalyst [72]. Here, it is aimed to produce graphene by using copper instead nickel as a catalyst. For that purpose, Cu foils (25μm, 1x1 cm-sized, treated with acetic acid) were heated under Ar/H_2 (1000/325-500 sccm). Samples were held 15 minutes at 990°C without altering the gas-flow. Graphene growth was achieved with the introduction of CH_4 (25-100 sccm) into that gas mixture for 5 minutes at 990°C (see Table 6). Different than the reported study, the effect of relative concentrations of H_2 and CH_4 to the growth was analyzed. Samples codes with CVD parameters and calculated intensity ratios of Raman bands are given in Table 7.

Table 7: Calculated intensity ratios of the Raman bands (I_D/I_G and I_{2D}/I_G) for Cu catalyzed CVD grown samples using procedure#2.

Procedure 2-25 μm Cu foil	I_D/I_G	I_{2D}/I_G
EK634- 5 min (at 990°C) (1000/325/25 sccm) ($Ar/H_2/CH_4$) + cooling until 200°C w/Ar,1000sccm	0.25	1.2
EK639- 5 min (at 990°C) (1000/325/25 sccm) ($Ar/H_2/CH_4$) + cooling until 200°C w/Ar,1000sccm	0.27	1.2
EK684- 5 min (at 990°C) (1000/500/25 sccm) ($Ar/H_2/CH_4$) + cooling until 200°C w/Ar,1000sccm	---	0.56
EK630-1st Area-5 min (at 990°C) (1000/325/100 sccm) ($Ar/H_2/CH_4$) and cooling until 200°C w/Ar,1000sccm	0.38	0.34
EK630-2nd Area-5 min (at 990°C) (1000/325/100 sccm) ($Ar/H_2/CH_4$) and cooling until 200°C w/Ar,1000sccm	0.43	0.34

Raman spectra of the samples depict that graphene was successfully grown on copper foil substrates by procedure#2 (Figure 40, Figure 42 and Figure 43). I_D/I_G values of the samples via procedure#2 (~0.2-0.4) are lower than the samples synthesized using procedure#1 and 1' (~0.6-1.0). Therefore it can be concluded that it was possible to grow lower-defective graphene compared to procedure#1 and 1' by procedure#2 described above. The reproducibility of the synthesis of growth with procedure#2 was checked by repeating the experiments with different batches. Figure 40 belongs to the samples of different batches (EK634 and EK639) with the same CVD parameters (5 minutes 990°C, $Ar/H_2/CH_4$ (1000/325/25 sccm). Corresponding Raman spectra of the samples give similar intensity ratios of D/G (~0.25-0.27) and 2D/G (~1.2) indicating the formation few-layered low defective graphene (Figure 40).

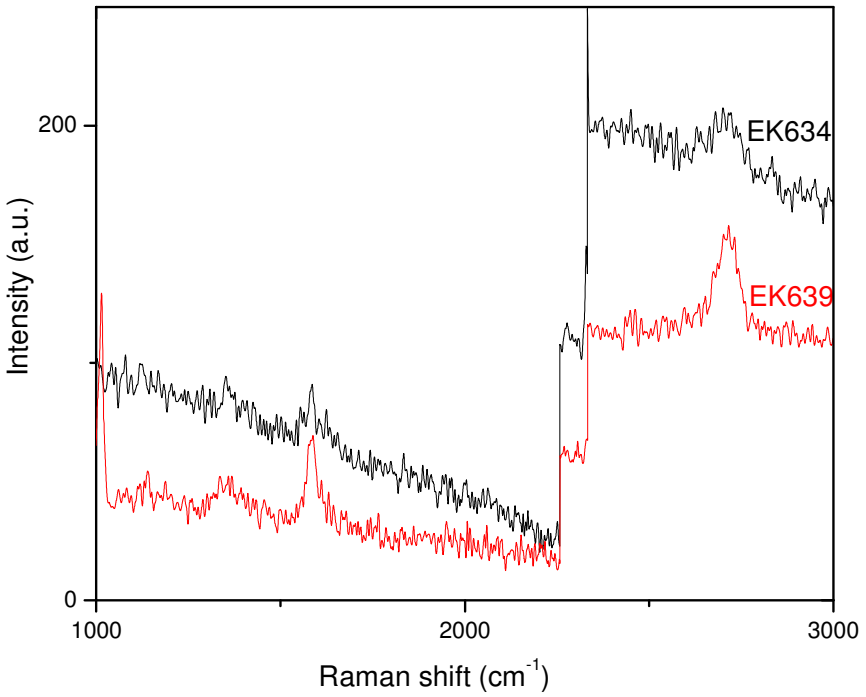

Figure 40: Raman spectra of two different batches of CVD grown samples on 25 μm thick Cu foils by procedure #2 with using same CVD parameters. Raman spectroscopy has an offset at 2250 cm^{-1} due to the grating in the spectrometer.

Wet-chemical pre-treatment of substrates with acetic acid was conducted to remove native oxide (CuO, Cu_2O) on the as-received Cu foils [48]. Moreover, it is also found crucial to further reduce the Cu substrate by annealing (at ~1000°C) under a hydrogen reducing atmosphere prior to introduction of carbon gas source in CVD process [73]. Although the copper oxide would be removed under hydrogen treatment, the use of acetic acid prior to that step eliminates the need for longer annealing times which would result in the deterioration of the copper film quality [71] (see Figure 41). It is stated that surface morphology is rearranged by introduction of atomic steps and elimination of surface structural defect during the annealing stage prior to deposition to facilitate graphene growth [74].

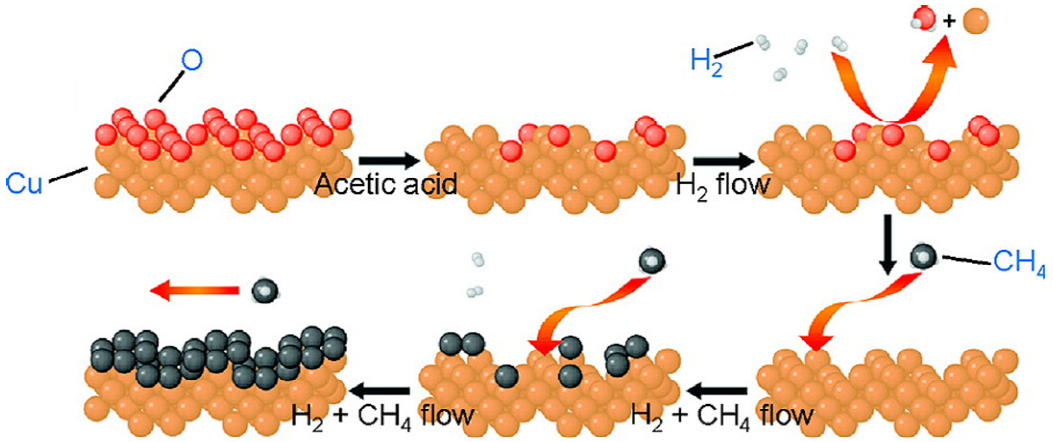

Figure 41: Graphene synthesis via copper as a catalyst. Pre-treatment of Cu prior to CVD growth and CVD growth steps are described [71].

The effect of H_2 amount on the quality of graphene was checked by increasing the amount from 325 sccm to 500 sccm prior to deposition and at deposition stages (EK684 is the sample code) (Figure 42). It is interesting to find out that D band (due to the defects in the structure of graphene) was not identified in the spectrum of the sample in which higher hydrogen concentration flow was used (500 sccm). This result can be attributed to the elimination of the defects on the graphene surface due to increased concentration of hydrogen. However, the 2D/G ratio decreases (from ~1.22 to 0.56) indicating that the number of layers gets higher with the higher hydrogen concentration. This can be attributed to the increased concentration of active carbon species formed by cracking of methane into the higher amount of hydrogen in CVD process.

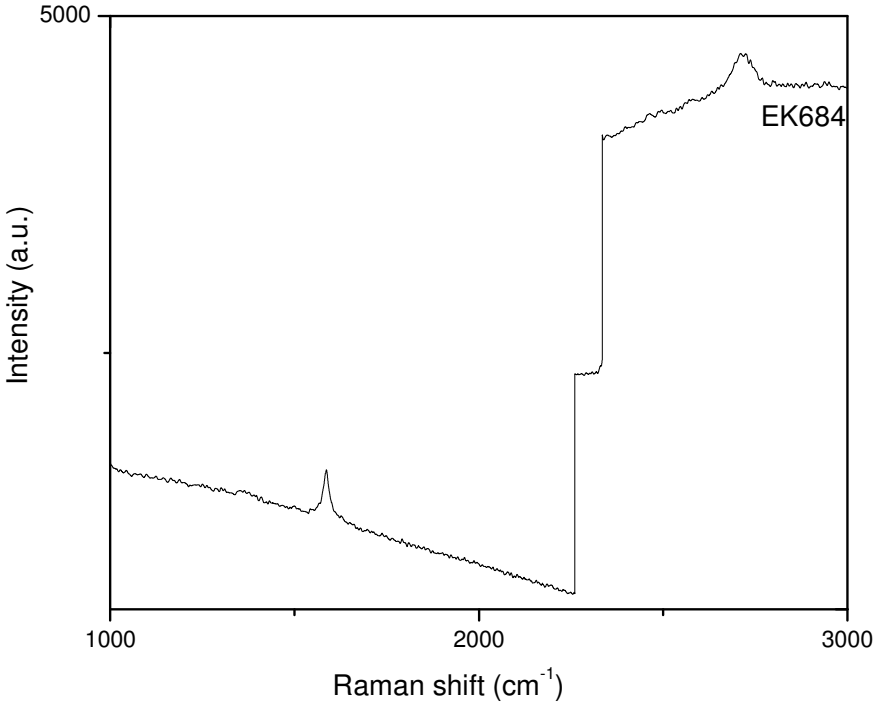

Figure 42: Raman spectrum of CVD grown sample (EK684) on 25 μm thick Cu foil by procedure #2. Raman spectroscopy has an offset at 2250 cm^{-1} due to the grating in the spectrometer.

Besides the hydrogen concentration, the role of using a higher amount of methane as a carbon source is analyzed (Figure 43) by applying 100 sccm methane instead 25 sccm (with the sample code of EK630). Similar to the findings when using a higher concentration of hydrogen, the number of graphene layers gets increases with an increase of methane amount (2D/G ratio decreases from ~1.2 to 0.38). Moreover, graphene becomes more defective (D/G ratio raises from ~0.25 to 0.43) if a higher amount of methane precursor is used.

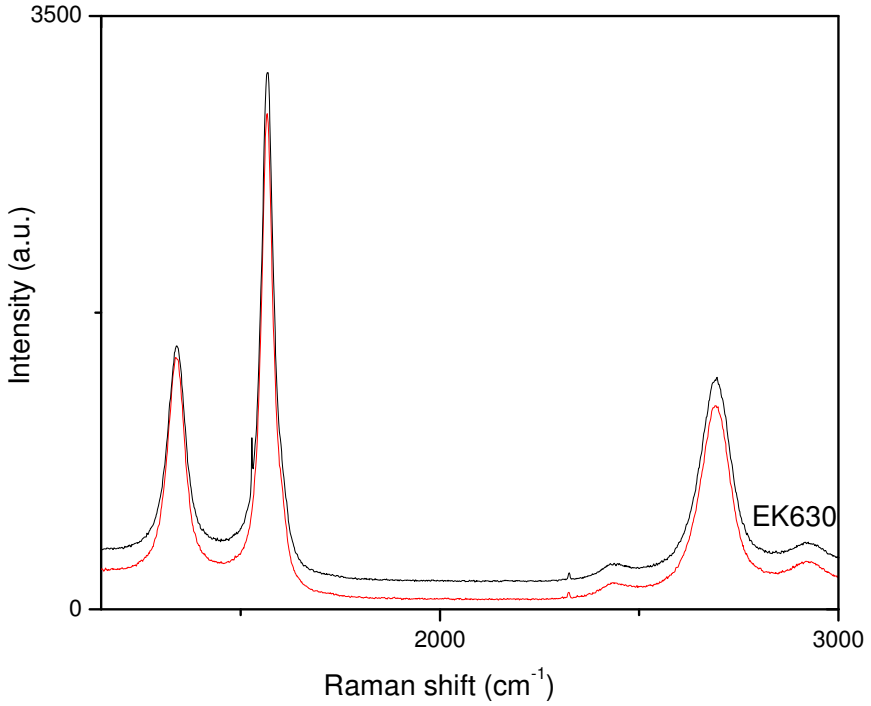

Figure 43: Raman spectra taken on two randomly chosen areas for CVD grown sample (EK630) catalyzed on 25μm thick Cu foil.

Comparing the results of samples obtained by procedure#2 and procedure#1 and 1', it can be seen that procedure#2 facilitates lower layered graphene (higher 2D/G ratio) on copper foils with lower defects (lower D/G ratio).

Procedure#3

Table 8: CVD growth procedure#3 for the synthesis of Cu catalyzed graphene

Procedure #, growth Pressure, Temperature	**Pre-annealing Conditions**	**H_2/CH_4 ratio, growth time**	**cooling step**	**Substrate**
#3, 760 Torr, 990°C	heating up to 990°C with Ar/H_2 (500/100 sccm) flow	5-15 min, $Ar/H_2/CH_4$ (500/100/50-200 sccm)	1. shock-cooling -dragging sample with magnet- with Ar/500 sccm or 2. slow-cooling under Ar/500 sccm	25 μm thick Cu foil

In this synthesis procedure, acetic acid cleaned copper foils were placed inside the CVD set-up and heated up to 990°C under Ar/H_2 (500/100 sccm). CH_4 (50-200 sccm) was added in that gas-mixture and flown for 5-15 minutes at 990°C. Then, the samples were taken out from the oven either by shock-cooling or slow-cooling under Ar of 1000 sccm flow (see Table 8). CVD was conducted at ambient pressure instead of a lower pressure of 9.3 Torr [75]. Moreover, growth time and effect of slow cooling were also monitored. The respective sample codes with the descriptions and calculated relative ratios of the bands of D/G and 2D/G are given in Table 9.

Table 9: Calculated intensity ratios of the Raman bands (I_D/I_G and I_{2D}/I_G) for Cu catalyzed CVD grown samples by using procedure#3.

Procedure 3- 25 μm Cu foil	I_D/I_G	I_{2D}/I_G
EK664-1st Area-15 min(at 990°C) (500/100/200 sccm) ($Ar/H_2/CH_4$) + shock-cooling w/1000 sccm of Ar	0.73	0.69
EK664-2nd Area-15 min(at 990°C) (500/100/200 sccm) ($Ar/H_2/CH_4$) + shock-cooling w/1000 sccm of Ar	0.77	0.67
EK665-15 min(at 990°C) (500/100/200 sccm) ($Ar/H_2/CH_4$) and slow cooling until 200°C w/1000 sccm of Ar	0.28	0.93
EK670-15 min(at 990°C) (500/100/50 sccm) ($Ar/H_2/CH_4$) and shock-cooling w/1000 sccm of Ar	0.35	0.57
EK674-5 min(at 990°C) (500/100/50 sccm) ($Ar/H_2/CH_4$) and shock-cooling w/1000 sccm of Ar	0.41	0.84
EK677-5 min(at 990°C) (500/100/50 sccm) ($Ar/H_2/CH_4$) and slow cooling until 200°C w/1000 sccm of Ar	0.34	0.92

Figure 44 corresponds to samples of which CVD parameters are all kept constant as described above but methane concentration (50-200 sccm) and growth time (5-15 min) vary in the samples. The existence of the characteristic Raman bands of graphene (D, G and 2D) depicts that graphene is grown on 25μm Cu foils by using that procedure as well. In agreement with the case in other procedures described so far, the sample produced by higher concentration methane is found to have higher defects with higher D/G intensity ratio (0.73-0.77 for EK664) than that of sample grown by lower concentration methane (0.35 and 0.41 for EK670 and EK674 respectively) too.

Growth time of graphene was increased from 5 min to 15 min. Both samples have close I_D/I_G ratio values (0.35 and 0.41 for EK670 and EK674). This means that the use of longer CVD growth time didn't lead to a significant difference in the quality of graphene.

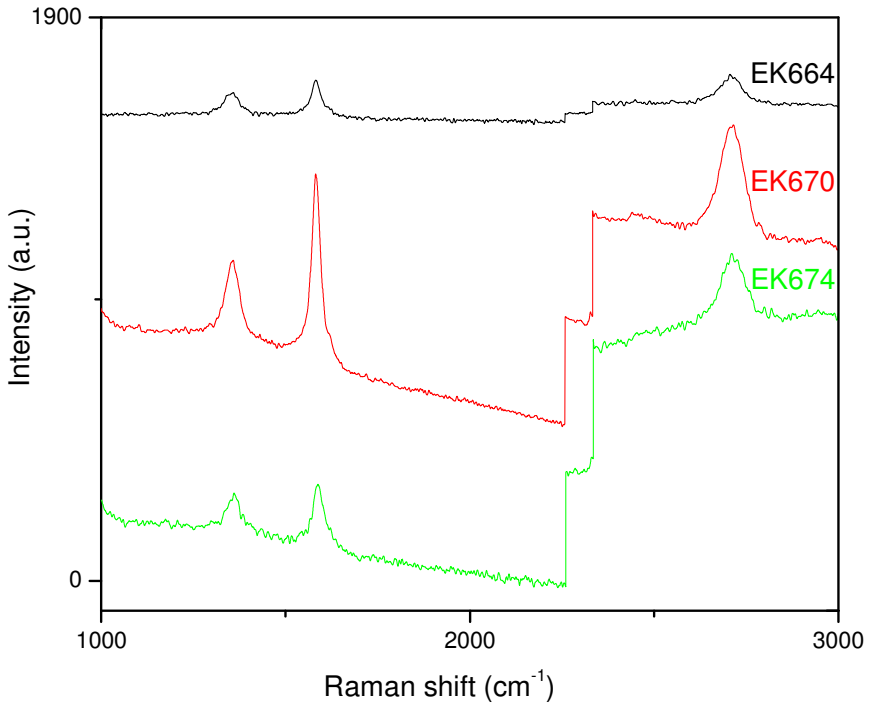

Figure 44: Raman spectra of CVD grown samples (EK664, EK670 and EK674) on 25 μm thick Cu foil by procedure #3. Raman spectroscopy has an offset at 2250 cm^{-1} due to the grating in the spectrometer.

The effect of cooling time was also checked by lowering the temperature of the samples after the CVD-growth step either by slow cooling to room temperature or by fast cooling while dragging the samples from the hottest zone to the cooler part of the oven under an Ar flow. Samples with different CVD conditions show that defects are more introduced to the graphene structure during shock cooling of the samples (Figure 45). Intensity ratio of D/G values are all smaller in the samples which have cooled slowly (0.28 and 0.34 for EK665 and EK677) compared to ones which were shock-cooled (0.73-0.77 and 0.41 for EK664 and EK674)

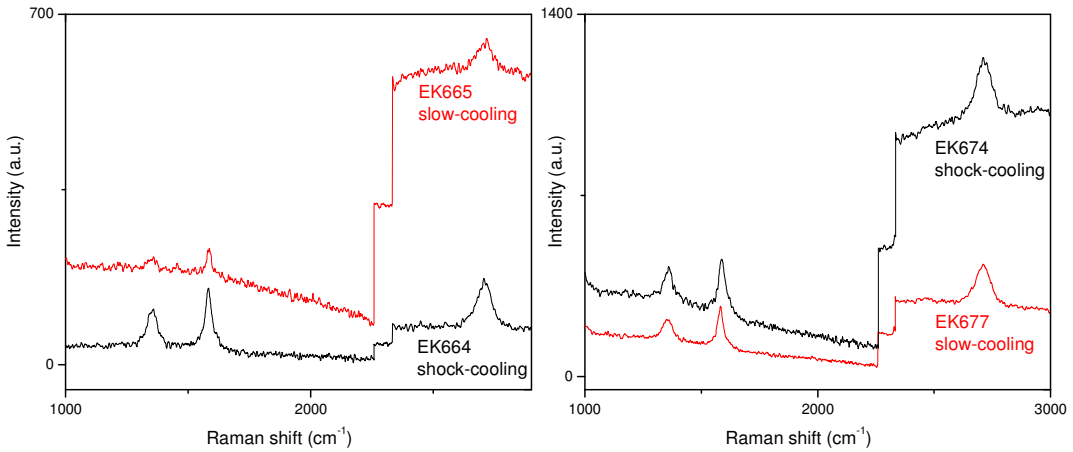

Figure 45: Raman spectra of CVD grown samples on 25 µm thick Cu foils by procedure#3. EK664 and EK665; EK674 and EK677 are with same CVD growth parameters except with the cooling rates. Raman spectroscopy has an offset at 2250 cm^{-1} due to the grating in the spectrometer.

Homogeneity of the samples was also checked by performing micro Raman spectra from randomly chosen areas on the CVD grown graphene samples. Figure 46 shows that spectra performed on different areas of graphene sample are similar concerning relative intensities of D, G and 2D Raman bands of graphene. This depicts that graphene is grown homogenous on copper substrate with similar defect density and number of layers.

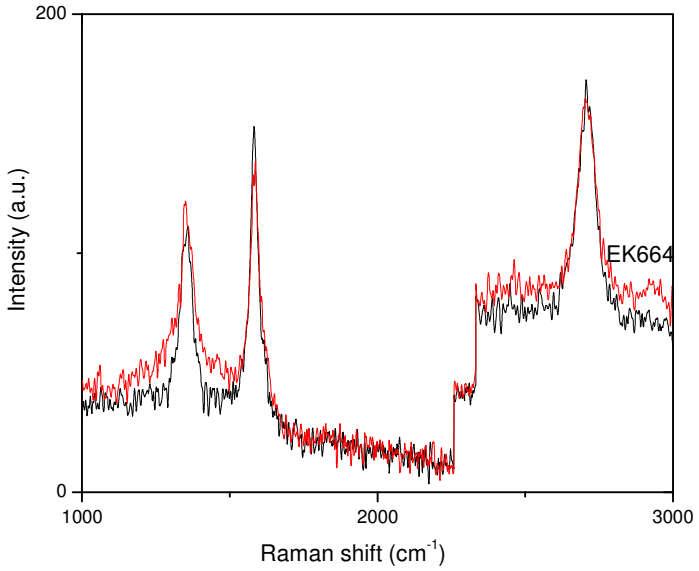

Figure 46: Raman spectra taken on two randomly chosen areas for CVD grown sample (EK664) catalyzed on 25μm thick Cu foil by procedure#3. Raman spectroscopy has an offset at 2250 cm^{-1} due to the grating in the spectrometer.

Procedure 3'

Table 10. CVD growth procedure#3' for the synthesis of Cu catalyzed graphene

Procedure #, growth Pressure, Temperature	**Pre-annealing Conditions**	**H_2/CH_4 ratio, growth time**	**cooling step**	**Substrate**
#3', 760 Torr, 990°C	heating up to 990°C with Ar/H_2 (1000/1000 sccm) flow	1-5-15-60 min, $Ar/H_2/CH_4$ (1000/1000/5-13-25-100 sccm)	slow cooling until RT under Ar/1000 sccm flow	25 μm thick Cu foil

Cu foils cleaned prior to CVD process were loaded into the CVD set-up and heated to 990°C with the mixture of H_2/Ar (1000/1000 sccm). CVD growth was conducted by introducing methane (5-13-25-100 sccm) to that gas mixture for certain time (1-5-15-60 min) at 990°C. Then the samples were cooled down slowly under Ar atmosphere (of 1000 sccm) (Table 10). Different than procedure#3, amounts of the H_2 and Ar gases were increased while CH_4 was decreased. The respective sample codes with the descriptions and calculated ratios of the bands of D/G and 2D/G are given in Table 11.

Table 11: Calculated intensity ratios of the Raman bands (I_D/I_G and I_{2D}/I_G) for Cu catalyzed CVD grown samples by procedure#3'.

Procedure 3'- 25 μm Cu foil	I_D/I_G	I_{2D}/I_G
EK737-15 min(at 990°C) (1000/1000/25 sccm) ($Ar/H_2/CH_4$)	--	2.2
EK738-60 min(at 990°C) (1000/1000/25 sccm) ($Ar/H_2/CH_4$)	--	1.8
EK778-1st Area-1 min(at 990°C) (1000/1000/100 sccm) ($Ar/H_2/CH_4$)	0.13	0.38
EK778-2nd Area-1 min(at 990°C) (1000/1000/100 sccm) ($Ar/H_2/CH_4$)	0.093	0.45
EK776-1st Area-transferred on SiO_2/Si-1 min(at 990°C) (1000/1000/100 sccm) ($Ar/H_2/CH_4$)	0.32	0.33
EK776-2nd Area-transferred on SiO_2/Si-1 min(at 990°C) (1000/1000/100 sccm) ($Ar/H_2/CH_4$)	0.34	0.30
EK774-5 min(at 990°C) (1000/1000/100 sccm) ($Ar/H_2/CH_4$)	0.12	0.40
EK773-transferred on SiO_2/Si-5 min(at 990°C) (1000/1000/100 sccm) ($Ar/H_2/CH_4$)	0.65	0.30

The procedure worked out using 100 sccm and 25 sccm CH_4. However, further decreasing methane concentration to 13 and 5 sccm was not sufficient to form graphene on copper foil. Only fluorescence due to copper is observed in the spectra of the samples where 5 and 13 sscm of methane were used (see 5. Appendix, Figure 133). Effect of methane concentration and growth time on the graphene formation was checked by performing CVD experiments for different time durations. Raman spectra taken after 15 and 60 minutes growth time ($H_2/Ar/CH_4$ (1000/1000/25 sccm, EK737 and EK738 respectively) as well as 1 and 5 minutes growth time ($H_2/Ar/CH_4$ (1000/1000/100 sccm, EK778 and EK774 respectively) are shown (Figure 47). As also found for all the other procedures#1 to #3, increased amount of methane gives a higher D/G ratio, which means more defective with the slightly lower 2D/G ratio, higher number of layers. The best sample has no D band and higher 2D/G ratio (2.2, 15 minutes growth with $H_2/Ar/CH_4$ (1000/1000/25 sccm), EK737) suggesting the existence of two to three layers of graphene. Besides, no significant differences in the band ratios (D/G and 2D/G) are found for the samples grown under different reaction time.

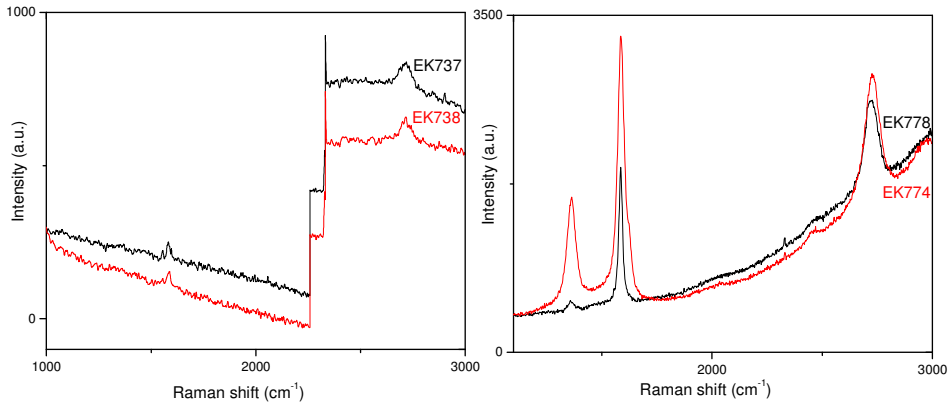

Figure 47: Raman spectra of CVD grown samples on 25 μm thick Cu foils by procedure #3. EK737 and EK738 (15 min and 60 min); EK778 and EK774 (1 min and 5 min) have same CVD growth parameters except growth time. Spectra shown at left were performed by Raman spectroscopy that has an offset at 2250 cm^{-1} due to the grating in the spectrometer.

Next, graphene samples grown on Cu-foils with $H_2/Ar/CH_4$ (1000/1000/100 sccm) mixture were transferred (as described in 2.1.4 Transfer of graphene) and placed on SiO_2/Si wafers. Figure 48 gives the spectra for the graphene samples on Cu foil substrate (EK778 and EK774) and samples that were separated from underlying Cu foil and transferred on SiO_2/Si wafers (EK776 and EK773). Fluorescence of copper is eliminated after the transfer process so no increase in the background of the spectra of transferred samples is seen (Figure 48). As expected, due to the transfer process defects were introduced most probably during the separation of the copper metal from the graphene. D/G ratios are thus higher in the transferred samples (from EK778 of 0.093 D/G to EK776 of ~0.30 and from EK774 of 0.12 D/G ratio to EK773 of 0.65). The number of layers might be also slightly changing due to the probable folding and sticking of the sites while transferring them. Therefore, 2D/G ratios are slighlty smaller in transferred samples compared to not-transferred ones (from 0.45 to 0.30). Moreover, the samples both before the transfer process as well as after were all found homogenous with values of I_D/I_G and I_{2D}/I_G which are very close. EK778 is an example for the sample on copper foil and EK776 is for the transferred one (see Table 11).

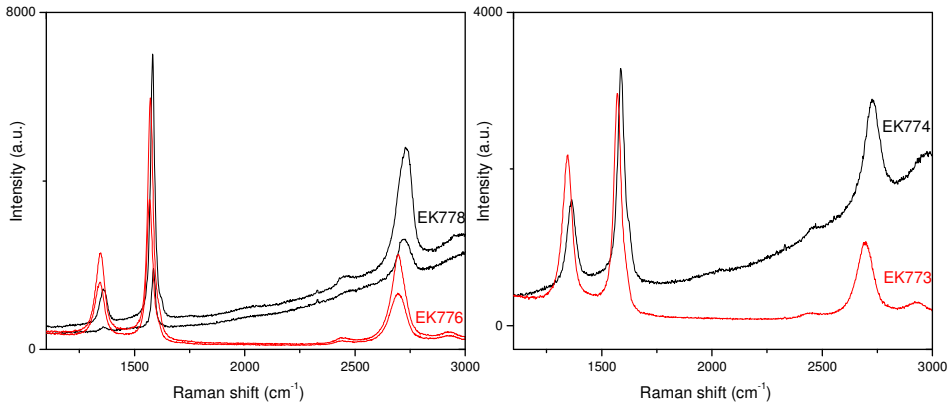

Figure 48: Raman spectra of, as CVD grown samples on 25 µm thick Cu foil by procedure #3' (in black, EK778 and EK774), and transferred CVD samples on Si/SiO_2 wafer (in red, EK776 and EK773).

Procedure#4

Table 12. CVD growth procedure#4 for the synthesis of Cu catalyzed graphene

Procedure #, growth Pressure, temperature	**Pre-annealing Conditions**	**H_2/CH_4 ratio, growth time**	**cooling step**	**Substrate**
#4, 760 Torr, 990°C	1. evacuated to a vacuum of 20 mTorr for 10 min 2. pump is switched off, 760 Torr with 500 sccm of Ar/H_2 (467/33 sccm) 3. 60 min, 990°C Ar/H_2 (467/33 sccm)	60-120 min, $H_2/CH_4/Ar$ (30/50/420 sccm)	slow-cooling under Ar/500 sccm	25 µm thick Cu foil

This procedure is also for the CVD growth graphene at atmospheric pressure like the other procedures described above (see Table 12). However, different than the procedures so far, the system is pumped until 10^{-1} mbar, flushed with Ar and pumped again multiple times prior to the CVD process. Then 500 sccm of Ar/H_2 (467/33 sccm) mixture is flown into the system while increasing the temperature to 990°C [76]. The temperature was held for 60 minutes without altering the gas flow. Then, 500 sccm mixture of $H_2/CH_4/Ar$ (30/50/420 sccm) is flown into the system for 60 minutes or 120 minutes. Samples were slowly cooled down under Ar gas flow (500 sccm).

Experiments on the CVD growth of graphene by using that procedure were successful for 60 and 120 minutes reaction times (Figure 49). The spectra were also performed on both side of the copper foil to check the growth of the graphene on the front and back sides (Figure 50). D/G and 2D/G ratios were calculated and given in Table 13.

Table 13: Calculated intensity ratios of the Raman bands (I_D/I_G and I_{2D}/I_G) for Cu catalyzed CVD grown samples by procedure#4.

Procedure 4- 25 μm Cu foil	I_D/I_G	I_{2D}/I_G
EK800-from front side-60 min (at 990°C) (420/30/50 sccm) ($Ar/H_2/CH_4$)	0.28	1.9
EK800-from back side-60 min (at 990°C) (420/30/50 sccm) ($Ar/H_2/CH_4$)	0.37	2.0
EK802-120 min(at 990°C) (420/30/50 sccm) ($Ar/H_2/CH_4$)	0.41	2.1

Intensity ratios of D/G (0.28-0.41) and 2D/G (1.9-2.1) are quite close to each other regardless of the CVD growth time and areas where the spectra were taken. So, this method also gives few layered graphene (<4 layers of graphene) with the relatively higher 2D/G ratios like procedure#3'. But, they are still not as good as the best sample of copper catalyzed graphene, EK737 by procedure#3, as judged by the lower D/G ratio of EK737. The reason for the higher D/G ratio in EK800 and EK802 samples than in EK737 can be related to the use of lower hydrogen concentration.

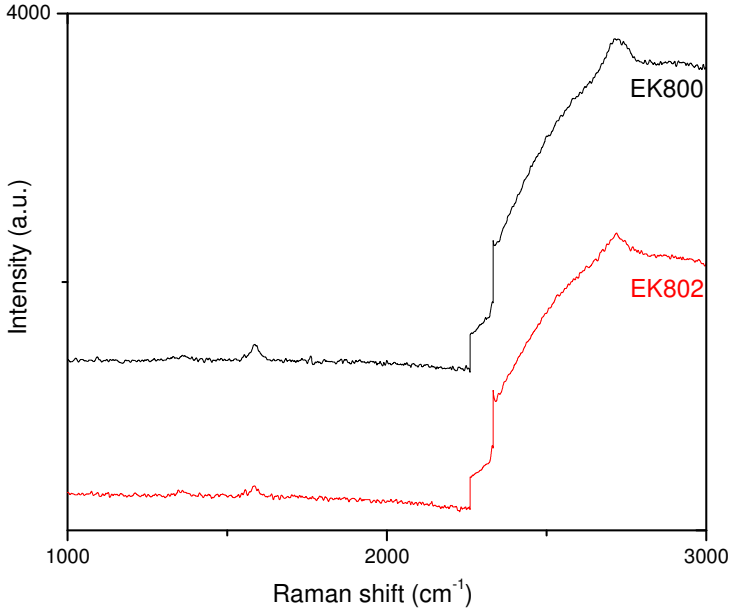

Figure 49: Raman spectra of CVD grown samples on 25 µm thick Cu foils (EK800 and EK802) by procedure #4. Raman spectroscopy has an offset at 2250 cm^{-1} due to the grating in the spectrometer.

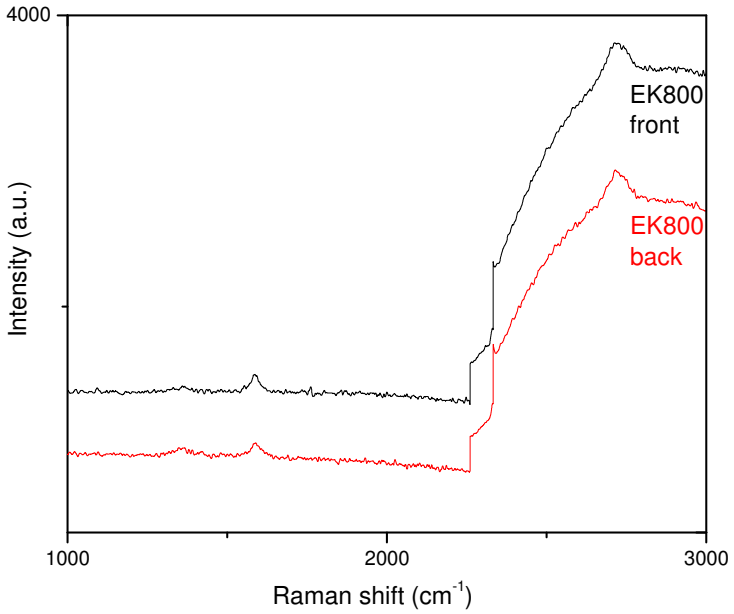

Figure 50: Raman spectra taken from front side and back side of CVD grown sample on 25 µm thick Cu foils by procedure #4. Raman spectroscopy has an offset at 2250 cm^{-1} due to the grating in the spectrometer.

In summary, growth of bilayer to multilayer graphene on Cu has been observed under ambient pressure CVD conditions [77]. Bhaviripudi *et al* argued that non-uniform multi-layer graphene is favored at ambient pressure due to the lowered mass transport rate of active carbon species through the boundary layer in the steady state gas flow [78]. Therein it has been stated that carbon precursor supply should be reduced to ppm levels to deposit uniform single-layer graphene on copper at ambient pressure. Under our ambient pressure CVD conditions in our set-up, compared to all other procedures that I applied so far, procedure#3' (EK737, 15 minutes at 990°C with 1000 sccm Ar/1000 sccm H_2/25 sccm CH_4) gives an even better quality graphene which is defect-free and bilayer. This can be probably attributed to the lower methane concentration with the optimized hydrogen gas flow [77a, 79]. Wu et al. reported that high CH_4 precursor concentration which increases the concentration of C adatom rapidly, results in a highly preferred dense nucleation of multi-layer graphene grains rather than of that single-layer graphene grains [77a]. Besides the concentration of methane, concentration of hydrogen is also crucial since cracking of methane to form active carbon species for graphene growth is promoted with hydrogen [79].

Procedure#5

Table 14. CVD growth procedure#5 for the synthesis of Cu catalyzed graphene

Procedure #, growth Pressure, temperature	**Pre-annealing Conditions**	**H_2/CH_4 ratio, growth time**	**cooling step**	**Substrate**
#5, 5-15 Torr, 990°C	1. heating up to 990°C with H_2 (1-5 sccm) 2. 30 min, 990°C with H_2 (1-5 sccm)	10 min, H_2/CH_4 (1-2/5 and 5/25 sccm)	shock-cooling -dragging sample with magnet- with H_2 (1-5 sccm)	25 µm thick Cu foil

The procedures #1 to #4 applied so far were for ambient pressure CVD (APCVD) growth of graphene. The reason for using mostly low pressure to grow graphene on copper might be attributed to the reaction conditions that decrease the oxidation probability of copper [80]. In this way, metallic copper serving as a catalyst for graphene growth would remain active during the CVD process. A study of carbon isotope labeling of the methane precursor used for the CVD growth has clarified the mechanism of graphene formation on copper surfaces. In particular, it has revealed that partial pressure of methane plays an important role to form single or multilayer graphene on copper surface [81]. It has been

shown that when higher partial pressure of the methane gas was used in CVD growth of graphene, nucleation density of active carbon species increased as well. This is followed by a multilayer seeding of carbon on the copper surface [79].

Low pressure CVD growth of graphene was examined by utilizing procedures#5 and 5' by studying the effect of pressure, growth time and concentration of precursor gases (Table 14).

Table 15: Calculated intensity ratios of the Raman bands (I_D/I_G and I_{2D}/I_G) for Cu catalyzed CVD grown samples by using Procedure#5.

Procedure 5	I_D/I_G	I_{2D}/I_G
EK849-1st area-2 min (at 990°C, 15 Torr) (2/5 sccm) (H_2/CH_4)	0.24	0.47
EK849-2nd area-2 min (at 990°C, 15 Torr) (2/5 sccm) (H_2/CH_4)	0.18	0.18
EK851-1st area-5 min (at 990°C, 15 Torr) (2/5 sccm) (H_2/CH_4)	0.16	0.16
EK851-2nd area-5 min (at 990°C, 15 Torr) (2/5 sccm) (H_2/CH_4)	0.14	0.17
EK861-1st area-2 min (at 990°C, 5 Torr) (2/5 sccm) (H_2/CH_4)	0.25	0.17
EK861-2nd area-2 min (at 990°C, 5 Torr) (2/5 sccm) (H_2/CH_4)	0.23	0.16
EK861-3rd area-2 min (at 990°C, 5 Torr) (2/5 sccm) (H_2/CH_4)	0.22	0.26
EK861-4th area-2 min (at 990°C, 5 Torr) (2/5 sccm) (H_2/CH_4)	0.31	0.30
EK861-5th area-2 min (at 990°C, 5 Torr) (2/5 sccm) (H_2/CH_4)	0.48	0.14
EK861-6th area-2 min (at 990°C, 5 Torr) (2/5 sccm) (H_2/CH_4)	0.22	0.38
EK861-7th area-2 min (at 990°C, 5 Torr) (2/5 sccm) (H_2/CH_4)	0.18	0.69
EK863-1st area-5 min (at 990°C, 5 Torr) (2/5 sccm) (H_2/CH_4)	0.26	0.15
EK863-2nd area-5 min (at 990°C, 5 Torr) (2/5 sccm) (H_2/CH_4)	0.51	0.19
EK863-3rd area-5 min (at 990°C, 5 Torr) (2/5 sccm) (H_2/CH_4)	0.80	0.48
EK864-5 min (at 990°C, 5 Torr) (2/5 sccm) (H_2/CH_4)	0.72	0.52
EK862-1st area-1 min (at 990°C, 2 Torr) (2/5 sccm) (H_2/CH_4)	0.22	--
EK862-2nd area-1 min (at 990°C, 2 Torr) (2/5 sccm) (H_2/CH_4)	0.43	--

Copper foils are cut and cleaned with acetic acid and loaded into the CVD set-up. CVD reactor is flushed with Ar flow (of 100 sccm) and pumped down to baseline pressure of ~1x10^{-2} Torr. That step is repeated three times and the Ar flow is stopped. A constant pressure (of 2, 5, 15, 20 and 70 Torr) is established by introducing hydrogen (1-2-5 sccm) to the system. The samples are heated up to 990°C and the temperature is held at 990°C for 30 min without altering the gas. After performing the growth with addition of methane to the flow (H_2/CH_4) (1-2/5 and 5/25 sccm)) (for 1-2-5-10 min), samples are shock-cooled -by dragging the sample holder with a magnet- under H_2 flow (of 1-2-5 sccm) out of the reaction zone [82].

Raman spectra of the samples synthesized at different pressures depict that graphene is formed on copper foils in that low pressure regime (Figure 51).

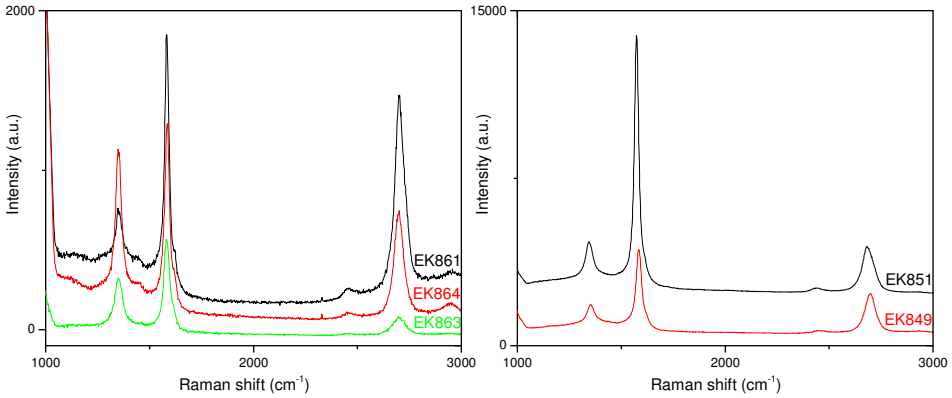

Figure 51: Raman spectra of low pressure CVD grown samples on 25 μm thick Cu foil (EK861, EK864, EK863 were grown at 5 Torr and EK851, EK849 were synthesized at 15 Torr) by procedure #5.

The effect of pressure (5-15 Torr) on the quality of graphene could not be determined because sample by procedure#5 is already not homogeneous as 2D/G ratios of spectra from randomly chosen areas vary (see Figure 52). The reason of the variation in the number of layers through the graphene surface might be attributed to the presence of different dense active carbon species adsorbed on copper surface that leads to growth of graphene islands with different number of layers [81].

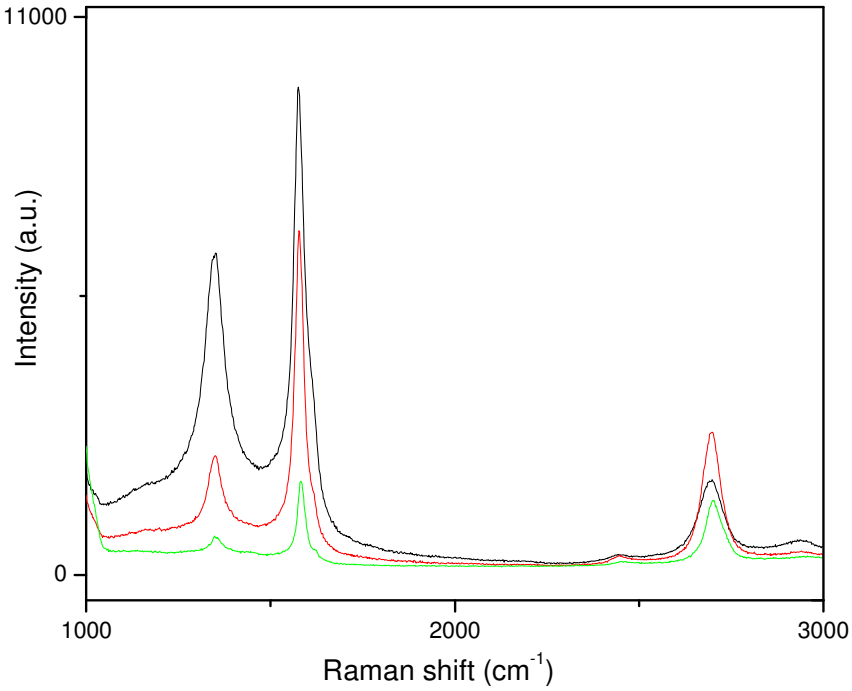

Figure 52: Raman spectra of three areas chosen randomly from CVD graphene sample (EK861) grown at low pressure 5 Torr on 25 μm thick Cu foil by procedure #5.

Growth of graphene could not be achieved at 2 Torr (EK862) with the same gas concentrations as for 5 and 15 Torr conditions (see Appendix, Figure 134). This can be associated with the lower partial pressure of hydrogen that is not sufficient to promote enough active carbon species for graphene formation. As shown theoretically by DFT calculations, chemisorption of methane even on the copper surface to form active carbon species of $(CH_3)_s$, $(CH_2)_s$, $(CH)_s$, or C_s is not thermodynamically favorable in the absence of hydrogen gas in the system [83]. The catalytic role of hydrogen in activating carbon is discussed in detail and illustrated by reactions 1 and 4 in reaction scheme (Figure 53)[79]. First dissociation of molecular hydrogen on copper into active hydrogen atoms that ensures the activation of physisorbed methane, takes place. Following the formation of $(CH_2)_s$, more active surface bound $(CH_2)_s$ and $(CH)_s$ species are formed in the subsequent dehydrogenation steps [79].

$$Cu + H_2 \Leftrightarrow 2H_s \quad (1)$$

$$Cu + CH_4 \rightarrow (CH_3)_s + H_s \text{ - slow} \quad (2)$$

$$Cu + CH_4 \Leftrightarrow (CH_4)_s \quad (3)$$

$$(CH_4)_s + H_s \Leftrightarrow (CH_3)_s + H_2 \quad (4)$$

$$(CH_3)_s + \text{graphene} \Leftrightarrow (\text{graphene}+C) + H_2 \quad (5)$$

$$H_s + \text{graphene} \Leftrightarrow (\text{graphene-C}) + (CH_x)_s \quad (6)$$

Figure 53: Illustration of catalytic role of hydrogen in activating carbon [79]. H_s represents active hydrogen atoms whereas $(CH_4)_s$ refers to physisorbed methane and $(CH_3)_s$ represents the surface bound radical derived from methane.

Moreover, a growth time of 1 min growth time is still not enough to cover the copper surface with a continuous carbon layer. Confocal microscope image on the transferred sample depicts that catalyst seeds are observed rather than a continuous film covering the surface (see Appendix, Figure 134).

Different growth time (2 and 5 min) didn't give difference in the number of layers with having close 2D/G ratios. It is also stated that once the multilayer seeds are nucleated due to the excess of supplied active carbon species at very early stage then the growth of graphene on the complete surface takes place [77a]. That means growth time only affects the time needed to form a complete layer. In line with that study, growth of graphene was suggested to start by the formation of a multilayer cluster during Cu-catalyzed chemical vapor deposition (at 0.35 Torr) using $^{12}CH_4$ and $^{13}CH_4$ precursor gases [81]. It is also reported that size of that seed increases and growth speed of a particular layer depends on its proximity to the copper surface. This leads to a fast growth of the layer close to the substrate with limiting growth rate of the upper layers that still continues to grow till to get a full blocking of all active copper surface [81].

Procedure#5'

Table 16. CVD growth procedure#5' for the synthesis of Cu catalyzed graphene

Procedure #, growth Pressure, Temperature	Pre-annealing Conditions	H_2/CH_4 ratio, growth time	cooling step	Substrate
#5', 2-5-15-20-70 Torr, 990°C	1. heating up to 990°C with H_2 (1-5 sccm) 2. 30 min, 990°C with H_2 (1-5 sccm)	10 min, H_2/CH_4 (1-2/5 and 5/25 sccm)	slow cooling with H_2 (1-5 sccm)	25 μm thick Cu foil

In that procedure, all the CVD steps before cooling are same with procedure#5. Differently, samples were cooled slowly to see the effect of cooling rate on the quality of graphene (see

Table 16). Samples codes with the descriptions and calculated intensity ratios of the bands of D/G are given in
Table 17.

Table 17: Calculated intensity ratios of the Raman bands (I_D/I_G and I_{2D}/I_G) for Cu catalyzed CVD grown samples by procedure#5'.

Procedure 5'	I_D/I_G	I_{2D}/I_G
EK840-1st area-10 min (at 990°C, 20 Torr) (1/5 sccm) (H_2/CH_4)	0.19	0.23
EK840-2nd area-10 min (at 990°C, 20 Torr) (1/5 sccm) (H_2/CH_4)	0.21	0.48
EK842-1st area-10 min (at 990°C, 70 Torr) (5/25 sccm) (H_2/CH_4)	0.36	0.43
EK842-2nd area-10 min (at 990°C, 70 Torr) (5/25 sccm) (H_2/CH_4)	0.23	0.39
EK850-1st area-5 min (at 990°C, 15 Torr) (2/5 sccm) (H_2/CH_4)	0.17	0.25
EK850-2nd area-5 min (at 990°C, 15 Torr) (2/5 sccm) (H_2/CH_4)	0.19	0.22
EK852-5 min (at 990°C, 5 Torr) (2/5 sccm) (H_2/CH_4)	0.14	0.27
EK837-10 min (at 990°C, 2 Torr) (1/5 sccm) (H_2/CH_4)	--	--

Samples synthesized at different pressures (5, 15, 20 and 70 Torr) with different growth time (5 and 10 min) before etching underneath copper (EK840) and after etching (EK842, EK850 and EK852) were analyzed by Raman spectroscopy (Figure 54). They all have close D/G ratios (0.14-0.36) and 2D/G ratios (0.22-0.48) suggesting the formation of few layer graphene.

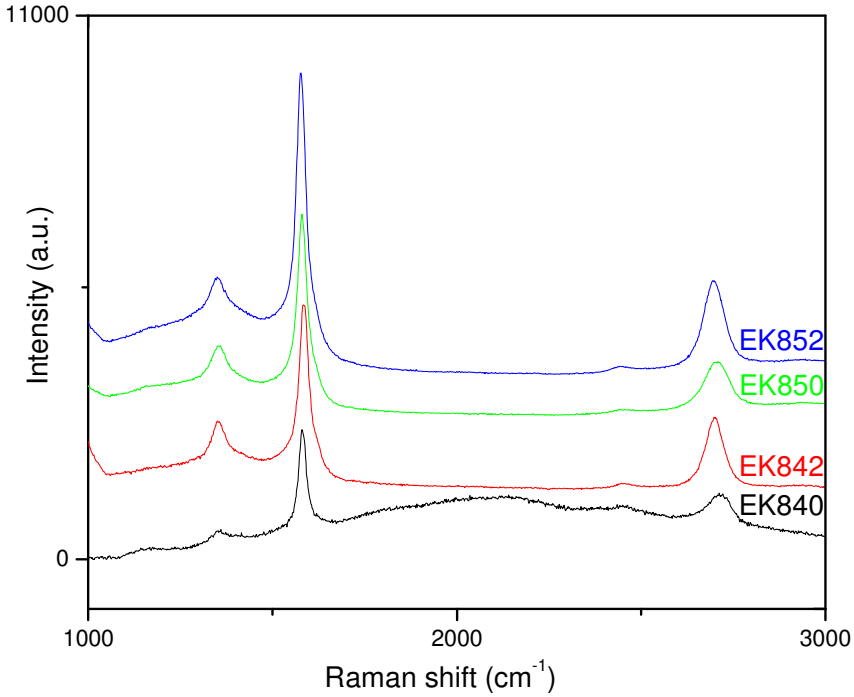

Figure 54: Raman spectra of low pressure CVD grown samples on 25 μm thick Cu foil (samples of EK852 at 5 Torr, EK850 at 15 Torr, EK840 at 20 Torr amd EK842 at 70 Torr were grown) by procedure #5'.

Higher I_{2D}/I_G values for the samples by procedure#5' than the ones by procedure#5 indicates the lower layered graphene formation by procedure#5'. This might be correlated to the use of hydrogen gas during slow cooling of the samples until room temperature in procedure#5'. Hydrogen has been reported to serve a dual role as an etching reagent of carbon layer as well as an activator of the surface bound carbon [79]. In this procedure, the flow of hydrogen during slow cooling in CVD process might allow etching the layers of graphene. So, the slowly cooled samples are found to have higher 2D/G ratios so lower number of layers compared to shock-cooled ones (see

Table 17). Similarly, the etching effect of hydrogen is mentioned during sample cooling [79]. Representative confocal images of the transferred low pressure CVD grown samples with procedure#5 (shock-cooled, EK851) and 5' (slowly cooled, EK850) are given in Figure 55. Both of the samples were grown with same CVD parameters (at 15mBar 990°C and 5 min of 2/5 sccm of H_2/CH_4) except cooling. In agreement with Raman results, confocal images also show that sample via shock cooling (EK851) consists of dominantly more graphene layers (darker pinkish areas) besides a few (light pinkish areas). However, a slow cooled sample (EK850) consists of significantly lighter pinkish areas suggesting the lower number of layers compared to EK851.

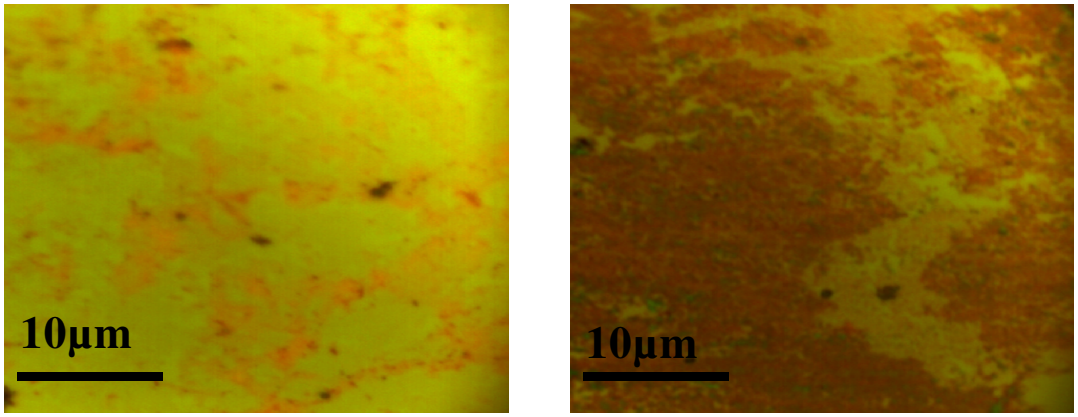

Figure 55: Confocal images of transferred samples (CVD grown on Cu foil) on Si/SiO_2 wafers. Slowly cooled sample by procedure#5' (left side, EK850) consists of dominantly pinkish areas while the shock cooled one by procedure#5 contains mostly darker pinkish areas (right side, EK851).

It should be also noted that graphene could not be obtained with the 1 min growth time which seems not sufficient to form graphene (see Appendix, Figure 135). The explanation might be attributed to low amount of hydrogen (1 sccm) that is insufficient to form active carbon species on the copper surface. Hydrogen catalyzes the reaction of methane dehydrogenation which is thermodynamically unfavorable process in the absence of hydrogen. Similar to the findings of procedure#5, different pressure growth samples (5-15-20-70 Torr) give similar quality of graphene with similar 2D/G and D/G ratios.

It can be concluded that despite the change in the concentrations of gases, growth time and pressure, due to the formation of mostly bi- and multilayer seeds most preferably, bi- to multilayer graphene was grown by during LPCVD conditions. Decreasing of the concentration of methane gas as carbon source to ppm levels (≤ 5 ppm) with sufficient

amount of hydrogen at pressure of ≤ 0.1 Torr is the requirement to get uniform single layer on copper by LPCVD process [77a].

2.1.4. Transfer of graphene

Once graphene is produced with CVD then the underlying metal catalyst layer is etched (in some cases, protecting the graphene layer by coating with 8%-15%PMMA/anisole) for further characterization and application [84].

Wet-chemical process was used to etch the underlying nickel or copper layer. HCl (5M), $FeCl_3$ (1M), $FeCl_3$ in HCl/H_2O (1-5M), HNO_3 (1M), H_2SO_4 (1M) and $CuSO_4$ in HCl/H_2SO_4 $/H_2O$ (5-10M) and HF (25M) were used as etchants. HF dissolves first SiO_2 layer under nickel in few seconds and graphene on nickel layer floats on the surface of the solution. Then HF continues to further etch SiO_2 layer in couple of hours. However, the other etchants except HF cannot etch the SiO_2 layer and it etches the nickel layer sandwiched between the substrate wafer and graphene. Oxygen containing acids are fast in the etching of metal layers but they introduce defects to graphene structure due to the formation of gases during etching. Therefore, HF (25M) is found to be an optimum etchant to transfer nickel catalyzed graphene on SiO_2/Si wafer.

For copper catalyzed graphene samples, $CuSO_4$ in HCl/H_2SO_4 $/H_2O$ (5-10M) is found a better etchant to transfer copper catalyzed graphene. The advantage of using $CuSO_4$ over other etchants is that it is relatively fast in etching process and doesn't contaminate graphene on copper. When graphene film floats over the solution, the solution is diluted and refreshed multiple times with distilled water and then graphene is transferred onto the desired substrate for further analyses.

The whole transfer process is illustrated in Figure 56 (without and with using protective polymer coating respectively).

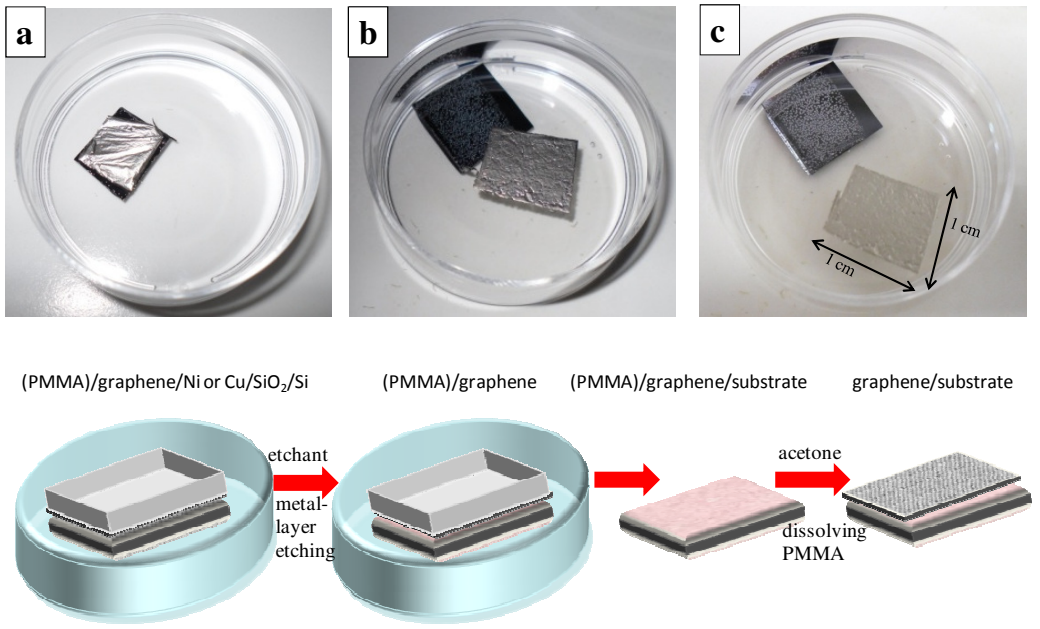

Figure 56: First row; photographs (a-c) showing the transfer process for a centimeter-large graphene film grown on a Ni/SiO_2/Si substrate. SiO_2, and Ni being etched in 48% HF aqueous solution, and floating graphene are shown in panels a, b and c, respectively [34]. Second row; scheme showing the transfer process in the case of polymer coating prior to etching process

Besides wet-chemical approach, underlying nickel layer was tried to be etched away by using CO (g). The idea behind that was to etch the underlying nickel metal layer by forming nickel tetracarbonyl $(Ni(CO)_4)_{(l)}$ from the reaction of nickel and CO (g). Optimal rate of that reaction is reported at 130°C[85]. Once $Ni(CO)_4$ is formed, it can be easily removed from the system since it is a volatile compound. The advantage of using CO(g) in the transfer process is that the possible contaminations due to the chemicals as in wet-etching process are prevented in this way.

After the formation of graphene on nickel at 950°C, the system was cooled down to 130°C under Ar flow and then 400 sccm of CO was passed for 3 hours to form $Ni(CO)_4$. By this way, it was aimed to transfer graphene on a desired substrate. The effect of CO (g) to graphene and nickel was investigated by grazing incidence X-ray diffraction (Figure 57). Five different samples with the following sample codes were analyzed. Two of the separated graphene samples from different batches were analyzed to check the reproducibility. Sample 1a. and Sample 1b.: graphene samples (from different batches) transferred on SiO_2/Si wafer, Sample 2: graphene prepared on Ni deposited on SiO_2/Si wafer, Sample 3: 500 nm Ni deposited SiO_2/Si wafer reacted with CO, Sample 4: graphene prepared on Ni deposited SiO_2/Si wafer reacted with CO(g) at 130°C.

Due to the existence of graphene flake or thin film, it is evident at the first glance that hump indicating the existence of carbon related structure was observed between 15° to 25° (2θ). This hump was not observed in sample 3, where not graphene but Ni was only deposited on wafer.

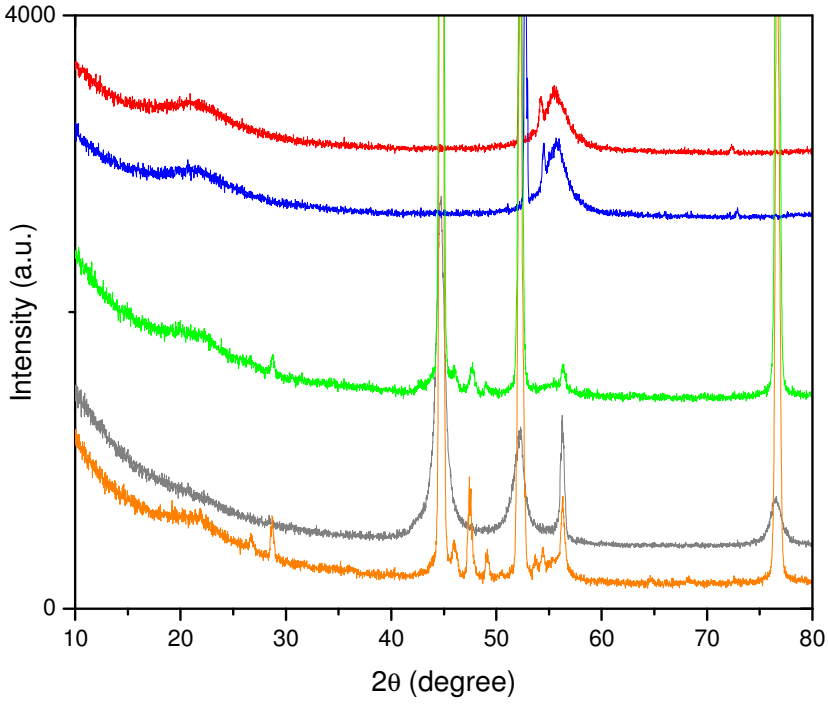

Figure 57: GIXRD pattern of, from top to bottom, transferred graphene on Si/SiO_2 (1a and 1b), graphene grown on $Ni\text{-}Si/SiO_2$ (2), CO reacted $Ni\text{-}Si/SiO_2$ (3) and CO reacted graphene grown on $Ni\text{-}Si/SiO_2$ (4)

Diffraction peak at about 45° (2θ) was indexed to nickel (111) reflection (JCPDS card 87-0712 given also below in Figure 58). Concerning CO reaction from sample 2 to 4, sample 3 shows a broader peak shape compared to the other two. Please see Figure 57. Comparing sample 2 and 4, though CO effect on graphene was difficult to identify, relative peak intensity of Ni (111) and Ni (220) reflections on Ni (200) was decreased after CO reaction. Nickel (111), (220) and (200) reflections are 44.496, 51.849, 76.381 degree, respectively, according to JCPDS card 87-0712 given also below in Figure 58.

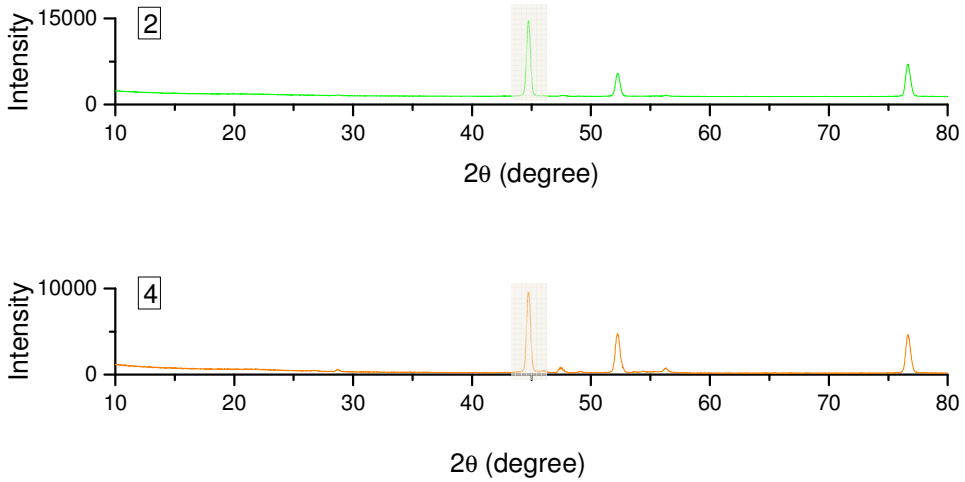

Figure 58: GIXRD pattern of CVD graphene grown on Ni-Si/SiO_2 (2), CO reacted graphene grown on Ni-Si/SiO_2 (4). Nickel (111) reflection at 44.496 degree is indicated with gray window in each pattern.

The effect of CO (g) on graphene was also examined by micro Raman and TEM analysis. Raman spectra of graphene and CO (g) reacted graphene on Ni-SiO_2/Si wafers were not similar when comparing the characteristic Raman bands of graphene (D, G and 2D) (Figure 59).

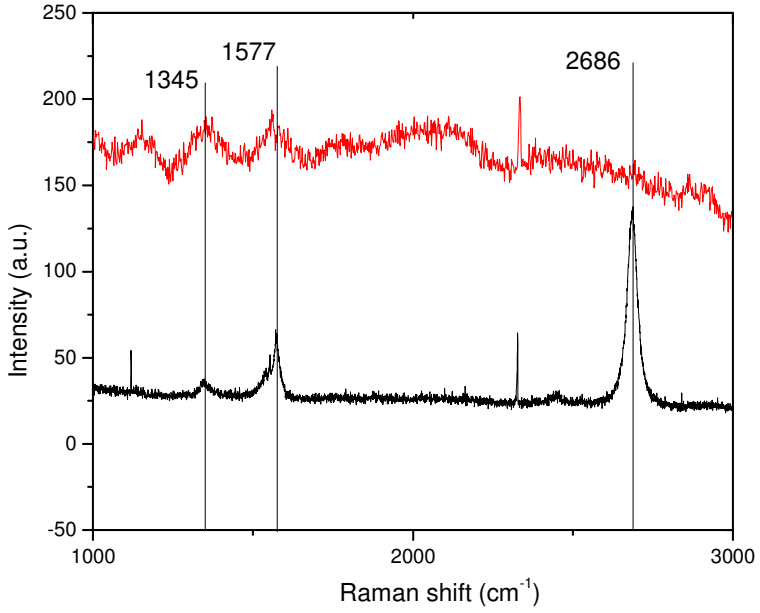

Figure 59: Raman spectra of graphene (in black) and CO reacted (in red) CVD graphene samples

During CO flow at 130°C, CO reacts with Ni and graphene preferentially at the edges that are easily accessible and energetically favorable sites. As Ni is etched from the edges,

graphene is peeled off from the edge and is transferred into a tube like morphology. TEM micrograph shows tubes formed at the edges of CO (g) treated sample (Figure 60).

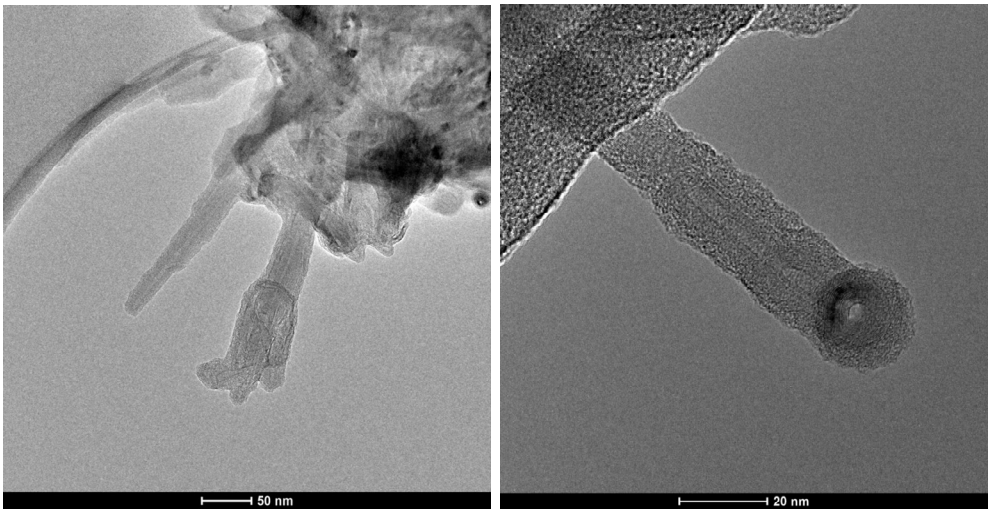

Figure 60: TEM images of a CVD graphene sample reacted with CO(g) for 3 hours at 130°C.

In summary, XRD data revealed that treating of graphene/Ni-SiO_2/Si sample with CO (g) layer was successful by partially etching underlying Ni layer. However, Raman and TEM results indicate that graphene structure was partly destroyed upon CO (g) exposure.

2.2. Post-treatment procedure

As the etching effect of hydrogen of graphene layers during cooling is mentioned in Procedure#5', it is aimed to use hydrogen to improve the quality of as-grown graphene on nickel film by etching the amorphous part. Minimum temperature for noticeably etching of graphene is found to be 850°C and even the holes are formed in the graphene grains due to the presence of impurities on the metal catalyst [79]. Therefore, in order to eliminate the possible deformation of the continuous layer, much lower temperature (500°C) required to etch the graphene layers is used in the post-treatment process to just etch the amorphous part. Transferred graphene sample (EK211) on SiO_2/Si wafer was heated to 500°C and held for 1 hour under 500 sccm of H_2 flow (EK235). Corresponding Raman spectra for the samples reveal that H_2 treatment slightly improved the quality of graphene sample by means of decreasing the defects (lowering D/G ratio from 0.13 to 0.063) (Figure 61).

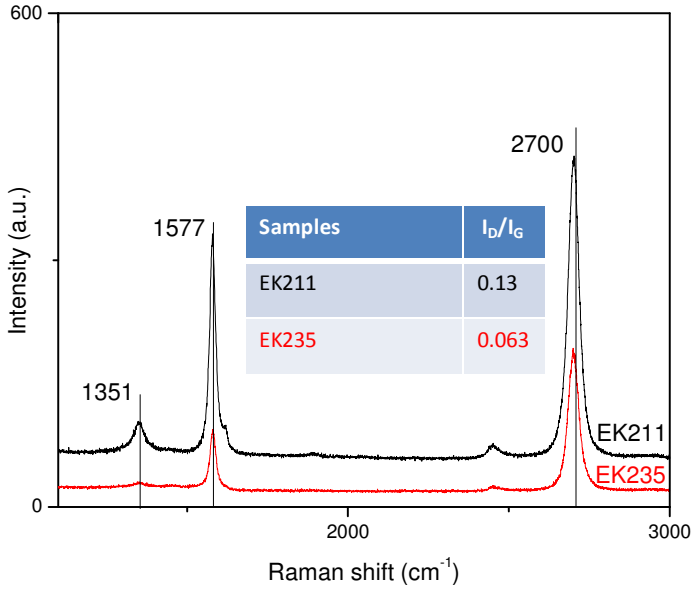

Figure 61: Raman spectra of transferred CVD graphene (EK211, in black) and hydrogen treated CVD graphene (EK235, in red) samples.

Besides hydrogen treatment, the transferred sample (EK253) was calcined at 500°C for 3 hours under air (EK253') with the aim of decreasing the amorphous carbon so the I_D/I_G ratio. As it can be seen from the Raman spectra in Figure 62, graphene turns out to be slightly less defective when employing the calcination process (I_D/I_G ratio decreases from 0.28 to 0.17).

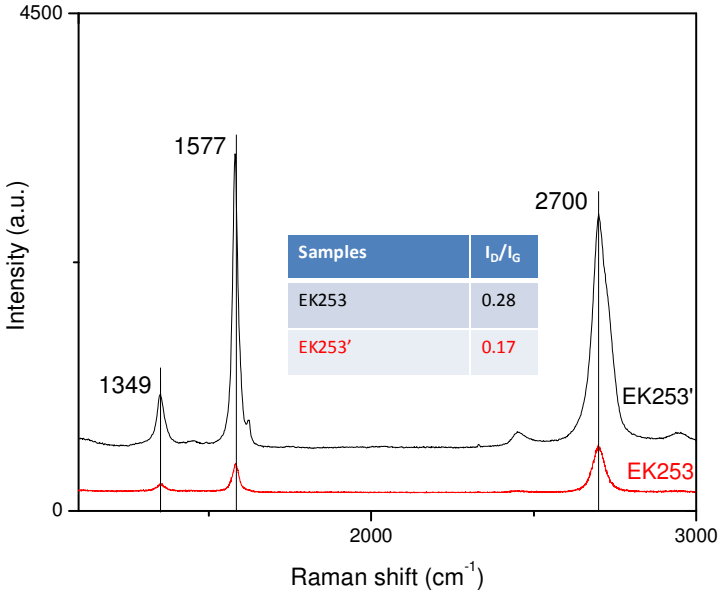

Figure 62: Raman spectra of transferred Ni catalyzed CVD graphene and calcined CVD graphene samples.

Similarly, same calcination procedure is applied to the copper catalyzed ambient pressure growth CVD graphene sample (Procedure#2). As in the case for the nickel catalyzed samples, I_D/I_G ratio (0.35 for EK634 and 0.10 for EK661) is becoming smaller by the calcination procedure (Figure 63).

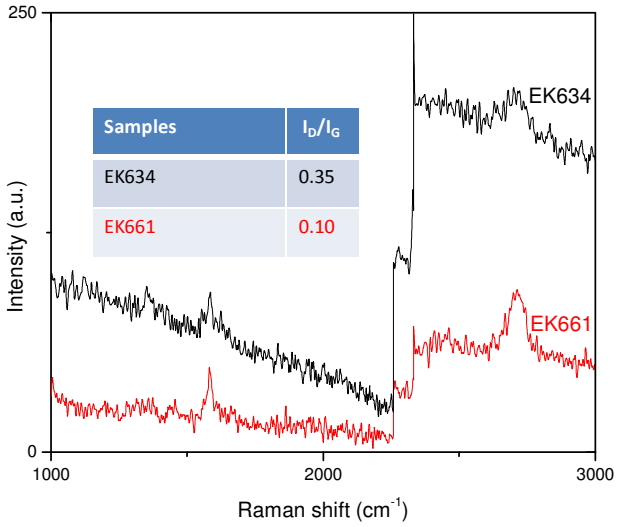

Figure 63: Raman spectra of transferred Cu catalyzed CVD graphene (EK634, in black) and calcined CVD graphene (EK661, in red) samples. Raman spectroscopy has an offset at 2250 cm^{-1} due to the grating in the spectrometer.

It can be concluded that hydrogen treatment and calcination of transferred graphene sample at 500°C improve the quality of graphene sample by healing the defects and eliminating the amorphous carbon from the structure.

2.3. Functional Properties of graphene

Graphene has potential applications in transistors [31b], flexible electronics [86] , and as gas-sensor material4 due to its exceptional electrical [2] mechanical [31b] and chemical [86] properties. Especially for the last application, its theoretical high surface area of approximately 2600 $m^2 g^{-1}$ [87] might allow altering its electrical conductivity to the ultimate limit of one molecule at a time.

Due to its low resistance and high integration capability in electronics, high impedance circuits necessary for metal-oxide gas sensors are not required for graphene-based gas-sensing devices [88]. Therefore, studies on functionalized graphene and bare graphene have revealed that graphene-based materials are promising candidates as gas sensors [37, 66, 72, 88-89]. Of these, it is important to analyze bare graphene to study the influence of adsorbant gases on the graphene surface without interference of a catalytically active metal or metal-oxide interface.

In the following part, electrical characterization of Ni-catalyzed few-layer CVD graphene and as well as studies on the gas-sensing properties towards low concentrations of CO and H_2 are reported.

2.3.1. Electrical characterization of chemical vapor deposition (CVD) derived graphene

Electrical characterization of the CVD-derived graphene was achieved by transferring individual graphene flakes onto a 10 mm×10 mm <100> silicon substrate coated with a 230 nm-thick silicon oxide (SiO_x) passivation layer. These graphene sheets were first electrically characterized by transmission line method (TLM). TLM is a widely used method for contact resistance evaluation of field effect transistors. In this method, several transistors with various channel lengths are constructed with a photolithographic mask by. Then the contact resistance is measured on each transistor and measured values are averaged [90]. In this work, a 200 nm-thick Ni metallization was sputtered on the top of the sample, patterned with the TLM mask by optical lithography and wet etched by HCl (32%) : H_2O_2 (30%) : H_2O (1:1:10) to define the final Ni-contacts. They had a size of 50 μm x 50 μm and a distance of 3, 6, 9, 12, 20 and 40 μm to each other (see Figure 64). These Ohmic contacts were characterized unannealed. The resistance between the different contacts was measured with an HP 4145 semiconductor parameter analyzer and plotted versus the contact distance (Figure 64). The graphene sample had a uniform sheet structure. Measurements performed by using TLM showed a sheet resistance of (R_{sheet}) of approximately 1435 Ω per □, a contact resistance (R_c) of about 127 Ω, and specific contact resistance (R_{sc}) of approximately $2.8\times10^{-4}\,\Omega\,cm^2$ (defined as $R_{sc}=R_c^2\,w^2/R_{sheet}$, in which w is contact width of 50 μm).

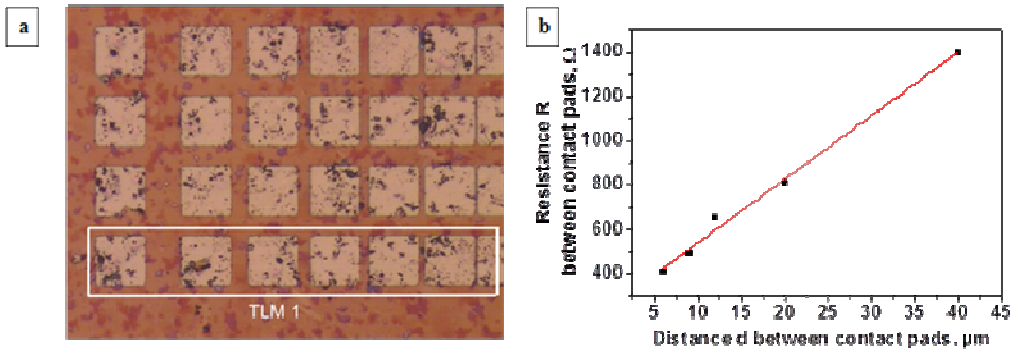

Figure 64: Four parallel TLM structures with Ni contacts on graphene (a) and resistance between contacts versus contact distance (b).

Afterwards, the bottom side of an n-doped-Si wafer was fixed to a metal electrode using a conducting silver paste to form a backside gate contact. The top side onto which the transparent graphene specimen was fixed, was partially O_2-plasma treated to etch some part of graphene and isolate the drain and source contacts from the bottom gate contact (Figure 65).

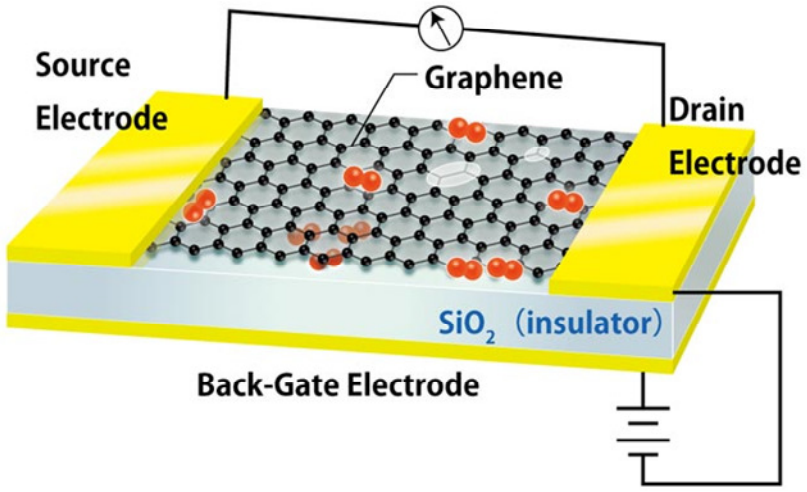

Figure 65. Schematical illustration of the set up of graphene based transistor used in the TLM studies.

Transistor output characteristics for the graphene sample demonstrated a linear current/voltage behavior with some gate modulation [I_{ds}(@V_{gs}=15 V)/I_{ds}(@V_{gs}=15 V)=1.5:1.25] (Figure 66 a). A current vs voltage (I_{ds}–V_{ds}) plot shows the response of a transistor for different values of gate voltage (Figure 66). Figure 66 clearly indicates the p

characteristics of graphene that upon application of a gate/source voltage led to a loss of drain current. The hysteresis behavior was also investigated for the sample. Only a small difference was measured for increased gate voltage (V_{gs} from −20 to 20 V) compared with decreased gate voltages (V_{gs} from 20 to −20 V; Figure 66 b).

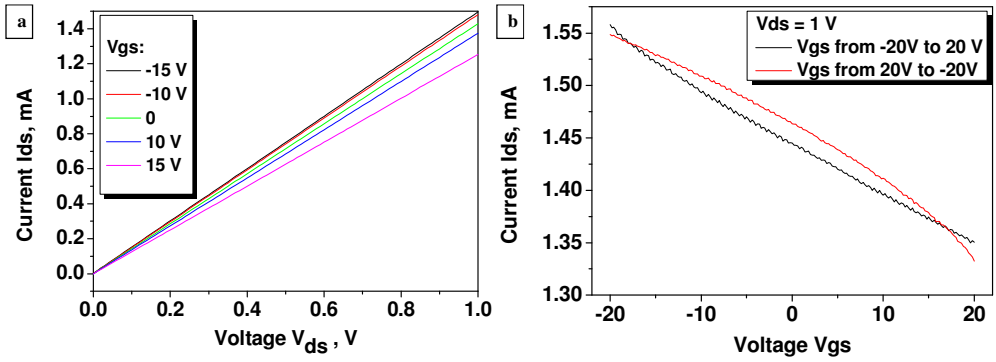

Figure 66: (a) Output current-voltage characteristics (b) and input current-voltage characteristics of the graphene sample [34].

2.3.2. Gas-sensor measurements on chemical vapor deposition (CVD) derived graphene

Its large surface area with unique electronic properties makes graphene an interesting candidate for gas-sensor applications [89a]. The conductivity of graphene (that arises from delocalized π electrons) is directly altered by the probe molecules adsorbed at the graphene surface [91]. Because graphene is a 2D material and exposes nearly its complete surface area to the gas atmosphere, the effect of adsorbing-gas molecules on the conductivity is rather large. Besides reports of gas-sensing properties of bare graphene towards H_2 and CO detection [37, 88-89, 92] studies of graphene gas sensors functionalized by metal and metal oxides, such as Pt [93] Pd [72], and ZnO [66], have been reported. Studies of bare graphene–gas interactions are important, because they allow examining the adsorbant/graphene influence without additional interference of the metal particle/graphene interface. The graphene specimen used for the sensoric measurements was a continuous film.

In this study, gas-sensor (DC electrical) measurements are performed to monitor the sensor response of graphene to CO and H_2 in dry nitrogen [94]. As shown previously in the AFM image of the specimen, the graphene film consists of micrometer-sized areas, which

are separated from each other by grains, however, the whole film specimen is continuous (Figure 17 B).

The sensing layer is deposited by immersing the alumina substrates with Pt-electrodes on the front side and a Pt-heater on the back side as shown in Figure 67. SEM micrographs of the Substrate after replacing the sample are shown as well (Figure 67). Contrast difference seen between two Pt fingers is due to the graphene flake.

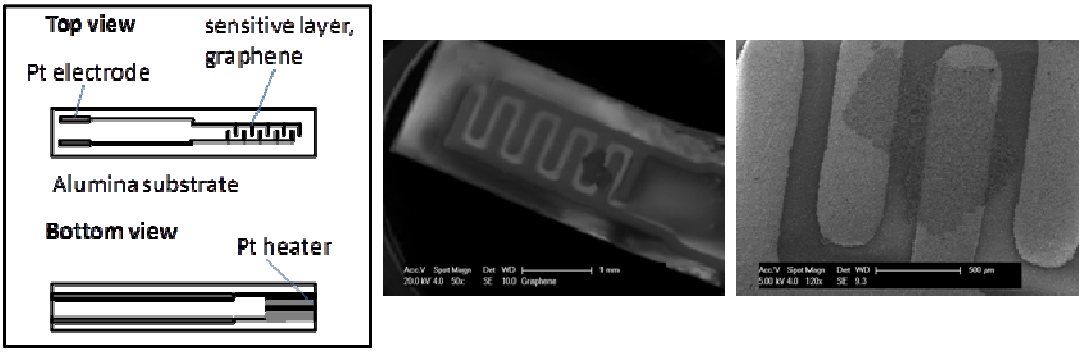

Figure 67: Layout of the planar alumina substrate with platinum electrodes and heater for sensor tests and SEM images of sample (CVD graphene here) transferred on that substrate.

Defined concentrations of H_2 (200, 500, 1000, 2500, 5000, and 10000 ppm) and of CO (50, 100 and 250 ppm) were obtained from a PC controlled gas mixing bench, which consists of a combination of computer controlled mass flow controllers and computer controlled valves, to mix the certified N_2 and H_2/N_2 and CO/N_2 test gas samples. Graphene samples were transferred onto an alumina substrate in a teflon-based test chamber and operated. Besides room temperature experiments, the studies were performed at 300°C. The sensor signal (S) is given as the resistance ratio; $S= 100\%x(R_{H2}-R_0)/R_0$ for H_2 and $100\%x(R_{CO}- R_0)/R_0$ for CO, where R_{H2} , R_{CO} and R_0 denote the sensors' resistances in the presence H_2, CO and in the absence of H_2 and CO, respectively.

Thin-layered graphene was exposed to CO or H_2 at different concentrations and its gas-sensing activity was studied by monitoring the resistance change. Exposure of reducing gases, such as CO and H_2 on a CVD-derived graphene surface resulted in an increase of the resistance of the graphene film (Figure 68a). This confirms p-type conductivity of the transferred CVD-derived graphene as was found in the electrical characterization studies. As was reported previously, chemically derived graphene (by exfoliation/reduction route) might give some contradictory results upon exposure to different types of e-donors (H_2 and CO). This can be attributed to an incomplete chemical reduction of graphene oxide

to graphene, if it is obtained by the exfoliation/reduction route [92]. However, this effect can be ruled out on CVD-derived graphene studied herein. The gas-sensing response of CVD graphene is similar to that of CNTs [95] and diamond surfaces [96]. At room temperature, no resistance change of our CVD-derived graphene was observed, if it is exposed to CO (Figure 68 a). DFT studies of CO adsorption on graphene [97] suggest small binding energies (0.008–0.02 eV), large adsorbate-surface distances (d; 3.70–2.80 Å), and small adsorption-energy values for CO (E_a; −0.12 to −0.05 eV). These findings indicate that CO undergoes a physical adsorption on graphene due to rather weak van der Waals interactions between the graphene surface and CO. However, a very small Mulliken charge transfer (0.01 |e|) from graphene to CO suggests that an electrostatic interaction between the graphene and CO does exist [97b, c].

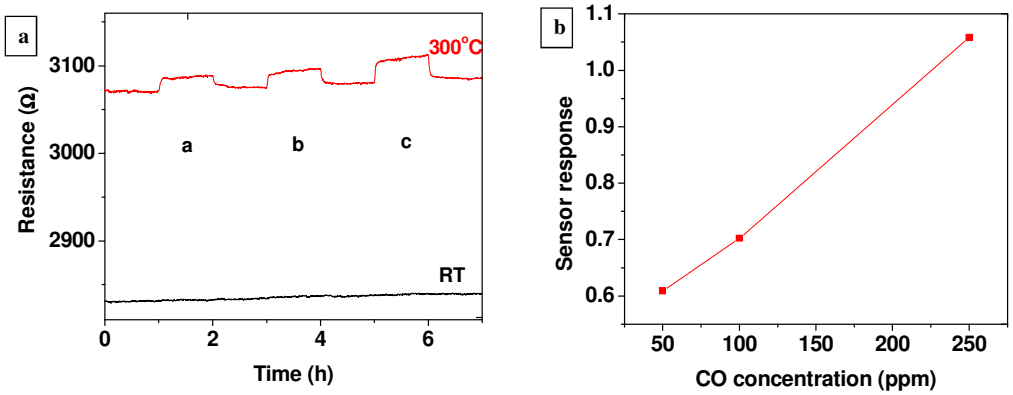

Figure 68: (a) Transient resistance of CVD-graphene film to CO (50-100-250 ppm) at RT and 300°C (b) sensor response of CVD-graphene (100 *(R_{gas}- R_0)/R_0) to CO (steps 50-100-250 ppm) at 300°C [34].

Exposure of graphene towards H_2 gas at room temperature induced a slight increase in the resistance; the latter did not show a concentration dependency. This behavior can be explained by the very weak interaction of H_2 with graphene under ambient conditions (Figure 69 a) [72, 98]. Again, as was shown by DFT computations, the adsorption of H_2 onto graphene is very weak with binding energies of <0.1 eV and adsorbate-surface separations between 5.07–5.50 Å [99]. Already at a low amount of adsorbed hydrogen, the graphene surface was saturated, leading to the same resistance change even with increasing hydrogen concentrations (Figure 69 a). In addition, due to the limited desorption at room temperature, the base-line resistance slightly increased upon hydrogen exposure. Similar behavior was observed required an annealing at 150 °C in vacuum to recover the initial graphene surface free of adsorbates [88-89, 100]. At 300 °C, a much higher sensor signal (ca. 29) to a lower H_2 concentration (1 vol %) was observed

than that reported recently on CVD-derived graphene (ca. 7 for 3.35 vol % H_2 at 200 °C [88])

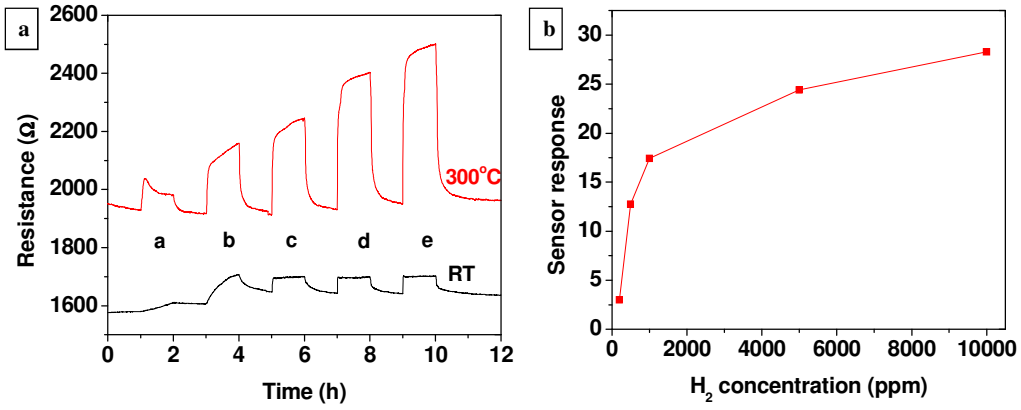

Figure 69: (a) Transient response and (b) sensor signal of CVD-graphene film to H_2 (steps of a, b, c, d and e; 200, 500, 1000, 5000 and 10000 ppm respectively) at room temperature (RT) and 300°C [34].

2.4. Conclusion

It could be demonstrated that single-layer to few-layer graphene can be obtained by a direct CVD method using Ni as catalyst layer. The material can be transferred to nonspecific substrates by a solvent-deposition process, which allowed its electrical characterization as p-type electronic material. Inhomogeneity in the number of layers of graphene on randomly selected areas of the graphene flakes is attributed to the formation of grain-boundaries on the Ni surface during thermal annealing. These have been studied by micro Raman spectroscopy. Gas-sensor measurements upon H_2 and CO exposition revealed an increase in the resistance of the graphene films, indicating that CVD graphene is a promising candidate as sensitive gas sensor towards both reducing gases at higher temperatures.

The CVD growth of graphene on Cu substrates has been considered to be surface mediated and somewhat self-limiting due to the extremely low carbon solubility in Cu, leading to the growth of predominantly single-layer films [49, 56]. However, that such self-limiting growth of graphene on copper surface as a single layer is broken under certain CVD conditions (e.g., high growth pressure and large amount of carbon precursor) resulting the growth of massive non-uniform multi-layer graphene films [77a, 81]. Under ambient pressure and low pressure CVD conditions, synthesis of bi- to multilayer graphene instead single layer was achieved on copper catalyst surfaces.

3. Chemically Derived (CD) Graphene

3.1. Introduction

The necessity of the formation of graphene in gram scale challenged me to synthesize graphene by using chemical synthesis methods. Generally, those methods consist of oxidation (of graphite into graphite oxide) and reduction (of graphite oxide to chemically derived graphene) steps. The common approach is the use of strong oxidizing agents for obtaining graphite exfoliation first (see Figure 70).

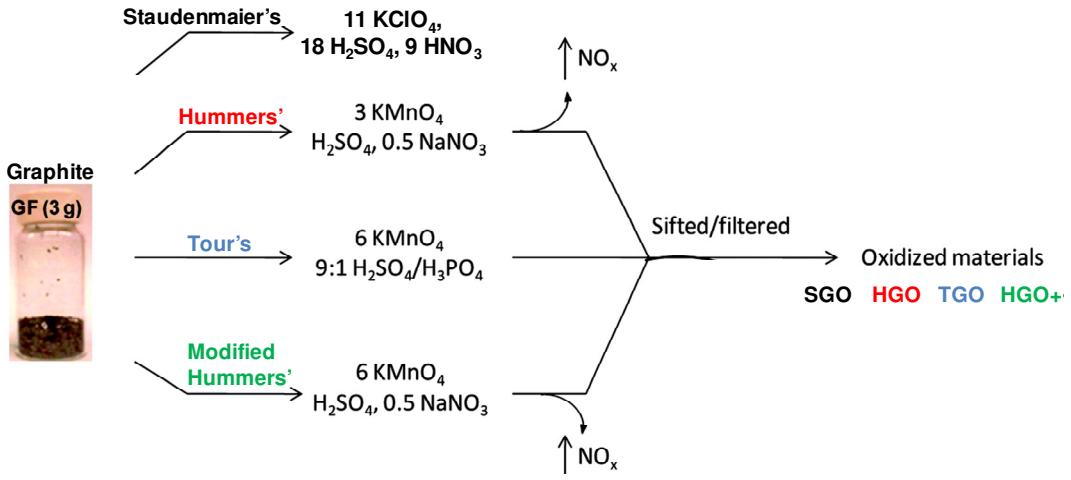

Figure 70: Methods used for the synthesis of graphene oxide (Modified scheme from[35])

As shown in Figure 70 above, Tour's method has an advantage over others in that it does not generate toxic gases and the reaction temperature is easily controlled during reaction. Once graphite oxide is produced, several methods including thermal (by shock or slow heat treatment) and chemical ways can be used to obtain graphene from graphite oxide. Synthesis of graphite oxide (GO by Staudenmaier's, Hummers', Modified Hummers' and Tour's Methods) and reduction of GO into graphene (CDG by chemical via hydrazine hydrate or hydroxylamine hydrochloride reductions, thermal and vacuum-assisted methods) were conducted and characterized comparatively. Re-reduction of CDG heating under hydrogen was also used to improve the quality of graphene. As synthesized samples were used as the precursors to form metal or metal oxide nanoparticles/CDG hybrid materials.

3.2. Synthesis

3.2.1. Synthesis of Graphene Oxide from Graphite

As it was mentioned above, the synthesis of graphene oxide is carried out by oxidizing graphite with strong oxidizing agents. During this work, four different synthesis methods were used (4.5 Experimental part for details). These are Staudenmeier's, Hummers', Modified Hummers' and Tour's Methods [13, 35].

The aim of this work is to compare the synthesis routes and evaluate, which method yields a better product with respect to the oxidation process. Two different forms of graphite as powder and flake versions were used to study the effect of precursor on the quality of graphite oxide as well.

The oxidation of graphite into graphite oxide process is illustrated with the pictures in Figure 71.

Figure 71: Synthesis of graphite oxide using Tour's method. Left: the reaction mixture before centrifugation. Middle: Dry untreated graphene oxide. Right: graphene oxide after mechanical grinding.

3.2.2. Comparison of results from graphene oxides obtained by different methods

Raman spectra of the graphene oxide samples from different methods are compared (Figure 72). Spectra belonging to flake and powder graphite were also recorded to show the change of Raman profile after oxidation. It is obvious to see the broadened, shifted (to higher cm^{-1}) G band due to the separation of the layers of graphite and stronger D band (due to the introduction of defects during oxidation process) in spectra of graphene

oxide samples compared to the ones of graphite. Broadening and shifting of G band is more significant in graphene oxide sample via Tour's method compared to all others. This suggests a better oxidation in Tour's method compared to the other methods studied. Besides, experiments were performed using powder graphite instead of flake graphite. No significant difference in Raman spectra was obtained for graphene oxide samples synthesized using flake graphite as a precursor.

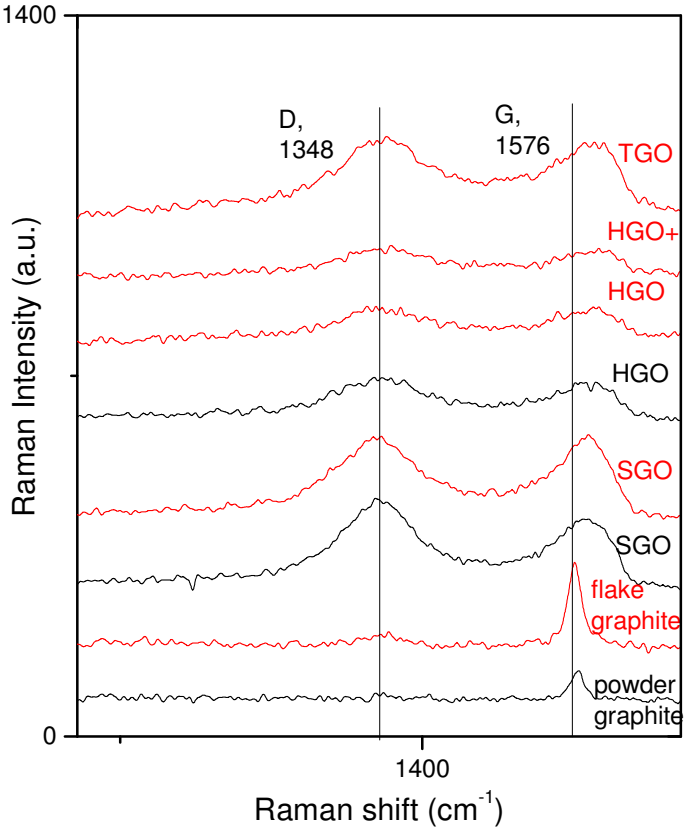

Figure 72: Raman spectra of graphite precursors (flake and powder) and graphene oxide samples derived by Tour's, Modified Hummers', Hummers' and Staudenmaier's methods. Black curves are the samples derived from powder graphite while red ones are from flake graphite

Thermal analysis was also performed for the graphene oxide samples via different methods. Figure 73 shows the TGA graphs of graphite and graphene oxides (GOs). No significant weight loss is observed for graphite as expected since pure graphite consists of no functional groups that would be burned out during thermal treatment. As clearly seen from the graph, weight loss gets more significant from SGO (Staudenmaier's graphene oxide) to TGO (Tour's graphene oxide) that means oxidation of the graphite is more

successful with Tour's method parallel to Raman results. TGO has a weight loss of 10% at 140°C and then 30% at 200°C corresponding to the removal of water and COOH groups, respectively. Next, a fast weight loss of GO takes place until 360°C due to the decomposition of the hydroxyl or epoxy groups.

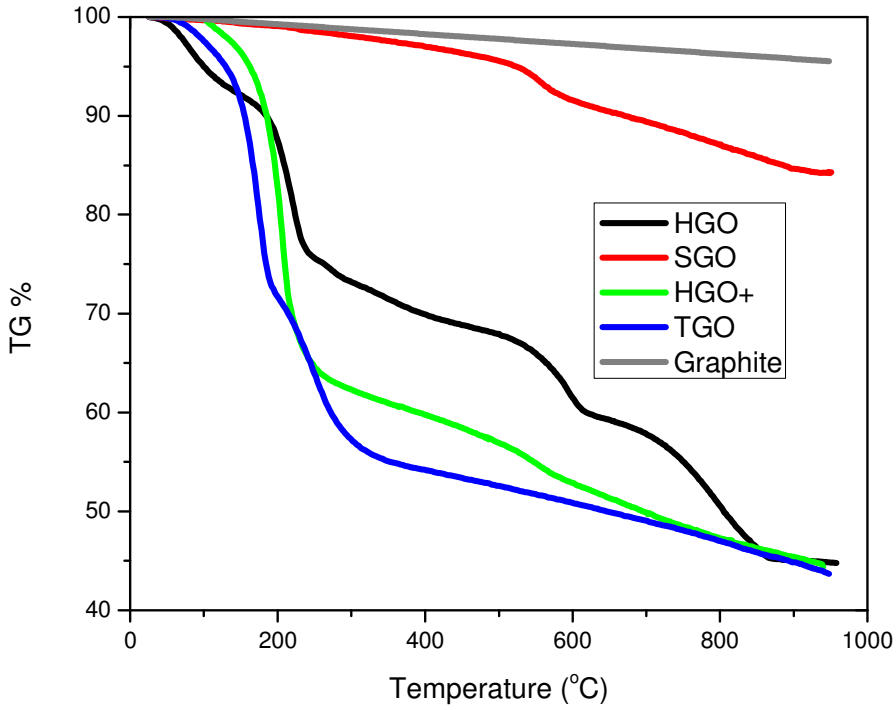

Figure 73: TGA data of graphite and graphene oxide samples derived by Tour's, Modified Hummers', Hummers' and Staudenmaier's methods under under helium atmosphere.

FTIR spectroscopy is also a powerful tool for characterization of the functional groups in GO samples. Spectra in Figure 74 support the presence of hydroxyl ((−OH), broad peak at 3050−3800 cm^{-1}), carbonyl ((−C═O), 1750−1850 cm^{-1}), carboxyl ((−COOH), 1650−1750 cm^{-1}), C=C (1500−1600 cm^{-1}), and ether or epoxide ((−O−), 1000−1280 cm^{-1}) groups. [101] Parallel to results so far, FTIR also suggests higher oxidation degree with more prominent bands in the Tour's method case compared to Staudenmaier's method for the production of graphene oxide.

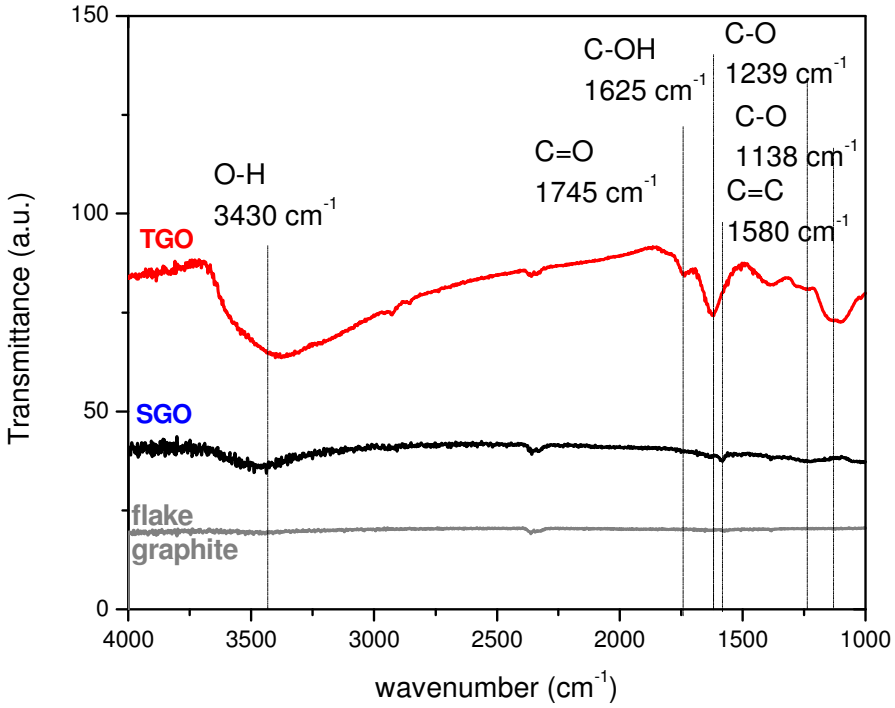

Figure 74: IR spectra of graphite and graphene oxide samples derived by Tour's and Staudenmaier's methods.

The UV-Vis spectra were recorded for a same concentration (of 0.04 mg/mL) of graphene oxide samples prepared with different methods (Figure 75). TGO, HGO+, HGO and SGO samples have all λ max band (located at the 225−232 nm) attributed to π→π* transitions (conjugation) and a shoulder around 300 nm assigned to the n→π* transitions of the carbonyl groups that means samples have similar structure in parallel to Raman and IR data given previously [102]. The degree of remaining conjugation can be determined by the λ_{max} of each UV-Vis spectrum [35]. As the number of π→π* transitions increases, the energy required for the electronic structure gets smaller. Therefore, λ_{max} gets more intense. When spectra are compared for the samples of the same concentrations, it is found that TGO has the most intense λ_{max} (so largest extinction coefficient) suggesting the more ordered structure due to greater retention of more aromatic carbon rings or isolated aromatic domains.

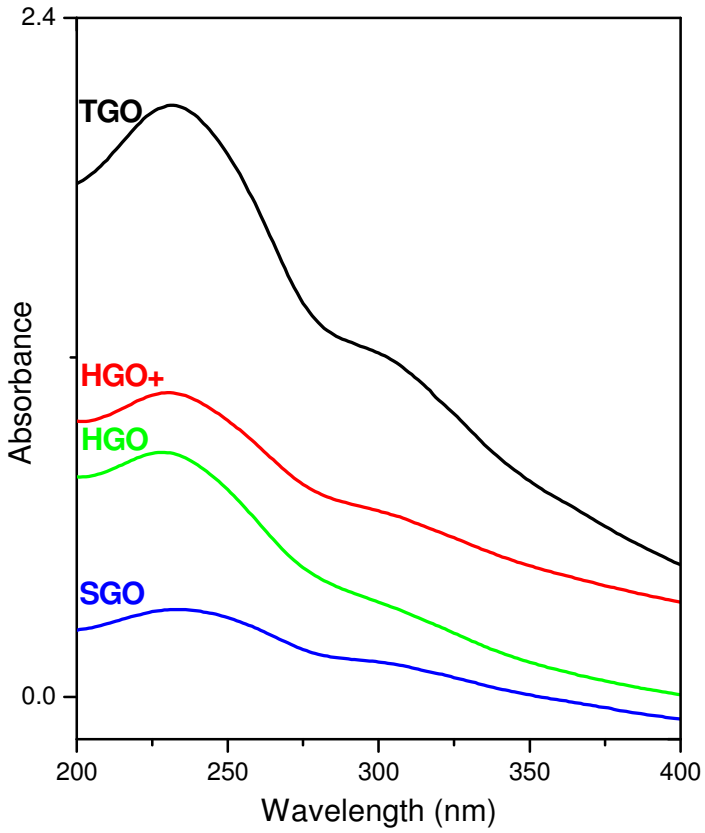

Figure 75: UV-Vis spectra for aqueous solutions of TGO, HGO+, HGO and SGO (same concentrations of 0.04 mg/mL).

SEM micrographs were also taken for graphite precursors and GO samples (Figure 76). Graphite samples both have stacked sheets and that sheets have similar size in flake graphite whereas these are more random in size for powder graphite. All samples were dispersed on SiO_2/Si wafers. Both types of graphites do not contain a detectable amount of impurity as found in their EDX analysis.

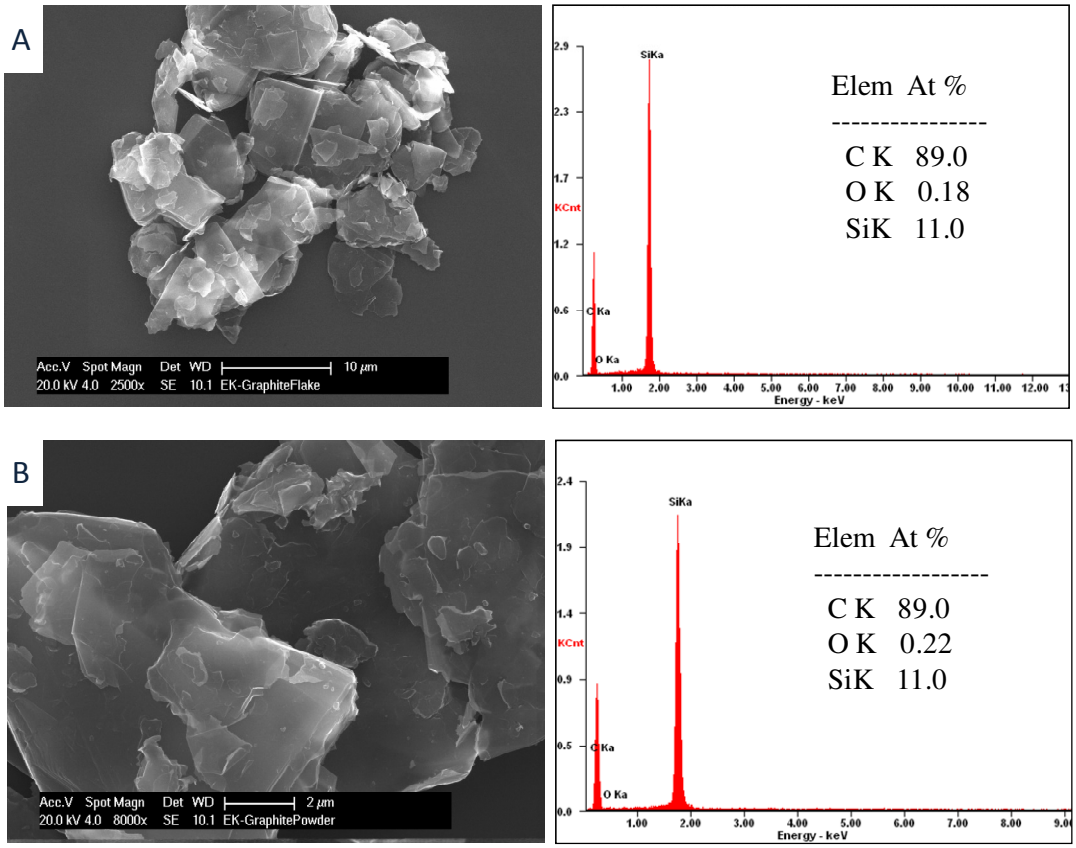

Figure 76: SEM images and EDX data of A. flake and B. powder graphite samples.

SEM micrographs GO samples via different procedures are shown in Figure 77. Samples where the starting material was flake graphite have a flat morphology whereas the ones with powder graphite display more crumbled parts. Different than graphite, EDX analysis shows that all GO samples contain some impurity left from the precursors used in oxidation process (e.g. Mn from $KMnO_4$). It should be noted that impurities are less pronounced in Tour's method derived GO (with negligible amount of S (0.15 at %)).

A

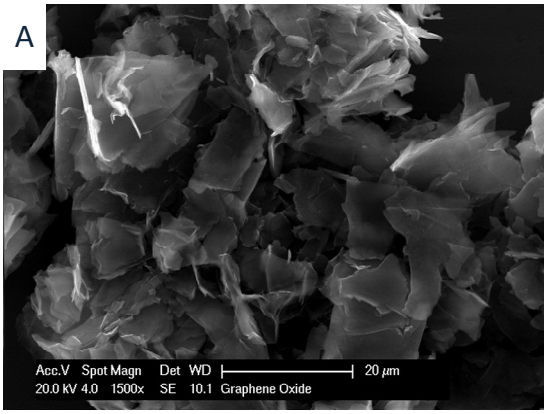
Acc.V Spot Magn Det WD 20 μm
20.0 kV 4.0 1500x SE 10.1 Graphene Oxide

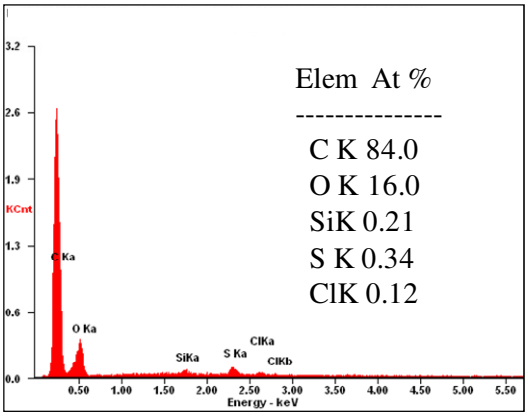
Elem At %
C K 84.0
O K 16.0
SiK 0.21
S K 0.34
ClK 0.12
KCnt
C Ka
O Ka
SiKa
S Ka
ClKa
ClKb
Energy - keV

B

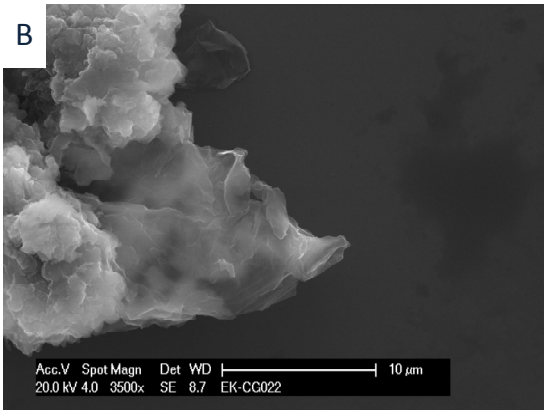
Acc.V Spot Magn Det WD 10 μm
20.0 kV 4.0 3500x SE 8.7 EK-CC022

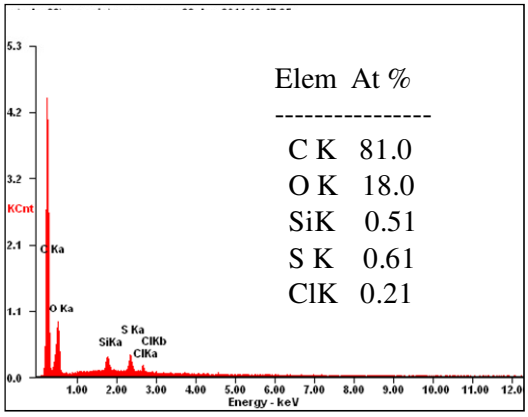
Elem At %
C K 81.0
O K 18.0
SiK 0.51
S K 0.61
ClK 0.21
KCnt
C Ka
O Ka
S Ka
SiKa
ClKb
ClKa
Energy - keV

C

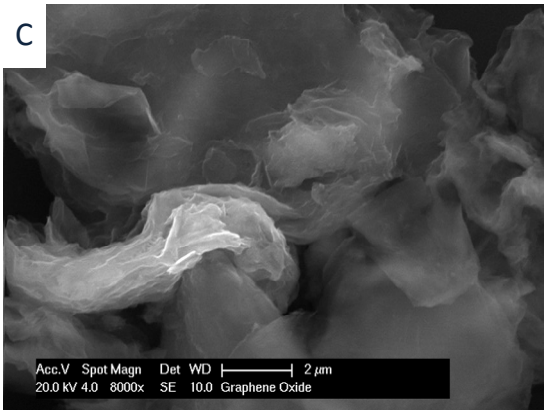
Acc.V Spot Magn Det WD 2 μm
20.0 kV 4.0 8000x SE 10.0 Graphene Oxide

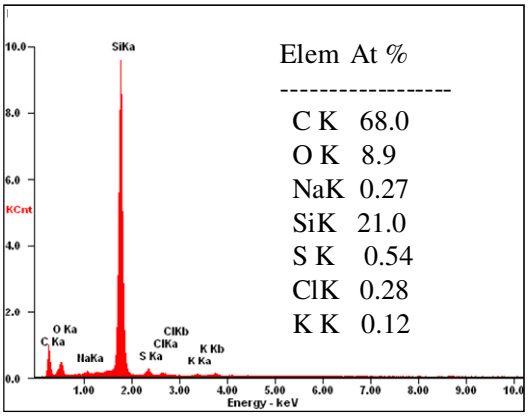
Elem At %
C K 68.0
O K 8.9
NaK 0.27
SiK 21.0
S K 0.54
ClK 0.28
K K 0.12
KCnt
SiKa
O Ka
C Ka
NaKa
ClKb
ClKa
S Ka
K Kb
K Ka
Energy - keV

D

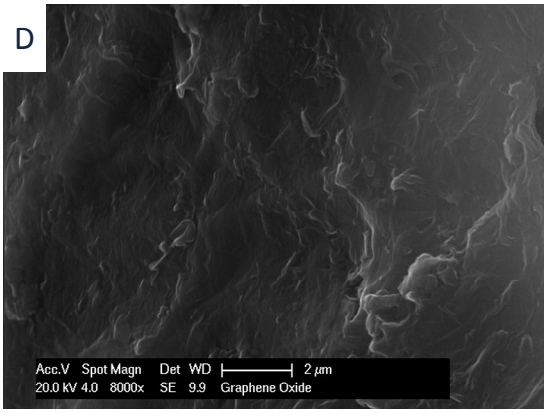
Acc.V Spot Magn Det WD 2 μm
20.0 kV 4.0 8000x SE 9.9 Graphene Oxide

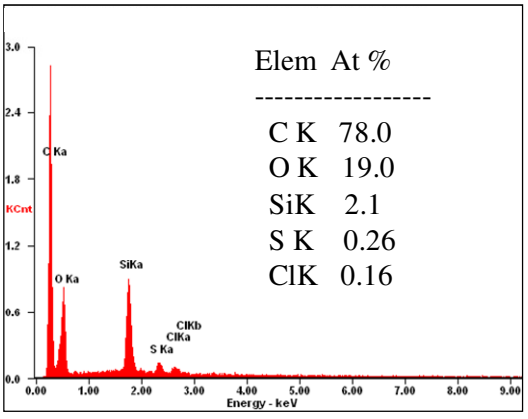
Elem At %
C K 78.0
O K 19.0
SiK 2.1
S K 0.26
ClK 0.16
KCnt
C Ka
O Ka
SiKa
ClKb
ClKa
S Ka
Energy - keV

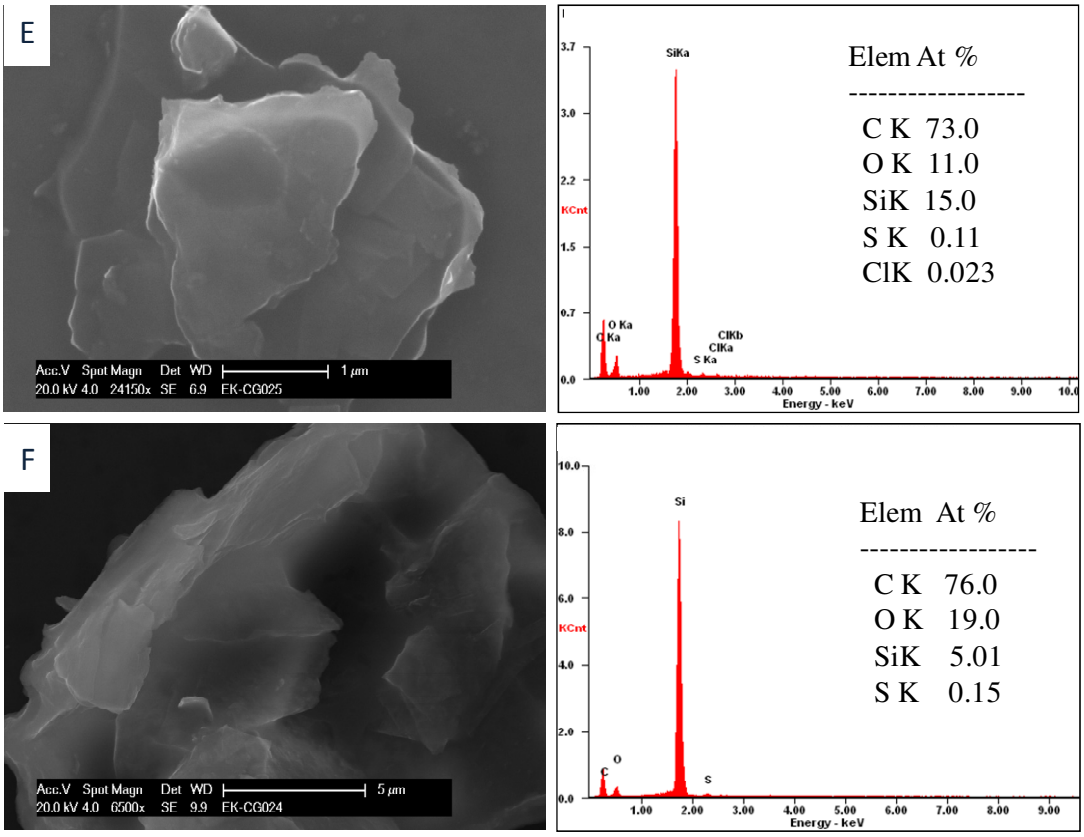

Figure 77: SEM images and EDX data of graphite oxide samples, A, B. SGO; C, D.HGO; E. HGO+; F. TGO. B and D were derived from powder graphite as precursor whereas the others were from graphite flake.

3.2.3. Synthesis of Graphene from Graphene Oxide

After graphene oxide is successfully synthesized by the oxidation of graphite, reduction of the samples are necessary to obtain graphene. Several reduction methods including wet chemical method (Ruoff's and Chen's methods), thermal reduction and vacuum-assisted methods were used to synthesize graphene from graphite oxide. In wet chemical reduction process, either hydrazine hydrate or hydroxylamine hydrochloride was used as a reducing agent. Besides reduction of graphite oxide with hydrazine hydrate, experiments including both poly(sodium 4-styrenesulfonate) (PSS) and hydrazine hydrate to get water dispersible graphene were also carried out. In a thermal reduction method, generally, samples were heated rapidly or slowly to 1050°C in the tubular or induction furnaces. To achieve GO reduction at lower temperatures, GO samples were heated at 145°C under vacuum. Besides all the reduction methods, the quality of

graphene was improved by re-reduction of the reduced GO samples under reducing gas environment (H_2 at 500^{o}C).

3.2.4. Comparison of results from graphene samples obtained by different methods

Raman spectra were performed to follow the change from GO to graphene. As shown in the analysis part for GO, as graphite is oxidized to GO, then intensity ratio of D/G raises. This is attributed to the formation of defects during oxidation process. Similarly, it is expected to observe further increase in the intensity ratio of D/G in the better reduction route. Therefore, Raman spectra belonging to graphene samples that are derived from different synthesis routes starting all from TGO are compared (Figure 78). In each spectrum, D and G bands are distinguishable and crucial to determine the quality of samples prepared by different reduction process. As I_D/I_G values are calculated for each, ratio increases from TGO to graphene (~1.1 to ~1.4). However, that increase is too small both for hydroxylamine hydrochloride reduced graphene (Chen's method) and vacuum-assisted graphene samples (~1.1) while the others all have the ratio of ~1.3. That ratio slightly increases to 1.4 in re-reduced graphene case where graphene (hydrazine hydrate reduced one) is further reduced under hydrogen atmosphere. Hence, re-reduced graphene sample is the better reduced form of graphene oxide among all other CDG samples in which TGO is the precursor for GO.

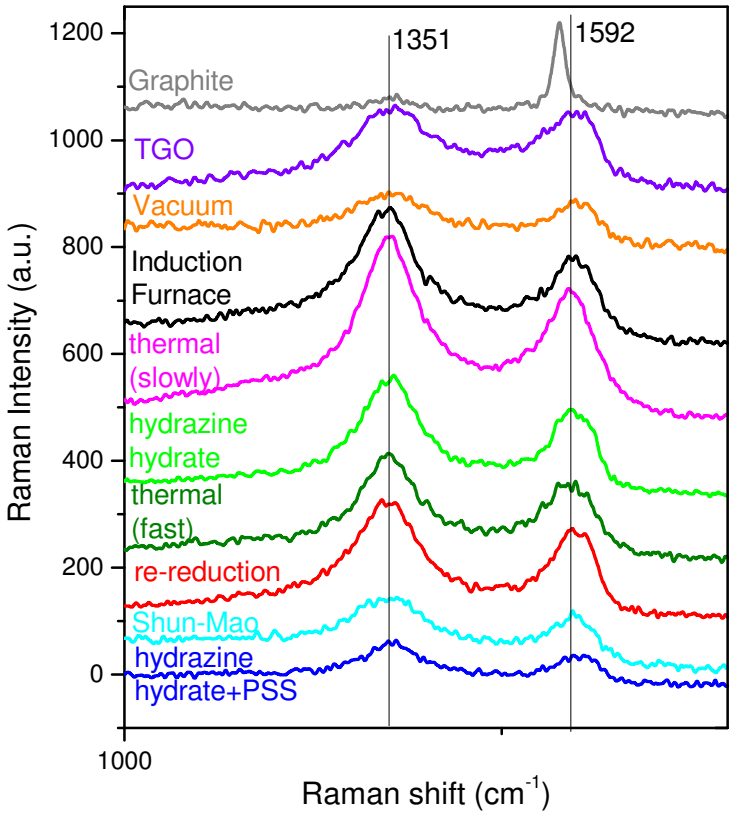

Figure 78: Raman spectra of graphite, TGO and CDG samples prepared by thermal, vacuum-assisted, chemical reduction methods from TGO as precursor.

FTIR analysis was also performed for chemically derived graphene samples (CDG). Spectra corresponding to graphite (gray color), TGO and SGO (black color) are also given in Figure 79 to observe the change in the spectra due to the reduction. It is obvious to see significantly reduced O-H streching band (~3430 cm^{-1}) due to deoxygenation, no noticable C=O stretching vibrations (~1745 cm^{-1}) and C–O peak (~1239 cm^{-1} and ~1138 cm^{-1}) showing less remaining carboxyl groups compared to literature data [103]. Vacuum assisted graphene sample compared to all the other graphene samples have a slightly noticeable C-O peak which is due to the remaining unreduced epoxide/ether groups in the structure. In agreement with Raman data, re-reduced graphene is found to be the best reduced CDG having a quite similar spectrum compared to graphite.

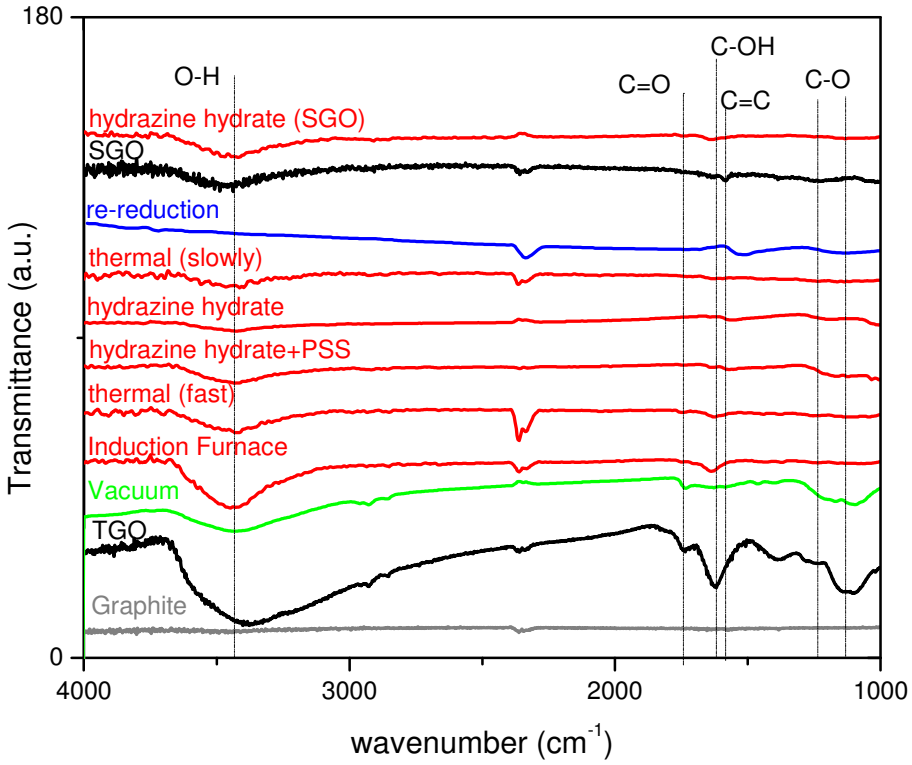

Figure 79: IR spectra of graphite, SGO, TGO and CDG samples prepared by thermal, vacuum-assisted, chemical reduction methods from TGO as precursor.

UV-Vis spectra were performed for water-dispersible graphene samples that were reduced by hydrazine hydrate reduction in the presence of PSS. UV-Vis analysis was also done for the solutions of bare PSS and GO (Figure 80). It can be seen in the figure that PSS-coated graphene dispersion has similar features as that of PSS. However, the intensity of signal arising from polymer is too small. This indicated that polymer is strongly attached to the graphene surface [104]. The absorption peak at 230 nm red-shifted to 270 nm, indicating that the electronic conjugation within the reduced graphene sheets was restored upon hydrazine hydrate reduction of graphene oxide in the presence of PSS [102a].

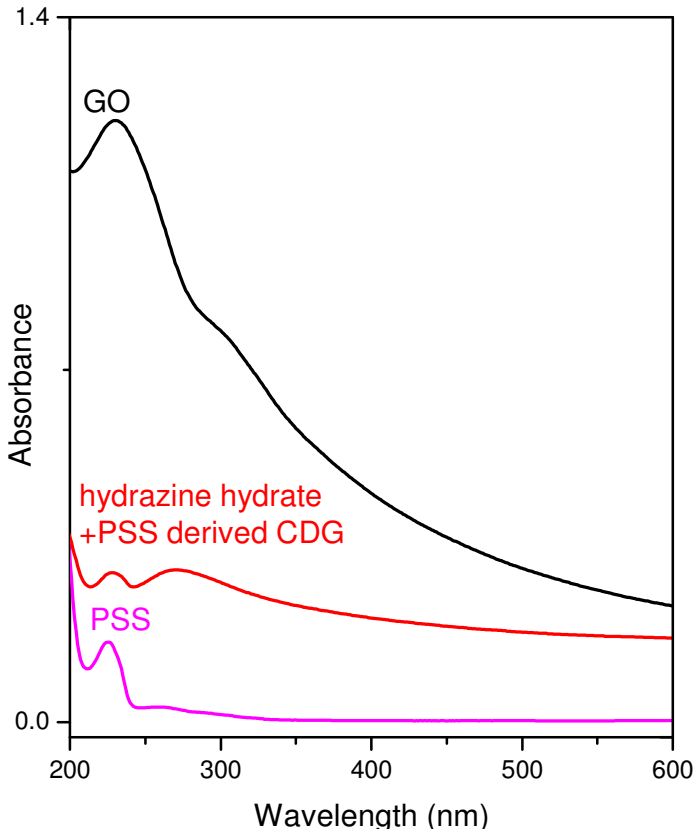

Figure 80: UV-Vis spectra of PSS, GO and CDG reduced by hydrazine hydrate in the presence of PSS.

TGA analysis was performed for TGO-derived graphene samples (Figure 81). Hydrazine hydrate mediated samples for different periods (1 day or 3 days) and thermally reduced sample show very similar trend in weight loss by temperature. Each has a weight loss <20 wt% in the temperature range of 25-1000°C like the natural graphite does. This means that reduced graphene oxide samples contain low number of functional groups due to the reduction of carboxyl, epoxide and hydroxyl groups in GO precursors.

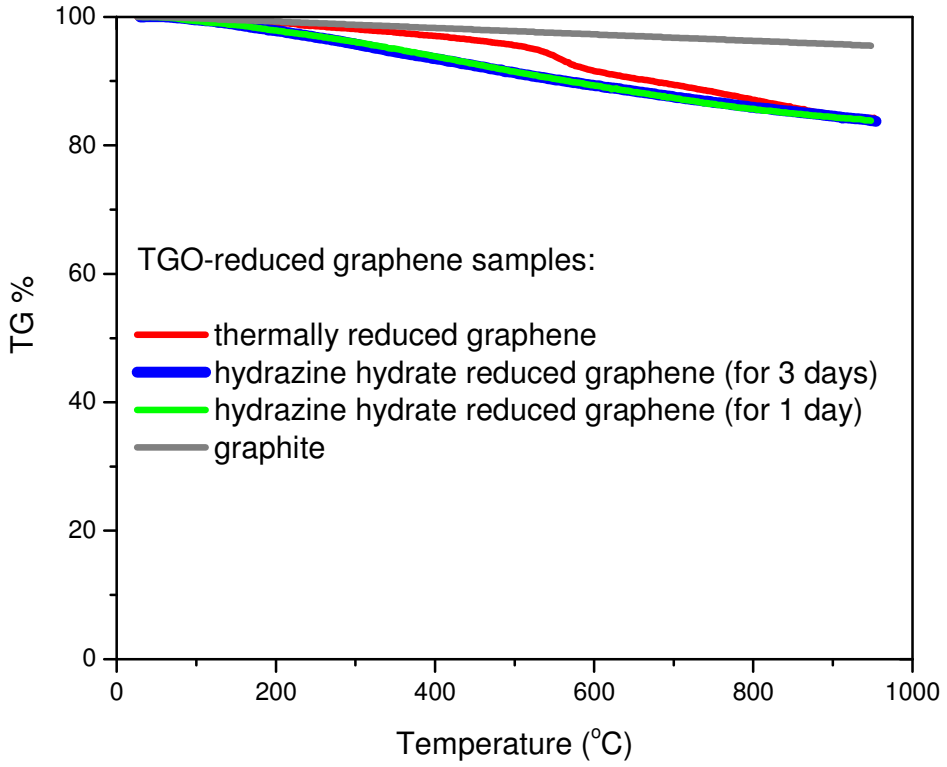

Figure 81: TGA data of graphite and CDG samples reduced by thermally and by hydrazine hydrate (for 1 day or 3 days), from TGO precursor, under He atmosphere.

Elemental analysis was conducted to follow the reduction process by comparing the carbon to oxygen ratio (C/O) of graphene oxide and chemically derived graphene samples (Table 18). As expected, C/O ratio increases (from 0.72 to 8.0) upon reduction of GO to CDG. Compared to hydrazine hydrate and thermally reduced CDG samples, re-reduced graphene has the highest C/O value (of 8.0). That result indicates that CDG was further reduced successfully with re-reduction method.

Table 18: Predicted formula and C/O ratio of TGO and CDG samples by Elemental Analysis.

Sample	Formula	C/O-ratio
Thermally CDG	$C_{77,48}HN_{0,12}O_{13,14}$	5,9
Re-reduced CDG	$C_{64,86}HN_{2,92}O_{8,09}$	8,0
TGO	$C_{11,84}HN_{0,02}O_{16,55}$	0,72
Hydrazine hydrate reduced CDG (1 day)	$C_{33,81}HN_{3,79}O_{8,77}$	4,0
Hydrazine hydrate reduced CDG (3 days)	$C_{33,73}HN_{3,55}O_{8,45}$	4,4

Moreover, BET nitrogen adsorption analyses (Figure 82), performed on graphite, GO and CDG samples after degassing at 80°C for 24 h, revealed that the re-reduced CDG has the largest surface area among them; ~600 $m^2.g^{-1}$ for re-reduced CDG, ~532 $m^2.g^{-1}$ for hydrazine hydrate reduced CDG, ~480 $m^2.g^{-1}$ for thermally reduced CDG, ~64 $m^2.g^{-1}$for GO and 1 $m^2.g^{-1}$ for graphite as expected.

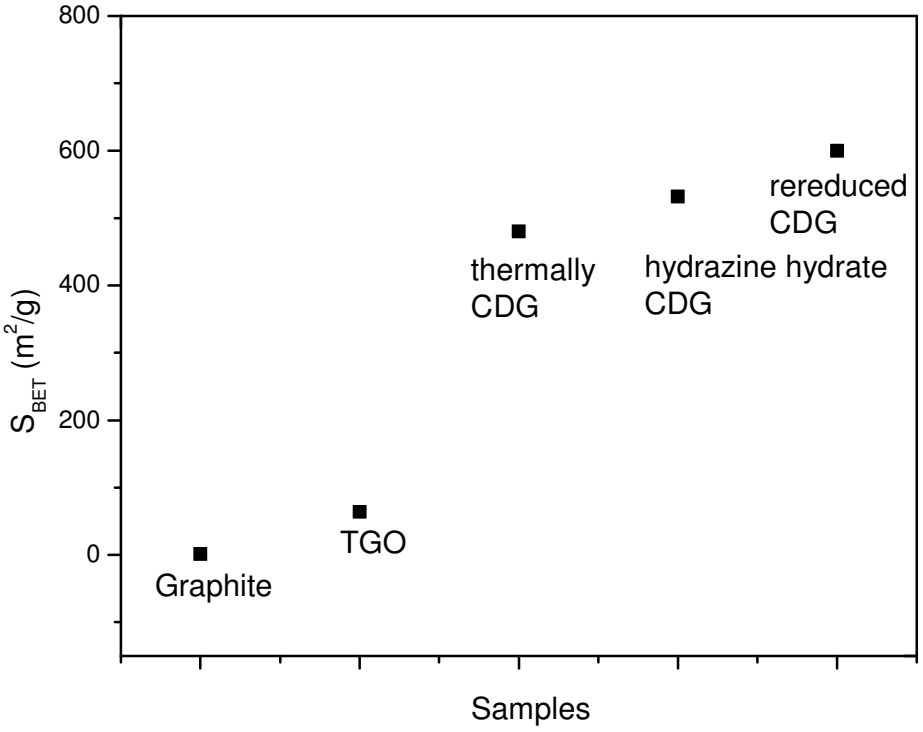

Figure 82: BET surface area results of graphite, TGO and CDG samples.

SEM micrographs for the SGO and TGO derived graphene samples were given in Figure 83. Moreover, the purity of the samples is also checked by means of EDX. SEM micrographs of SGO derived graphene samples by wet chemical (with hydrazine hydrate and hydroxylamine hydrochloride), thermal and vacuum-assisted methods are given in Figure 83 from A-E, respectively. Graphene samples via wet-chemical ways (A, B) look different than the ones by thermally reduced (C, D). Chemically reduced ones have curly edges with nonflat parts formed during chemical reduction process where the thermally ones have mostly flat, exfoliated layers. Thermal and vacuum assisted ones (C, D and E) have more pronounced impurities than the chemically reduced ones (A, B). This is most probably due to the washing the samples intensively after chemical reduction process that is missing in the thermally and vacuum assisted ones.

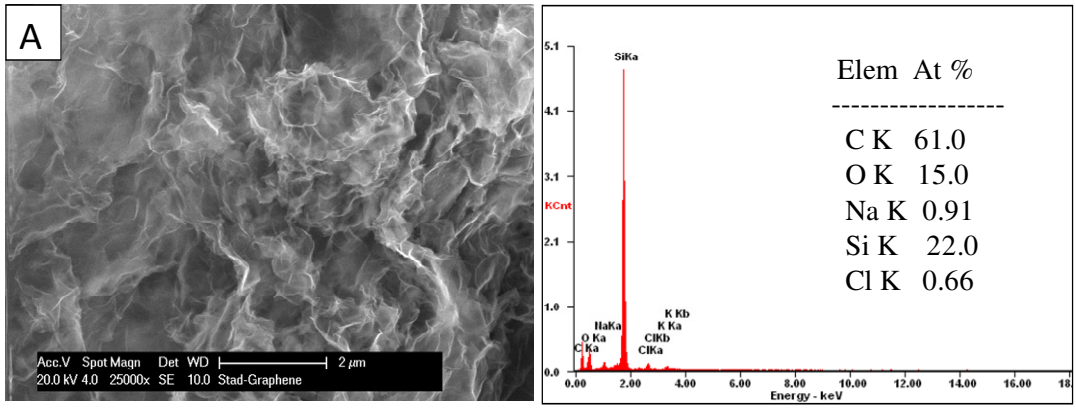
A
Acc.V Spot Magn Det WD 2 μm
20.0 kV 4.0 25000x SE 10.0 Stad-Graphene
SiKa
NaKa
O Ka
C Ka
K Kb
K Ka
ClKb
ClKa
KCnt
Energy - keV
Elem At %
C K 61.0
O K 15.0
Na K 0.91
Si K 22.0
Cl K 0.66

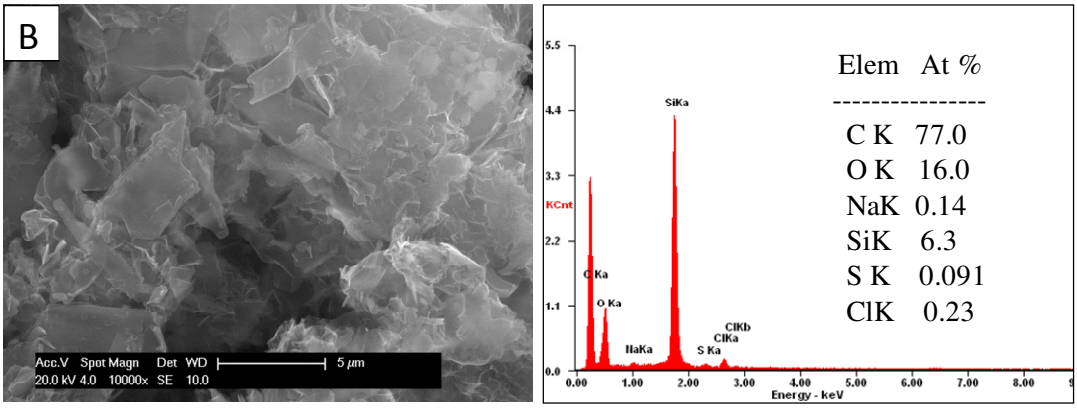
B
Acc.V Spot Magn Det WD 5 μm
20.0 kV 4.0 10000x SE 10.0
SiKa
C Ka
O Ka
NaKa
ClKb
ClKa
S Ka
KCnt
Energy - keV
Elem At %
C K 77.0
O K 16.0
NaK 0.14
SiK 6.3
S K 0.091
ClK 0.23

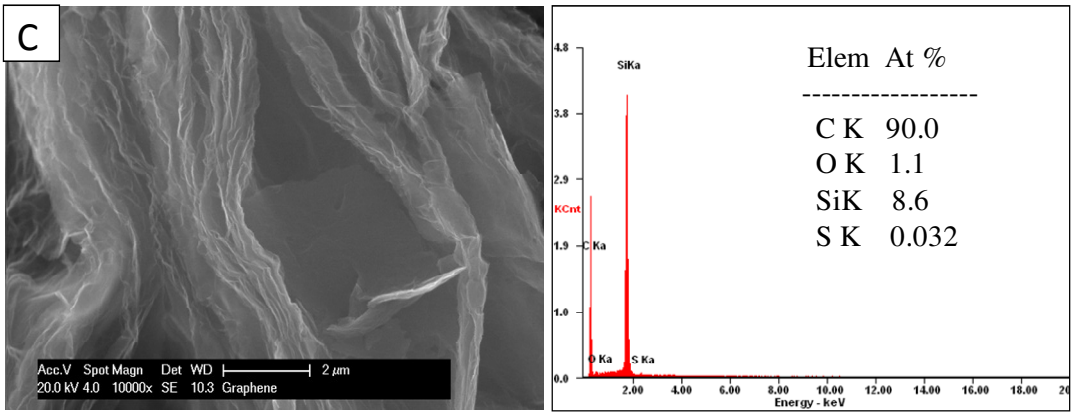
C
Acc.V Spot Magn Det WD 2 μm
20.0 kV 4.0 10000x SE 10.3 Graphene
SiKa
C Ka
O Ka
S Ka
KCnt
Energy - keV
Elem At %
C K 90.0
O K 1.1
SiK 8.6
S K 0.032

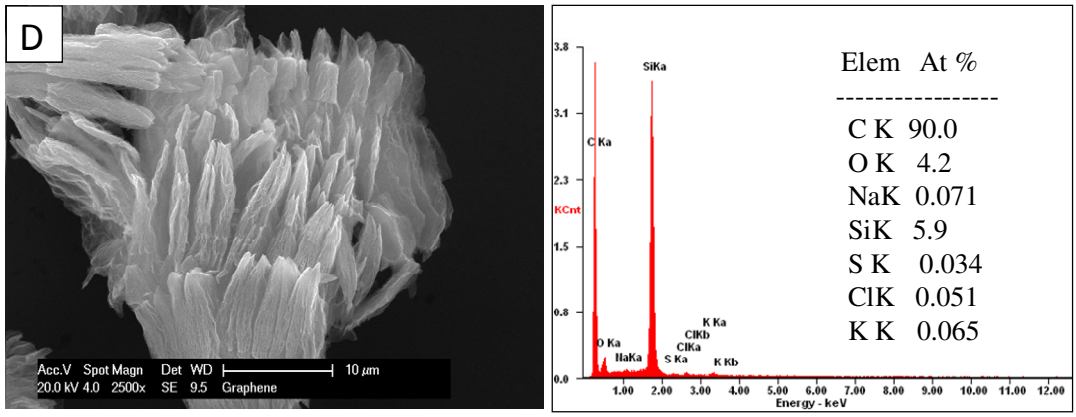
D
Acc.V Spot Magn Det WD 10 μm
20.0 kV 4.0 2500x SE 9.5 Graphene
SiKa
C Ka
O Ka
NaKa
S Ka
K Ka
ClKb
ClKa
K Kb
KCnt
Energy - keV
Elem At %
C K 90.0
O K 4.2
NaK 0.071
SiK 5.9
S K 0.034
ClK 0.051
K K 0.065

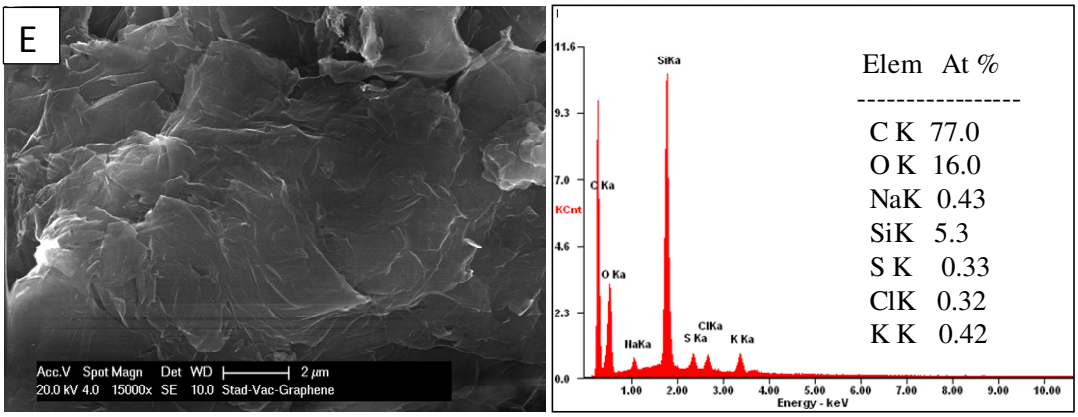

Figure 83: SEM images of CDG samples derived from SGO as precursor, corresponding EDX data of each area was given next to the SEM image. A. hydrazine hydrate reduced CDG; B. hydroxylamine hydrochloride reduced CDG; C, D. thermally reduced CDG (rapid and slow heating) and E. vacuum-assisted CDG.

SEM micrographs for graphene samples reduced from TGO samples are also given below in Figure 84. Different than SGO derived ones, even the thermally derived graphene samples (D-F) have nonflat areas. This is due to the difference in the GO precursors that are used for the reduction. As shown in the discussion for GO part, SGO is poorly oxidized from graphite than TGO case and SGO has similar looking like graphite. So, SGO does not result an obvious difference in the morphology during reduction (Figure 83 A-E), reduction of TGO ones look different than graphite. In summary, oxidation-reduction steps for TGO and TGO derived CDG samples are more successful compared to SGO and SGO derived ones. Similar to findings of graphene from SGO, wet-chemical derived graphene samples (A, C) except PSS introduced one (B) have less impurities than thermal and vacuum-assisted ones (D-G). This is again due to the washing step at the end of chemical reduction process. Nevertheless, hydrazine hydrate reduced samples in the presence of PSS contains some other elements besides C due to the PSS polymer itself (Figure 83 B).

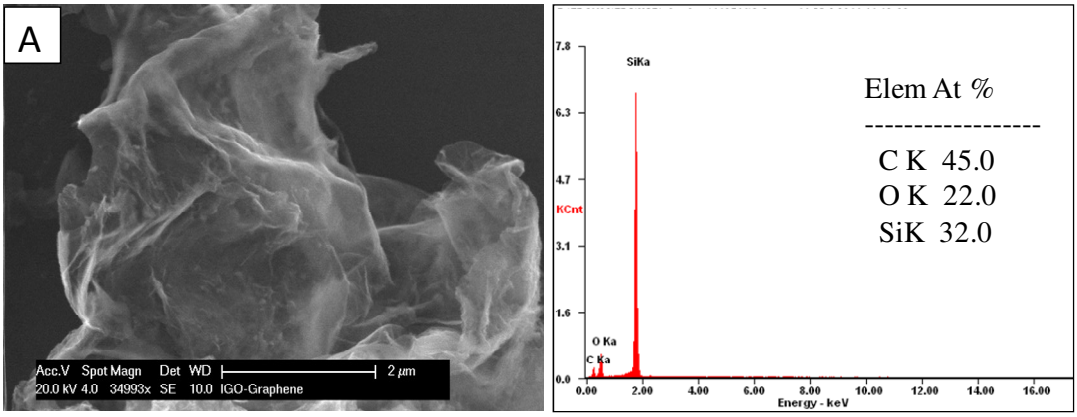
A
Acc.V Spot Magn Det WD 2 μm
20.0 kV 4.0 34993x SE 10.0 IGO-Graphene
SiKa
O Ka
C Ka
KCnt
Energy - keV
Elem At %
C K 45.0
O K 22.0
SiK 32.0

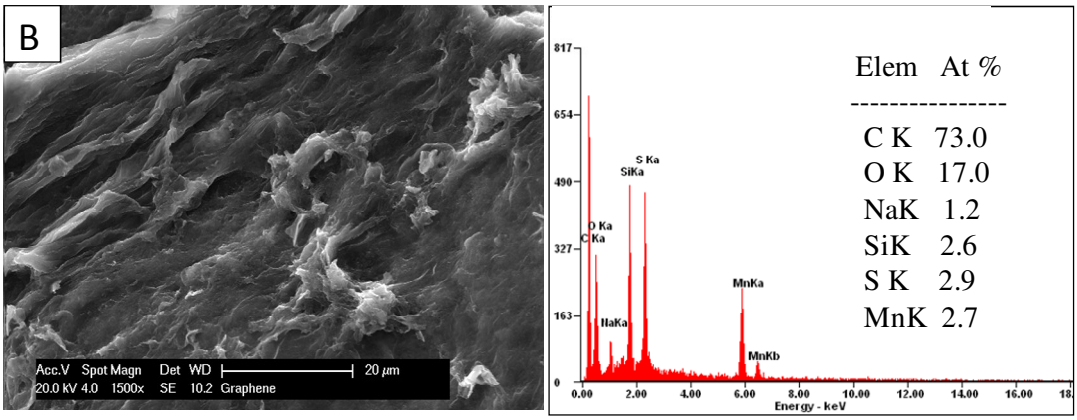
B
Acc.V Spot Magn Det WD 20 μm
20.0 kV 4.0 1500x SE 10.2 Graphene
S Ka
SiKa
O Ka
C Ka
MnKa
NaKa
MnKb
Energy - keV
Elem At %
C K 73.0
O K 17.0
NaK 1.2
SiK 2.6
S K 2.9
MnK 2.7

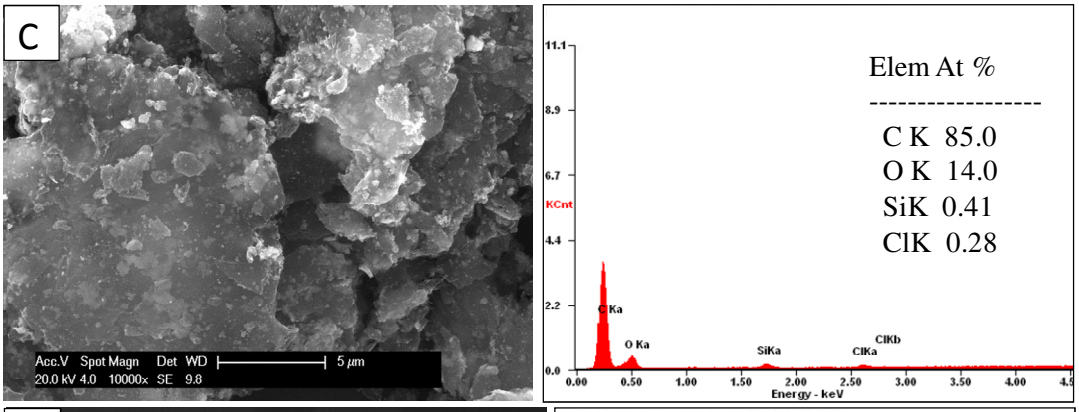
C
Acc.V Spot Magn Det WD 5 μm
20.0 kV 4.0 10000x SE 9.8
Cl Ka
O Ka
SiKa
ClKb
ClKa
KCnt
Energy - keV
Elem At %
C K 85.0
O K 14.0
SiK 0.41
ClK 0.28

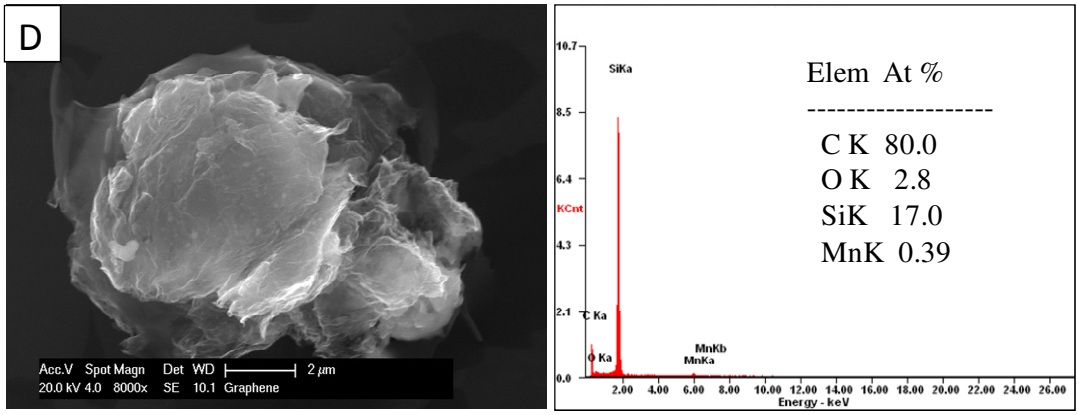
D
Acc.V Spot Magn Det WD 2 μm
20.0 kV 4.0 8000x SE 10.1 Graphene
SiKa
C Ka
O Ka
MnKb
MnKa
KCnt
Energy - keV
Elem At %
C K 80.0
O K 2.8
SiK 17.0
MnK 0.39

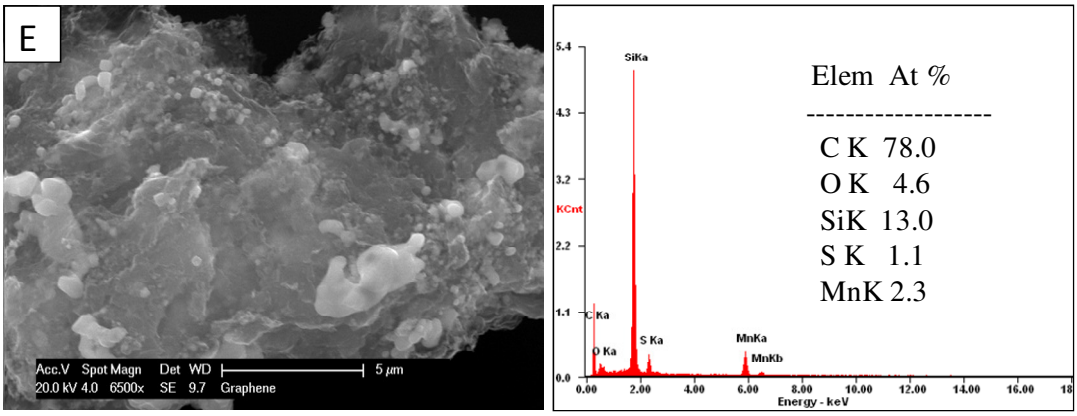

Figure 84: SEM images of CDG samples derived from TGO as precursor. Corresponding EDX data of each area was given next to the SEM image. A. hydrazine hydrate reduced; B. hydrazine hydrate reduced in the presence of PSS; C. hydroxylamine reduced; D-F. thermally reduced (via rapid or slow heating); G. vacuum-assisted CDG.

Figure 85 shows the TEM and HRTEM images of the sonificated hexane dispersion of CDG. The thin layered and transparent structure of CDG can nicely be seen from the TEM image in Figure 85 a. The number of the graphitic layers could be calculated as 8-10 from the wrinkle of the CDG layers in the HRTEM image in Figure 85 b, which indicates a few layered structure of the 2D graphene [51]. Additionally, the distance between the CDG layers was calculated as 0.38 nm from the wrinkle observed in the HRTEM image, which is consistent with the reported values [57b].

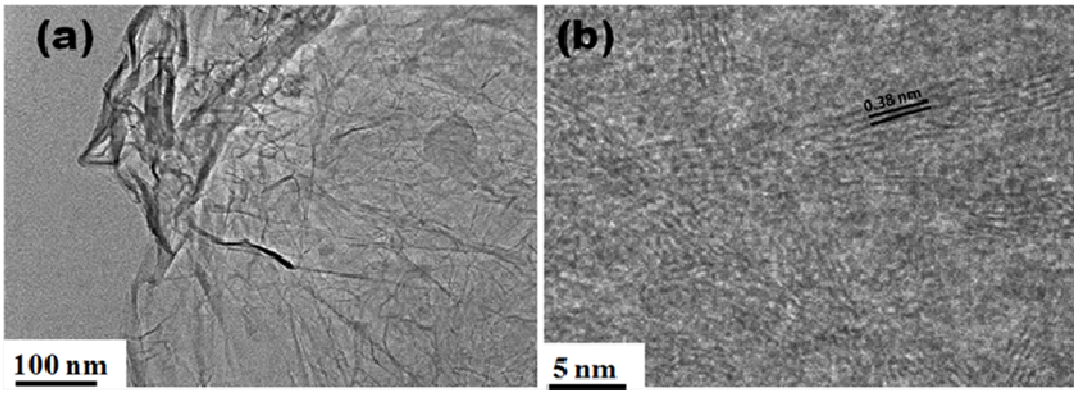

Figure 85: (a) TEM and (b) HRTEM images of CDG [38].

4. Chemically derived graphene hybrid materials

4.1. Graphene with Metal Nanoparticles

Chemically derived graphene (CDG) is used to produce hybrid materials of CDG derived metal and metal oxide NPs to utilize the outstanding properties of graphene such as high surface area with defects and conductivity that is essential for applications such as catalysis and gas sensors. To illustrate, the use of graphene as support for developing novel heterogeneous catalysts with enhanced activity is desired due to its huge surface area (theoretical value 2600 m^2/g) [105] and excellent chemical stability [106]. Recently, many examples of using graphene as support for noble metal nanoparticles such as Ag [107], Pt [108] , Pd [109], and Au [110] have been reported. Among them, palladium nanoparticles (Pd NPs) are especially important due to their extensive applications in a variety of industrial reactions such as hydrogenation [111], Suzuki-Miyaura [112], Heck [113] and Stille [114] coupling reactions. In a recent study, the Pd NPs supported on graphite oxide (GO) or chemically derived graphene (CDG) have been employed as catalyst in the Suzuki-Miyaura coupling reaction, whereby the CDG supported Pd NPs were *in situ* generated from the reduction of Pd^{2+}-exchanged GO by hydrazine hydrate in aqueous solution [115]. However, the kinetic control of the *in situ* generated Pd NPs on CDG has been found to be difficult in this procedure. A literature survey resulted in no hit on CDG supported Pd NPs generated *ex situ* and then supported on CDG.

In this regard, the preparation of Pd NPs in a separate step (*ex situ*) and then supporting them on CDG would be more advantageous to control the size and dispersion of the nanoparticles, which are very important issues on enhancing the catalytic activity of nanoparticles catalyst.

Storing hydrogen in a lightweight material is of great of interest especially for mobile applications. Ammonia borane (AB, $H_3N{\bullet}BH_3$) is considered to be a promising candidate for "on-board" hydrogen storage applications [116] owing to its impressive gravimetric hydrogen content of 19.6% wt (6.5% wt and 13.1% wt for the first and second equivalents of H_2, respectively), stability in the solid state under ambient conditions, and nontoxicity [117]. The hydrogen stored in the AB can be released through different routes including solid state thermolysis [118], solvolyis [119] and dehydrogenation [120].

Among these routes, the dehydrogenation of AB in organic solvents (Eq.1) and hydrolysis (Eq. 2) are considered to be the most convenient methods [121].

$$n\ H_3NBH_3 \rightleftharpoons (H_2NBH_2)_n + nH_2 \quad (1)$$

$$H_3NBH_3(aq) + 2H_2O(l) \longrightarrow (NH_4)BO_2(aq) + 3H_2(g) \quad (2)$$

However, a suitable catalyst is needed for hydrogen generation from AB in both the dehydrogenation and hydrolysis routes. Many transition metals or their alloys have been tested as catalysts in the dehydrogenation [122] and hydrolysis of AB [123] but there is no example of a catalyst inducing the hydrogen generation from both reactions. Additionally, there are only a few examples of supported metal nanoparticles used in the dehydrogenation and hydrolysis of AB. In a previous study, it is reported that palladium(0) nanoparticles stabilized by a water soluble polymer are highly active catalyst in hydrogen generation from the hydrolysis of AB [124]. In a more recent study, it is also shown that oleylamine stabilized palladium(0) nanoparticles are active catalyst in the dehydrogenation of AB [125]. However, both palladium(0) nanoparticle catalysts were *in situ* generated during the hydrolysis or dehydrogenation of AB that caused a problem in recovery and reusability of the catalysts. In this regard, supporting Pd NPs on a high surface area material such as CDG would be a feasible solution to the recovery problem for both catalytic reactions.

In the following I report the synthesis and application of CDG/Metal NPs. Au, Ni and Pd metal nanoparticles were synthesized, Au was in-situ deposited on CDG whereas Ni and Pd were ex-situ supported on CDG. As synthesized ex-situ supported Pd-CDG samples were used in dehydrogenation and hydrolysis of ammonia borane reactions.

4.1.1. Results for Chemically Derived Graphene/Metal Nanoparticles (NPs) Hybrid Materials

The well characterized CDG was used as support materials for the Ni and Pd NPs. The Ni NPs (of 3.2 nm) and Pd NPs (of 4.5 nm) were obtained from the reduction of Nickel(II) acetylacetonate (in the presence of OAm and oleic acid) or palladium(II) acetylacetonate by borane tert-butylamine complex (BTB; $C_4H_{14}BN$) (in the presence of oleylamine (OAm; $C_{18}H_{37}N$)). In our protocol, OAm acts the solvent and surfactant while BTB serves as reductant. Figure 86 A shows TEM image of the Ni NPs stabilized by oleic acid

($C_{18}H_{34}O_2$) and OAm while Figure 86 B shows a TEM image of the Pd NPs stabilized by OAm. The Ni NPs have 3.2 nm of size. The Pd NPs of 4.5 nm size have a narrow size distribution with a standard deviation of 7% in the diameter.

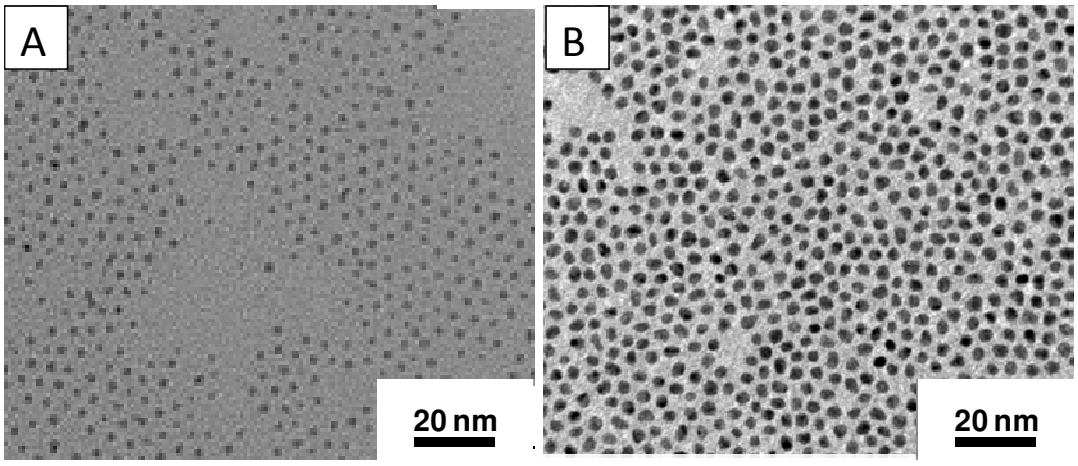

Figure 86: TEM image of the (A) OAm and oleic acid stabilized nickel nanoparticles (B) OAm stabilized palladium nanoparticles (TEM images were taken at Middle East Technical University/Central Lab, Turkey).

The OAm stabilized Pd NPs were impregnated on CDG to employ them as catalyst in hydrogen generation from the hydrolysis and dehydrogenation of AB. Figure 87 shows the TEM and HRTEM images of the CDG supported Pd NPs. As clearly seen from the TEM image in Figure 87a, Pd NPs are well dispersed on CDG and preserved their particle size distribution. The crystallinity of the Pd NPs was examined after supporting them on CDG by the HRTEM image given in Figure 87b. A typical interfringe distance of 0.221 nm was calculated from the HRTEM images, which is close to the lattice spacing of the (111) planes of the fcc palladium (0.223 nm) [124].

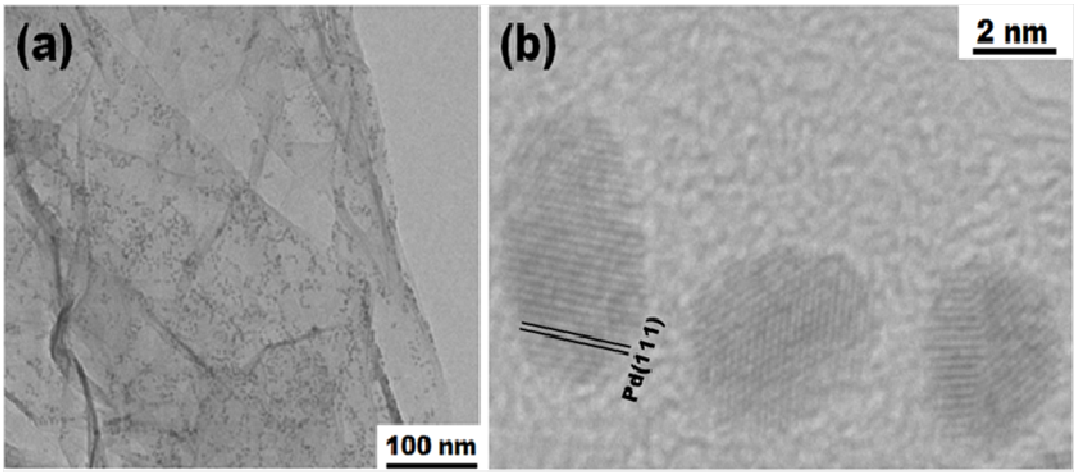

Figure 87: (a) TEM and (b) HRTEM image of the chemically derived graphene supported OAm stabilized palladium nanoparticles [38].

For Au NPs on graphene oxide and graphene samples (hydrazine hydrate reduced CDG and re-reduced CDG), SEM-EDX analysis was performed. Although 5 wt% Au was used for each supports, the amount of Au on the supports decreases from graphene oxide to CDG graphene and re-reduced CDG (see 5. Appendix, Figure 136). Therefore, Au reduction on graphene oxide is more feasible than on graphene. This can be attributed to the presence of functional groups on graphene oxide which can favor the linking of Cetyl trimethylammonium bromide (CTAB ($(C_{16}H_{33})N(CH_3)_3Br$) stabilized Au. The more CTAB-stabilized-Au particles are supported on graphene oxide, the higher content of Au NPs (3.7 wt% Au) through in-situ reduction on the support is expected to be formed.

4.2. Graphene with Metal Oxide Nanoparticles

As a crucial part of sustainable chemistry, photodegradation is a green process for the dissociation of unwanted pollutants. The molecule to be photodegraded in this study is methylene blue (MB; $C_{16}H_{18}N_3SCl$), which is often released along with waste water during the dyeing and printing textiles process and subsequently pollutes our ecosystem.
In the process of photodegradation of MB catalyzed by semiconducting metal oxides, electrons in the valence band are excited and jump across the band gap into the conduction band, thereby leaving behind a positive "hole" [126]. Therefore, electrons (e^-) and holes (h^+) are generetad at the semiconducting metal oxide (MO) surface (here, TiO_2 and WO_3). Photocatalytic reaction of water (H_2O) with h^+ and, photocatalytic reaction of oxygen (O_2) with e^- yield the formation of $OH^\bullet$ and $O_2^{-\bullet}$ radicals that carry strong

oxidation capability. O_2 that is generated by decomposition of $HO_2^{\bullet}$ (protonated superoxide), irreversibly oxidizes MB to H_2O, CO_2 and mineral acid [127]. Besides that, second possible mechanism for the bleaching of MB is simple reversible reduction of MB to the leuco form (LMB) [127b, 128][129] [130](see Figure 88).

$$MO + h\nu \longrightarrow h^+ + e^- \quad (1)$$

$$H_2O + h^+ \longrightarrow OH^{\bullet} + H^+ \quad (2)$$

$$O_2 + e^- \longrightarrow O_2^{-\bullet} \quad (3)$$

$$O_2^{-\bullet} + H^+ \longrightarrow HO_2^{\bullet} \quad (4)$$

$$2HO_2^{\bullet} \longrightarrow H_2O_2 + O_2 \quad (5)$$

$$C_{16}H_{18}N_3SCl + 25\ ½O_2 \longrightarrow 6H_2O + 16CO_2 + HCl + H_2SO_4 + 3HNO_3 \quad (6)$$

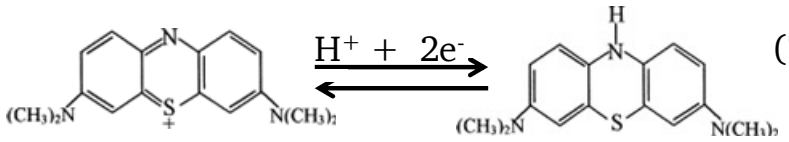

(7)

(Methylene blue) (Leuco Methylene blue)

Figure 88. Possible reaction pathway of photocatalytic degradation of methylene blue ($C_{16}H_{18}N_3SCl$) in the presence of UV-irradiated semiconductor metal oxide (MO).

Of course, the subject of photodegradation does not have to be methylene blue; the concept can be transferred and applied to other organic pollutants which are photodegradable.

I have performed experiments with some of the most prominent photocatalysts. These include titanium oxide which has a band gap of 3.2eV, active in the UV region [131]. It is known for its low toxicity and long term thermodynamic stability [126]. The crystallinity of titanium dioxide is also crucial, as it is well known that the anatase phase is more active than the rutile phase [132]. A common commercial TiO_2 under the name of AEROXIDE TiO_2 P25 (it is referred to as P25), which is a mixture of anatase (85%) and rutile (15%), was tested.

A recent study reports the use of tungsten trioxide as a valuable photocatalyst due to its photoactivity within the visible range (~500 nm), stable physicochemical properties, and resilience to photo-corrosions [133]. Although it may not be as viable as titanium dioxide, which is known to offer more cost efficient performance within the UV range, there is a

possibility that the synthesis of metal oxide composites with an optimized amount of tungsten trioxide will be able to both extend photoactivity into the visible range [133]. The major problem hindering photocatalysis is that the excited electron in the conduction band will recombine with the positively charged "hole" in the valence band [133] [134] [126]. Often the recombination happens rapidly than the time it takes for the catalyst to chemically interact with the organic pollutant. This problem is common to all the aforementioned catalysts. For instance, trap sites in titania may be generated due to the structural imperfections in the lattice. Those sites act as recombination centers so that electrons and holes concentrations decrease [135]. Inclusion of electron accepting species such as Mn^{2+}, Cr^{3+}, Ni^{2+}, Cu^{2+}, Co^{2+}, SiO_2 and V_2O_5 to titania has been found to improve the performance of the photocatalysts [136]. Transition metal ions increase the photocatalytic activity either by scavenging electrons that will go through the recombination process. Those ions may also modify the catalyst surface while introducing active sites so that the adsorption of the organic dye to be degraded increases. Moreover, there have been suggestions that the synthesis of a coupled semiconductor such as WO_x-TiO_2 will be able to prolong the recombination time due to the charge separation [131]. It has been found that an optimum WO_3 content (considering costs and efficiency) in WO_x-TiO_2 composites is 3% [131]. Another popular suggestion is to synthesize metal oxide graphene composites as this is expected to yield more promising results [134] [137]. By incorporating graphene into metal oxide catalysts, its high specific surface area and high charge carrier mobility allows it to act as an electron acceptor thereby supporting the formation of electron-hole pairs [126, 134, 137-138].

It has already been shown that the photocatalytic performance of titanium dioxide catalyst was improved when supported on graphene [137]. This can be explained by a flow of electrons from the titanium dioxide to graphene; due to the energy level difference at the interface, a Schottky barrier is formed which inhibits the recombination of electron-hole pairs [126]. Similarly this concept has been extrapolated to tungsten trioxides; in this case the principle remains the same: the graphene acts as an electron transfer channel to remove photogenerated electrons [133].

In an effort to improve on the photoactivity of extensively used photocatalysts, in particular titanium dioxide, two properties must be achieved: 1) extension of the energy range of photoexcitation to include the visible range and 2) hinder the recombination of electron-hole pairs. I have aimed to test the effects of coupling titanium dioxide to WO_3 and also compositing metal oxides with graphene. Both of these methods have received attention for their ability to achieve both of the above desired properties, thereby

enhancing photoactivity. I wish to investigate into the photoactivity of titanium dioxide (P25 and TiO_2 samples), and synergistic effect formed with graphene and tungsten oxide addition to titania. The idea of supporting WO_3 in the composites is the ability of WO_3 to improve and extend photoactivity into the visible range as well.

Besides CDG/Metal NPs systems discussed in the previous section, CDG/metal oxide NPs were also synthesized and characterized. For that purpose, titania was in-situ (via photodegradation process) and ex-situ (by hydrothermal method) formed with CDG. Similarly, WO_3/CDG and WO_3/titania (P25 and TiO_2) samples were prepared by sonochemical methods. Moreover, ZnO/CDG samples that were also prepared by thermal decomposition of a zinc oximato complex ($[CH_3ONCCH_3COO]_2Zn.2H_2O$ [139]) in the presence of CDG under reflux, were used to sense hydrogen at room temperature, 200 and 300°C. Ex-situ supported titania and tungsten oxide based CDG samples were applied in photodegradation of methylene blue under UV light.

4.2.1. TiO_2/Graphene

TiO_2/graphene samples were prepared with a photocatalytic method (UV-assisted) and by a hydrothermal synthesis method. In both of the cases, graphene oxide was used as the source for graphene formation and titanium (IV) isopropoxide (in UV-assisted synthesis) and TiO_2 (anatase, Merck) or P25 (anatase and rutile mixture, Evonik) (in hydrothermal method) were the precursors for titania. Hydrothermally synthesized samples were used as a catalyst for photodegradation of methylene blue.

4.2.2. Results for Chemically Derived Graphene/Metal Oxide Hybrid Materials

TiO_2/Graphene (by UV-assisted/ photocatalytic method)

Graphene oxide due to its functional groups is dispersible in polar solvent giving brown color. Reduction of graphene oxide in ethanol results in graphene with an indication of color change from brown to black. Here, UV-assisted method (photocatalytic method) was used for the reduction of functional groups (epoxides, hydroxyl groups, carboxylic acids) of the graphene oxide into chemically derived graphene in the presence of titanium species [140]. Before and after the photocatalysis procedure, ethanol suspensions of the samples were dried on a watch glass under air at room temperature. Figure 89 shows TiO_2−TGO (before the reaction) and TiO_2−CDG (after the reaction) samples after being

dried. Photos taken before and after UV irradiation clearly indicates the reduction of graphene oxide (brown) into graphene (black) in the presence of titanium species.

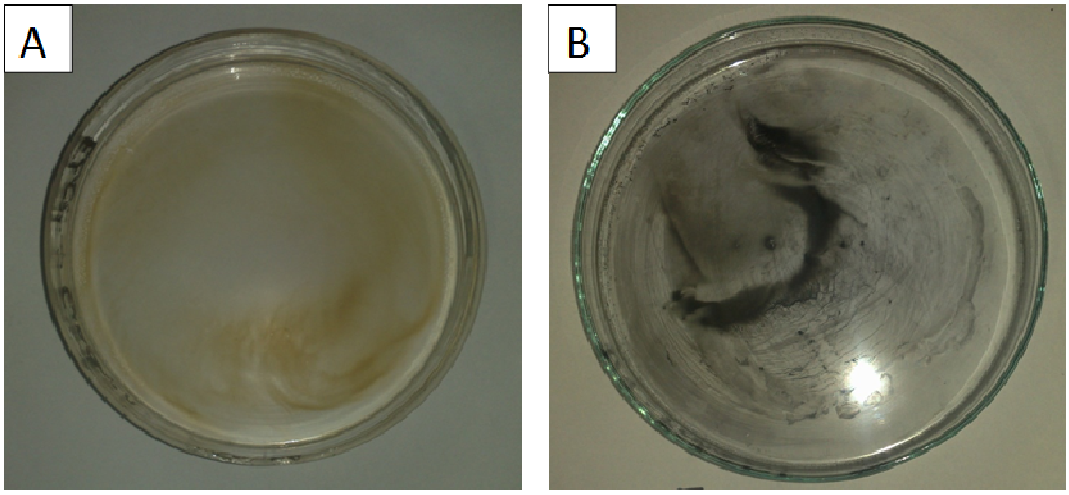

Figure 89: Photos of A. TiO_2 on Tour's graphene oxide (TiO_2–TGO) (before UV-irradiation) and B. TiO_2 on chemically derived graphene (TiO_2–CDG) powders (after UV-irradiation) obtained after solvent evaporation and drying the samples at room temperature.

The photocatalytic properties of semiconducting TiO_2 particles are reported in detail [141]. Charge separation into valence band holes (h) and conduction bands electrons (e) occurs upon band gap UV-irradiation of the semiconductor TiO_2 in suspension. Recombination of holes and electrons is prevented since holes are used to produce ethoxy radicals in the presence of ethanol. So, the electrons that accumulate within the titania particles reduce the functional groups during interaction with graphene oxide (reaction 1). The reaction proceeds as in the following proposed mechanism given in the equation below.

$$TiO_2 + h\nu \longrightarrow TiO_2(h + e) \xrightarrow{C_2H_5OH} TiO_2(e) + \dot{C}_2H_4OH + H^+$$

$$TiO_2(e) + \text{graphene oxide} \longrightarrow TiO_2 + \text{graphene}$$

Figure 90: Proposed mechanism of UV-assisted reduction of GO to CDG in the presence of TiO_2 to form TiO_2/CDG [140].

The UV-assisted reduction process of graphene oxide in the presence of titania nanoparticles is summarized in the following scheme as well.

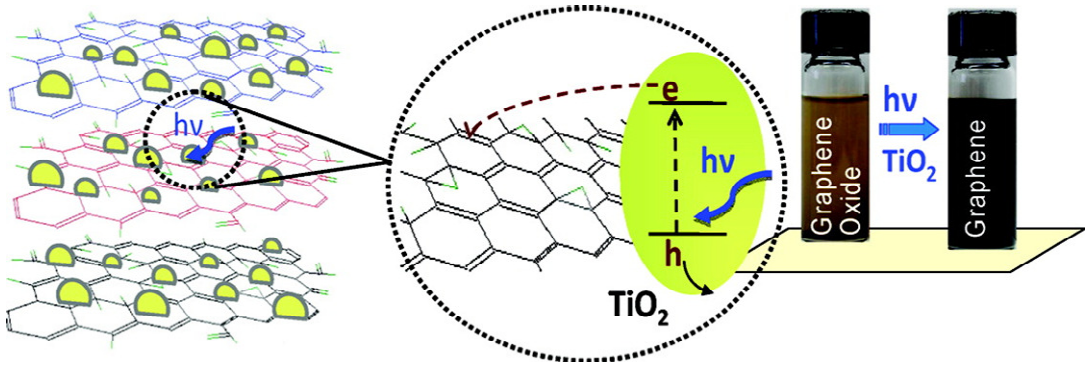

Figure 91: UV-assisted reduction process of graphene oxide in the presence of titania given visually from [140].

Raman spectra taken for the sample after UV-irradiation process is given in comparison to TGO. The change in the fingerprint bands; D and G (D-relative intensity increases and G-shifts to lower frequency bands after the reaction) clearly indicates that graphene oxide is reduced into graphene with the help of titania through the photocatalytic process. Besides D (~1351 cm^{-1}) and G (~1592 cm^{-1}) bands for graphene, some other features at 201, 397, 512 and 622 can be also seen in the figure below. These bands are assigned to anatase [142].

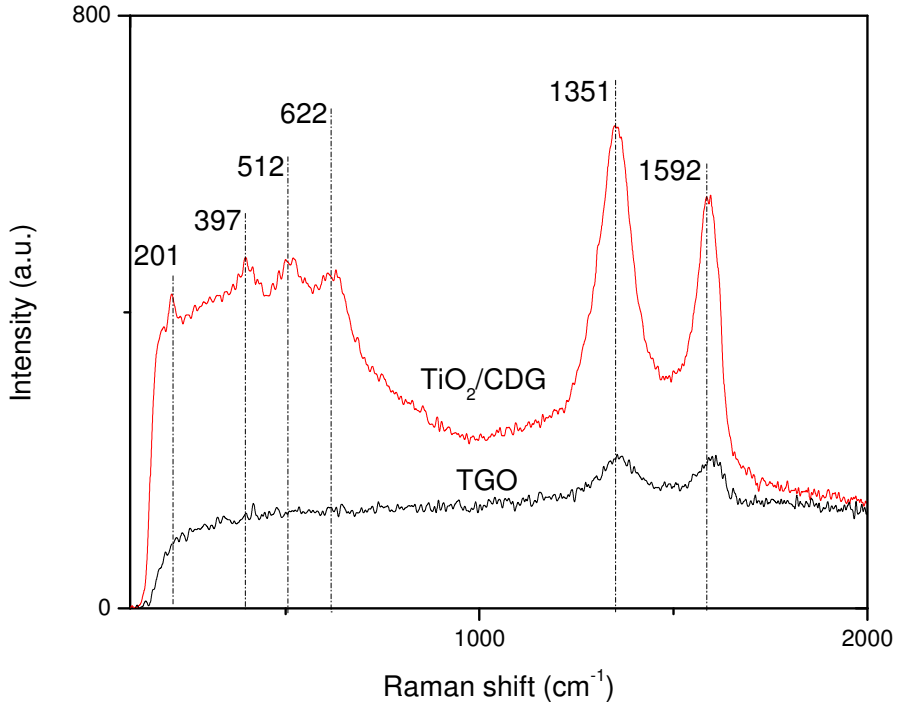

Figure 92: Raman spectra of TGO and UV-assisted TiO_2/CDG samples.

SEM and EDX analysis of TiO_2 particles shows the presence of Ti, O and Si peaks and no impurities (Figure 93 A). TiO_2 particles are agglomerated but still have a size below 100 nm. It should be noted that that size does not represent the individual particle size because TiO_2 particles quickly agglomerate when the mixing of the suspension is stopped. That can be also realized from the color change when the mixing is interrupted.

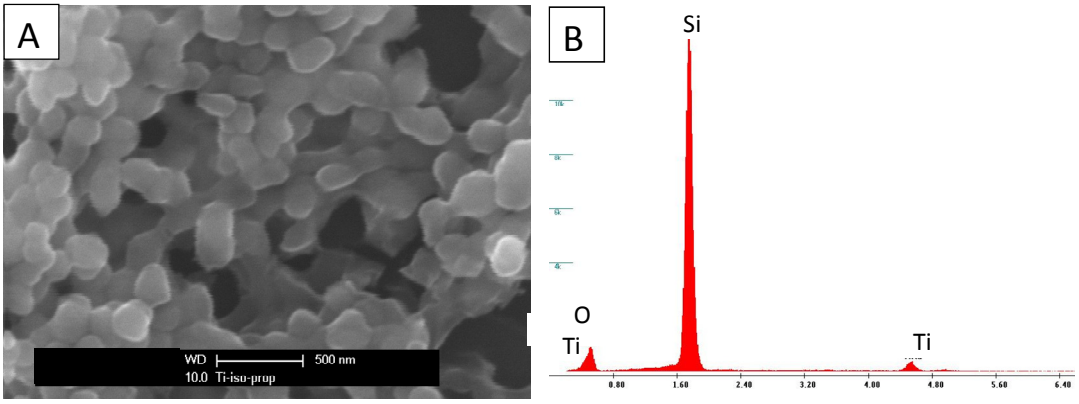

Figure 93: TiO_2 nanoparticles obtained with the addition of titanium isopropoxide into ethanol is put on SiO_2 wafer dropwise and dried.

TiO_2 nanoparticles are hardly visible in the SEM image of TiO_2/TGO sample prior to UV irradiation (Figure 94 A). The presence of titania however is confirmed by EDX (Figure 94 B).

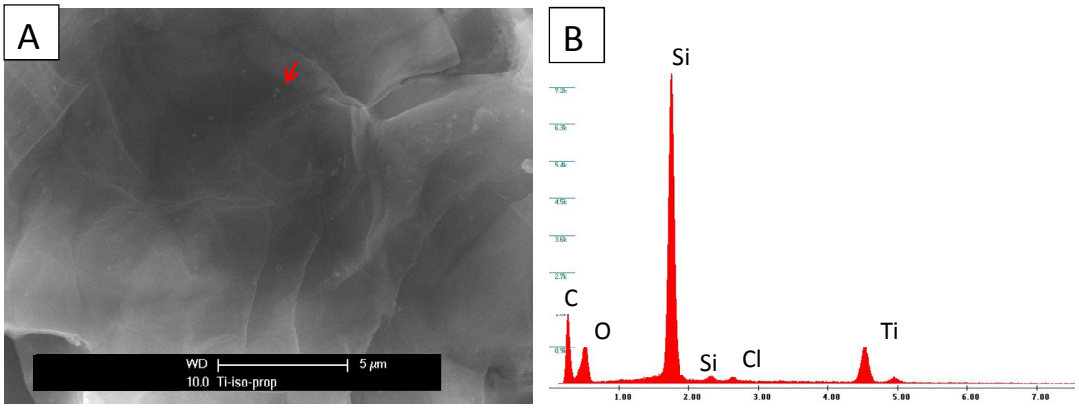

Figure 94: SEM image and EDX spectrum or UV-assisted TiO_2/TGO.

Similar to TiO_2/TGO sample, titania species can be also seen in SEM image of the TiO_2/CDG sample. Titania particles become more visible due to the scattering of titania

particles in BSE (backscattered electron) mode. Titanium signals are seen in EDX spectrum as well.

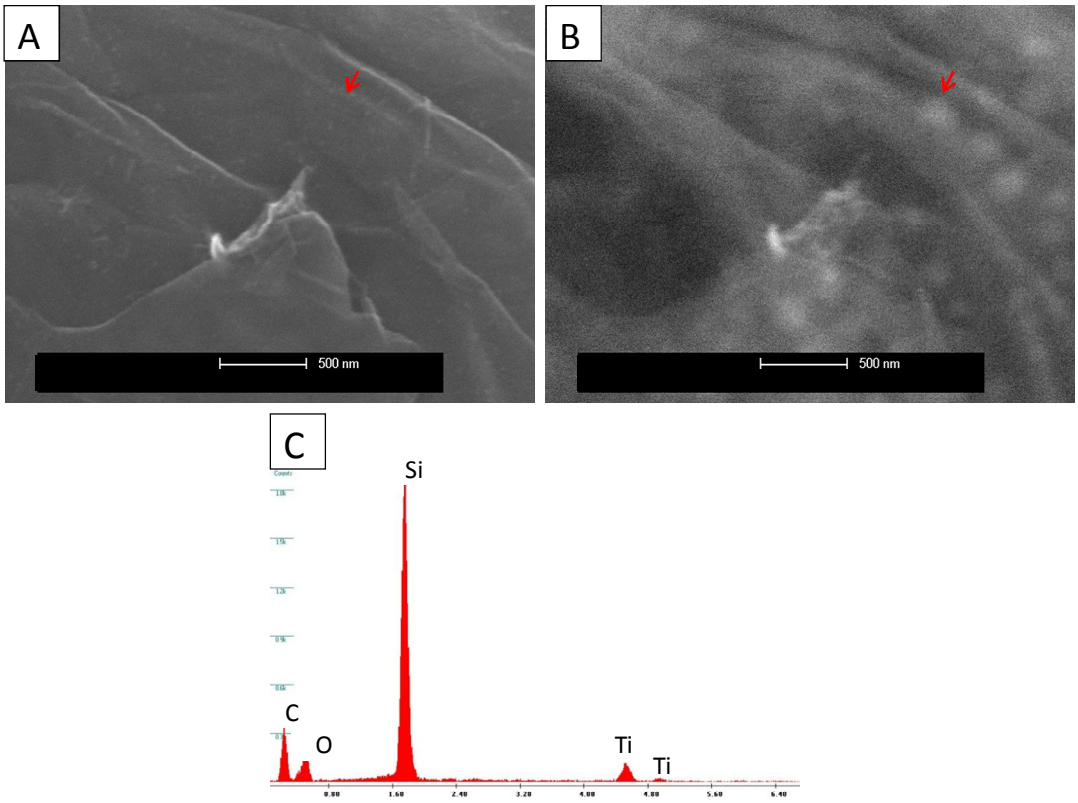

Figure 95: A. SE-image, b. BSE-image, and C. EDX spectrum of UV-assisted TiO_2/CDG.

TiO_2/Graphene (by hydrothermal method)

Two different types of commercial titania (P25 (Degussa) and TiO_2 (Merck KGaA)) were supported on chemically derived graphene by hydrothermal method. P25 is claimed to be a mixture of anatase and rutile phases while TiO_2 consists of only anatase. To clarify this, Raman analysis was performed to investigate P25 and TiO_2 samples. For both of the titania precursors, six bands at 143, 194, 395, 513, 519 and 636 cm^{-1} assigned for anatase are seen in Figure 96. Different than TiO_2 sample, small shoulders at 445 and 609 cm^{-1} referred to the typical features for rutile phases is detected for P25 sample. Therefore, it is confirmed with Raman spectra that different than TiO_2 sample (anatase), P25 is composed of the mixture of anatase and rutile phases.

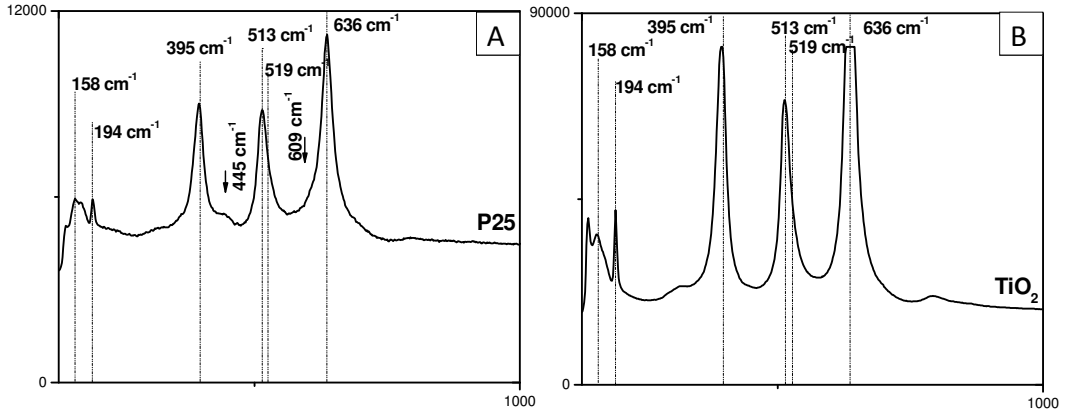

Figure 96. Raman spectra of titania samples A. P25 and B. TiO_2

Morphological analysis for the bare TiO_2 and TiO_2/graphene 1 wt% was conducted by SEM and TEM as well. TiO_2 particles have particle size in the wide range of 50-200 nm as shown in Figure 97 A-B.

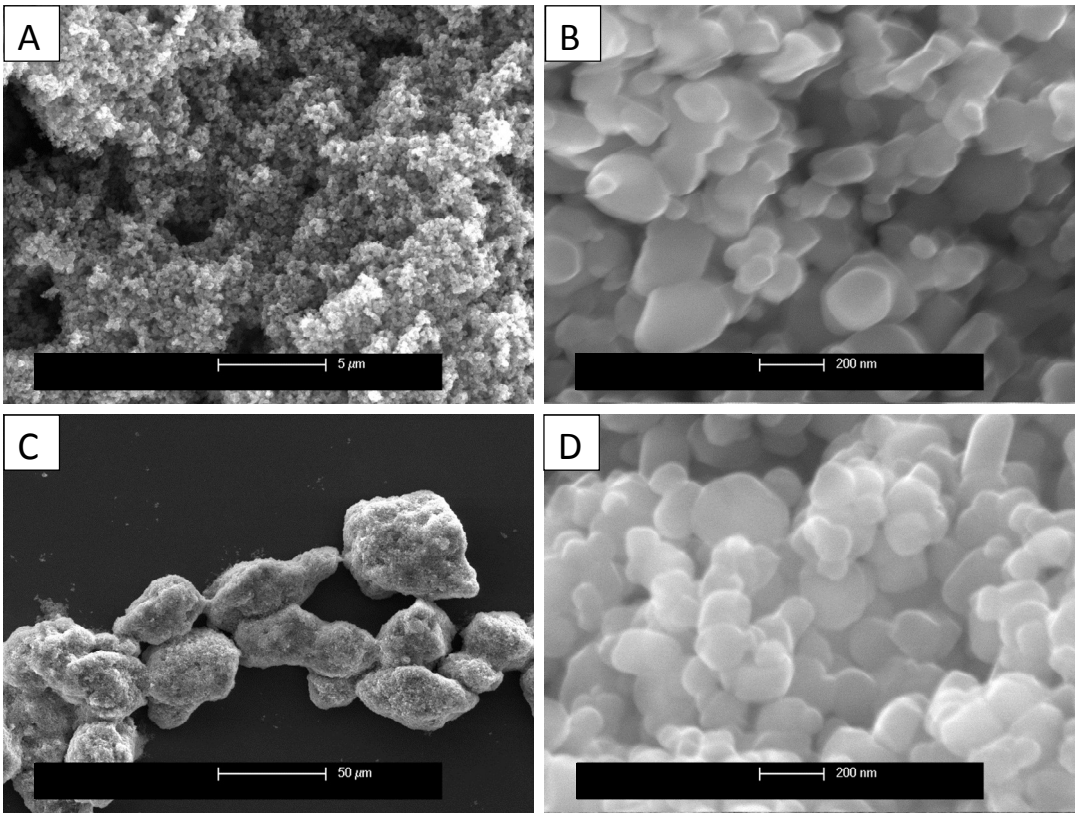

Figure 97: SEM images of, A, B. TiO_2 and C, D. TiO_2/CDG 1wt% samples.

When titania particles are hydrothermally supported on graphene oxide to form TiO_2/graphene 1 wt%, no detectable increase in the particle size of TiO_2 particles is seen as given in SEM and TEM images of TiO_2/graphene 1 wt% sample (Figure 97, Figure 98).

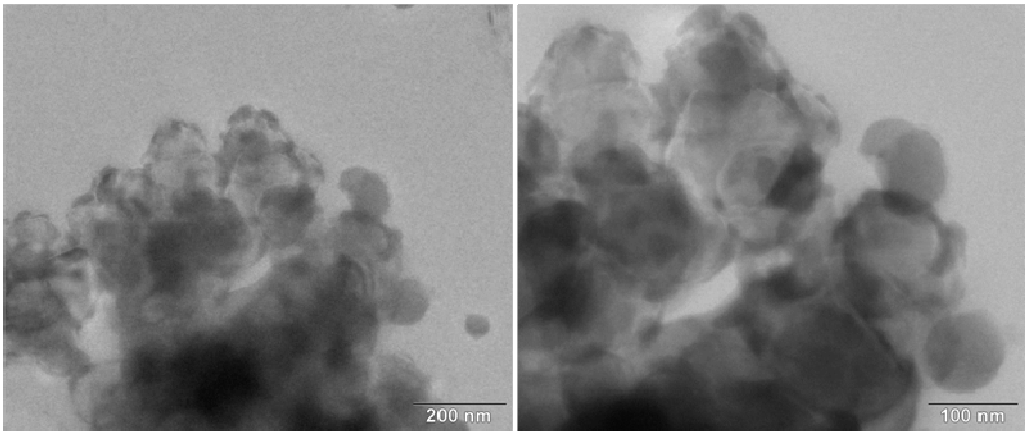

Figure 98: TEM images of TiO_2/CDG 1wt% sample prepared by hydrothermal method.

Hydrothermally formed bare graphene (Figure 99 A), P25 (Figure 99 B) and P25/graphene 1 wt% samples (Figure 99 C-D) were also investigated by SEM. Particle size of P25 is in the narrower range of 5-20 nm that is more uniform and smaller compared to TiO_2/graphene sample.

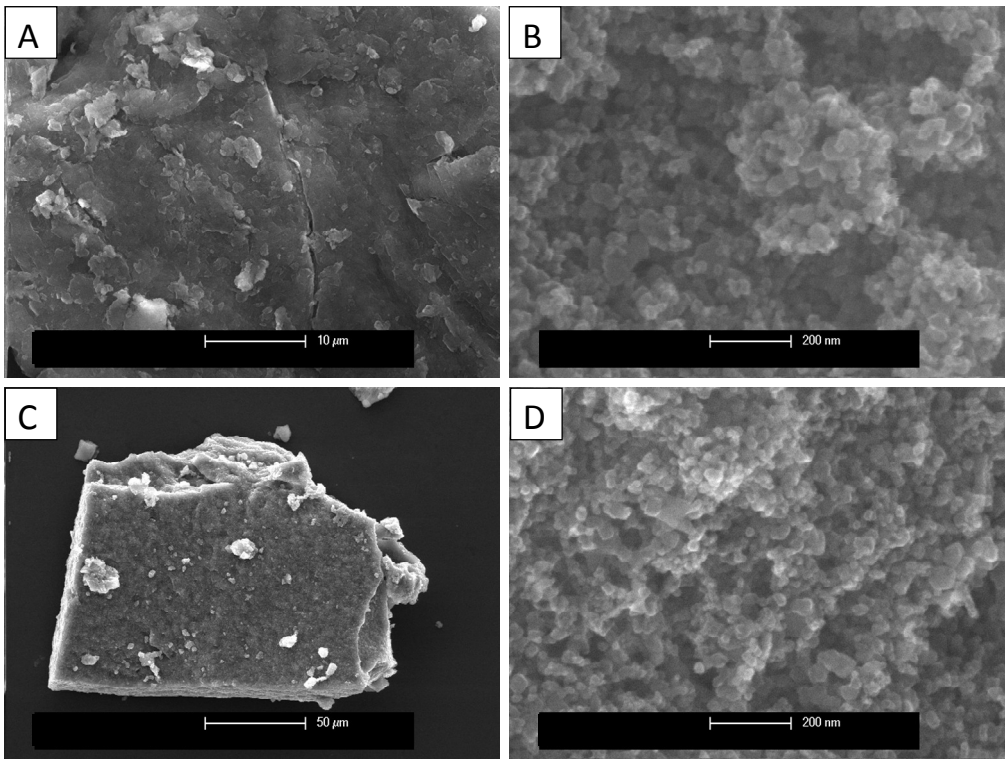

Figure 99: SEM images of A. CDG by hydrothermal method, B. P25, C, D. P25/CDG 1wt% samples.

Figure 100 gives TEM micrograph of P25/CDG sample. Particle size of P25 is still in the range of 5-20 nm. Similar to TiO_2/graphene sample, particle size of P25 didn't get larger after being supported on graphene.

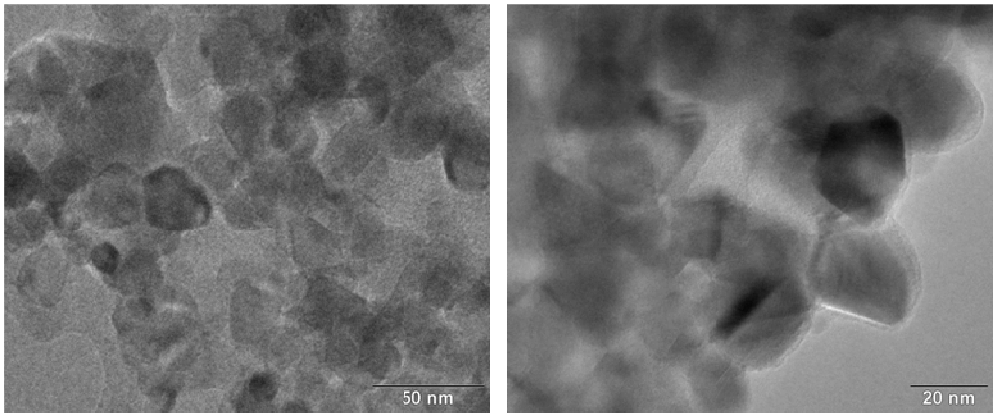

Figure 100: TEM images P25/CDG 1wt% samples.

Complementary to the Raman findings of TiO_2/CDG and P25/CDG samples, XRD plot shows that TiO_2/CDG sample has only the reflections of anatase phase while P25/CDG sample has both anatase and rutile phases (Figure 101). This also proves that P25 consists of anatase and rutile structures. The intensity of titania reflections in P25/CDG sample is much weaker than that of TiO_2/CDG. This indicates that P25/CDG has smaller crystalline titania nanoparticles than of TiO_2/CDG which is in agreement with TEM data (Figure 98 and Figure 100).

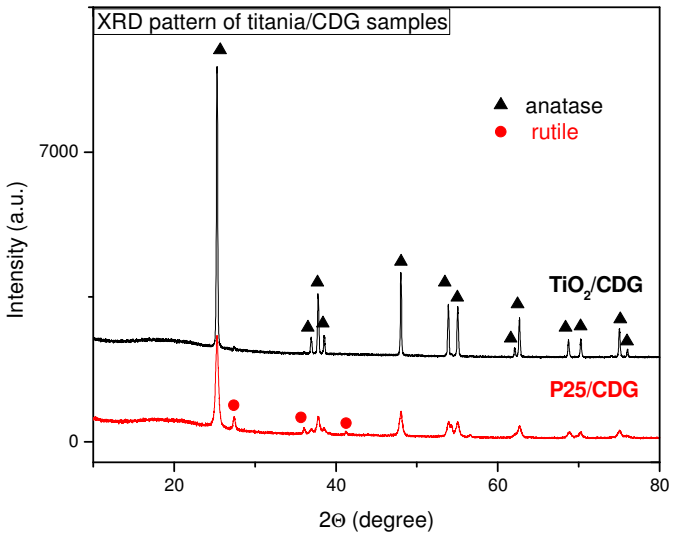

Figure 101: XRD pattern of TiO_2/CDG and P25/CDG samples.

WOx/Graphene

WO_x/graphene samples were prepared by using a sonochemical method where graphene oxide and phosphotungstic acid were precursors. The sonochemical method starts with the sonication of precursors in aqueous media followed by centrifugation and heating (at 550°C for 3 hours under Argon flow) process.

Two different loadings of WO_x were prepared as WO_x/graphene (1 wt %) and 1 mol% WO_x-graphene (95 wt %) using the sonochemical method. The aim was to compare WO_x/graphene 1 wt % with titania (TiO_2 or P25) /graphene 1 wt % composites. Moreover, 1 mol% WO_x/graphene was prepared to see the effect of 1 mol% WO_x that have been heralded in the literature as a way for extending the photocatalytic activity into the visible range [131] on titania-graphene 1 wt % samples. Briefly, WO_x/graphene 1 wt% was synthesized such that the graphene will consist of 1% of its overall weight. As this has been the case with all preceding metal oxide graphene composites, it would allow us to put WO_x/graphene up for comparison with other metal oxide graphene composites.

WO_3 crystallographic structure in all the phases is composed of corner-sharing [WO_6] octahedra having different degree of distortion in three dimensional network (Figure 102 A). Alternating planes of O and WO_2 in the octahedral environment is shown (Figure 102 B).

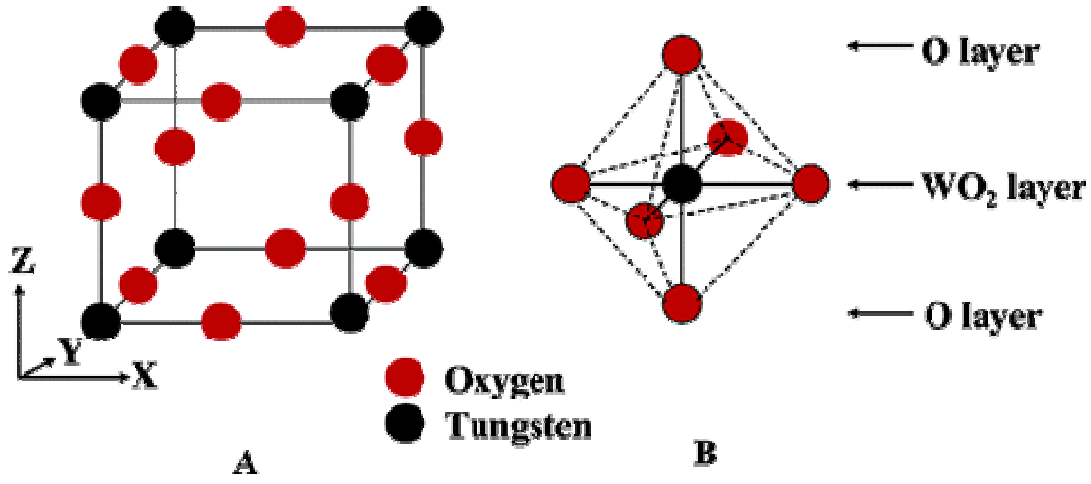

Figure 102. A. The ideal cubic structure of WO_3. (B) alternating WO_2 and O planes in WO_6 octahedra [143].

Figure 103 shows a Raman spectra of pure WO_x, chemically derived graphene and WO_x/graphene composite samples. Raman vibrations centered at around 232, 664 and 802 cm^{-1} are detected for WO_x and WO_x-related samples that are characteristic bands for O-W-O stretching modes in WO_6 octahedra [133, 143-144]. All the bands are broadened in WO_x-graphene samples compared to bare WO_x. It is attributed to the formation of C-O-W bonds that makes the initial O-W-O bonds weaker [133]. When spectrum of WO_x/graphene is compared to that of graphene, G-band up-shift that is evidence for the chemical doping of carbon materials is observed. That up-shift can be attributed to the charge transfer between of WO_x and graphene. This means interaction of WO_x with graphene is not just physical adsorption. WO_x was grafted on graphene surface in WO_x/graphene hybrid material by forming a bonding between graphene and WO_x [133].

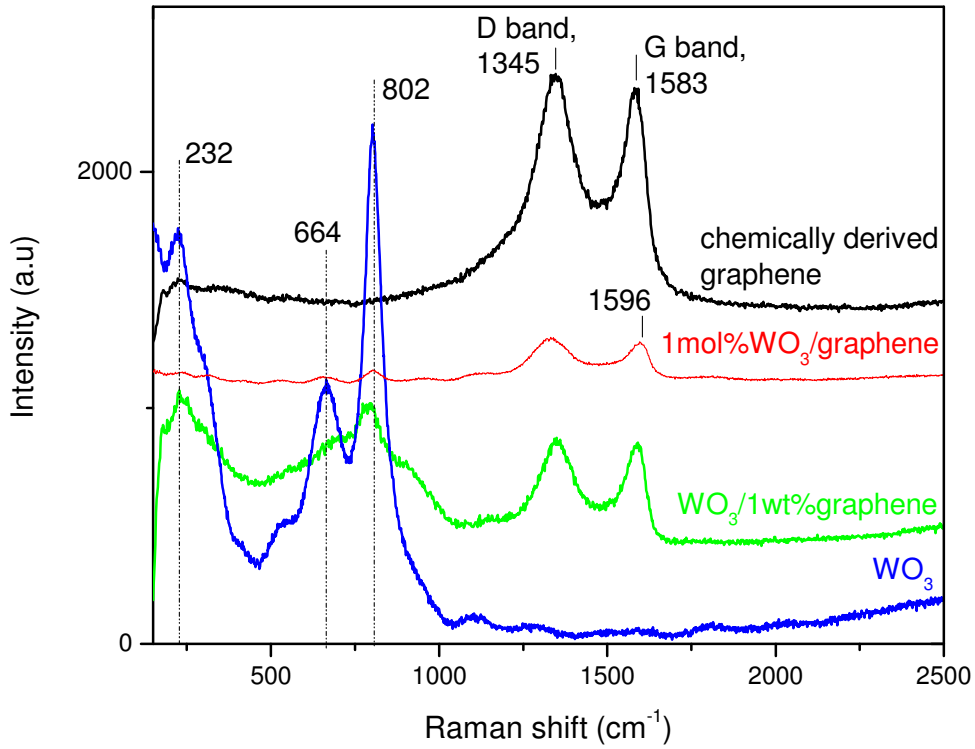

Figure 103: Raman spectra of CDG, sonochemically synthesized 1mol%WO_3/CDG, WO_3/1wt%CDG and WO_3 samples.

The structure of as-synthesized WO_x sample was further characterized by using SEM and TEM. WO_x sample consists of agglomerated μm sized particles with sharp and defined

edges as shown in SEM micrograph. TEM analysis clarifies that the sample is a layered morphology and composed of 5 nm to 20 nm crystalline elongated particles (Figure 105). High resolution TEM (Figure 105, lower left, lower right) show the crystalline nature of this layered structure.

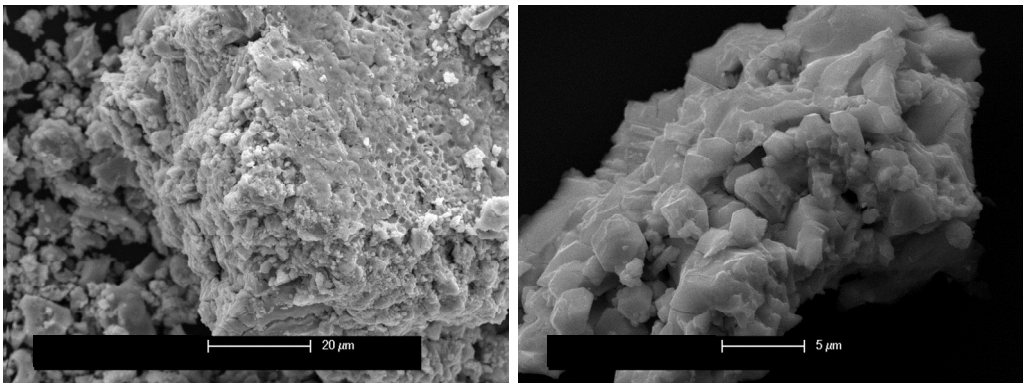

Figure 104: SEM images of as-synthesized WO_3 sample.

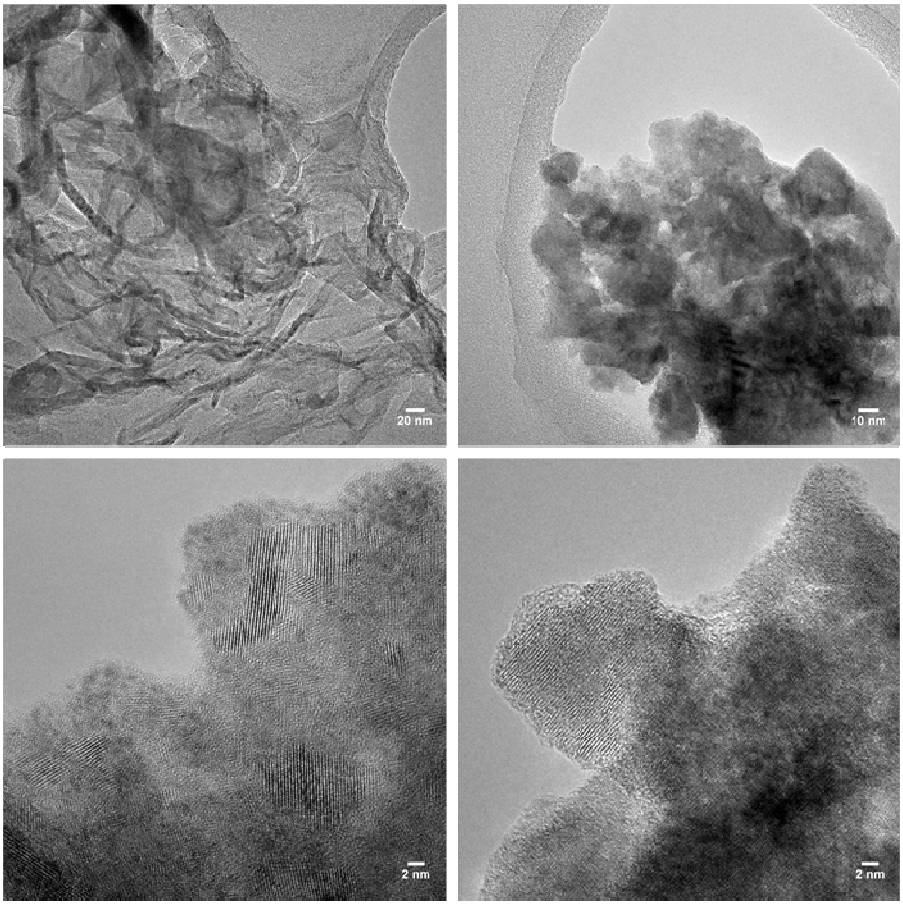

Figure 105: TEM images of as-synthesized WO_3 sample.

XRD pattern of WO_3 and WO_3-based graphene samples is given in Figure 106. Reflections due to the crystalline WO_3 structure are seen in WO_3 and WO_3/CDG 1wt% whereas not visible in 1 mol% WO_3/CDG sample. This can be attributed to the lower loading of WO_3 (<5 wt%) on CDG. Therefore, only a broad signal between 20 and 30° is observed and attributed to graphene structure for 1 mol% WO_3/CDG sample. WO_3 is orthorhombic, which is stable at 330-740°C [145], and is formed due to the heat treatment of WO_3-based samples at 550°C.

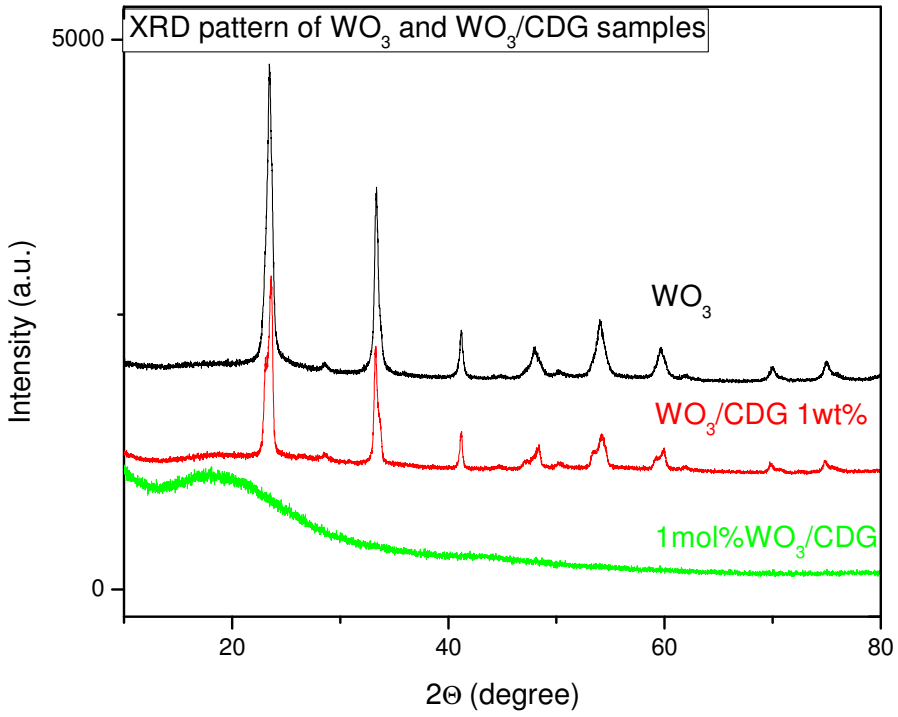

Figure 106: XRD pattern of WO_3 and WO_3/CDG samples.

SEM image of WO_x/graphene (1wt%) sample is given below (Figure 107C, D). SEM micrographs for the bare graphene produced by sonochemical way are also given in Figure 107 below (A and B). From the image, WO_3 particles on the wavy graphene can be seen, however the size of the particles is not detectable. Therefore WO_x supported graphene samples were also analyzed via TEM. Similar to the WO_x case, the WO_x/graphene (1wt%) sample has a layered structure (Figure 108).

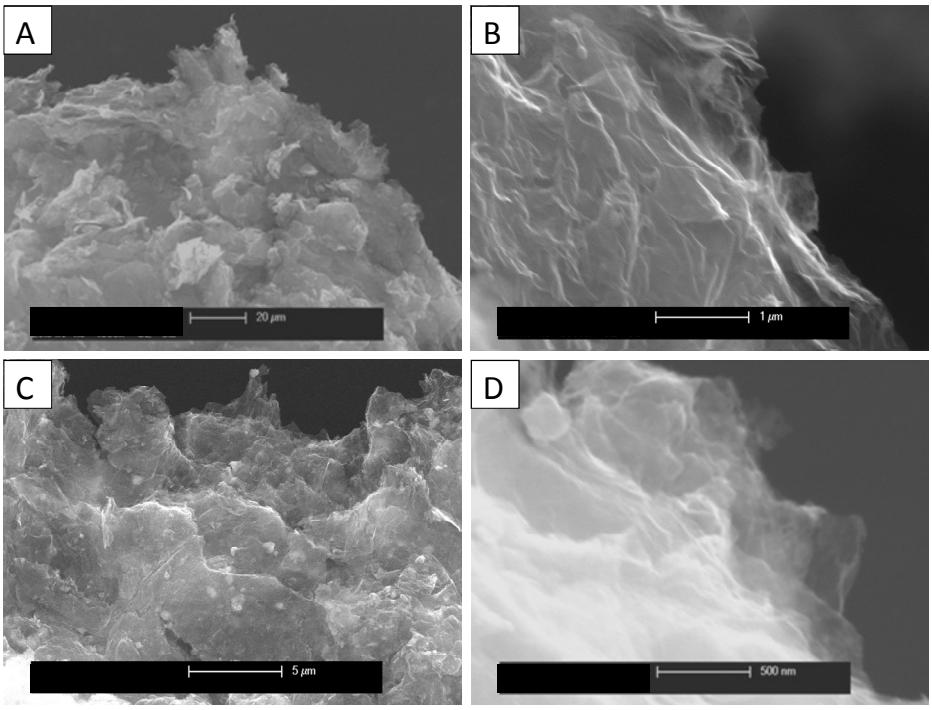

Figure 107: SEM images of CDG via sonochemical method (A, B) and WO_3/1wt%CDG (C, D) samples.

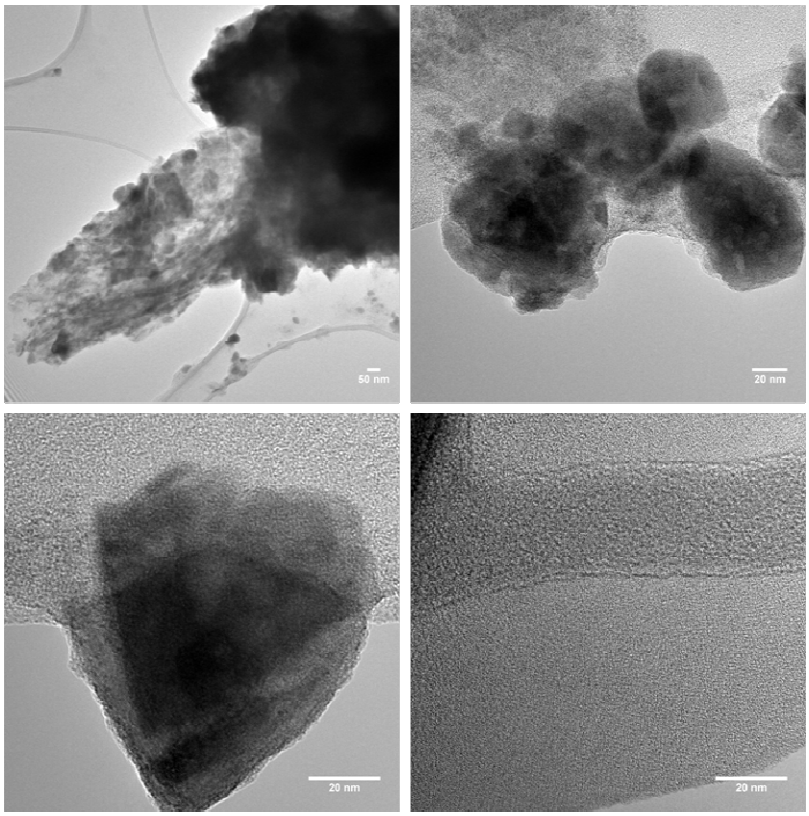

Figure 108: TEM images of WO_3/1wt%CDG sample.

In 1 mol% WO_x/graphene case, TEM micrograph depicts the higher coverage of graphene with the dispersed nanoparticles. Those particles of mostly sub 2 nm size and minor amount of 20 nm size are much smaller and better dispersed than that of WO_x/graphene 1 wt% due to the higher amount of graphene compared to WO_x/graphene 1 wt% sample above.

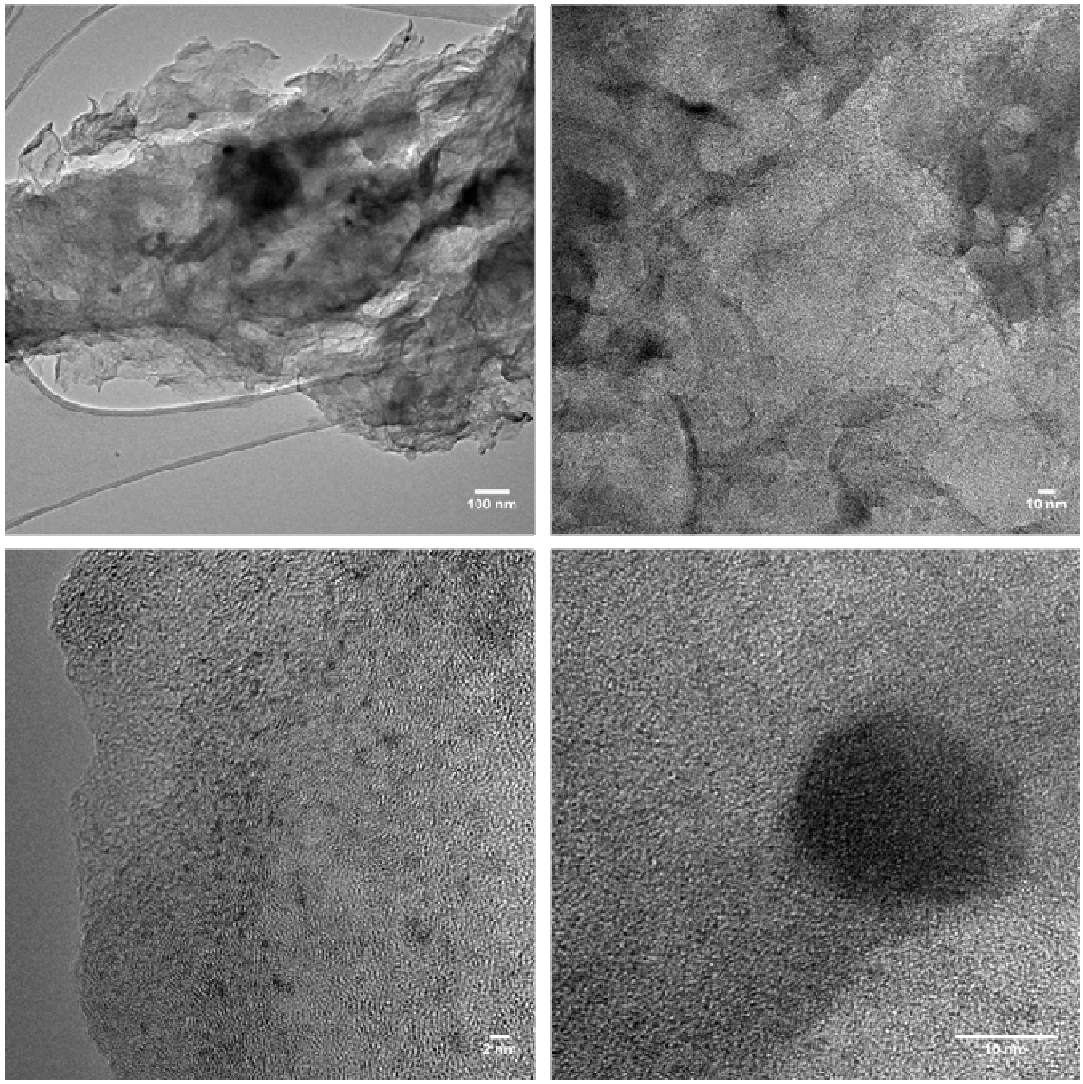

Figure 109: TEM images of 1mol%WO_3/CDG sample.

WO_x-titania (P25 or TiO_2)/graphene

1 mol% WO_x was supported on P25/chemically derived graphene (CDG) 1wt% to yield WO_x-P25/CDG and was supported on TiO_2/CDG 1wt% as well to yield WO_x-TiO_2/CDG samples.

Figure 110 gives the Raman analysis performed on P25, P25/graphene 1 wt%, 1 mol% WO_x/P25 and 1 mol% WO_x-P25/graphene as well. Spectra were given into two different selected regions as till 1000 cm^{-1} and 1000-2000 cm^{-1} to better identify oxide and graphene related Raman bands. As found for the titania precursor used (P25, mixture of anatase and rutile), six bands at 143, 194, 395, 513, 519 and 636 cm^{-1} assigned for anatase and while small shoulders at 445 and 609 cm^{-1} referred to the typical features for rutile phases can be easily seen in each sample. All titania related bands downshifts and get broader from P25 to P25/graphene and gets even broader in WO_x/P25/graphene sample. This can be attributed to the formation of Ti-O-C bond that makes the Ti-O bond weaker so the Ti-O related bands broaden similar to the findings for WO_x related samples discussed above.

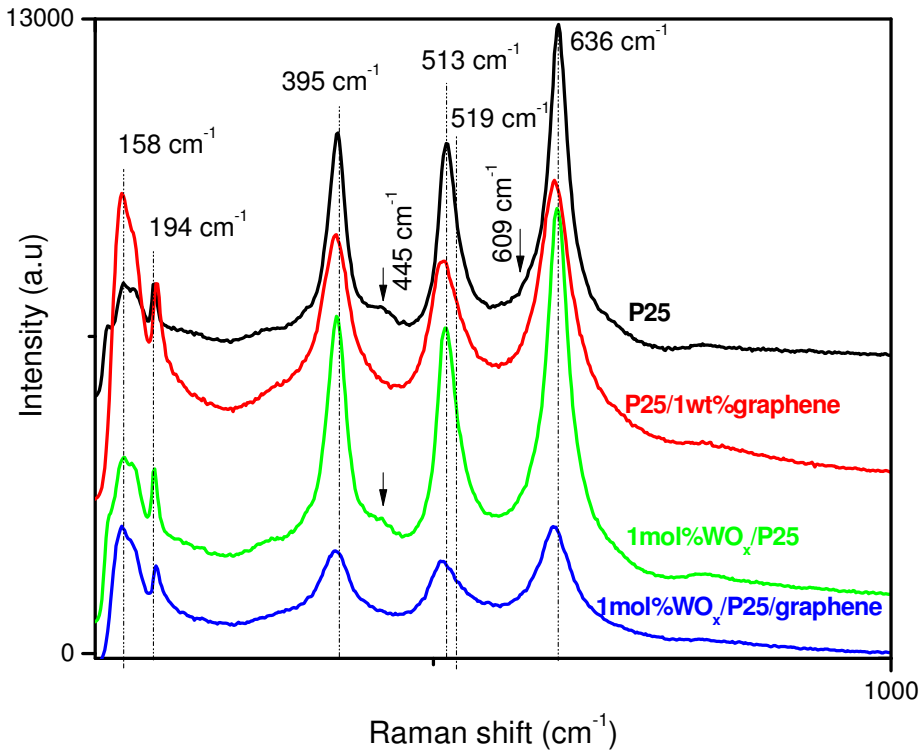

Figure 110: Raman spectra of P25, P25/1wt%CDG, 1mol%WO_3/P25, 1mol%WO_3-P25/CDG samples.

Similar to P25-based samples, Raman spectra of TiO_2-based hydrothermally synthesized samples show that titania bands get broader upon being supported on graphene or WO_3 (Figure 111). However, interestingly typical rutile bands at 405 and 609 cm^{-1} become visible in WO_x/TiO_2/graphene sample. This is due to the heat treatment of the sample after sonochemical synthesis of WO_x containing samples at 550°C that leads to anatase to rutile phase transformation. In agreement with XRD findings, in none of the sample, WO_x related reflections were detected most probably lower loading of WO_x compared to P25 or TiO_2. Similar to WO_x loaded samples discussed so far, broadening is seen in the anatase bands due to the interaction of the WO_x species with titania to yield Ti-O-W bonds as observed in sample WO_x-P25/CDG as well.

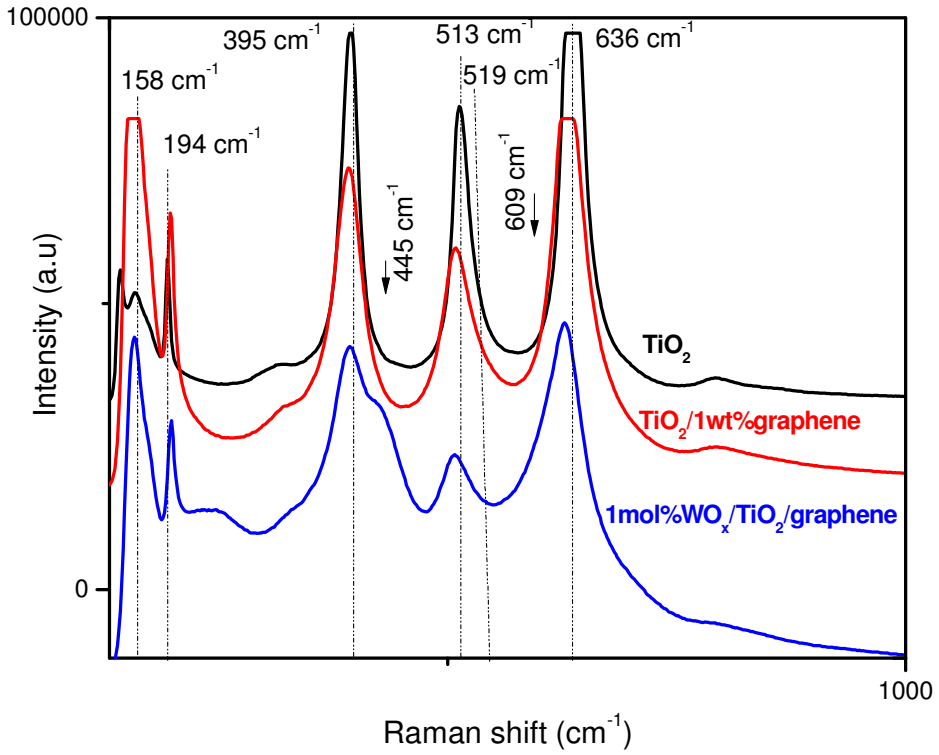

Figure 111: Raman spectra of TiO_2, TiO_2/1wt%CDG, 1mol%WO_3/TiO_2/CDG samples.

Selected Raman spectra in 1000-2000 cm^{-1} region for graphene including samples show characteristic bands of graphene (D and G). This indicates that graphene is formed successfully through the hydrothermal process. Similar to the findings for WO_x-graphene, G-band up-shift, which is observed in both P25/graphene, TiO_2/graphene and WO_x-P25/graphene, WO_x-TiO_2/graphene hybrid materials, shows the chemical bonding of the hybrid materials with graphene upon hydrothermal and sonochemical reactions.

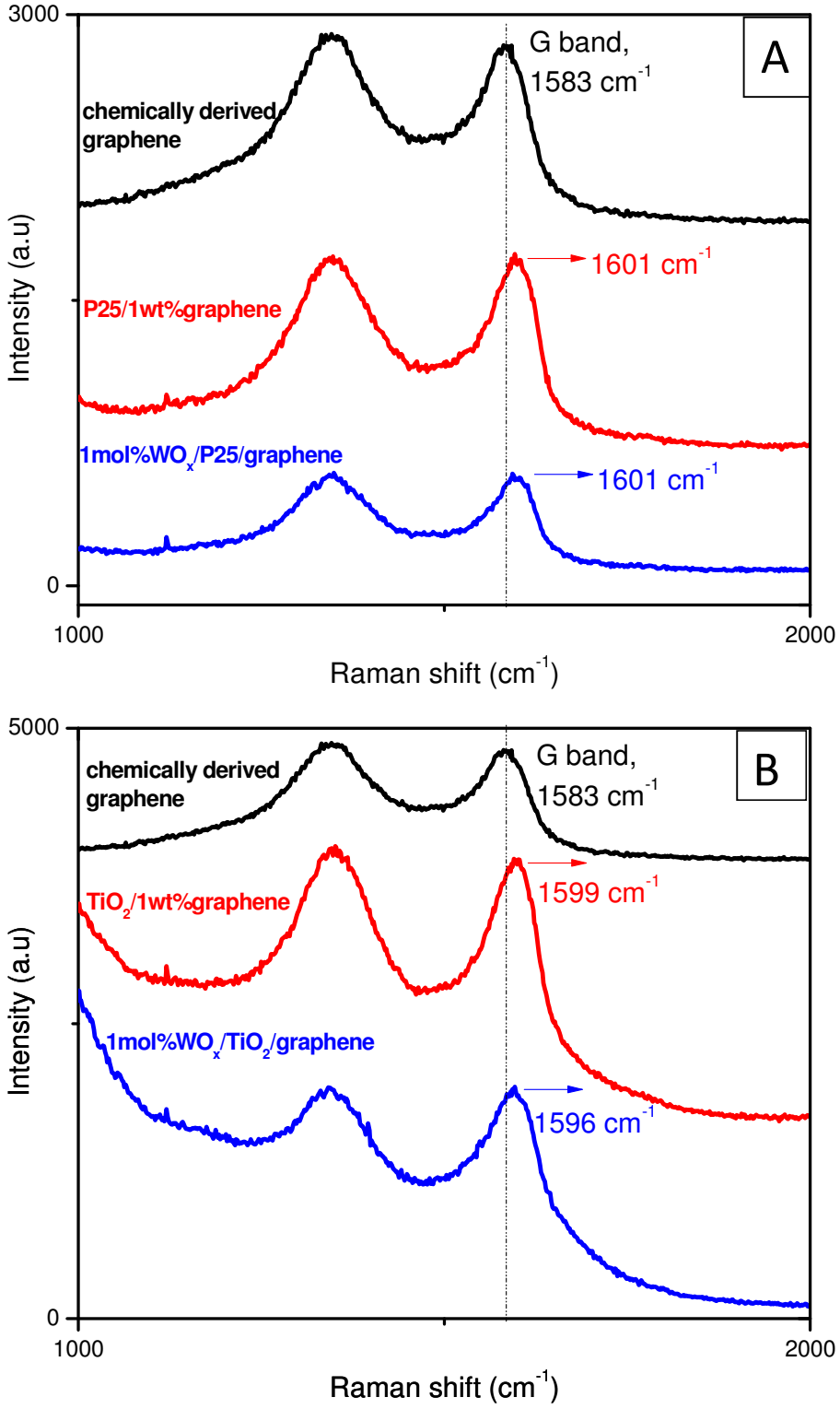

Figure 112: Selected Raman spectra of graphene including samples. A. CDG, P25/1wt%CDG, 1mol%WO_3-P25/CDG and B. same set in A, TiO_2 instead P25.

In TEM image of WO_x-P25/graphene sample, mostly 5-20 nm size of P25 nanoparticles can be seen besides minor amount of elongated particles of WO_x (of 20-30 nm size) and wavy-like graphene that is more visible at the edge. Upon supporting of P25 and WO_x on graphene, their particle sizes did not increase suggesting that nanoparticles were successfully dispersed on graphene surface.

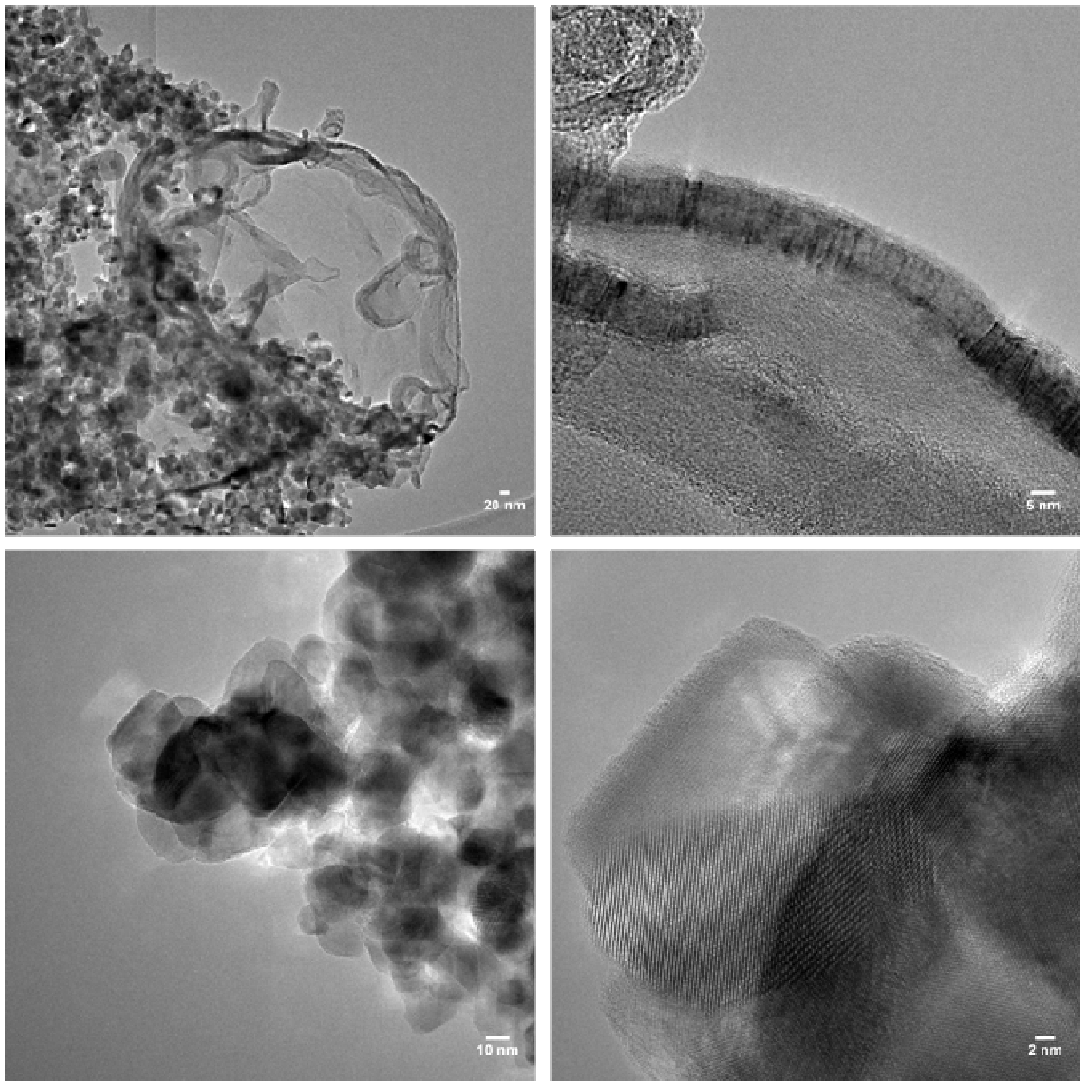

Figure 113: TEM images of 1mol%WO_3-P25/CDG 1wt% samples.

XRD pattern is shown for TiO_2, WO_3-TiO_2/CDG and WO_3-P25/CDG samples (Figure 114). The bands are assigned as anatase for TiO_2-based sample and anatase and rutile for P25 based one. No WO_x attributed signals are detectable in WO_3-TiO_2/CDG and WO_3-P25/CDG as well due to lower content of WO_3 (< 5wt %) under detection limit of XRD.

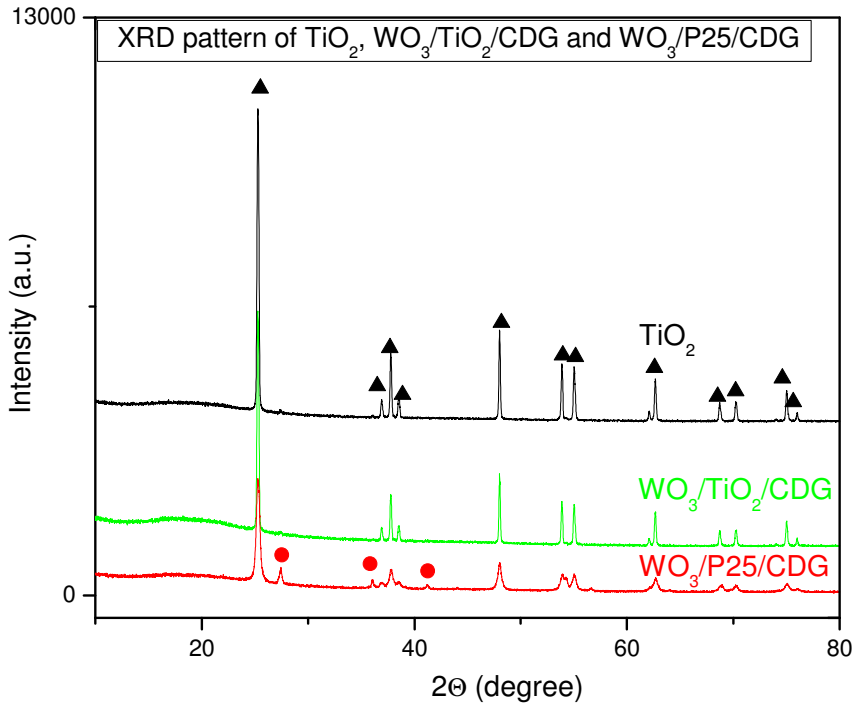

Figure 114: XRD pattern of TiO_2, 1mol%- WO_3-TiO_2/CDG 1wt% and WO_3-P25/CDG 1wt% samples. Anatase (▲) and rutile (●) reflections are shown in the pattern.

Chemically Derived Graphene Samples via chemical and hydrothermal methods

XRD pattern of graphite, TGO and CDG samples (derived from hydrothermal and hydrazine hydrate reduction) are given in Figure 115. Plot reveals that 2 theta at around 26.4° corresponds to <200> reflection that is the major signal of graphitic structure. That band shifts to lower 2 theta values (~11.5°) upon oxidation of graphite into graphite oxide (TGO) by Tour's method. That means interlayer spacing between carbon layers is increased due to the introduction of functional groups in oxidation process. When TGO is reduced to chemically derived graphene (CDG) via hydrothermal and hydrazine hydrate reduction processes, broad hump between 20 and 30° (<200> reflection) can be seen. Besides that, reflection indexed to <101> at around 42.4° slightly shifts to higher 2 theta values to 43.0° upon hydrothermal process and 43.6° upon hydrazine hydrate reduction. That shift refers to the decrease of interlayer spacing due to the removal of functional groups in reduction process. Slightly higher shift in hydrazine hydrate reduced CDG depicts that reduction is better by this method than hydrothermal process.

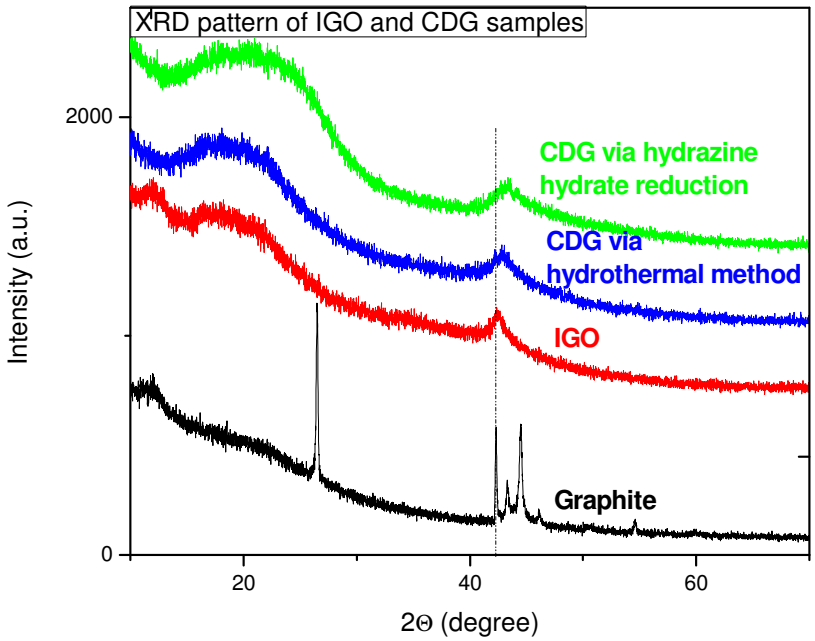

Figure 115: XRD pattern of graphite, TGO, and CDG (via hydrothermal and hydrazine hydrate reduction methods) samples.

BET surface area of samples

Specific surface area measurements utilizing BET theory was performed on the synthesized samples (see Table 19.). Hydrazine hydrate reduced graphene is found to have a higher specific surface area (532 m^2/g) than hydrothermally reduced one (60 m^2/g That might be attributed to the better exfoliation of graphitic layers that exposes larger surface during hydrazine hydrate reduction process in agreement to XRD data). Graphene via sonochemical reaction followed by heat treatment has a surface area (of 241 m^2/g) in between two other types of graphene samples.

P25 having a specific surface area that is almost five times higher than that of TiO_2 (51 m^2/g to 10 m^2/g) might be attributed to the smaller particle size (shown by TEM) or higher porosity of P25. It is observed that surface area of metal oxide precursors (P25 and TiO_2) slightly decreases after hydrothermal reaction. This might be attributed to an increase in particle size during the hydrothermal process. Surface area of titania samples upon being supported to graphene increases slightly (since graphene amount is just 1wt%). When tungsten oxide is combined with titania samples (WO_x/TiO_2 and WO_x/P25), surface area gets smaller compared to bare titania samples due to the lower surface area of tungsten oxide itself. Combination of two low surface area oxides

(WO_x/TiO_2) results sample with the lowest surface area (3 m^2/g). As given in the experimental section, different than the synthesis of titania related samples, WO_x procedure involves heating up step (at 550°C for 3 hrs under 200 sccm of Ar flow) right after the hydrothermal reduction. So, the better exfoliation of graphene layers (surface area of 241 m^2/g) during thermal treatment can explain why 1 mol% WO_x-graphene has the BET surface area of 157 m^2/g that is the highest value of the hybrid samples.

Table 19: BET specific surface areas of CDG, P25-, TiO_2- and WO_3-based samples.

Sample	Specific Surface area (m^2/g)
graphene via hydrazine reduction (CDG)	532
graphene via hydrothermal reduction	59.8
graphene via sonochemical reaction and calcination	241
P25 (Evonik, AEROXIDE TiO_2)	57.1
P25 after hydrothermal reduction	51.3
P25-graphene 1wt% via hydrothermal reduction	55.6
TiO_2 (Merck KGaA)	11.5
TiO_2 after hydrothermal reduction	10.4
TiO_2-graphene 1wt% via hydrothermal reduction	11.1
WO_x via sonochemical reaction and calcination	11.9
1 mol% WO_x-graphene	157
1 mol% WO_x-TiO_2	2.74
1 mol% WO_x-TiO_2-graphene 1wt% after calcination	23.5
1 mol% WO_x-P25 after calcination	42.7
1 mol% WO_x-P25-graphene 1wt% after calcination	55.3

4.3. Studies towards the functional properties of Graphene Hybrid Materials

CDG and CDG-hybrid materials (with metal/metal oxide nanoparticles) are investigated with respect to their functional properties such as catalysis and gas sensor. Basically, employment of CDG supported Pd NPs (CDG-Pd) in the dehydrogenation and hydrolysis of ammonia borane (AB) and TiO_2/P25/WO_x-CDG in photodegradation of methylene

blue are described here. Preliminary results obtained for ZnO/CDG in gas sensor are also discussed.

4.3.1. Catalysis

4.3.1.1. Dehydrogenation and Hydrolysis Reaction (Pd/Graphene (Modified Hummers' Method))

In the following we report, the preparation of CDG supported Pd NPs (CDG-Pd) and their employment as catalysts in the dehydrogenation and hydrolysis of AB. Pd NPs were prepared from the reduction of palladium(II) acetylacetonate in the presence of oleylamine (OAm) by borane *tert*-butylamine complex (BTB) using a modified version of oleylamine mediated synthesis [146]. The support material CDG was prepared by a two step procedure; (i) preparation of graphite oxide from the oxidation of natural graphite flakes by a modified Hummers' method [14], (ii) the exfoliation and then reduction of graphite oxide by hydrazine hydrate in aqueous solution [105]. Next, OAm stabilized Pd NPs were supported on CDG by impregnation. The CDG and CDG-Pd were characterized by transmission electron microcopy (TEM), high resolution TEM (HRTEM), scanning electron microscopy (SEM), electron dispersive X-ray (EDX), Brunauer-Emmett-Teller (BET) surface area analysis, Raman spectroscopy, thermal gravimetric analysis (TGA) and inductively coupled plasma mass spectroscopy (ICP-MS). CDG-Pd samples were used as catalyst in the dehydrogenation and hydrolysis of AB without any further treatment and found to be highly active and stable.

Catalytic activity of chemically derived graphene supported palladium nanoparticles in the dehydrogenation and hydrolysis of ammonia borane

CDG-Pd were tested as catalyst in hydrogen generation from the dehydrogenation and hydrolysis of AB and found to be highly active in both reactions. The (mol H_2/mol AB) ratio vs time during the catalytic dehydrogenation and hydrolysis of 2.0 mmol AB in the presence of CDG-Pd catalyst at 25 ± 0.5°C is shown (Figure 116). The loading of Pd on CDG is 2.1 % wt Pd, as determined by ICP-OES. The hydrogen generation rate was determined from the linear portion of each plot. Totally one equivalent of hydrogen was generated from the dehydrogenation of AB while 3 equivalents of hydrogen were

generated from the hydrolysis of AB in the presence of CDG-Pd catalyst. The initial TOF values for the dehydrogenation and hydrolysis of AB in the presence of CDG-Pd catalyst were calculated as 170 h^{-1} and 933 h^{-1}, respectively (Figure 116). These values are comparable with the catalyst systems tested for the dehydrogenation [147] and hydrolysis of AB [148]. However, it is noteworthy to compare the recent supported catalysts (Ni/SiO_2 and CoPd/C) tested in the hydrolysis of AB with CDG-Pd catalyst in terms of their catalytic activities to emphasize the state-of-the-art for readers. In a recent study, it is reported that OAm stabilized Ni NPs of 3.2 nm supported on SiO_2 provide a TOF value of 13.2 min^{-1}, which is the highest TOF value ever reported for the hydrolysis of AB using Ni catalysts [148]. In a very recent study, Sun et al have reported that CoPd NPs supported on Ketjen carbon provide a TOF of 35.7 min^{-1} in the hydrolysis of AB [149]. The TOF of CDG-Pd catalyst (15.5 min^{-1}) is higher than that of Ni/SiO_2 catalyst but lower than that of CoPd catalyst. It can be concluded that with respect to the catalytic hydrolysis of AB palladium is a more active metal than nickel and the alloying cobalt with palladium enhances the activity of palladium.

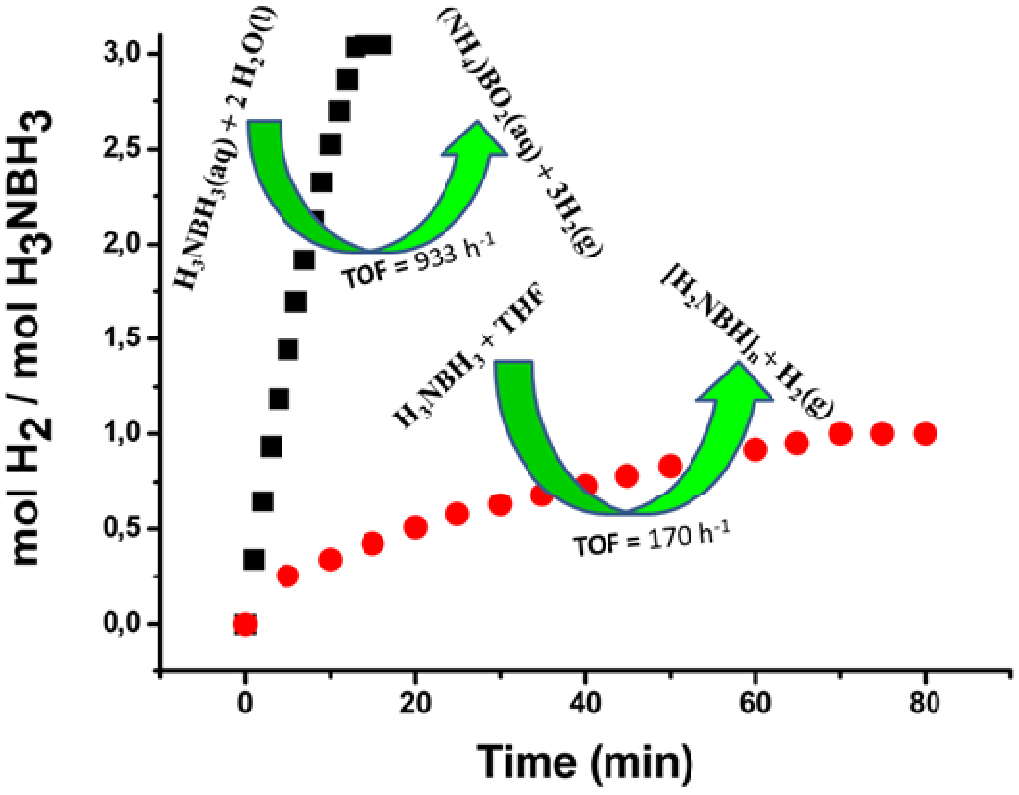

Figure 116: The dehydrogenation and hydrolysis processes of AB catalyzed by CDG-Pd [38].

Figure 117 shows the mol H_2/mol AB versus time plots for the dehydrogenation and hydrolysis of AB catalyzed by CDG-Pd catalyst at different catalytic run. CDG-Pd catalyst maintain 85% of its initial activity after the 5th catalytic run in the dehydrogenation of AB (Figure 9a) and 95 % of its initial activity after the 10th run in the hydrolysis of AB at 25 ± 0.5 ^{o}C (Figure 117 b).

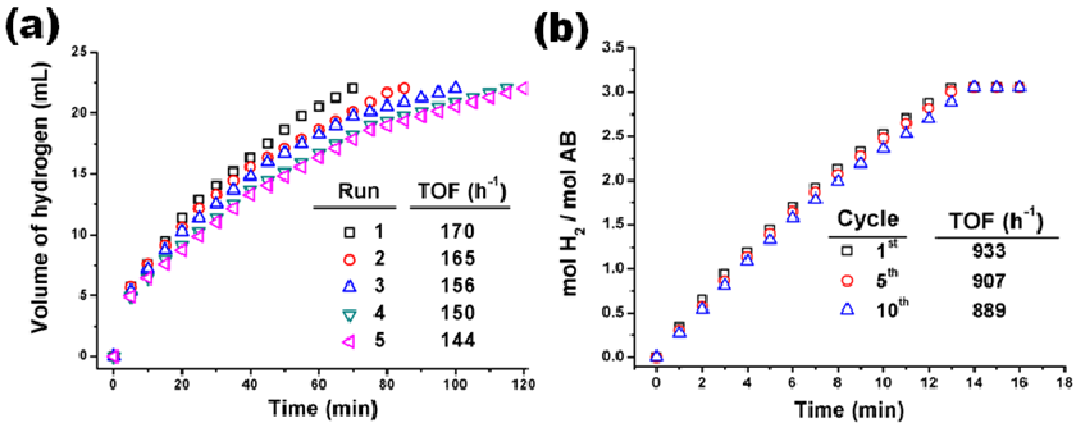

Figure 117: The plots of mol H_2/mol AB versus time for hydrogen generation from (a) dehydrogenation of AB and (b) the hydrolysis of AB catalyzed by CDG-Pd catalyst at different catalytic runs [38].

These results indicate that CDG-Pd is highly active and reusable catalyst in hydrogen generation from both dehydrogenation and hydrolysis of AB. See Figure 118 for the TEM image of CDG-Pd catalyst after the reusability test.

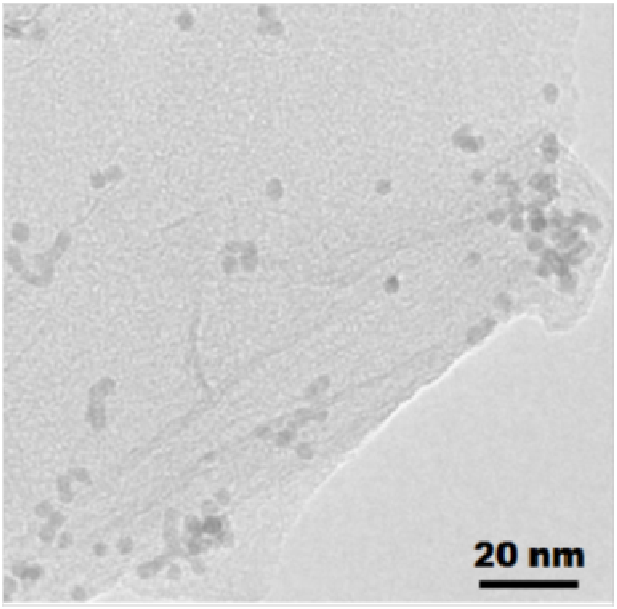

Figure 118: A representative TEM image of the CDG-Pd catalyst after the reusability test (ten runs) in the hydrolysis of AB (TEM image was taken at Middle East Technical University/Central Lab, Turkey).

4.3.1.2. Photodegradation of Methylene-Blue

4.3.1.2.1. Photocatalytic Measurements

P25-, TiO_2- (prepared via hydrothermal method) and WO_x- (prepared via sonochemical method followed by heat treatment) related graphene hybrid materials were used as photocatalysts in the photodegradation of methylene blue (MB) reaction under UV light. The photocatalytic activities of the samples were measured by UV-Visible spectroscopy that we obtain a set of data with absorption scans in the 500 nm to 750 nm range at various time intervals. All of these scans at various time intervals pertaining to the same catalyst for the reaction are plotted together. Figure 119 belongs to WOx/P25/graphene catalyst is one example.

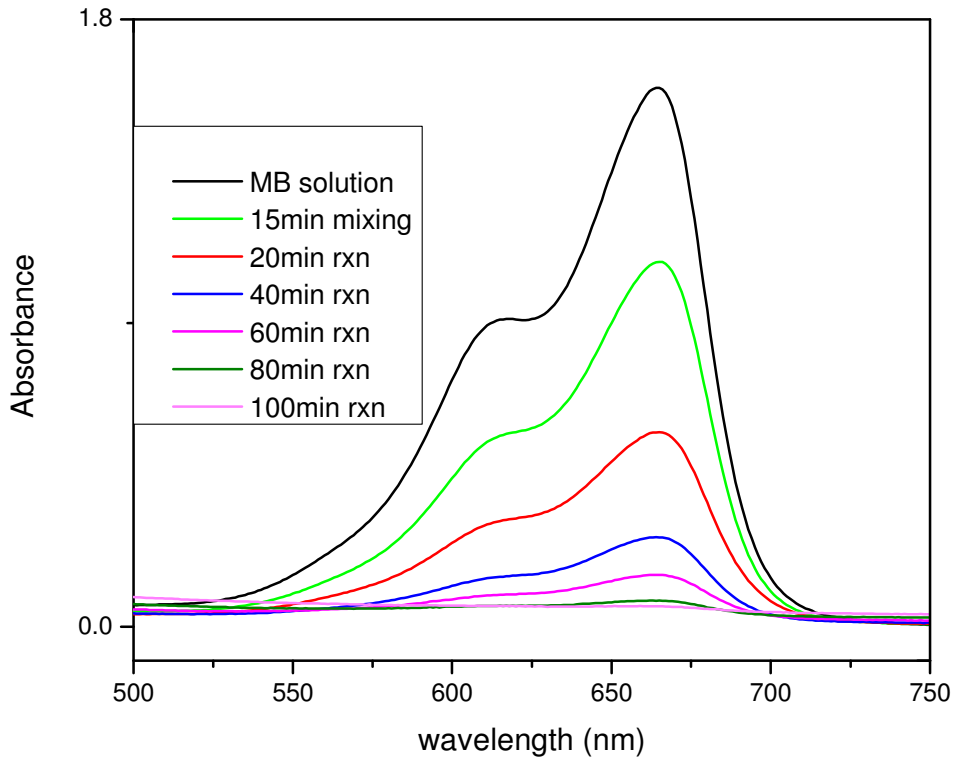

Figure 119: UV-Vis spectra taken by time from the mixture of MB and 1mol%WOx/P25/CDG catalyst under UV light photodegradation reaction.

We note the maximum absorbance of methylene blue as initial absorbance A_o that occurs at 665 nm. Then, the decrease in the absorbance of methylene blue at 665 nm is taken as A. The ratio of that absorbance values (at each time interval) to the initial absorbance of methylene blue is plotted versus time. A/A_o versus time plot is given in Figure 120 below. Under UV radiation, the WO_x-P25-graphene composite was found to have the highest photoactivity –with what appears to be 90% degradation in 60 minutes and full decomposition after 100 minutes– followed closely by WO_x-TiO_2-graphene. Essentially, what distinguishes these two catalysts is simply particle size and phase. These results then suggest that P25 with its dominantly anatase and rutile mix and smaller nanosized particles is the optimum choice of titanium dioxide to use when coupled with tungsten oxide and graphene.

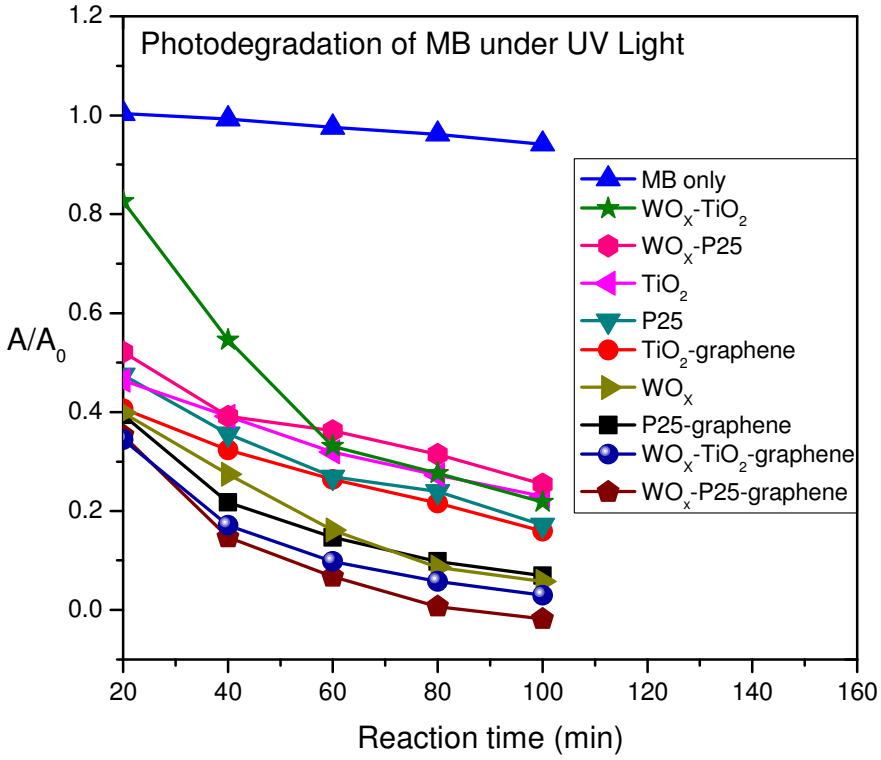

Figure 120: All the results of photodegradation of MB in the presence of metal oxide/CDG hybrid catalysts (P25-, TiO_2-, WO_3-based) under UV light.

To differentiate the effect of WO_x and graphene on the activity of titania samples, corresponding plots are given separately below. Parallel to the literature findings [137], photocatalytic performance both titania (P25 and TiO_2) samples is enhanced upon

supporting the titania on graphene. For instance, comparing P25 (0.18 at 100 min) with P25-graphene (0.09 at 100 min). Moreover, including WO_x into titania-graphene composite materials results further improvement in the photocatalytic activity. The improvement can be explained that titania is bonded to graphene that is required for carbon to act as dopant to titania as confirmed by the shifts of the Raman bands. This ensures that titania is more effective by lowering the minimum photon energy required to generate the electron-hole pair [150]. Graphene due to the larger surface area and conductivity is an excellent scavenger of electrons generated during the UV irradiation and that's why lifetime of the holes is extended with the help of graphene.

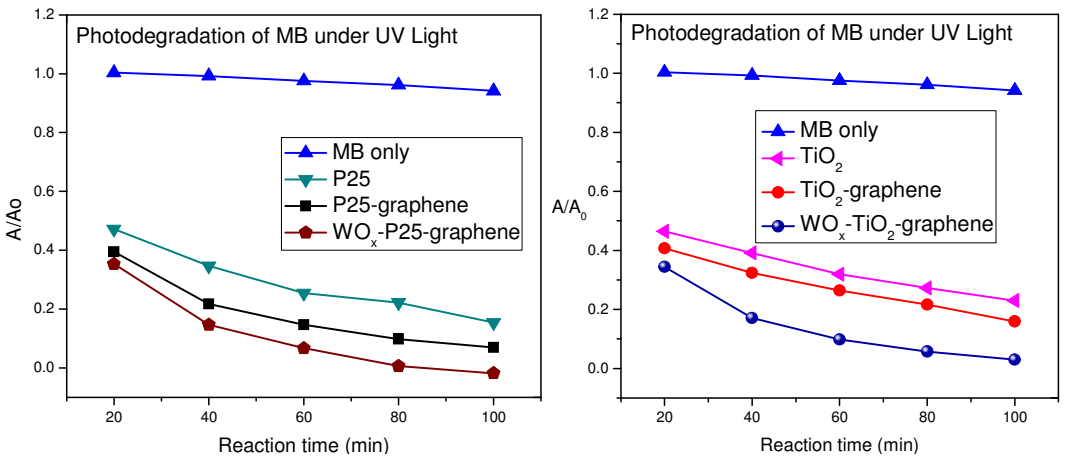

Figure 121: Photodegradation of MB with WO_3/P25-based (plot at the left side) and WO_3/ TiO_2-based (plot at the right side) under UV light.

Experiments were conducted under dark conditions for the catalysts mixing into the MB solution to examine the adsorption of MB on catalyst prior to photodegradation reaction under UV light. Hereby, the results obtained under UV light would be evaluated whether these are due to the photocatalytic activity of the catalysts or just the adsorption of MB on the catalyst. Adsorption experiments under dark conditions show that MB has different tendencies to adsorb on the different catalysts (Figure 122). For most catalysts, adsorption accounts for less than 40% of the absorbance decrease, as evidenced by the majority of the graphs being above the 0.6 A/A_o ratio. However, it seems that methylene blue has much higher affinity for WO_x–graphene than others that suggests the better interaction of MB with the catalyst surface of the highest BET surface area (157 m^2/g) among all the hybrid materials. However, WO_x–graphene sample cannot be used as a catalyst in the photodegradation reaction of MB since it does not fulfill the reusability

requirement for the efficient catalyst. Besides that, one can easily see that supporting of titania (TiO_2 or P25) or tungsten oxide on graphene increases the adsorption of MB. BET surface areas of the samples just slightly increase with the inclusion of graphene to the system (1-3 m^2/g). It is not simply attributed to the increase in the surface area of the titania or tungsten oxide catalyst samples upon supporting on graphene. Moreover, although BET surface area of WOx-TiO_2-graphene is more than double of TiO_2-graphene, adsorption of MB is lower than that of TiO_2-graphene. These results point out to the fact that adsorption of MB on the catalyst is not only affected by surface area of the samples. It is also evident that the higher decrease in the A/A_o ratio of MB with respect to time under UV light for WO_x-P25-graphene can be accounted by the degradation process rather than physically adsorption of MB. Having lower adsorption degree of that sample compared to P25/graphene clearly indicates that insertion of WO_x to P25/graphene sample increases the photocatalytic activity of the sample. A similar relation is also found between WO_x-TiO_2-graphene and TiO_2-graphene samples.

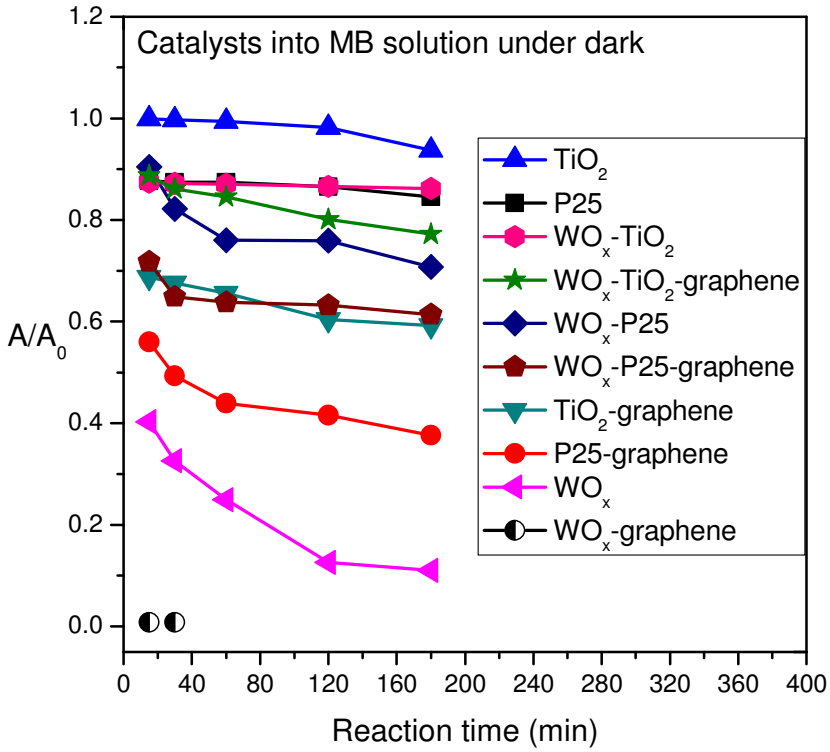

Figure 122: Results for metal oxide/CDG hybrid catalysts (P25-, TiO_2-, WO_3-based) samples into MB solution under dark.

Diffuse reflectance spectra of the powder samples were also performed to see the effect of graphene and WO_x on titania samples. In Figure 123, red shift in the absorption edges and increase in the absorption intensities of WO_3/P25/graphene and P25/graphene compared to bare P25 are observed. Same trend is also found for TiO_2 samples (see Figure 123).

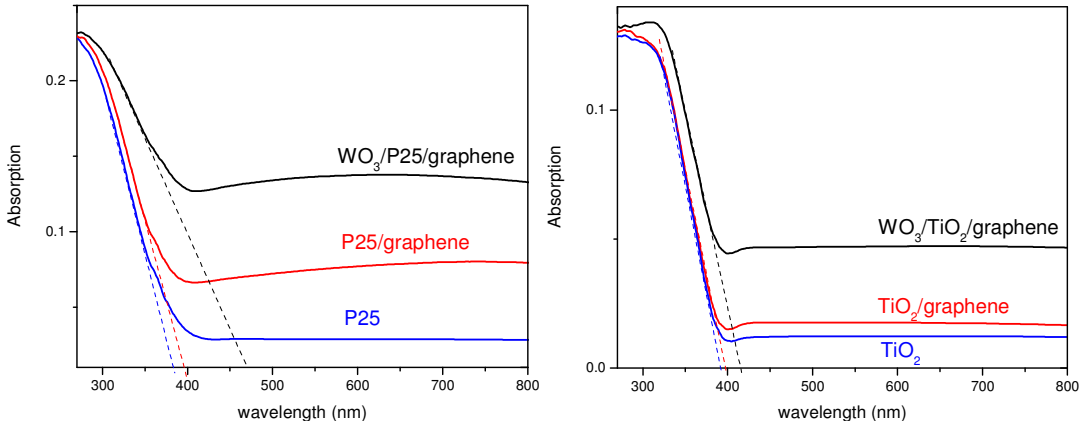

Figure 123: Diffuse reflectance spectra of the P25- and TiO_2-based metal oxide/CDG hybrid catalyst samples.

4.3.2. Gas-sensors

In the field of gas sensors, tin oxide (SnO_2) and zinc oxide (ZnO) are widely used in nanostructured systems due to their high sensitivity, chemical stability and low production costs [151]. However, the need for high operation temperature of metal oxide systems results in high power consumption. Attempts to use metal oxides gas sensors at room temperature have been conducted for instance by coating SnO_2 on CNTs for room temperature sensing. On the other hand, metal oxide structures have been also used to improve the selectivity of CNTs and/graphene based gas sensors that work at room temperature. Besides, p-type semiconductor graphene (in ambient atmosphere) and n-type semiconductor ZnO due to the oxygen vacancies and zinc interstitials [152] form n-p heterostructure. Photoluminescence studies show that a blue shift of 0.15 eV was measured in ZnO-graphene sample compared to bare graphene [66].

In our group, ZnO decorated on CNTs was reported with higher sensing response compared to bare CNTs (and smaller sensing response compared to ZnO) for sensing CO at 400°C [94a]. In that study, the zinc oximato complex ($[CH_3ONCCH_3COO]_2Zn.2H_2O$) was decomposed at 150°C in the presence of MWCNTs to get ZnO nanoparticles of 2-10 nm size densely deposited along the complete periphery of the MWCNTs.

The advantage of using zinc oximato precursor as a precursor is that it decomposes in dimethylformamide (DMF) completely with high purity at low temperatures (~150°C) by yielding ZnO nanoparticles in the narrow size range of 3-5 nm [139]. During decomposition process, zinc-carbonato intermediate is formed by a loss of CH_3CN and further converted into ZnO by the additional loss of H_2O and CO_2 (Figure 124).

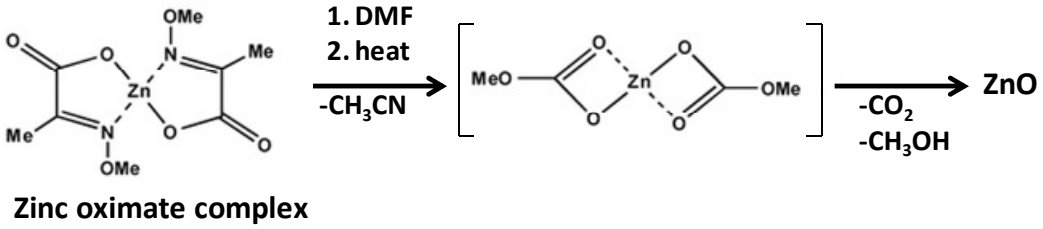

Figure 124. Decomposition pathway of the zinc oximate precursor [139].

Due to the interruption of sp^2 clusters by oxygen functional groups in as-oxidized state of graphene (graphene oxide), the creation of e–h pairs upon excitation is decreased. So, it is electrically insulating in nature to use it in resistance based sensors [153]. However, conductivity and aromatic double-bonded carbons are recovered upon hydrazine hydrate reduction of graphene oxide to yield chemically derived graphene [66]. While that resulting reduced graphene oxide still contains some oxygen groups acting as active defect sites, is a promising candidate as gas sensor.

In these studies, the aim is to synthesize a ZnO decoration on chemically derived graphene in the similar synthesis manner by using zinc oximato complex and with the insertion of CNTs with CDG. Similarly, different loadings of ZnO/graphene samples were prepared besides bare ZnO and graphene. Then, sensing behavior of the samples towards hydrogen gas at room temperature and elevated temperatures (200-300°C) could be measured. Sensor responses/signals (S) of the samples could be calculated according to the relation ($S= 100\%x(R_{H2}- R_0)/R_0$ for H_2) where R_{H2} and R_0 denote the sensors' resistances in the presence H_2, and in the absence of H_2, respectively.

4.3.2.1. Characterization of ZnO/CD Graphene

SEM micrographs of the ZnO/CDG samples with varying ZnO loadings (5.7%, 11%, 20% and 33 wt%ZnO/CDG) are given in the Figure 125, from A to D respectively. Agglomerated nanoparticles of 30-150 nm size on graphene are found. As the loading of the ZnO increases from A to D, coverage of the particles on the graphene raises as well.

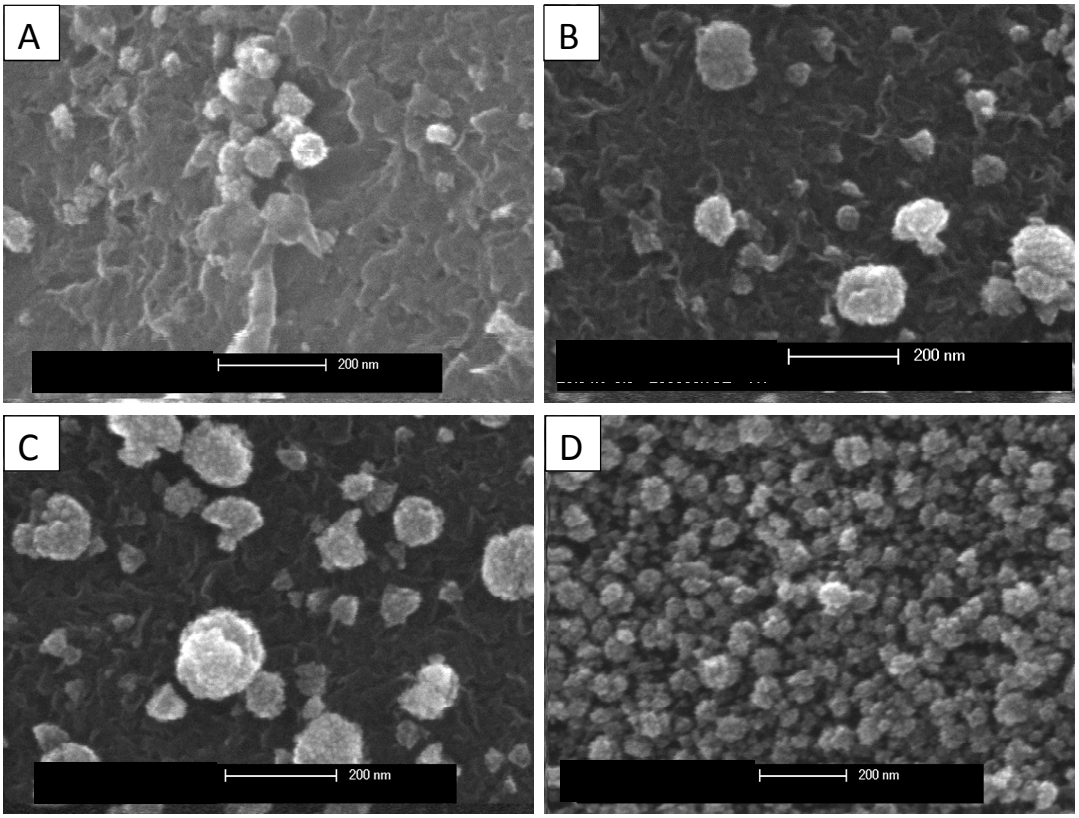

Figure 125: ZnO/CDG samples of lower to higher loadings of ZnO. 5.7%, 11%, 20% and 33% ZnO in A, B, C and D respectively.

XRD pattern of ZnO/CDG sample shows the formation of crystalline ZnO nanoparticles (zincite).

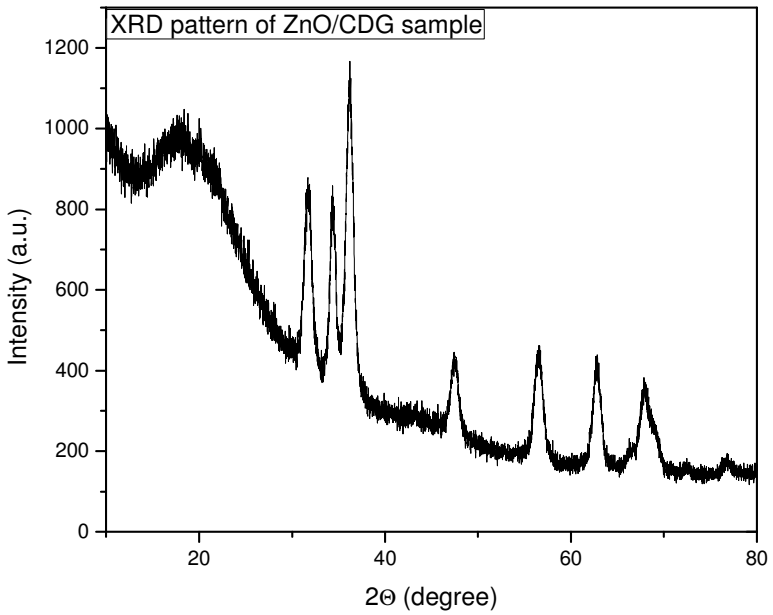

Figure 126: XRD pattern of 33wt%ZnO/CDG sample

A TEM analysis was performed on the ZnO/CDG sample (33 wt%ZnO/CDG) with the highest ZnO loading. In line with the findings from SEM, ZnO nanoparticles almost cover the whole surface of graphene in Figure 127 where mostly ZnO nanoparticles are visible in the image besides small areas of bare graphene. The sample consists of ZnO agglomerates of about 5 nm size.

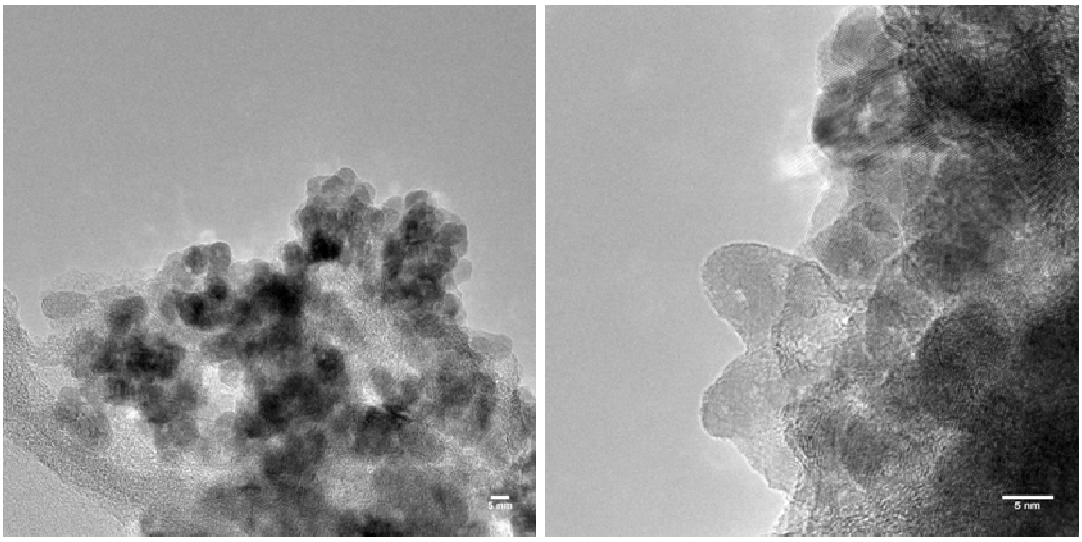

Figure 127: TEM images of ZnO/CDG sample (33wt%ZnO/CDG).

4.3.2.2. Sensoric studies of ZnO/chemically derived graphene towards H_2

Sensing measurements of a ZnO/CDG hybrid (6 wt% ZnO/CDG) towards H_2 were performed at room temperature and at 300°C. Room temperature experiments were done within two different H_2 flow regime from 50 ppm-2000 ppm and 100 ppm-10000 ppm respectively. Regardless of initial concentration of hydrogen introduced, sample shows p-type semiconducting behavior at room temperature was observed due to the resistance increase when hydrogen gas is introduced. When the sensing curve is analyzed further, two regions indicating rapid and slow responses can be differentiated with the slope change in the curve. Slow response is due to the weak adsorption on sp^2 hybridized sites[153]. Rapid response can be attributed to irrecoverable adsorption on sp^3 hybridized sites where strong adsorption takes place. Therefore, baseline increases and the sensor response gets lower after initial adsorption of H_2. The response slightly increases again but seems like remains almost constant due to the saturation of the adsorption sites. Sensing experiments at 300°C shows that the sensor response increases possibly due to desorption of adsorbed H_2 on the sp^2 sites. However, initial sensor response of the sample to 100 ppm H_2 at 300°C is slightly smaller than the one observed at room temperature (~4 % versus ~6 %). This can be attributed to the higher adsorption affinity of the hydrogen at room temperature compared to that at elevated temperatures. Besides that, resistance of the sample decreases from room temperature to 300°C by a more than tenfold degree. This can be explained by an Arrhenius model suggesting that thermally excited carriers starts dominating electrical conduction at temperatures >300 K [154].

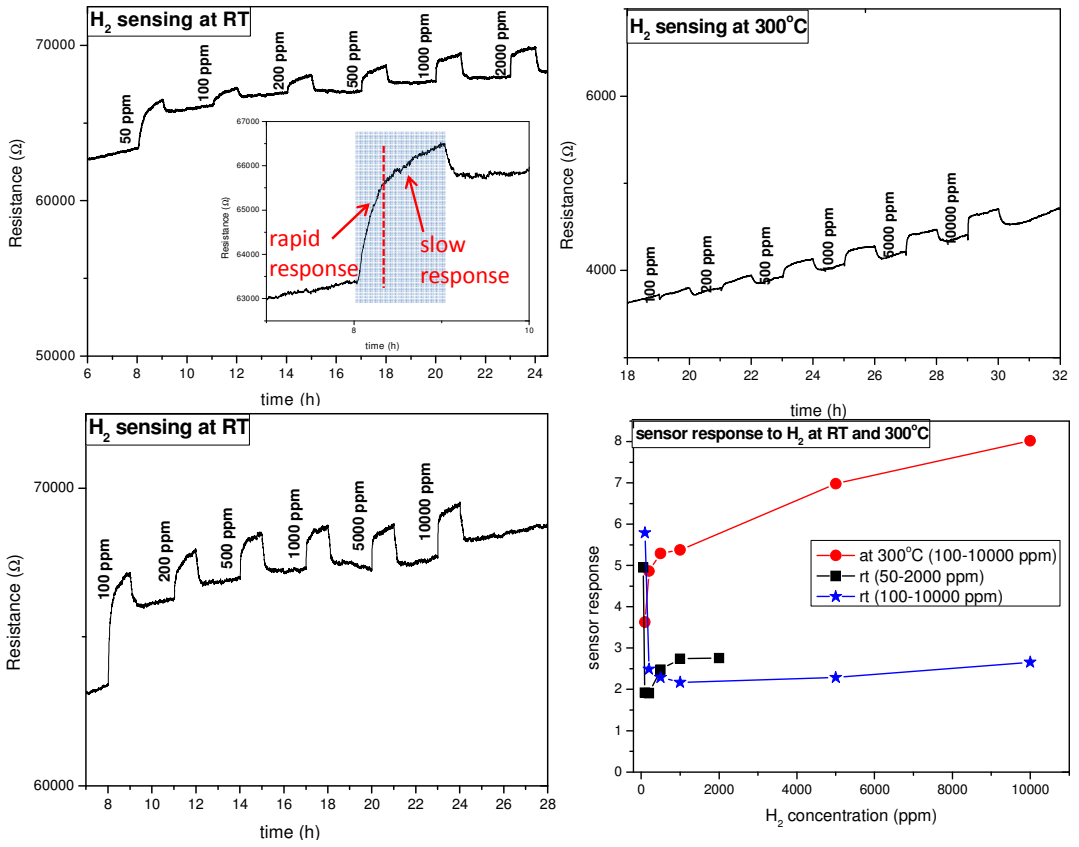

Figure 128: Sensing results and sensor response of CDG sample towards H_2 at room temperature and 300°C.

Figure 129 depicts that ZnO/CDG sample dominantly shows increase in resistance upon exposure to H_2 so the p-characteristics. That can be explained by a combination of an n-type behavior of ZnO combined with the p-type behavior of graphene. Even after reduction of graphene oxide to graphene, oxygen functionalities such as epoxide and carboxyl groups still exist in CDG and since they are electron-withdrawing groups, they promote some holes into the conduction band. The introduction of e-donors (like H_2, here) results in depletion of holes from the conduction band and hence the resistance increases [155]. Sensing behavior of bare graphene at room temperature follows a quite similar trend as the sample ZnO/graphene sample (6 wt%ZnO/CDG) (Figure 129). First the adsorption sites are satured upon exposure to hydrogen. That behavior can be attributed to the graphene itself. Sensor response of graphene is slightly higher than ZnO/graphene sample (8 % versus 6 %). As ZnO loading increases to 33 wt%, the sensor response even decreases more (to ~0.4 %) since ZnO is not active at room temperature but the graphene.

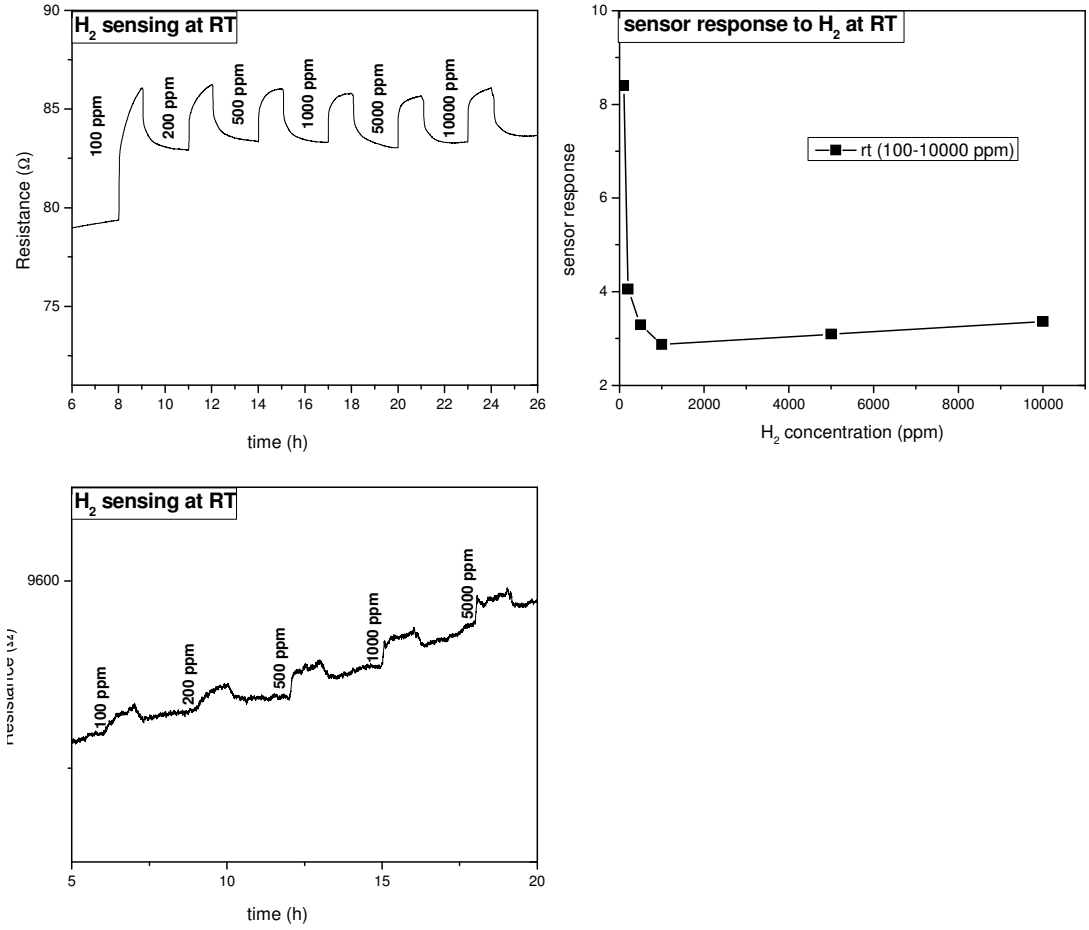

Figure 129: Sensing results and sensor response of 6wt% ZnO/CDG sample towards H_2 at room temperature, at the top and sensing result of 33wt% ZnO/CDG sample towards H_2 at room temperature, at the bottom.

Sensing measurements were also conducted for bare ZnO sample. Figure 130 shows that ZnO sample is an n-type semiconductor as expected for ZnO. That sensing mechanism is based on the formation of Schottky barrier due to chemisorbed oxygen on metal-oxide surface [151]. Upon exposure of reducing gases (like H_2 in our case) to the sample, partial pressure of oxygen decreases so the surface trapped electrons are released back to conductance band of ZnO. That process results in the decrease of the sensor resistance as was observed in Figure 130 [66].

Measurement was not possible for ZnO sample at room temperature due to very high resistance. Sensing behavior of ZnO at 200°C is slightly better than the behavior of the sample at 300°C, however no significant change in sensing response was observed. This could be due to gas saturation at adsorption sites.

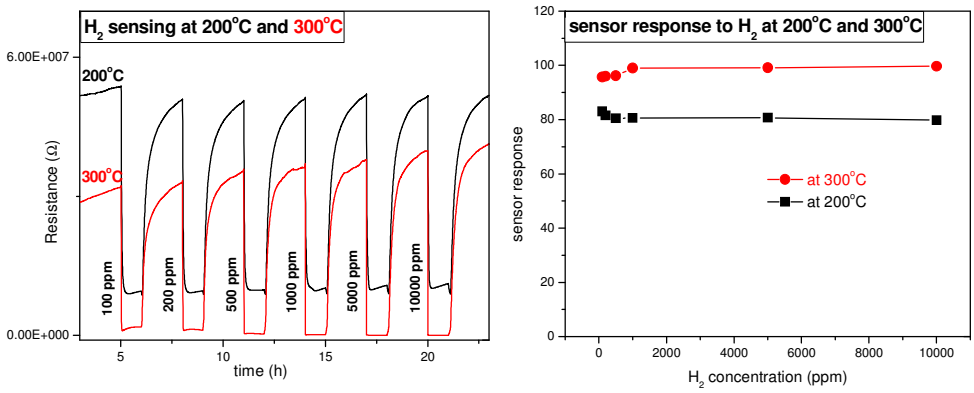

Figure 130: Sensing results and sensor response of ZnO sample towards H_2 at 200°C and 300°C.

It can be summarized that bare ZnO has a higher sensor response (96-99%) than the other samples studied (bare graphene and ZnO/graphene (6 wt% and 33 wt% ZnO/CDG). However, discrimination of different concentrations of H_2 was not possible due to the very fast saturation. Despite the lower sensing response, the use of graphene with ZnO allowed the sensing of hydrogen at room temperature which bare ZnO did not show. The response was even increased at 300°C. The sensing behavior of ZnO/graphene samples is dominantly attributed to graphene rather than ZnO. The reason might be due to the hindering of ZnO particles between the graphene sheets that prevents the adsorption of gases on ZnO sites.

4.4. Conclusion

In summary, wet synthesis of chemically derived graphene was performed. For that purpose first the oxidation of graphite to graphene oxide was carried out by various methods to achieve as much as high oxidation of graphite as possible. Staudenmaier's, Hummers', Modified Hummers' and Tour's Methods were applied to get graphene oxide. Tour's synthesis method was found to be the best way giving the better quality of graphene oxide in the means of oxidation.

Chemically derived graphene was synthesized by reducing the graphene oxide in different ways. Hydrazine hydrate (with and without PSS), hydroxylamine hydrochloride, thermal (slow and fast heating) and vacuum-assisted reduction processes were studied. Hydrazine hydrate reduction resulted in a sample with a high amount of reduced functionality and

further re-reduction of the sample in the presence of hydrogen at 500°C resulted in a further improvement.

Metal (Au, Ni and Pd) and metal oxide (TiO_2, P25 and WO_3) nanoparticles were supported on chemically derived graphene so that hybrid nanoparticles were formed. Some of the hybrid samples were used in catalysis reaction as well as gas sensor material towards H_2 and CO.

Hydrazine hydrate reduced chemically derived graphene sample was used as support for the in-situ synthesized Au NPs and *ex -situ* synthesized Ni and Pd NPs with controllable particle size and dispersion. The chemically derived graphene supported Pd NPs were characterized by using a variety of analytical techniques. They were employed as catalysts in the dehydrogenation and hydrolysis of ammonia borane (AB) in organic solvents and aqueous solutions, respectively. Monodisperse Pd NPs of 4.5 nm were prepared from the reduction of palladium(II) acetylacetonate ($Pd(acac)_2$) in the presence of oleylamine (OAm) by borane tert-butylamine complex (BTB) and easily impregnated on chemically derived graphene (CDG) which has Brunauer Emmett Teller (BET) surface area of 500 $m^2.g^{-1}$. This is the first example of the preparation of CDG-Pd where the Pd NPs were generated ex-situ and then supported on CDG. Pd NPs preserved their particle size dispersion and stability when supported on CDG. The resulting CDG-Pd proved to be highly active and stable catalyst for the dehydrogenation and hydrolysis of AB which are the most promising routes for hydrogen generation from AB complex. In addition to its high activity and stability, CDG-Pd was also found to be reusable catalyst in both dehydrogenation and hydrolysis of AB preserving its 85% and 95% of initial activity after 5^{th} and 10^{th} runs, respectively. The kinetics of CDG-Pd catalyzed dehydrogenation and hydrolysis of AB were studied. Easy preparation using environmentally benign materials, the high catalytic performance, high stability and the reusability of the CDG-Pd make it promising candidate among the precious metals to be employed as a catalyst in developing highly efficient portable hydrogen generation systems using AB as solid hydrogen storage material.

Besides supporting metal nanoparticles on graphene, different metal oxide-graphene hybrid materials were also successfully synthesized. Photocatalytic reduction of graphene oxide to graphene was successfully achieved in the presence of TiO_2 nanoparticles via UV-assisted set-up with Ar flow through the reaction mixture and water cooling.

Moreover, synthesis of titanium dioxide (TiO_2 and P25) graphene composites by hydrothermal reduction have been verified by a variety of characterization methods, particularly with Raman spectroscopy, X-ray diffraction and SEM, TEM microscopic

techniques. In situ preparation of WO_x-graphene hybrid material was achieved using a sonochemical reaction followed by heating process. WO_x was also introduced to the titania-graphene systems and photodegradation of methylene blue in the presence of the home made catalysts were applied. Photoactivities of catalysts correlate with that predicted by literature [156], with titania (in both TiO_2 and P25 cases) loaded on graphene having better catalytic performance than their bare metal oxide counterparts. Moreover, P25-graphene with smaller titania nanoparticles showed better activity than TiO_2-graphene. To the best of my knowledge, it has been for the first time reported that the photoactivity was even increased with the inclusion of WO_x into the titania-graphene samples. This can be attributed to the extension of the absorption range in UV spectrum in the presence of tungsten oxide. WO_x-P25-graphene sample was found to be as the best photocatalyst among P25-based (P25, P25-graphene, P25-WO_x and P25-TiO_2), TiO_2-based (TiO_2, TiO_2–graphene, WO_x-TiO_2–graphene) and WO_x-based (WO_3 and WO_3-graphene) samples.

In addition to these findings, ZnO/chemically derived graphene (CDG) samples were also prepared via in-situ formation of ZnO nanoparticles (of around 5 nm size) from a zinc oximato complex ($[CH_3ONCCH_3COO]_2Zn.2H_2O$) in the presence of CDG. As prepared ZnO/CDG, bare CDG and bare ZnO samples were used in sensing of hydrogen. It is found that a bare ZnO sample has the highest sensitivity at 300°C with lower selectivity to variable concentrations. The selectivity problem of ZnO was solved by forming hybrid of ZnO with graphene. Despite the low sensor response, selectivity of the sample towards different concentrations of hydrogen is higher.

4.5. Experimental Section

4.5.1. Methods for oxidation of Graphite into Graphene Oxide

4.5.1.1. Staudenmaier's Method

5 g graphite was added in a solution of 90 ml concentrated H_2SO_4 (96%) and 45 ml fuming nitric acid (HNO_3, 100%) [13]. This mixture was stirred until a homogeneous suspension was obtained. While stirring the suspension with ice-cooling, 55 g Potassium chlorate ($KClO_4$) was very slowly added whereas a and green colored gas evolved (Cl_2). The black mixture was stirred more than 72 hours, dispersed in 4 L of H_2O, washed with HCl (5%) to remove remaining sulfate ions from the product. Sulfate test was examined with the addition of $CaCl_2$ since $CaSO_4$ was precipitated in presence of sulfate ions. Afterwards, the product was filtrated, vacuum-dried at 60°C overnight and scraped off with a spatula from the filter paper and then homogenized in a mortar. The resulting product was powdery and black.

4.5.1.2. Hummers' Method

In a typical synthesis of graphite oxide, natural graphite flakes (3.0 g, 1 wt equiv) were dispersed in 69.0 mL of H_2SO_4 in a 500 mL erlenmeyer flask. Next, $NaNO_3$ (1.5 g, 0.5 wt equiv) was added into the mixture under continuous stirring at 600 rpm [14]. The Erlenmeyer flask was placed into the ice-bath to decrease the reaction temperature in the range of 0-3 °C since an exothermic reaction occurs upon addition of $KMnO_4$ in the following step. Once everything has settled down, $KMnO_4$ (9.0 g, 3 wt equiv) was added partially by controlling the temperature of the reaction via a thermometer placed into the reaction mixture. Then, the resulting mixture was stirred at 600 rpm for 30 minutes in the ice-bath. After the removal of ice-bath, the solution was heated to 35°C and stirred for 3 hours. A thick paste was formed after 3 h stirring at 35°C. Then, the solution was placed into ice-bath again and 138.0 mL of water was added dropwise (causion, a severe exothermic reaction occurs upon addition of water into the reaction mixture and the reaction temperature may increase up to ~98°C). A dark-brown slurry was formed after stirring of the solution for 30 minutes at room temperature. Finally, 420 mL of water and 3.0 ml of 30 % H_2O_2 were added dropwise into the dark-brown slurry until observation of a permanent yellow color indicating the complete oxidation of graphite. The resultant

solution was filtered and washed with deionized water many times and dried under vacuum at 60°C.

4.5.1.3. Modified Hummers' Method

The method is the use of Hummers' method with doubling the amount of $KMnO_4$ and called as Hummers+. The product is called as HGO+. All of the steps in the synthesis were same with Hummers', the only difference is after adding $KMnO_4$ to the mixture, the slurry was mixed for 7 hrs and additional 9 g of $KMnO_4$ was added into the mixture at once. Further steps to get product is same like in Hummers' method [35].

4.5.1.4. Tour's Method

Tour's method is a further development of the Hummers' method, in which the amount of $KMnO_4$ was doubled, H_3PO_4 was also included to the system besides H_2SO_4 with excluding $NaNO_3$ [35]. Briefly, a 9:1 mixture of concentrated sulfuric and phosphoric acid (360 ml H_2SO_4 (96%)/40 ml H_3PO_4 (100%)) was swiftly added to a mixture of 3 g graphite (flake graphite, natural, -325 mesh, 99.9%, metal basis) and 18 g potassium permanganate ($KMnO_4$) in a 500 ml Erlenmeyer flask, giving a slight exotherm to 40 °C. The reaction was heated to 50°C and stirred for 12 h resulting in the color change of the reaction mixture from black to purple. Then, reaction mixture was cooled to room temperature and poured into a mixture of 300 ml ice and 4 ml H_2O_2 (30%). Here, the color of the reaction mixture changed from dark purple to yellowish. The resulting suspension was centrifuged at 4500 rpm for 5 min. The liquid phase was then decanted and the solid residue washed with 40 ml water and centrifuged again at 4500 rpm for 5 min. The product was washed with HCl (30%) and excessive washing with copious amounts of distilled water was used during filtration. Further filtrating with ethanol, brown color product was yielded, dried at 60°C in vacuum. Since in this experiment concentrated acids have been used in the experiment, it was too difficult to separate the product from the filter paper. For that reason, the filter paper is placed into acetone and graphene oxide was peeled off. Finally, the product was ready for the characterization after grinding.

4.5.2. Methods for reduction of graphene oxide into graphene

4.5.2.1. Hydrazine Hydrate Reduction: Ruoff's Method

500 mg of dried GO was dispersed in 500 mL of water and the mixture was sonicated to exfoliate GO in water until no visible particle was observed in the solution [33] . Then, the resultant solution was connected to reflux system. 5.0 mL of hydrazine hydrate was added into the aqueous dispersion of GO when the temperature was reached to 100°C and the system was refluxed at 100°C over a day. Due to the reduction of graphite oxide, the floating black particles were observed at the end of the reflux process indicating the formation of graphene nanosheets. Finally, the graphene nanosheets were filtered by suction filtration and washed three times with 150 mL of water and 300 mL of methanol, respectively. The powder samples were dried in a Schlenk tube under vacuum at 60°C.

4.5.2.2. Hydrazine Hydrate reduction in the presence of poly(sodium 4-styrenesulfonate): Ruoff's Second Method

This method aims to produce stable aqueous dispersion of graphitic nanoplatelets with the help of poly(sodium 4-styrenesulfonate) (PSS) [104]. Reduction of graphene oxide into graphene was carried out in the same way as described above in Stankovith method. Differently, PSS (10 mg PSS/1 mL GO suspension) was added to the graphite oxide aqueous dispersion prior to reflux at 100°C over a day. Product was collected with filtration and excessive washing with distilled water and methanol.

4.5.2.3. Hydroxylamine hydrochloride reduction: Chen's Method

Initially, 36 mg of graphite oxide was dispersed in 50 mL of distilled water with ultrasonic bath for two hours [157]. 18 g of hydroxylamine hydrochloride was added into that brown dispersion with further addition of 850 mL of water. The reaction mixture was stirred for 24 h under reflux at 80°C. The resulting clear solution, in which black flakes were floating, was filtered with 200 ml methanol and plenty of water washing and followed by vacuum drying at 60°C overnight.

4.5.2.4. Thermal reduction: Boehm's Method

For the thermal synthesis of graphene, required amount of well-ground graphene oxide was replaced into a ceramic boat for tube furnace and boron nitride crucible for induction furnace treatments. Then basically, heating the sample exfoliated and reduced graphene oxide yielding a black powder [15]. Mainly rapid heating of the sample in tube furnace or induction furnace with the heating rate of >2000°C and slow heating with a heating rate of 1.5°C/min in tube furnace were used. Four different thermal treatments were applied under Ar flow comparably. These are; rapid heating of the GO sample to 1050°C into preheated quartz tube under Ar flow (tube furnace), rapid heating of the GO sample and quartz tube to 1050°C under Ar flow (tube furnace), rapid heating of the GO sample to 1050°C under Ar atmosphere (induction furnace) and slow heating the GO sample to 1050°C under Ar flow with a heating rate of (1.5°C/min).

Rapid heating of graphene oxide into preheated quartz tube in tube furnace:

Quartz tube was pre-heated to 1050°C in tube furnace and then graphene oxide was inserted into the hot quartz tube under 180 sccm of Argon flow for two minutes. Then the quartz tube with the sample was removed from the oven under Ar flow.

Rapid heating of graphene oxide and quartz tube in tube furnace:

Graphene oxide sample was placed into quartz tube and then inserted into preheated tube furnace at 1050°C under Ar flow. The sample was removed from the oven with quartz tube under Ar flow as well.

Rapid heating of graphene oxide into induction furnace:

Graphene oxide in boron nitride crucible was put into reactor of induction furnace. After several times flushing with Ar, pressure was set to 700 mbar. Then the sample was heated to 1050°C in few minutes and kept for two minutes. Then the system was cooled to room temperature in few minutes and then the sample was taken out from the system.

Slow heating the graphene oxide sample to 1050°C in tube furnace:

Graphene oxide sample was put into quartz tube and oven was set to 1050°C with a heating rate of 1.5°C/min under Ar flow. After keeping the sample at 1050°C for two minutes, system was cooled down to room temperature under Ar flow and sample was removed from the oven.

4.5.2.5. Vacuum-assisted reduction: Yu's Method

Required amount of well-ground graphene oxide (produced by Tour's or Staudenmaier's methods) was put into a necked flask that was placed in an oil bath and connected to the Schlenk line. The flask was evacuated and temperature of the flask in oil-bath was set to145°C [158]. After applying vacuum for 24 hours by keeping the temperature at 145°C, product was taken out for characterization.

4.5.3. Re-reduction of chemically derived graphene

In order to ensure complete reduction, the resulting graphene samples (where Tour's graphene oxide were precursors and reduced by Ruoff's method) were heated to 500°C with a heating rate of 18°C/min in a tube furnace and annealed at 500°C for 3 hours under the mixture of Ar/H_2 (180:20 sccm) flow. Then temperature was cooled down to room temperature and sample was taken out to be analyzed.

4.5.4. Metal Nanoparticle Synthesis

Pd: Oleylamine mediated synthesis of palladium nanoparticles

Pd NPs were prepared using a modified version of the oleylamine mediated synthesis [146]. In a typical synthesis, 73.3 mg palladium(II) acetylacetonate (($Pd(acac)_2$, 99%), 0.25 mmol Pd) and 12.0 mL of oleylamine (OAm, >70%) were mixed and stirred at 1000 rpm under continuous nitrogen flow in a special three-necked reactor shown in the figure below. Owing to jacketed heater and connected thermocouple placed into the reactor, the mixture was heated up to 75°C slowly. Next, 300 mg of BTB dissolved in 3.0 mL of OAm was injected into the system when the temperature settled down to 75°C. Next, the resulted mixture was heated up to 100°C expeditiously and the system was kept at this temperature for 30 min. Then, the resulted solution was cooled down to 40°C and centrifuged at 8500 rpm for 10 min after the addition of ethanol into the each nanoparticle solution separated into four centrifuge tubes. After a second centrifugation step at 9000 rpm for 10 min, the resulted Pd NPs were dispersed and collected in hexane.

Ni: Oleylamine and oleic acid mediated synthesis of nickel nanoparticles

Similar to the preparation of Pd-NP described above and stated in literature [159]. Briefly, 0.26 g (1 mmol) of $Ni(acac)_2$ and 0.32 mL (1 mmol) of oleic acid were introduced into a

three-necked flask. 15 mL oleylamine was added under inert gas. Then the reaction mixture was heated for one hour at 120° C and green color referred to Ni-oleate complex formation was observed. Thereafter, the mixture was cooled to 95°C and 0.32 g BTB dissolved in 2 ml oleylamine was added to the reaction mixture resulting in a visible color change from green to a dark-brown. The temperature was kept for one hour at 95°C. Then, the system was cooled to room temperature. Reaction mixture was centrifuged at 8500 rpm for 10 min after the addition of ethanol into the each nanoparticle solution separated into four centrifuge tubes. After a second centrifugation step at 9000 rpm for 10 min, the resulted Ni NPs were dispersed and collected in hexane.

4.5.5. Metal Nanoparticles/Graphene Systems

Pd/Graphene (ex-situ): Supporting palladium nanoparticles on chemically derived graphene

Accurate weight of Pd NPs dispersed in hexane was calculated via gravimetric method before their impregnation on CDG and desired amount of them was mixed with dried CDG to ensure the ratio of 2.5 % Pd (w/w) for application in dehydrogenation and hydrolysis of AB, 5 % and 10 % Pd (w/w) for Suzuki-Miyaura coupling reactions. Then, the mixture was diluted with ~5-10 mL of hexane and stirred overnight. After centrifugation (6000 rpm for 10 min), the solid was transferred into a schlenk tube and dried in vacuum. The resulted powder of CDG-Pd was stored for using as catalyst in the dehydrogenation and hydrolysis of AB. The palladium contents of CDG-Pd samples were determined by ICP-OES after each sample was completely dissolved in the mixture of HNO_3/HCl (1/3 ratio). The weight ratio of Pd metal in monodisperse Pd NPs was found as 30% by series ICP-OES analysis performed on colloidal NPs. Monodisperse Pd NPs consist of 70% wt OAm as surfactant.

Ni/Graphene (ex-situ): Supporting palladium nanoparticles on chemically derived graphene

Same procedure given for supporting Pd NPs on CDG was followed. Three different amounts of Ni NPs on CDG as 2.5%-5%-10% (w/w) were prepared.

Au/Graphene (in-situ) Synthesis:

The synthesis of gold nanoparticles on different graphene and graphite oxide was conducted [160]. It is a method in which a surfactant (stabilizer), in this case, cetyltrimethylammonium bromide (CTAB) was used to allow emulsification to control particle size with specific shapes. 5% and 10% (w/w) Au NPs were formed and supported in-situ on graphite oxide (by Tour's method) and graphene samples (one of them was the sample where Tour's graphene oxide were precursors and reduced by Stankovitch method and the other one was the re-reduced (with H_2+Ar) form of that Stankovitch graphene). For the synthesis, 30 mg of graphene oxide or graphene sample was dispersed in 16 mL of water for two hours in an ultrasonic bath until a homogeneous solution was formed. Subsequently, 1.166 g CTAB and 17mM aurochloric acid ($HAuCl_4$) solution (0.47 mL of $HAuCl_4$ solution for 5% and 0.94 mL of that solution for 10% Au loading) were added to that suspension. The reaction mixture was treated in an ultrasonic bath for an hour. 5 mg of $NaBH_4$ was added into the mixture resulting into a color change from brown to gray-black suddenly and formation of foam by the nascent hydrogen (as shown in Figure 131). After further stirring for two minutes, solution was filtered, washed with water and ethanol and the resulting black powder was dried in the air.

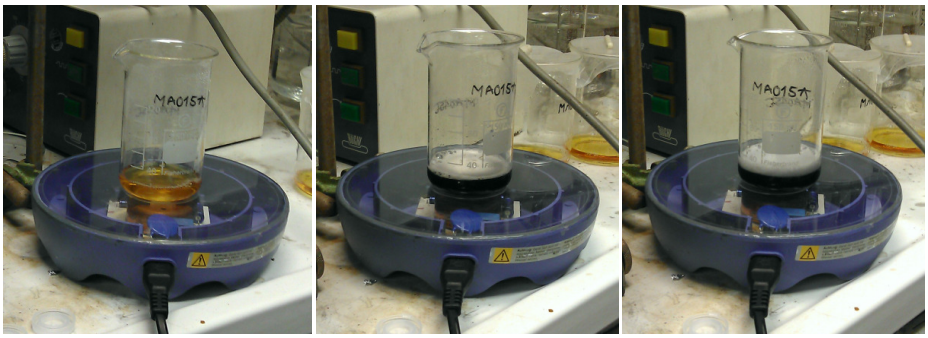

Figure 131: Synthesis of Au NPs by using $NaBH_4$ (5mg) and CTAB. Pictures left to right showed the reaction and foaming (poor) by time.

Control experiments for Au/Graphene (in-situ) Synthesis:

To examine the influence of sodium borohydride as reducing agent, control experiments were carried out, wherein the amount of $NaBH_4$ and the reaction time of reduction varied. By using $NaBH_4$, Au NPs with the particle sizes up to 1 nm was reported [161]. By

increasing the reduction more gold nuclei are formed, which leads to a smaller particle size, and an increasing concentration of nanoparticles in the solution. Therefore, synthesis steps were kept same as detailed in Table 20 besides the amount of $NaBH_4$ was chosen as 5 mg and 600 mg and reduction time was chosen as 2 minutes and 48 hours. The following table presents the experiments carried out.

Table 20: Control experiments performed for Au/graphene synthesis.

Sample	Substances							Reaction time
MA015A			$HAuCl_4$	+	CTAB	+	5 mg $NaBH_4$	2 min
MA015B			$HAuCl_4$	+	CTAB	+	600 mg $NaBH_4$	2 min
MA015C			$HAuCl_4$	+	CTAB	+	600 mg $NaBH_4$	48 h
MA016A	TGO	+	$HAuCl_4$	+	CTAB	+	5 mg $NaBH_4$	2 min
MA016B	TGO	+	$HAuCl_4$	+	CTAB	+	600 mg $NaBH_4$	2 min
MA016C	TGO	+	$HAuCl_4$	+	CTAB	+	600 mg $NaBH_4$	48 h
MA017A	Hydrazinehydrate reduced CDG	+	$HAuCl_4$	+	CTAB	+	5 mg $NaBH_4$	2 min
MA017B	Hydrazinehydrate reduced CDG	+	$HAuCl_4$	+	CTAB	+	600 mg $NaBH_4$	2 min
MA017C	Hydrazinehydrate reduced CDG	+	$HAuCl_4$	+	CTAB	+	600 mg $NaBH_4$	48 h
MA018A	re-reduced CDG	+	$HAuCl_4$	+	CTAB	+	5 mg $NaBH_4$	2 min
MA018B	re-reduced CDG	+	$HAuCl_4$	+	CTAB	+	600 mg $NaBH_4$	2 min
MA018C	re-reduced CDG	+	$HAuCl_4$	+	CTAB	+	600 mg $NaBH_4$	48 h

4.5.6. Metal Oxide Nanoparticles/Graphene Systems

TiO_2/Graphene (by UV-assisted method):

10mM colloidal suspension of TiO_2 in ethanol was prepared by hydrolysis of titanium isopropoxide, (20.9 μL per 10 mL of ethanol) through the dropwise addition of 98% titanium (IV) isopropoxide ($Ti(OCH(CH_3)_2)_4$) to a vigorously stirred ethanol [140]. To that, graphene oxide (1 mg graphene oxide for 1 mL ethanol) was added and sonicated for half an hour to produce TiO_2 coated graphene oxide dispersion.

UV-irradiation of the TiO_2 and TiO_2−graphene oxide was carried out for 2 hours in the apparatus using a 150W Mercury lamp (emitting in the UV and Visible range) with a built-in cooling system (as shown in Figure 132). This apparatus allows continuous mixing of the sample and argon flow through the sample during reaction. The total volume of this apparatus is about 420 mL. UV-VIS spectra of the samples before and after the UV irradiation were received, and compared with the colloidal suspension of titania. The used amount was calculated to give 38 wt% TiO_2/GO or 50 wt% TiO_2/CDG (formula of GO was taken as $C_{2.19}H_{0.80}O_{1.00}$ [162].

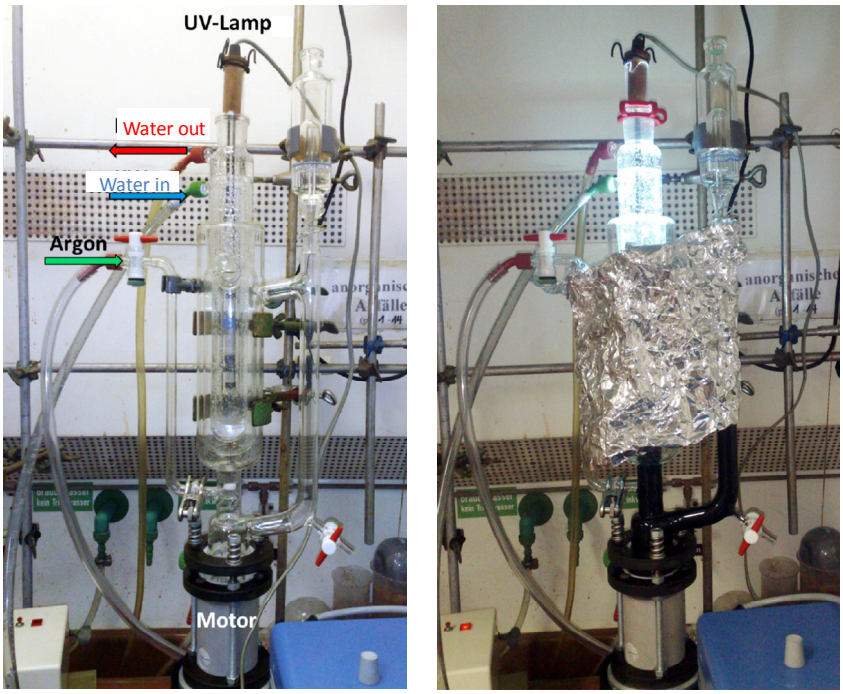

Figure 132: Left: Apparatus equipped with Ar flow and water cooling for UV-irradiation of the samples UV equipment, right: running UV apparatus filled with graphene oxide and titania suspension

TiO_2/Graphene (hydrothermal synthesis):

4 mg of graphene oxide was dispersed in 40 mL deionized water and 20 mL ethanol mixture and sonicated for one hour [137]. Then 0.4 g of TiO_2 (Merck) was added and sonicated for another 2 hours. The reaction mixture was then transferred to a Teflon autoclave and heated to 120°C for 3 hours. The mixture was then cooled to room temperature and centrifuged at 4500 rpm for 10 minutes to be decanted. The resulting precipitate was dried in the desiccator and ground. Besides, bare TiO_2 sample was also prepared by following the same procedure with excluding graphene oxide.

P25/Graphene (hydrothermal synthesis):

The synthesis of P25-graphene also followed the same procedures as that of P25-graphene. The P25 used falls under the brand name AEROXIDE TiO_2 P25 manufactured by Evonik. Bare P25 sample was synthesized as well for comparison.

WO_x/Graphene (sonochemical method):

Two loadings of WO_x were prepared as WOx-graphene (1 wt %) and 1 mol% WO_x-graphene (95 wt %) with sonochemical method [133].

For 1wt%WO_x/graphene sample, 10.35 g phosphotungstic acid (PTA) was sonicated in 86 mL ethanol while at the same time 0.1 g graphene oxide was sonicated in 4 mL deionized water for 8 hours. The mixtures were then stirred overnight separately and subsequently combined for 3 hours of sonication. The resulting mixture was centrifuged and rinsed with ethanol and deionized water. The precipitate was then dried under vacuum and calcined at 550°C for 3 hours under Argon at a flow rate of 200 sccm.

In WO_x-graphene (1 mol% WO_x case), tungsten constituted 1 mol % of the final synthesized product. The synthetic procedure – as well as that of all the tungsten-titanium oxide based catalysts – was exactly the same as that listed for WO_3-graphene 1 wt %. The only difference being that 0.011 g PTA is used with 0.2 g GO. Subsequently the amount of solvent was also adjusted to maintain the correct ratio.

Besides WO_x/graphene samples, as a control experiment bare WO_x sample was also produced by following the same steps described above except using graphene oxide.

WO_x/TiO_2/Graphene:

1 mol% WO_3-TiO_2-graphene (1 wt %) was prepared from 0.006 g PTA and 0.2 g TiO_2-graphene (synthesized beforehand). The TiO_2-graphene was sonicated in ~8mL water. Besides this, the rest of the procedure remained the same with WO_x/graphene preparation. Moreover, 1 mol% WO_3-TiO_2 was prepared from 0.006 g PTA and 0.2 g TiO_2 by using sonochemical method described for WOx/TiO_2/graphene samples.

WO_x/P25/Graphene:

1 mol% WO_3-P25-graphene (1 wt %) was prepared from 0.006 g PTA and 0.2 g P25-graphene (synthesized beforehand). The same procedure with the preparation of WO_3-TiO_2-graphene was followed. In this case, P25-graphene was used instead of TiO_2-graphene. Besides, control experiment was also carried out by preparing 1 mol% WO_3-P25 sample in a same way given for 1 mol% WO_3-TiO_2.

ZnO/Graphene:

To see the effect of using graphene instead of MWCNTs, ZnO/graphene samples were prepared by the same zinc-precursor complex $[CH_3ONCCH_3COO]_2Zn.2H_2O$ (zinc oximato complex)) with as reported [94a]. Briefly, 20 mg of graphene (Stankovitch graphene using Tour's graphene oxide as precursor) was sonicated into 40 ml of DMF for a couple of hours. A defined amount of the zinc oximato precursor given in the table below was added into graphene dispersion. After the complex was dissolved (maximum solubility of zinc oximato complex in DMF is 11 wt %), mixture was refluxed at 150°C for 3 hours. Then, the resulting mixture was filtered, washed with ethanol and dried at 80°C for couple of hours. Besides ZnO/graphene samples, bare ZnO sample was also prepared without using graphene.

Table 21: Amount of the precursors for the preparation of ZnO/CDG samples. Loadings of ZnO are calculated in wt%.

amount of Zn-oximato (mg)	n of Zn oximato (mmol)	amount of graphene (mg)	ZnO/graphene (wt%)
5	0.015	20	5.7
10	0.030	20	11.0
20	0.060	20	20.0
40	0.120	20	33.0

4.5.7. Experimental for Ammonia Borane Hydrogenation and Dehydrogenation Reactions

Dehydrogenation of ammonia borane catalyzed by palladium nanoparticles supported on chemically derived graphene:

The catalytic activity of Pd NPs supported on CDG in the dehydrogenation and hydrolysis of AB were determined by measuring the rate of hydrogen generation. The dehydrogenation and hydrolysis of AB were performed in a typical jacketed, three necked reaction flask connected to the water-filled cylinder glass tube.

Before starting a typical catalytic dehydrogenation of AB, the jacketed reaction flask was kept under vacuum at least for 15 min and filled with nitrogen to remove any trace of oxygen and water present before all the catalytic reactions. 50.0 mg of CDG-Pd catalyst (2.5 wt % Pd) was dispersed in 3 mL of THF in the jacketed reactor thermostated at 25.0 ± 0.5 °C under nitrogen gas atmosphere. Next, 1.0 mmol of AB dissolved in 2.0 mL of THF was injected into the jacketed reactor with a gastight syringe under vigorous stirring and hydrogen gas evolution started immediately.

Hydrogen gas generation from the catalytic reaction solution was followed by using a typical water-filled gas burette system and recording the displacement of water level in the gas burette every minute until no more hydrogen evolution observed. When no more hydrogen generation was observed, the experiment was stopped, the reactor was disconnected from the water-filled tube and the hydrogen pressure was released. Next, an approximately 0.5 mL aliquot of the reaction solution in the reactor was withdrawn with

a glass Pasteur pipette and added to 1 g of $CDCl_3$ in a quartz NMR sample tube (Norell S-500-QTZ), which was subsequently sealed. The ^{11}B-NMR spectrum of this solution showed the complete conversion of H_3NBH_3 (quartet at -23 ppm) to products giving peaks at 1.0 and 16.8 ppm for the dehydrogenation and 11.5 ppm for the hydrolysis reactions.

Hydrolysis of ammonia borane catalyzed by palladium nanoparticles supported on chemically derived graphene:

50.0 mg CDG-Pd catalyst (2.1 wt % Pd) was dispersed in 7.0 mL of water in the jacketed reactor thermostated at 25.0 ± 0.5 °C. Next, 2.0 mmol AB dissolved in 3.0 mL of water was injected into the catalyst solution via gastight syringe under vigorous stirring and hydrogen gas evolution started immediately. The catalytic hydrolysis reaction was followed by measuring the hydrogen generation with time. Hydrogen gas generation from the catalytic reaction solution was followed by using a typical water-filled gas burette system and recording the displacement of water level in the gas burette every minute until no more hydrogen evolution observed. Next, an approximately 0.1 mL aliquot of the reaction solution in the reactor was withdrawn with a glass Pasteur pipette and added to 0.5 mL of D_2O in a quartz NMR sample tube (Norell S-500-QTZ), which was subsequently sealed. The ^{11}B-NMR spectrum of this solution showed the complete conversion of H_3NBH_3 (quartet at -23 ppm) to ammonium metaborate giving a peak at 11.5 ppm.

Reusability of the palladium nanoparticles supported on chemically derived graphene in the dehydrogenation and hydrolysis of ammonia borane:

In a typical reusability test, CDG-Pd catalyst was isolated from the catalytic reaction solution by filtration after all of the AB present in solution was consumed for each cycle. The isolated CDG-Pd catalyst was washed several times with water or THF to remove the residuals from the surface of the catalyst. Next, a new catalytic reaction was started by dispersing the isolated CDG-Pd catalyst in a solution containing a new batch of 1.0 mmol AB for dehydrogenation or 2.0 mmol AB for the hydrolysis as described in the section 2.7 and 2.8, respectively.

4.5.8. Photocatalytic Experiments

Experiments were performed in a customized photodegradation setup, employing two quartz vessels, each containing initially 20 mL of Argon saturated methylene blue aqueous solution (0.01 g/L) along with the tested catalyst (15 mg). The entire setup is kept oxygen free by being closed off to the ambient environment and having Argon being flown into the setup, as well as with the Argon exhaust line. In fact, a cooling condenser is used to seal off the quartz vessels as this is crucial in preventing any sort of evaporation of sample when subjected to the light source. Both quartz vessels are kept at a distance of 12 cm from the light source; each quartz vessel also has its own stirring plate to ensure even mixing of the sample. This entire setup allows the simultaneous photodegradation of two methylene blue samples, allowing the evaluation of two catalysts at the same time.
Two different experiments were performed for each catalyst: dark adsorption and degradation under UV. Common to all experiments, a sample of aqueous solution of methylene blue is measured first by UV-Vis Spectroscopy to obtain the initial concentration value. The spectrum of interest is from 500 nm to 750 nm, with the expected peak to be around 665 nm. Afterwards, the methylene blue solution and the tested catalyst were added into the quartz vessel and mixed for 15 minutes under dark conditions –by simply wrapping the quartz vessels with aluminum foil. After this mixing period, 4 mL of each sample was taken from the quartz vessels and centrifuged for 5 minutes at 4500 rpm in order to separate the catalyst from the solution. Then the solution was transferred to UV cuvette by syringe for UV-Vis Spectroscopy analysis. After this, the methylene blue was thoroughly mixed with the metal catalyst previously separated by centrifuging, and the mixture was returned to the corresponding reaction vessel.
The dark adsorption experiments were performed to determine the initial amount of physisorbed methylene blue adsorption onto the catalyst. In this setup, the quartz vessels were covered with aluminum foil at all times to prevent photodegradation. On top of the 15 minutes of initial mixing, at 30, 60, 120 and 180 minutes of mixing, the procedure of retrieving 4 mL of sample for centrifuging and UV-Vis measurement as described above was repeated.
In the UV experiments, a 150W Mercury lamp emitting in the UV and Visible range was used with a built-in cooling system. After 15 minutes of initial mixing, the Mercury lamp was turned on and samples were taken at 20, 40, 60, 80, and 100 minutes for UV-Vis measurement. It should be noted out that the solutions and the separated catalyst by

centrifuge were put into the reaction vessels during UV degradation experiments as well to ensure the initial volume and concentration constant.

4.5.9. Chemicals

Alfa-Aesar: 25μm thick Ni foil *(99.5%, annealed)* and 25μm thick Cu foils with different purity (*99.8% (metals basis)* and *Puratronic®, 99.999% (metals basis) were used as a substrate for CVD graphene synthesis.*
Acros Organics: *Graphite flake, natural, -325 mesh, 99.8% (metals basis),* 98% titanium (IV) isopropoxide ($Ti(OCH(CH_3)_2)_4$), Hydrazine hydrate, 100% (Hydrazine, 64%), Cetyltrimmethylammoniumbromide (CTAB), Phosphotungstic acid hydrate
Sigma Aldrich: palladium(II) acetylacetonate ($Pd(acac)_2$, 99%), nickel (II) acetylacetonate ($Pd(acac)_2$, 99%)oleylamine (OAm, >70%), oleic acid, HNO_3 (100%), 30 % H_2O_2, H_2SO_4 (96%) and H_3PO_4 (100%)
Merck KGaA: TiO_2
Degussa Evonik: P25
Si-Mat, Silicon Materials: Two different types of wafers as Si and SiO_2/Si (600 nm thermally oxide layer on Si) having a <100> crystal orientation (p-type, light boron doped)

4.5.10.Characterization techniques:

4.5.11.Microscopy:

Electron microscopic characterization was performed by SEM (Philips XL 30 FEG) that is equipped with a LaB6 electron gun, a vacuum SE detector, an elevated pressure SE detector, a backscattering electron detector (BSD), and a Bruker AXS XFlash 4010 detector. SEM images were obtained using a vacuum SE detector where electron acceleration voltage of the incident beam was varied within 10-20 kV and the samples were kept typically at $\leq 5 \times 10^{-5}$ Torr inside the SEM chamber. All of the EDX data were collected using an electron acceleration voltage of 20 kV and a working distance of 10 mm.
Samples for TEM and HRTEM analyses were prepared by two different ways for CVD and CD-graphene samples. CVD samples that are films, transferred directly on the lacy carbon coated TEM grids by fishing the catalyst-free floating graphene flakes onto. CD-related

powder samples were prepared by depositing a single drop of sonificated graphene or graphene-hybrid metal/metal oxide samples that are dispersed in absolute ethanol (for palladium nanoparticles or CDG-Pd dispersed in hexane) on amorphous carbon coated copper grids. Images were obtained by a JEOL 2100 TEM (200 kV) or TEM (FEI Titan 80–300@300 keV),

Atomic Force Microscopy (AFM) analysis of the samples was performed using CP II, Veeco Instruments in non contact mode. A 5μm scanner with standard scanning rate of 0.8 to 1 Hz and silicon cantilevers (Phosphor doped Si tip, 40N/m, 300kHz, Symmetric Tip, Al Reflective Coating, MPP-11120-10 type, Veeco Instruments) were used in the analysis.

4.5.12.X-ray Diffraction (XRD)

X-ray diffraction was carried out using two different instruments. For powder samples, normal 2θ scan, Siemens D5000 (copper Kα) or STADI P, STOE diffractometer (copper Kα) were used. The scan range was in between 10° to 90° (2θ) with step size of 0.02°.

Gracing incidence X-ray diffraction (GIXRD) was carried out for CVDD graphene sample using a PANalytical X´Pert PRO 2-theta scan system equipped with a linear detector (X'Celerator) (in EMPA, Switzerland). The incident X-rays had a wavelength of 1.5418 Å (Cu-Kα-radiation). The diffraction patterns were scanned from 10° to 80° (2θ) with an angular step interval of 0.02° and counting time of 15 second. It takes 14 hour 35 minute to get one pattern.

4.5.13.Raman spectroscopy:

Two different Raman spectroscopy were used. In one of them, micro Raman spectra (ten scans, each lasting 3 s) were recorded in back-scattering smode with a Horiba LabRam HR 800 micro Raman spectrometer (Horiba Jobin Yvon, Bensheim, Germany) equipped with an air-cooled Ar^+ ion laser (emission line λ=514.5 nm). The excitation line has its own interference filter (to filter out the plasma emission) and a Raman notch filter (for laser-light rejection). The measurements were performed with a spectrometer grating of 1800 g mm^{-1} and a confocal microscope (long-working-distance objective, magnification ×50; numerical aperture (NA) 0.5; focused laser-spot diameter ca. 2 μm). The laser power (ca. 20 mW) was attenuated on the sample in the range of 2 mW–20 μW by using

neutral density (ND) filters. Spectral resolution at the conditions was about 1 cm^{-1} and the spatial resolution was about 1 μm.
In the second one, Raman spectroscopy analyses were performed on using an argon laser (Melles Griot) at 514 nm and an excitation power of 7 mW measured at the position of the sample.

4.5.13.1.Infrared Spectroscopy

Nicolet IR100 Instrument was used to perform IR spectrum of solid samples in a range of 400 to 4000 cm^{-1} wavenumbers. Standart potassium bromide (KBr) pellet technique was used. Powder samples were mixed with potassium bromide (KBr) that acts as a binding agent and pressed in a pellet form.

4.5.14.TGA analysis

TGA analysis was performed on STA449C Jupiter (Netzsch) at a heating rate of 10 K/min in aluminum crucibles under helium atmosphere.

4.5.14.1.BET Analysis

BET surface area analysis is performed using a NovaWin2 system (Quantachrome) after degassing all of the samples for 24 h at 80 °C.

4.5.15.Inductively coupled plasma optical emission spectrometry (ICP-OES)

Palladium content of the CDG-Pd samples were determined by using Thermo X series ICP-OES (in METU, Turkey) after each sample was completely dissolved in the mixture of HNO_3/HCl (1/3 ratio).

5. Appendix

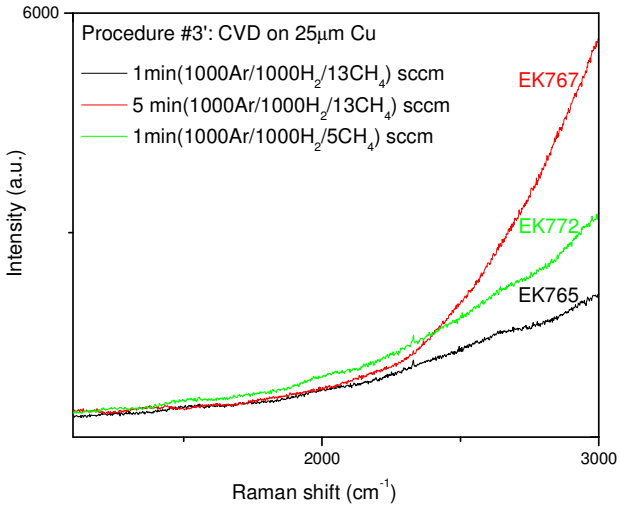

Figure 133: Raman spectra of CVD grown samples on 25 μm thick Cu foil by procedure #3'.

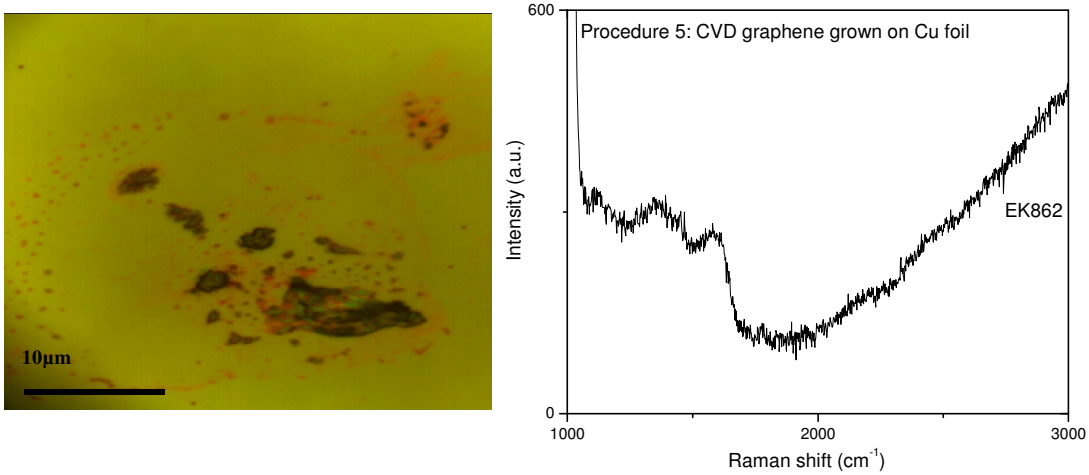

Figure 134: Confocal image of CVD grown sample on Cu foil (left side), Representative Raman spectrum performed on randomly chosen area (at right).

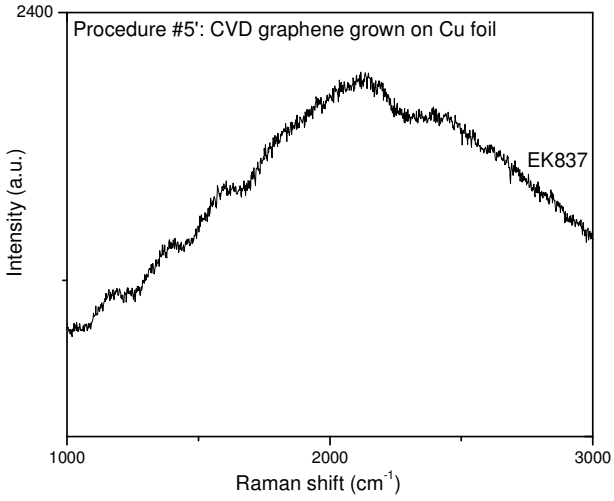

Figure 135: Raman spectrum of CVD grown sample of only 1 min growth time on 25 μm thick Cu foil by procedure #5'.

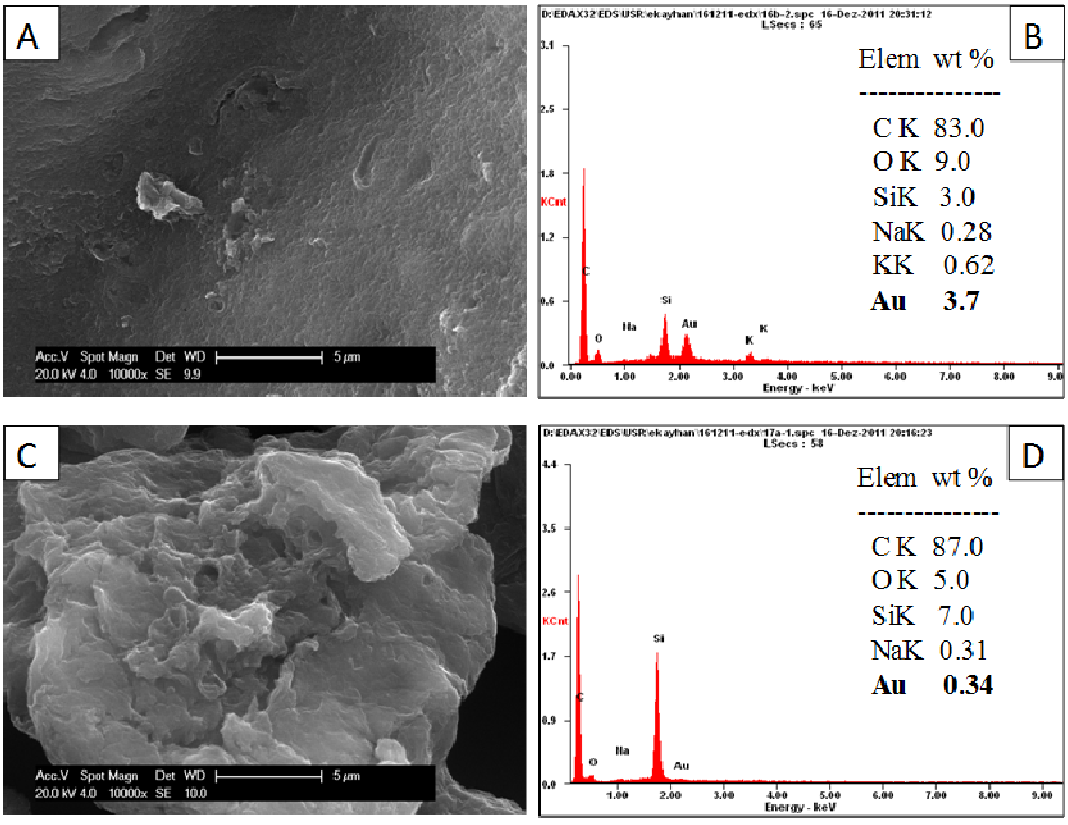

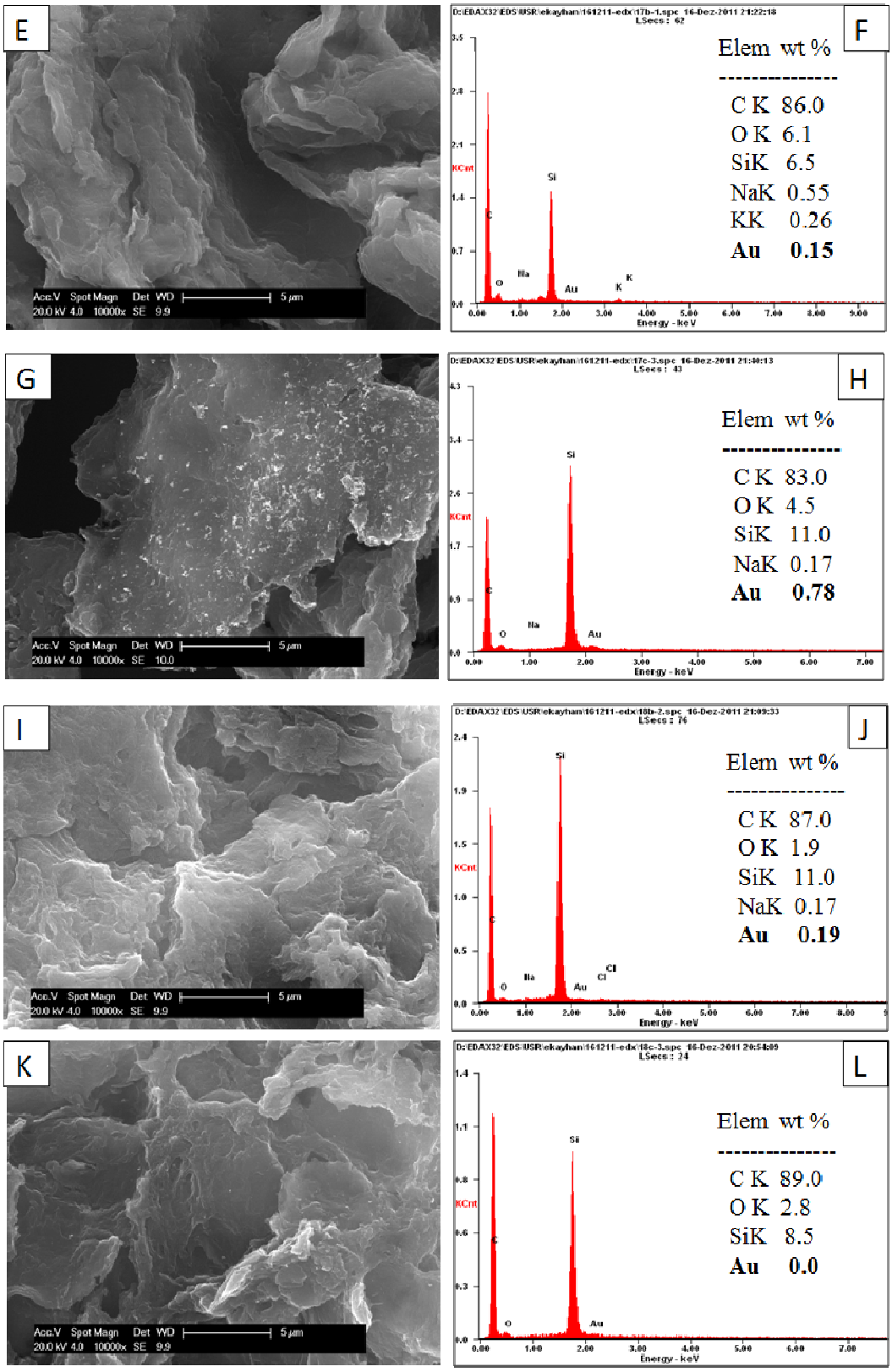

Figure 136: SEM micrographs and EDX data for Au/Graphene samples. TGO (A, B), CDG (C-G) and re-reduced CDG (I-L) were used as precursors.

6. References

[1] H. P. Boehm, R. Setton and E. Stumpp, *Carbon* **1986**, *24*, 241-245.
[2] A. K. Geim and K. S. Novoselov, *Nat Mater* **2007**, *6*, 183-191.
[3] H. W. Kroto, J. R. Heath, S. C. O'Brien, R. F. Curl and R. E. Smalley, *Nature* **1985**, *318*, 162-163.
[4] S. Iijima, *Nature* **1991**, *354*, 56-58.
[5] P. R. Wallace, *Physical Review* **1947**, *71*, 622-634.
[6] J. W. McClure, *Physical Review* **1956**, *104*, 666-671.
[7] G. W. Semenoff, *Physical Review Letters* **1984**, *53*, 2449-2452.
[8] R. E. Peirls, *Helv. Phys. Acta* **1934**, *7*, 81-83.
[9] N. D. Mermin, *Physical Review* **1968**, *176*, 250-254.
[10] K. S. Novoselov, A. K. Geim, S. V. Morozov, D. Jiang, Y. Zhang, S. V. Dubonos, I. V. Grigorieva and A. A. Firsov, *Science* **2004**, *306*, 666-669.
[11] C. Schafhaeutl, *Philosophical Magazine Series 3* **1840**, *16*, 570-590.
[12] B. C. Brodie, *Philosophical Transactions of the Royal Society of London* **1859**, *149*, 249-259.
[13] L. Staudenmaier, *Berichte der deutschen chemischen Gesellschaft* **1898**, *31*, 1481-1487.
[14] W. S. Hummers and R. E. Offeman, *Journal of the American Chemical Society* **1958**, *80*, 1339-1339.
[15] H. P. Boehm, A. Clauss, G. O. Fischer and U. Hofmann, *Zeitschrift für anorganische und allgemeine Chemie* **1962**, *316*, 119-127.
[16] A. K. Geim, *Physica Scripta* **2012**, *2012*, 014003.
[17] a) J. T. Grant and T. W. Haas, *Surface Science* **1970**, *21*, 76-85; b) R. Rosei, M. De Crescenzi, F. Sette, C. Quaresima, A. Savoia and P. Perfetti, *Physical Review B* **1983**, *28*, 1161-1164; c) T. A. Land, T. Michely, R. J. Behm, J. C. Hemminger and G. Comsa, *Surface Science* **1992**, *264*, 261-270; d) J. M. Blakely, J. S. Kim and H. C. Potter, *Journal of Applied Physics* **1970**, *41*, 2693-2697; e) C. F. McConville, D. P. Woodruff, S. D. Kevan, M. Weinert and J. W. Davenport, *Physical Review B* **1986**, *34*, 2199-2206.
[18] a) A. J. Van Bommel, J. E. Crombeen and A. Van Tooren, *Surface Science* **1975**, *48*, 463-472; b) A. Nagashima, K. Nuka, K. Satoh, H. Itoh, T. Ichinokawa, C. Oshima and S. Otani, *Surface Science* **1993**, *287–288, Part 2*, 609-613; c) M. Terai, N. Hasegawa, M. Okusawa, S. Otani and C. Oshima, *Applied Surface Science* **1998**, *130–132*, 876-882; d) I. Forbeaux, J. M. Themlin and J. M. Debever, *Physical Review B* **1998**, *58*, 16396-16406.
[19] A. M. Affoune, B. L. V. Prasad, H. Sato, T. Enoki, Y. Kaburagi and Y. Hishiyama, *Chemical Physics Letters* **2001**, *348*, 17-20.
[20] K. Seibert, G. C. Cho, W. Kütt, H. Kurz, D. H. Reitze, J. I. Dadap, H. Ahn, M. C. Downer and A. M. Malvezzi, *Physical Review B* **1990**, *42*, 2842-2851.
[21] T. W. Ebbesen and H. Hiura, *Advanced Materials* **1995**, *7*, 582-586.
[22] L. Xuekun, Y. Minfeng, H. Hui and S. R. Rodney, *Nanotechnology* **1999**, *10*, 269.
[23] a) Y. Ohashi, T. Koizumi, T. Yoshikawa, T. Hironaka and K. Shiiki, *TANSO* **1997**, *1997*, 235-238; b) Y. Ohashi, T. Hironaka, T. Kubo and K. Shiiki, *TANSO* **2000**, *2000*, 410; c) E. Dujardin, T. Thio, H. Lezec and T. W. Ebbesen, *Applied Physics Letters* **2001**, *79*, 2474-2476.
[24] Y. Gan, W. Chu and L. Qiao, *Surface Science* **2003**, *539*, 120-128.
[25] C. Berger, Z. Song, T. Li, X. Li, A. Y. Ogbazghi, R. Feng, Z. Dai, A. N. Marchenkov, E. H. Conrad, P. N. First and W. A. de Heer, *The Journal of Physical Chemistry B* **2004**, *108*, 19912-19916.
[26] D. R. Dreyer, R. S. Ruoff and C. W. Bielawski, *Angewandte Chemie International Edition* **2010**, *49*, 9336-9344.

[27] X. Du, I. Skachko, A. Barker and E. Y. Andrei, *Nat Nano* **2008**, *3*, 491-495.
[28] M. C. Lemme, *Solid State Phenomena* **2010**, *156-158*, 499-509.
[29] Z. H. Ni, H. M. Wang, J. Kasim, H. M. Fan, T. Yu, Y. H. Wu, Y. P. Feng and Z. X. Shen, *Nano Letters* **2007**, *7*, 2758-2763.
[30] Y. Zhu, S. Murali, W. Cai, X. Li, J. W. Suk, J. R. Potts and R. S. Ruoff, *Advanced Materials* **2010**, *22*, 3906-3924.
[31] a) G. Van Lier, C. Van Alsenoy, V. Van Doren and P. Geerlings, *Chemical Physics Letters* **2000**, *326*, 181-185; b) C. Lee, X. Wei, J. W. Kysar and J. Hone, *Science* **2008**, *321*, 385-388.
[32] S. Chen, Q. Wu, C. Mishra, J. Kang, H. Zhang, K. Cho, W. Cai, A. A. Balandin and R. S. Ruoff, *Nat Mater* **2012**, *11*, 203-207.
[33] S. Stankovich, D. A. Dikin, R. D. Piner, K. A. Kohlhaas, A. Kleinhammes, Y. Jia, Y. Wu, S. T. Nguyen and R. S. Ruoff, *Carbon* **2007**, *45*, 1558-1565.
[34] E. Kayhan, R. M. Prasad, A. Gurlo, O. Yilmazoglu, J. Engstler, E. Ionescu, S. Yoon, A. Weidenkaff and J. J. Schneider, *Chemistry – A European Journal* **2012**, *18*, 14996-15003.
[35] D. C. Marcano, D. V. Kosynkin, J. M. Berlin, A. Sinitskii, Z. Sun, A. Slesarev, L. B. Alemany, W. Lu and J. M. Tour, *ACS Nano* **2010**, *4*, 4806-4814.
[36] S. Bae, H. Kim, Y. Lee, X. Xu, J.-S. Park, Y. Zheng, J. Balakrishnan, T. Lei, H. Ri Kim, Y. I. Song, Y.-J. Kim, K. S. Kim, B. Ozyilmaz, J.-H. Ahn, B. H. Hong and S. Iijima, *Nat Nano* **2010**, *5*, 574-578.
[37] R. K. Joshi, H. Gomez, F. Alvi and A. Kumar, *The Journal of Physical Chemistry C* **2010**, *114*, 6610-6613.
[38] Ö. Metin, E. Kayhan, S. Özkar and J. J. Schneider, *International Journal of Hydrogen Energy* **2012**, *37*, 8161-8169.
[39] X. Zhao, C. M. Hayner, M. C. Kung and H. H. Kung, *Advanced Energy Materials* **2011**, *1*, 1079-1084.
[40] N. Li, Z. Chen, W. Ren, F. Li and H.-M. Cheng, *Proceedings of the National Academy of Sciences* **2012**, *109*, 17360-17365.
[41] a) G. Flagship in *http://www.graphene-flagship.eu/GF/MediaKit2.php*, *2013* **2013**; b) Technical University of Manchester in *http://www.graphene.manchester.ac.uk/story/*, *2013* **2013**.
[42] J. Chen, M. Duan and G. Chen, *Journal of Materials Chemistry* **2012**, *22*, 19625-19628.
[43] Y. Hernandez, V. Nicolosi, M. Lotya, F. M. Blighe, Z. Sun, S. De, I. T. McGovern, B. Holland, M. Byrne, Y. K. Gun'Ko, J. J. Boland, P. Niraj, G. Duesberg, S. Krishnamurthy, R. Goodhue, J. Hutchison, V. Scardaci, A. C. Ferrari and J. N. Coleman, *Nat Nano* **2008**, *3*, 563-568.
[44] V. Alzari, D. Nuvoli, S. Scognamillo, M. Piccinini, E. Gioffredi, G. Malucelli, S. Marceddu, M. Sechi, V. Sanna and A. Mariani, *Journal of Materials Chemistry* **2011**, *21*, 8727-8733.
[45] D. Nuvoli, L. Valentini, V. Alzari, S. Scognamillo, S. B. Bon, M. Piccinini, J. Illescas and A. Mariani, *Journal of Materials Chemistry* **2011**, *21*, 3428-3431.
[46] C. Berger, Z. Song, X. Li, X. Wu, N. Brown, C. Naud, D. Mayou, T. Li, J. Hass, A. N. Marchenkov, E. H. Conrad, P. N. First and W. A. de Heer, *Science* **2006**, *312*, 1191-1196.
[47] a) J. Hass, W. A. d. Heer and E. H. Conrad, *Journal of Physics: Condensed Matter* **2008**, *20*, 323202; b) J. Kedzierski, H. Pei-Lan, P. Healey, P. W. Wyatt, C. L. Keast, M. Sprinkle, C. Berger and W. A. De Heer, *Electron Devices, IEEE Transactions on* **2008**, *55*, 2078-2085.
[48] C. Mattevi, H. Kim and M. Chhowalla, *Journal of Materials Chemistry* **2011**, *21*, 3324-3334.
[49] X. Li, W. Cai, L. Colombo and R. S. Ruoff, *Nano Letters* **2009**, *9*, 4268-4272.

[50] O. C. Compton and S. T. Nguyen, *Small* **2010**, *6*, 711-723.
[51] M. J. Allen, V. C. Tung and R. B. Kaner, *Chemical Reviews* **2009**, *110*, 132-145.
[52] Y. Xu, Z. Liu, X. Zhang, Y. Wang, J. Tian, Y. Huang, Y. Ma, X. Zhang and Y. Chen, *Advanced Materials* **2009**, *21*, 1275-1279.
[53] K. S. Kim, Y. Zhao, H. Jang, S. Y. Lee, J. M. Kim, K. S. Kim, J.-H. Ahn, P. Kim, J.-Y. Choi and B. H. Hong, *Nature* **2009**, *457*, 706-710.
[54] J. Coraux, A. T. N`Diaye, C. Busse and T. Michely, *Nano Letters* **2008**, *8*, 565-570.
[55] P. W. Sutter, J.-I. Flege and E. A. Sutter, *Nat Mater* **2008**, *7*, 406-411.
[56] X. Li, W. Cai, J. An, S. Kim, J. Nah, D. Yang, R. Piner, A. Velamakanni, I. Jung, E. Tutuc, S. K. Banerjee, L. Colombo and R. S. Ruoff, *Science* **2009**, *324*, 1312-1314.
[57] a) Z. Ni, Y. Wang, T. Yu and Z. Shen, *Nano Research* **2008**, *1*, 273-291; b) A. C. Ferrari, J. C. Meyer, V. Scardaci, C. Casiraghi, M. Lazzeri, F. Mauri, S. Piscanec, D. Jiang, K. S. Novoselov, S. Roth and A. K. Geim, *Physical Review Letters* **2006**, *97*, 187401.
[58] L. G. Cançado, A. Reina, J. Kong and M. S. Dresselhaus, *Physical Review B* **2008**, *77*, 245408.
[59] Y. Y. Wang, Z. H. Ni, Z. X. Shen, H. M. Wang and Y. H. Wu, *Applied Physics Letters* **2008**, *92*, 043121.
[60] J. S. Bunch, A. M. van der Zande, S. S. Verbridge, I. W. Frank, D. M. Tanenbaum, J. M. Parpia, H. G. Craighead and P. L. McEuen, *Science* **2007**, *315*, 490-493.
[61] C. Thomsen and S. Reich, *Physical Review Letters* **2000**, *85*, 5214-5217.
[62] M. A. Pimenta, G. Dresselhaus, M. S. Dresselhaus, L. G. Cancado, A. Jorio and R. Saito, *Physical Chemistry Chemical Physics* **2007**, *9*, 1276-1290.
[63] A. Ismach, C. Druzgalski, S. Penwell, A. Schwartzberg, M. Zheng, A. Javey, J. Bokor and Y. Zhang, *Nano Letters* **2010**, *10*, 1542-1548.
[64] A. Reina, X. Jia, J. Ho, D. Nezich, H. Son, V. Bulovic, M. S. Dresselhaus and J. Kong, *Nano Letters* **2008**, *9*, 30-35.
[65] Q. Yu, J. Lian, S. Siriponglert, H. Li, Y. P. Chen and S.-S. Pei, *Applied Physics Letters* **2008**, *93*, 113103.
[66] G. Singh, A. Choudhary, D. Haranath, A. G. Joshi, N. Singh, S. Singh and R. Pasricha, *Carbon* **2012**, *50*, 385-394.
[67] W. Eck, A. Küller, M. Grunze, B. Völkel and A. Gölzhäuser, *Advanced Materials* **2005**, *17*, 2583-2587.
[68] X. Wang, H. You, F. Liu, M. Li, L. Wan, S. Li, Q. Li, Y. Xu, R. Tian, Z. Yu, D. Xiang and J. Cheng, *Chemical Vapor Deposition* **2009**, *15*, 53-56.
[69] S. Kumar, N. McEvoy, T. Lutz, G. P. Keeley, V. Nicolosi, C. P. Murray, W. J. Blau and G. S. Duesberg, *Chemical Communications* **2010**, *46*, 1422-1424.
[70] S. J. Chae, F. Güneş, K. K. Kim, E. S. Kim, G. H. Han, S. M. Kim, H.-J. Shin, S.-M. Yoon, J.-Y. Choi, M. H. Park, C. W. Yang, D. Pribat and Y. H. Lee, *Advanced Materials* **2009**, *21*, 2328-2333.
[71] M. P. Levendorf, C. S. Ruiz-Vargas, S. Garg and J. Park, *Nano Letters* **2009**, *9*, 4479-4483.
[72] W. Wu, Z. Liu, L. A. Jauregui, Q. Yu, R. Pillai, H. Cao, J. Bao, Y. P. Chen and S.-S. Pei, *Sensors and Actuators B: Chemical* **2010**, *150*, 296-300.
[73] Y. N. Trehan, *Zeitschrift für anorganische und allgemeine Chemie* **1962**, *318*, 107-112.
[74] C. H. See and A. T. Harris, *Industrial & Engineering Chemistry Research* **2007**, *46*, 997-1012.
[75] G. Ruan, Z. Sun, Z. Peng and J. M. Tour, *ACS Nano* **2011**, *5*, 7601-7607.
[76] L. Liu, H. Zhou, R. Cheng, Y. Chen, Y.-C. Lin, Y. Qu, J. Bai, I. A. Ivanov, G. Liu, Y. Huang and X. Duan, *Journal of Materials Chemistry* **2012**, *22*, 1498-1503.
[77] a) W. Wu, Q. Yu, P. Peng, Z. Liu, J. Bao and S.-S. Pei, *Nanotechnology* **2012**, *23*, 035603; b) A. W. Robertson and J. H. Warner, *Nano Letters* **2011**, *11*, 1182-1189; c) Y.

Yao, Z. Li, Z. Lin, K.-S. Moon, J. Agar and C. Wong, *The Journal of Physical Chemistry C* **2011**, *115*, 5232-5238.
[78] S. Bhaviripudi, X. Jia, M. S. Dresselhaus and J. Kong, *Nano Letters* **2010**, *10*, 4128-4133.
[79] I. Vlassiouk, M. Regmi, P. Fulvio, S. Dai, P. Datskos, G. Eres and S. Smirnov, *ACS Nano* **2011**, *5*, 6069-6076.
[80] Y. Lee, S. Bae, H. Jang, S. Jang, S.-E. Zhu, S. H. Sim, Y. I. Song, B. H. Hong and J.-H. Ahn, *Nano Letters* **2010**, *10*, 490-493.
[81] M. Kalbac, O. Frank and L. Kavan, *Carbon* **2012**, *50*, 3682-3687.
[82] W. Cai, Y. Zhu, X. Li, R. D. Piner and R. S. Ruoff, *Applied Physics Letters* **2009**, *95*, 123115.
[83] W. Zhang, P. Wu, Z. Li and J. Yang, *The Journal of Physical Chemistry C* **2011**, *115*, 17782-17787.
[84] A. M. v. d. Zande, R. A. Barton, J. S. Alden, C. S. Ruiz-Vargas, W. S. Whitney, P. H. Q. Pham, J. Park, J. M. Parpia, H. G. Craighead and P. L. McEuen, *Nano Letters* **2010**, *10*, 4869-4873.
[85] K. Lascelles, L. G. Morgan, D. Nicholls and D. Beyersmann in *Nickel Compounds*, *Vol.* Wiley-VCH Verlag GmbH & Co. KGaA, **2000**.
[86] D. C. Elias, R. R. Nair, T. M. G. Mohiuddin, S. V. Morozov, P. Blake, M. P. Halsall, A. C. Ferrari, D. W. Boukhvalov, M. I. Katsnelson, A. K. Geim and K. S. Novoselov, *Science* **2009**, *323*, 610-613.
[87] A. Peigney, C. Laurent, E. Flahaut, R. R. Bacsa and A. Rousset, *Carbon* **2001**, *39*, 507-514.
[88] M. Gautam and A. H. Jayatissa, *Materials Science and Engineering: C* **2011**, *31*, 1405-1411.
[89] a) F. Schedin, A. K. Geim, S. V. Morozov, E. W. Hill, P. Blake, M. I. Katsnelson and K. S. Novoselov, *Nat Mater* **2007**, *6*, 652-655; b) K. S. Subrahmanyam, S. R. C. Vivekchand, A. Govindaraj and C. N. R. Rao, *Journal of Materials Chemistry* **2008**, *18*, 1517-1523; c) L.-S. Zhang, W. D. Wang, X.-Q. Liang, W.-S. Chu, W.-G. Song, W. Wang and Z.-Y. Wu, *Nanoscale* **2011**, *3*, 2458-2460.
[90] a) Y. Xu, R. Gwoziecki, I. Chartier, R. Coppard, F. Balestra and G. Ghibaudo, *Applied Physics Letters* **2010**, *97*, 063302; b) C. Christopoulos, *Synthesis Lectures on Computational Electromagnetics* **2006**, *1*, 1-132.
[91] H. Mousavi, *Communications in Theoretical Physics* **2011**, *56*, 373.
[92] R. Arsat, M. Breedon, M. Shafiei, P. G. Spizziri, S. Gilje, R. B. Kaner, K. Kalantar-zadeh and W. Wlodarski, *Chemical Physics Letters* **2009**, *467*, 344-347.
[93] A. Kaniyoor, R. Imran Jafri, T. Arockiadoss and S. Ramaprabhu, *Nanoscale* **2009**, *1*, 382-386.
[94] a) J. Khanderi, R. C. Hoffmann, A. Gurlo and J. J. Schneider, *Journal of Materials Chemistry* **2009**, *19*, 5039-5046; b) T. Sahm, A. Gurlo, N. Barsan and U. Weimar, *Particulate Science and Technology* **2006**, *24*, 441-452.
[95] a) H. Chang, J. D. Lee, S. M. Lee and Y. H. Lee, *Applied Physics Letters* **2001**, *79*, 3863-3865; b) J. Zhao, A. Buldum, J. Han and J. P. Lu, *Nanotechnology* **2002**, *13*, 195.
[96] R. K. Joshi, J. E. Weber, Q. Hu, B. Johnson, J. W. Zimmer and A. Kumar, *Sensors and Actuators B: Chemical* **2010**, *145*, 527-532.
[97] a) O. Leenaerts, B. Partoens and F. M. Peeters, *Physical Review B* **2008**, *77*, 125416; b) Y.-H. Zhang, Y.-B. Chen, K.-G. Zhou, C.-H. Liu, J. Zeng, H.-L. Zhang and Y. Peng, *Nanotechnology* **2009**, *20*, 185504; c) Y. Zou, F. Li, Z. Zhu, M. Zhao, X. Xu and X. Su, *The European Physical Journal B - Condensed Matter and Complex Systems* **2011**, *81*, 475-479.
[98] A. Z. Sadek, C. Zhang, Z. Hu, J. G. Partridge, D. G. McCulloch, W. Wlodarski and K. Kalantar-zadeh, *The Journal of Physical Chemistry C* **2009**, *114*, 238-242.

[99] a) J. S. Arellano, L. M. Molina, A. Rubio and J. A. Alonso, *The Journal of Chemical Physics* **2000**, *112*, 8114-8119; b) Y. Okamoto and Y. Miyamoto, *The Journal of Physical Chemistry B* **2001**, *105*, 3470-3474.
[100] G. Ko, H. Y. Kim, J. Ahn, Y. M. Park, K. Y. Lee and J. Kim, *Current Applied Physics* **2010**, *10*, 1002-1004.
[101] a) Y. Si and E. T. Samulski, *Nano Letters* **2008**, *8*, 1679-1682; b) D. W. Lee, L. De Los Santos V, J. W. Seo, L. L. Felix, A. Bustamante D, J. M. Cole and C. H. W. Barnes, *The Journal of Physical Chemistry B* **2010**, *114*, 5723-5728; c) A. Bagri, C. Mattevi, M. Acik, Y. J. Chabal, M. Chhowalla and V. B. Shenoy, *Nat Chem* **2010**, *2*, 581-587.
[102] a) D. Li, M. B. Muller, S. Gilje, R. B. Kaner and G. G. Wallace, *Nat Nano* **2008**, *3*, 101-105; b) X. Gao, J. Jang and S. Nagase, *The Journal of Physical Chemistry C* **2009**, *114*, 832-842.
[103] E.-Y. Choi, T. H. Han, J. Hong, J. E. Kim, S. H. Lee, H. W. Kim and S. O. Kim, *Journal of Materials Chemistry* **2010**, *20*, 1907-1912.
[104] S. Stankovich, R. D. Piner, X. Chen, N. Wu, S. T. Nguyen and R. S. Ruoff, *Journal of Materials Chemistry* **2006**, *16*, 155-158.
[105] S. Stankovich, D. A. Dikin, G. H. B. Dommett, K. M. Kohlhaas, E. J. Zimney, E. A. Stach, R. D. Piner, S. T. Nguyen and R. S. Ruoff, *Nature* **2006**, *442*, 282-286.
[106] E. Yoo, T. Okata, T. Akita, M. Kohyama, J. Nakamura and I. Honma, *Nano Letters* **2009**, *9*, 2255-2259.
[107] G. Lu, S. Mao, S. Park, R. Ruoff and J. Chen, *Nano Research* **2009**, *2*, 192-200.
[108] S. Guo, D. Wen, Y. Zhai, S. Dong and E. Wang, *ACS Nano* **2010**, *4*, 3959-3968.
[109] H. M. A. Hassan, V. Abdelsayed, A. E. R. S. Khder, K. M. AbouZeid, J. Terner, M. S. El-Shall, S. I. Al-Resayes and A. A. El-Azhary, *Journal of Materials Chemistry* **2009**, *19*, 3832-3837.
[110] R. Muszynski, B. Seger and P. V. Kamat, *The Journal of Physical Chemistry C* **2008**, *112*, 5263-5266.
[111] Á. Mastalir, Z. Király, Á. Patzkó, I. Dékány and P. L'Argentiere, *Carbon* **2008**, *46*, 1631-1637.
[112] F. Durap, Ö. Metin, M. Aydemir and S. Özkar, *Applied Organometallic Chemistry* **2009**, *23*, 498-503.
[113] C. C. Cassol, A. P. Umpierre, G. Machado, S. I. Wolke and J. Dupont, *Journal of the American Chemical Society* **2005**, *127*, 3298-3299.
[114] J. K. Stille, *Angewandte Chemie International Edition in English* **1986**, *25*, 508-524.
[115] G. M. Scheuermann, L. Rumi, P. Steurer, W. Bannwarth and R. Mülhaupt, *Journal of the American Chemical Society* **2009**, *131*, 8262-8270.
[116] S.-i. Orimo, Y. Nakamori, J. R. Eliseo, A. Züttel and C. M. Jensen, *Chemical Reviews* **2007**, *107*, 4111-4132.
[117] T. B. Marder, *Angewandte Chemie International Edition* **2007**, *46*, 8116-8118.
[118] F. Baitalow, J. Baumann, G. Wolf, K. Jaenicke-Rößler and G. Leitner, *Thermochimica Acta* **2002**, *391*, 159-168.
[119] H. Erdogan, O. Metin and S. Ozkar, *Physical Chemistry Chemical Physics* **2009**, *11*, 10519-10525.
[120] C. A. Jaska, K. Temple, A. J. Lough and I. Manners, *Chemical Communications* **2001**, *0*, 962-963.
[121] C. W. Hamilton, R. T. Baker, A. Staubitz and I. Manners, *Chemical Society Reviews* **2009**, *38*, 279-293.
[122] C. A. Jaska, K. Temple, A. J. Lough and I. Manners, *Journal of the American Chemical Society* **2003**, *125*, 9424-9434.
[123] Ö. Metin and S. Özkar, *Energy & Fuels* **2009**, *23*, 3517-3526.

[124] Ö. Metin, Ş. Şahin and S. Özkar, *International Journal of Hydrogen Energy* **2009**, *34*, 6304-6313.
[125] Ö. Metin, S. Duman, M. Dinç and S. Özkar, *The Journal of Physical Chemistry C* **2011**, *115*, 10736-10743.
[126] K. Zhou, Y. Zhu, X. Yang, X. Jiang and C. Li, *New Journal of Chemistry* **2011**, *35*, 353-359.
[127] a) R. W. Matthews, *Journal of the Chemical Society, Faraday Transactions 1: Physical Chemistry in Condensed Phases* **1989**, *85*, 1291-1302; b) T. Tatsuma, S.-i. Tachibana and A. Fujishima, *The Journal of Physical Chemistry B* **2001**, *105*, 6987-6992.
[128] T. Tatsuma, S.-i. Tachibana, T. Miwa, D. A. Tryk and A. Fujishima, *The Journal of Physical Chemistry B* **1999**, *103*, 8033-8035.
[129] K.-i. Ishibashi, A. Fujishima, T. Watanabe and K. Hashimoto, *The Journal of Physical Chemistry B* **2000**, *104*, 4934-4938.
[130] A. Mills and J. Wang, *Journal of Photochemistry and Photobiology A: Chemistry* **1999**, *127*, 123-134.
[131] X. Z. Li, F. B. Li, C. L. Yang and W. K. Ge, *Journal of Photochemistry and Photobiology A: Chemistry* **2001**, *141*, 209-217.
[132] J. Zhang, M. Li, Z. Feng, J. Chen and C. Li, *The Journal of Physical Chemistry B* **2005**, *110*, 927-935.
[133] J. Guo, Y. Li, S. Zhu, Z. Chen, Q. Liu, D. Zhang, W.-J. Moon and D.-M. Song, *RSC Advances* **2012**, *2*, 1356-1363.
[134] O. Akhavan, M. Choobtashani and E. Ghaderi, *The Journal of Physical Chemistry C* **2012**, *116*, 9653-9659.
[135] M. A. Rauf, M. A. Meetani, A. Khaleel and A. Ahmed, *Chemical Engineering Journal* **2010**, *157*, 373-378.
[136] E. B. Gracien, J. Shen, X. Sun, D. Liu, M. Li, S. Yao and J. Sun, *Thin Solid Films* **2007**, *515*, 5287-5297.
[137] H. Zhang, X. Lv, Y. Li, Y. Wang and J. Li, *ACS Nano* **2009**, *4*, 380-386.
[138] X. Li, *Journal of Photochemistry and Photobiology A: Chemistry* **2001**, *141*, 209-217.
[139] J. J. Schneider, R. C. Hoffmann, J. Engstler, O. Soffke, W. Jaegermann, A. Issanin and A. Klyszcz, *Advanced Materials* **2008**, *20*, 3383-3387.
[140] G. Williams, B. Seger and P. V. Kamat, *ACS Nano* **2008**, *2*, 1487-1491.
[141] P. V. Kamat, *Chemical Reviews* **1993**, *93*, 267-300.
[142] S. M. Andonova, G. S. Senturk, E. Kayhan and E. Ozensoy, *The Journal of Physical Chemistry C* **2009**, *113*, 11014-11026.
[143] C. V. Ramana, S. Utsunomiya, R. C. Ewing, C. M. Julien and U. Becker, *The Journal of Physical Chemistry B* **2006**, *110*, 10430-10435.
[144] S.-H. Lee, H. M. Cheong, C. E. Tracy, A. Mascarenhas, D. K. Benson and S. K. Deb, *Electrochimica Acta* **1999**, *44*, 3111-3115.
[145] M. P. Thi and G. Velasco, *Solid State Ionics* **1984**, *14*, 217-220.
[146] V. Mazumder and S. Sun, *Journal of the American Chemical Society* **2009**, *131*, 4588-4589.
[147] T. Ayval, M. Zahmakran and S. Ozkar, *Dalton Transactions* **2011**, *40*, 3584-3591.
[148] Ö. Metin, V. Mazumder, S. Özkar and S. Sun, *Journal of the American Chemical Society* **2010**, *132*, 1468-1469.
[149] D. Sun, V. Mazumder, Ö. Metin and S. Sun, *ACS Nano* **2011**, *5*, 6458-6464.
[150] G. Pyrgiotakis and W. M. Sigmund in *Raman Spectroscopy of Anatase Coated Carbon Nanotubes*, *Vol.* John Wiley & Sons, Inc., **2009**, pp. 197-208.
[151] M. E. Franke, T. J. Koplin and U. Simon, *Small* **2006**, *2*, 36-50.
[152] D. C. Look, J. W. Hemsky and J. R. Sizelove, *Physical Review Letters* **1999**, *82*, 2552-2555.

[153] J. T. Robinson, F. K. Perkins, E. S. Snow, Z. Wei and P. E. Sheehan, *Nano Letters* **2008**, *8*, 3137-3140.
[154] G. Eda, C. Mattevi, H. Yamaguchi, H. Kim and M. Chhowalla, *The Journal of Physical Chemistry C* **2009**, *113*, 15768-15771.
[155] J. D. Fowler, M. J. Allen, V. C. Tung, Y. Yang, R. B. Kaner and B. H. Weiller, *ACS Nano* **2009**, *3*, 301-306.
[156] J. S. Lee, K. H. You and C. B. Park, *Advanced Materials* **2012**, *24*, 1084-1088.
[157] S. Mao, K. Yu, S. Cui, Z. Bo, G. Lu and J. Chen, *Nanoscale* **2011**, *3*, 2849-2853.
[158] H.-B. Zhang, J.-W. Wang, Q. Yan, W.-G. Zheng, C. Chen and Z.-Z. Yu, *Journal of Materials Chemistry* **2011**, *21*, 5392-5397.
[159] Ö. Metin, S. Özkar and S. Sun, *Nano Research* **2010**, *3*, 676-684.
[160] B. Nikoobakht and M. A. El-Sayed, *Chemistry of Materials* **2003**, *15*, 1957-1962.
[161] E. Dulkeith in *Optische Charakterisierung von Hybridsystemen aus Gold Nanopartikeln und Farbstoffmolekülen*, *Vol.* **2004**.
[162] D. R. Dreyer, S. Park, C. W. Bielawski and R. S. Ruoff, *Chemical Society Reviews* **2010**, *39*, 228-240.

Curriculum Vitae

Personal Information

Name: Emine Kayhan

Date of Birth: June 8, 1984

Marital Status: Married with one daughter

Adress: Orhaniye Mah. Yagci Ibrahim Sok. No: 7 16400 Inegol-Bursa/TURKEY

Work experience

2006 – 2007	Senior Study at Chemistry Department, Bilkent University, Ankara/Turkey
2005 – 2006 Summer	Internship at Silvio O. Conte National Center for Polymer Research, University of Massachusetts, Amherst/US
2005 – 2006 Mid-Break	Internship in Chemistry Department, Erciyes University, Kayseri/Turkey
2004 – 2005 Summer	Internship in Natural Science Department, Sabanci University, Istanbul/Turkey
2004 – 2005 Summer	Internship in Chemistry Department, Bilkent University, Ankara/Turkey

Education

08/2013 – till date: Doktor rerum naturalium (Dr. rer. nat.)

"Graphene: Synthesis, Characterization,
Properties and Functional Behavior as Catalyst Support and Gas Sensor"
Technische Universität Darmstadt, Darmstadt Germany

2007 – 2009	Master of Science in Chemistry Department, Bilkent University, Ankara/Turkey "Structure and NO_x Uptake Properties of Fe-Ba/Al_2O_3 As a Model NO_x Storage Material"
2002 – 2007	Bachelor of Science in Chemistry Department, Bilkent University, Ankara/Turkey
1998 – 2002	Samsun Milli Piyango Anatolian High School, Samsun/Turkey
1995 – 1998	Afyon Kocatepe Anatolian High School, Afyon/Turkey
1990-1995	Afyon Ataturk Primary School, Afyon/Turkey

Emine Kayhan
Kaupstrasse 47
64289, Darmstadt

03/06/2013

Eidesstattliche Erklärung

Ich erkläre hiermit an Eides Statt, dass ich meine Dissertation selbständig und nur mit den angegebenen Hilfsmitteln angefertigt habe.

Emine Kayhan

Emine Kayhan
Kaupstrasse 47
64289, Darmstadt

03/06/2013

Erklärung

Ich erkläre hiermit, noch keinen Promotionsversuch unternommen zu haben.

Emine Kayhan